Six-Dimensional Quantum Dynamics of Dissociative Chemisorption of Hydrogen on Metal Surfaces

Somers, M.F.

Citation

Somers, M. F. (2004, March 31). *Six-Dimensional Quantum Dynamics of Dissociative Chemisorption of Hydrogen on Metal Surfaces*. Retrieved from https://hdl.handle.net/1887/3250648

Six-Dimensional Quantum Dynamics of Dissociative Chemisorption of Hydrogen on Metal Surfaces

PROEFSCHRIFT

ter verkijging van

de graad van Doctor aan de Universiteit Leiden,

op gezag van de Rector Magnificus dr. D. D. Breimer,

hoogleraar in de faculteit der Wiskunde en

Natuurwetenschappen en die der Geneeskunde,

volgens besluit van het College voor Promoties

te verdedigen op woensdag 31 maart 2004

klokke 16:15 uur

door

Mark Frans Somers

geboren te Heerlen in 1975

Promotiecommissie:

Promotor: Prof. dr. G.J. Kroes

Referent: Dr. D. Lemoine   (CNRS, Toulouse)

Overige leden: Prof. dr. A.W. Kleyn
                   Prof. dr. J. Reedijk
                   Dr. M.C. van Hemert
                   Prof. dr. E.J. Baerends   (Vrije Universiteit Amsterdam)
                   Dr. D.A. McCormack   (Vrije Universiteit Amsterdam)

Ondanks dat het onderzoek beschreven in dit proefschrift veel tijd heeft gekost en er voor heeft gezorgd dat ik ruim vier jaar lang achter een computer heb doorgebracht, heeft mijn gevoel voor humor daar niet onder geleden. Ik kan dus ook niets anders zeggen dan:

"Je kunt niet op alle computers rekenen!"

Mark Somers.

Contents

Chapter 1

Introduction

1.1. Molecule-surface reactions

In everyday life, we all encounter molecule-surface interactions. Whether it is in cleaning a window, writing on a piece of paper or glueing two parts together, a clear interaction of the dirt, the ink or the glue molecules is present with the surface. Not only molecules interact with surfaces. Light, for example, also shows a clear interaction with surfaces in everyday life, for instance when one observes a mountain scenery through a pair of binoculars. Not only does the sunlight scatter from the mountain towards the binoculars, the light is also focused and scattered by the lenses in the binoculars, the end result being a more detailed picture of the mountain and the mountaineer trying to reach the top of the mountain. Ironically, by using the interactions of the sunlight with the various surfaces, looking at the mountaineer and the way he overcomes gravity by using the friction between his equipment and the mountain itself, again presents a clear example of interactions of molecules with surfaces.

Focusing more on molecules and surfaces, besides interactions of molecules with surfaces that might cause the molecules to stick on the surface thereby causing friction, molecule-surface interactions can also lead to reactions. The molecule, being composed of atoms connected by bonds, might break some of its bonds and form new bonds, either with atoms of another surface absorbed molecule or with the surface itself. A nice example we all know about that shows that reactions do take place in presence of a surface is the corrosion of a coin. Clearly, the oxygen molecules in the air interact with

the metal surface atoms, bonds are broken and new bonds are formed, changing the appearance of the coin by leaving a layer of oxidised material on the metal.

In the fields of Chemistry and Physics, reactions of molecules on surfaces are of particular interest. Not only does research from a physical or chemical perspective lead to a better understanding of the fundamentals of molecule surface reactions, it has also lead to numerous applications. For instance, think about the exhaust gasses from a car engine. Some of the gasses, expelled directly from the engine (CO and NO_x), are known to be harmful to the environment and by making use of a car catalyst, these gasses are converted into a less harmful exhaust mixture before being ejected into the air. The harmful gasses from the engine are reactive and would eventually convert to less harmful gasses but at the same time lead to environmental problems. The metal particles in the car catalyst enable the harmful molecules to react with each other and oxygen before they are able to affect nature. Here, the surface atoms of the metal particles participate in the conversion reaction by making sure the reactions occur within the time scale of the harmful gasses reaching and leaving the catalyst (i.e. before ejection into the air). However, in the process of conversion, the metal particles in the car catalyst do not deplete. In Chemistry this is known as catalysis and the catalyst evidently has lowered the large energetic barriers of the conversion reaction to such a level that these reactions take place on a fast enough time scale. In industry, a large number of applications are found of catalysis. For instance in the production of NH_3 ruthenium and iron are used to catalyse the hydrogenation of nitrogen. In another example of a catalytic process, dehydrogenation, in which an H atom is effectively extracted from a molecule, occurs in for example the upgrading of the octane rating of gasoline.

Research on molecule-surface reactions has revealed several reaction mechanisms. For instance, on a surface atoms or molecules can react with one another through the Langmuir-Hinshelwood (LH) mechanism, the Eley-Rideal (ER) mechanism and the Hot-Atom (HA) or Harris-Kasemo mechanism. In the Langmuir-Hinshelwood mechanism (Figure 1.1A), the most common mechanism of the three, two atoms or molecules are adsorbed on the surface and fully equilibrated. When they meet, they react. In the Eley-

Rideal mechanism (Figure 1.1B), one of the reactants is adsorbed on the surface and the other collides with it coming from the gas phase, upon which reaction is immediate. In the intermediate mechanism, the Hot-Atom mechanism (Figure 1.1C), the reaction takes place between an equilibrated reactant and a reactant which has not fully equilibrated yet, but has recently arrived from the gas phase and has completed a few bounces on the surface.
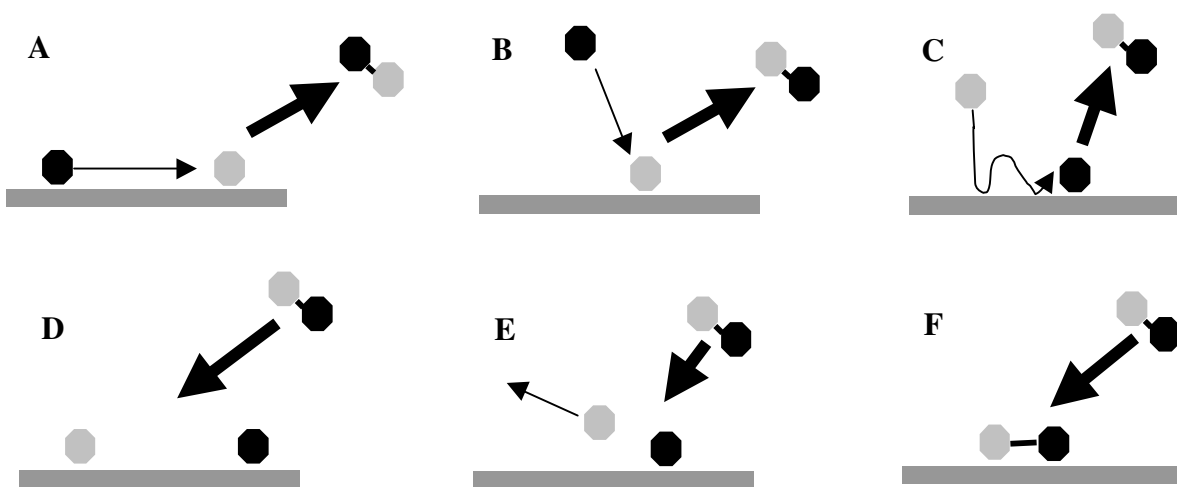
Figure 1.1: A) The Langmuir-Hinshelwood mechanism, **B)** the Eley-Rideal mechanism and **C)** the Hot-Atom mechanism for molecule-surface reactions. **D)** the dissociative chemisorption mechanism, **E)** the abstraction mechanism and **F)** the molecule-surface adsorption mechanisms.

In all of the three reaction-mechanisms described above, at least one of the reactants, whether it is a molecule or a single atom, is already adsorbed on the surface. The process of adsorption of molecules or atoms on surfaces, which must precede these reactions, is one of the key steps in molecule-surface reactions. The adsorption of a molecule or atom can also take place through several mechanisms. The molecule might break apart into two fragments which both form chemical bonds to the surface. This is called dissociative chemisorption (Figure 1.1D) and can be regarded to be the reverse of the Langmuir-Hinshelwood reaction mechanism followed by desorption (this is called associative desorption, see Figure 1.1A). The molecule may also break into two with one fragment

remaining on the surface and one escaping to the gas phase. This is called abstraction (Figure 1.1E) and can be identified as the reverse of the Eley-Rideal reaction mechanism (Figure 1.1B). Finally, a molecule might get adsorbed on the surface, either by chemisorption or physisorption, depending on the strength of the molecule-surface bond, and remain intact (Figure 1.1F). The dissociative adsorption process (Figure 1.1D) is particularly interesting because it is relevant to a number of industrial applications. It is a fundamental step in corrosion and hydrogen storage in metals and can be the rate-limiting step of an overall reaction in the field of heterogeneous catalysis (for instance the dissociation of N_2 in the production of NH_3[1]).

1.2. Hydrogen scattering from metal surfaces

As was explained above, the first step in understanding reactions between molecules on surfaces is to study the adsorption process. Such a study begins with the investigation of how a relative simple molecule like hydrogen scatters from and can get adsorbed on a clean and structured metal surface. Such investigations form the fundamental basis in the understanding of molecule-surface reactions and catalysis.

The hydrogen-metal surface system serves as an ideal model system for reactive scattering. There are two reasons for this. First, theoretical[2] and experimental[3,4] work on activated dissociation has shown that the movement of the metal surface atoms does not affect the reaction in a major way, and that the effect of the surface temperature on reaction can be easily modelled[5]. Second, it is reasonable to assume that electron-hole pair excitations can be neglected, so that the dissociation process is governed by the lowest adiabatic potential energy surface. These two approximations (freezing the surface atoms and applying the Born-Oppenheimer approximation with the use of the ground state potential energy surface (PES)) make a full quantum dynamical treatment of the reactive scattering process feasible[6]. This allows for a fundamental study of the adsorption of molecules on surfaces and at the same time opens up the possibility to test

current state of the art density functional theory (DFT) by comparing scattering probabilities calculated using DFT PESs to experimental results[6].

1.2.1. Hydrogen in the gas phase

When hydrogen is located far away from a metal surface, the molecule is considered to be in the gas phase and quantum mechanics is needed to fully understand the characteristics of the molecule. In a quantum mechanical picture of hydrogen, the molecule can be in several electronic states of which one is the electronically bound ground state $X^1\Sigma_g^+$ and the other is the first excited anti-bonding state $^3\Sigma_u^+$. In molecular-orbital theory these states correspond to the $1\sigma_g^2$ ($X^1\Sigma_g^+$) and the $1\sigma_g1\sigma_u$ ($^3\Sigma_u^+$) configurations respectively. The $1\sigma_g$ and the $1\sigma_u$ are often referred to as σ and σ^*, respectively.

The formation of the $1\sigma_g$ and $1\sigma_u$ single-electron molecular orbitals can be understood from Figure 1.2A. When two hydrogen atoms approach each other, the two 1s atomic ground state wave functions will start to show overlap and, as can be understood from perturbation theory, the single-electron molecular orbitals $1\sigma_g$ and $1\sigma_u$ are formed. As a consequence, the closer the two hydrogen atoms get, the more bound the $X^1\Sigma_g^+$ state becomes and the more the electronic energy is lowered. However, if the two atoms approach each other too much, the Coulomb repulsion between the two nuclei starts to dominate and the $X^1\Sigma_g^+$ state's electronic energy will again increase. Shown in Figure 1.2B are the two electronic energy levels of the hydrogen molecule as a function of the distance between the atoms, r.

A   **B**
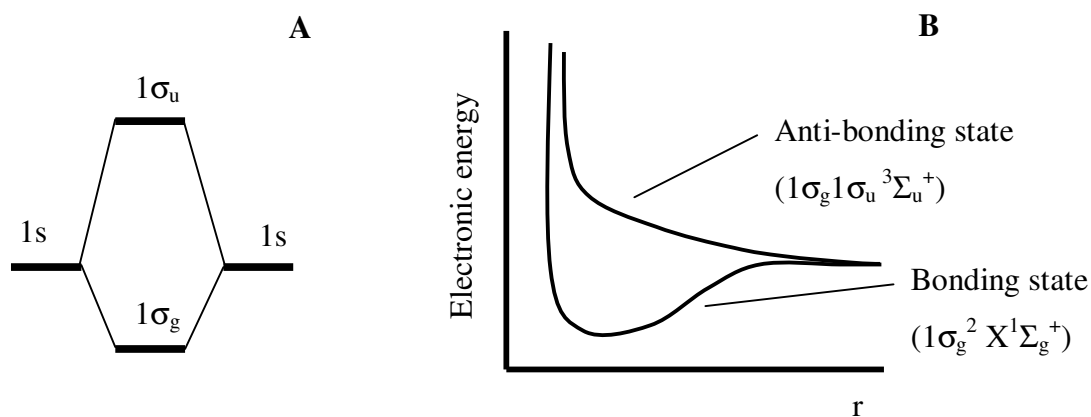
Figure 1.2: A) The overlap of the two approaching 1s atomic hydrogen wave functions causes the formation of the $1\sigma_g$ and $1\sigma_u$ single-electron molecular orbitals. **B)** The formation of the bonding ($1\sigma_g^2 \ X^1\Sigma_g^+$) and anti-bonding ($1\sigma_g1\sigma_u \ ^3\Sigma_u^+$) electronic ground states of H_2 when the distance between the two hydrogen atoms (r) is varied.

So far only the electronic states of the hydrogen molecule have been considered. The movement of the two nuclei should also be described by quantum mechanics and within the Born-Oppenheimer approximation, the motion of the two electrons can be separated from the motion of the two nuclei. The two nuclei can then be considered to move in a force field derived from the potential energy curve or surface (PES) that corresponds to the electronically bound ground state ($1\sigma_g^2 \ X^1\Sigma_g^+$). Moreover, the molecular wave function can be taken as a product of the electronic ground state wave function and a nuclear wave function. The rules of quantum mechanics dictate that for such a bound PES, quantisation occurs in the inter-nuclear distance co-ordinate (r). The molecule can be in a specific vibrational state, specified by the quantum number v, and will have a fixed amount of vibrational energy. The nuclear part of the full molecular wave function in the Born-Oppenheimer approximation should therefore be labelled with v.

The vibrational motion, being quantised, is only one of the six degrees of freedom needed to fully describe the movement of the two nuclei. In the gas phase, the hydrogen molecule can also rotate and the quantum mechanical treatment of the rotation also leads to quantisation with two quantum numbers (j, m_j) associated with the rotational motion.
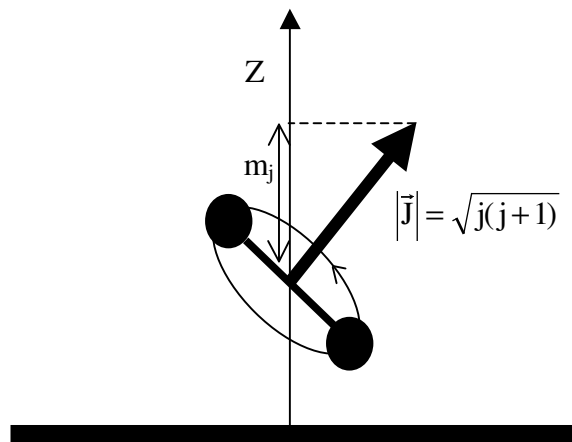
Figure 1.3: Shown is the rotating hydrogen molecule with the angular momentum vector $\vec{J}$, with the length being specified by the rotational quantum number j. The projection of $\vec{J}$ onto an arbitrary Z axis, m_j, the rotational magnetic quantum number, is also shown. When considering a molecule interacting with a surface, the Z axis is usually chosen to be the surface normal.

In Figure 1.3 the rotating hydrogen molecule is shown together with the angular momentum vector $\vec{J}$ and its projection m_j onto an arbitrary Z axis. $\vec{J}$ is oriented perpendicular to the plane of rotation and has a length, in atomic units, equal to $\sqrt{j(j+1)}$. Here, j is called the rotational or angular momentum quantum number and can take on any positive integer value. The kinetic energy associated with the rotational motion is given by $\left|\vec{J}\right|^2/(2\mu r^2)$ in which r is the inter-nuclear distance and μ is the reduced mass of the hydrogen molecule. The projection of $\vec{J}$, m_j, the rotational magnetic quantum number, can take on any integer value between -j and j, for a given j quantum number. In total, for a given j value, there are 2j+1 different m_j states for the nuclear wave function that are degenerate.

The vibrational and rotational motions of the hydrogen molecule account for three of the six degrees of freedom. In the gas phase, the molecule not only vibrates and rotates, it also moves translationally in three directions. The molecule has translational kinetic energy associated with it. The application of quantum mechanics to the translational

degrees of freedom does not lead to quantisation if the molecule is situated in the gas phase. The nuclear wave function will therefore have a plane-wave contribution to describe the translational motion in these remaining degrees of freedom. Therefore, to fully specify the nuclear wave function of the hydrogen molecule in the gas phase, taken the Born-Oppenheimer approximation and neglecting the spins of the protons, three quantum numbers (v, j, m_j) and a momentum vector (k_0^X, k_0^Y, k_0^Z) are needed.

1.2.2. Hydrogen approaching a metal surface

When the hydrogen molecule, situated in the gas phase, has translational energy towards the metal surface, it will eventually interact with the metal surface. Several things can then happen to the molecule and the surface:

-        Elastic and inelastic scattering.
-        Diffraction.
-        Dissociative chemisorption and physisorption.
-        Energy transfer to phonons and electron-hole pair excitations.

These possibilities will now be discussed.

Elastic and inelastic scattering

When the total energy, the sum of the vibrational, rotational and translational energy, of the hydrogen molecule in the gas phase is too small to overcome any barrier to reaction, the molecule can bounce back into the gas phase. This process is called *scattering* and two cases can be distinguished: (i) the scattering takes place without energy exchange, and (ii) the scattering takes place while energy is exchanged among some of the degrees

of freedom of the system. The former process is called *elastic scattering* (Figure 1.4A), while the latter is called *inelastic scattering*.
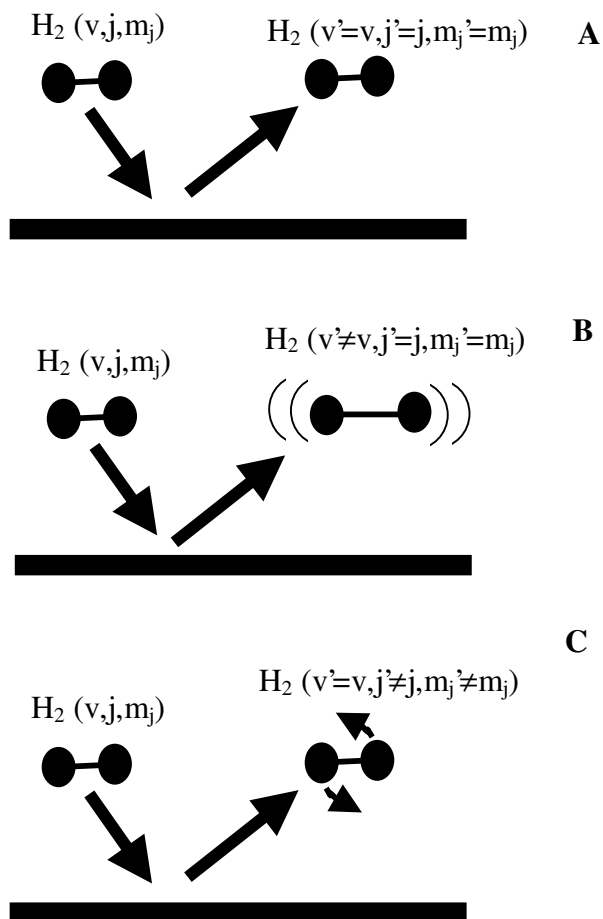
Figure 1.4: A) Elastic scattering, **B)** vibrationally inelastic scattering and **C)** rotationally inelastic scattering of H_2 from a surface. Here, (v,j,m_j) specifies the initial state of the hydrogen molecule and (v',j',m_j') the final state after the scattering event.

When the atoms of the metal surface are taken to be fixed at their ideal lattice positions, energy can only be redistributed among the hydrogen degrees of freedom. The inelastic scattering events can therefore be subdivided into *vibrationally inelastic scattering* (Figure 1.4B) and *rotationally inelastic scattering* (Figure 1.4C). Because of the quantisation of the rotational and vibrational motions of the hydrogen molecule, the

energy transfer is only allowed if at least a full quantum is exchanged. The translational motion is not quantised and can therefore exchange any amount of energy with other degrees of freedom. Energy transfer involving the translational degrees of freedom corresponding to the motion parallel to the surface may also be called (diffractive) inelastic scattering and will be the subject of the next section. For rotationally inelastic scattering to occur, the molecule-surface potential should be anisotropic, and for vibrationally inelastic scattering to occur, the molecule-surface potential should show a curvature in the reaction path in front of the barrier to reaction[7-10].

In molecule-surface collisions, rotationally inelastic scattering was first proposed as a possibility in the mid 1930s by Jackson and Howarth[11] and experimental confirmation was obtained forty years later for H_2 scattering from LiF(001)[12,13] and HD scattering from MgO(001)[14,15]. The vibrational inelastic scattering process was first confirmed in experiments for NO scattering from Ag(111)[16] and NH_3 from Au(111)[17]. For H_2 scattering from Cu(111) very efficient virbational inelastic scattering has been observed[18,19].

Diffraction

When the metal surface is considered to be flat, the translational degrees of freedom corresponding to motion parallel to the surface are not coupled to any of the other degrees of freedom and the energy of motion parallel to the surface will be conserved. If, however, the metal surface has periodicity (with a few surface atoms grouped into a surface unit cell, which is repeated infinitely (Figure 1.5)), the molecule-surface interaction potential should exhibit the same periodicity. The translation of the molecule into the same configuration within another surface unit cell does not change the interaction with the surface and Bloch's theorem[20-22] then states that the wave function for motion in the degrees of freedom that show periodicity should also be periodic, to within a phase factor.

As a result of Bloch's theorem and the restriction that the wave function be periodic in the degrees of freedom for translation parallel to the surface, the parallel momentum of the molecule can only change an integer times a diffraction quantum. Given the X and Y degrees of freedom that show the periodicity, the final parallel momentum of the molecule, with initial parallel momentum (k_x, k_y), can be written as $(k_x+n\Delta k, k_y+m\Delta k)$. Here, $\Delta k = 2\pi/L$ is the diffraction quantum for a square shaped surface unit cell defined by the lengths $(L_x=L_y=L)$ and (n,m) correspond to the diffraction quantum numbers. The latter label the diffraction channel (Figure 1.5). For a non-square shaped surface unit cell, the final momentum is given by $(k_x+n\Delta k_x, k_y+m\Delta k_y)$, with $\Delta k_x=2\pi/L_x$ and $\Delta k_y=2\pi/L_y$.
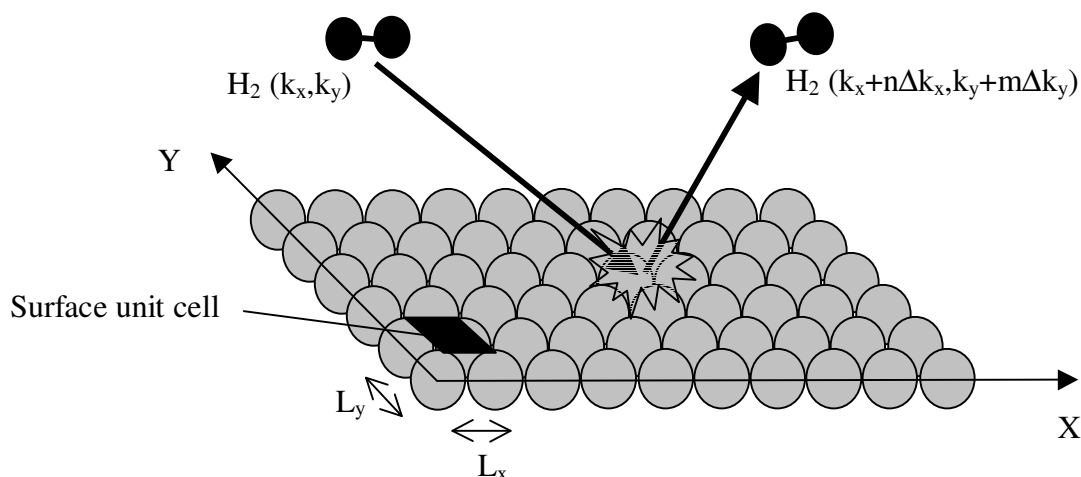
Figure 1.5: Shown is the surface unit cell and the diffraction process. The hydrogen molecule with initial parallel momentum (k_x, k_y) can have a final parallel momentum of $(k_x+n\Delta k_x, k_y+m\Delta k_y)$ due to the periodicity in X and Y, the two translational degrees of freedom of H_2 for motion parallel to the surface. Here, n and m are the diffraction quantum numbers and $\Delta k_x=2\pi/L_x$, $\Delta k_y=2\pi/L_y$ are the diffraction quanta, L_x and L_y being the lengths of the surface unit cell.

This purely quantum mechanical phenomenon is called *molecular diffraction* and was first observed in 1930 by Estermann and Stern[23] in experiments on scattering of H_2 and He from a LiF surface. Their experiments confirmed the wave nature of atoms and small molecules. It can be regarded as a beautiful example of the matter-wave duality, which touches the very heart of quantum mechanics.

Dissociative chemisorption and physisorption

Apart from the hydrogen molecule scattering and diffracting from a metal surface, it can also dissociate if enough energy is available to overcome the barrier to reaction. The H-H bond is broken and new bonds between the hydrogen atoms and the surface atoms are formed (Figure 1.1D). To understand how transition metals like Pt, Cu and Pd can lead to dissociation of the hydrogen molecule, the same Molecular Orbital (MO) concepts used to understand the formation of H_2 from two hydrogen atoms can be used[24,25].
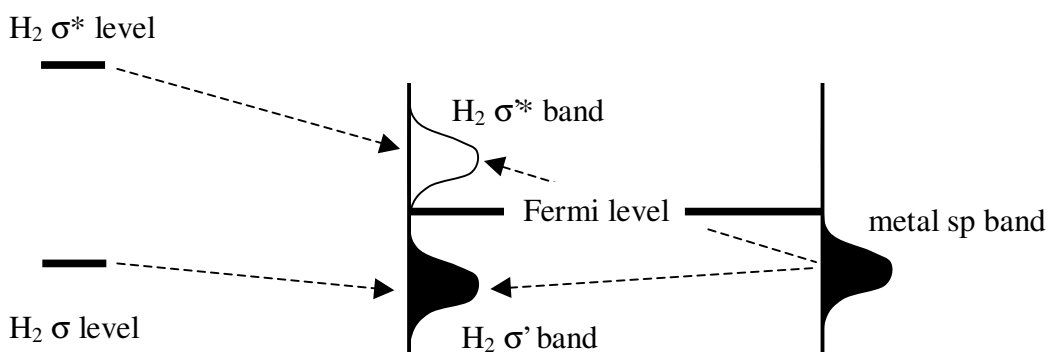
Figure 1.6: The electrostatic interaction of the hydrogen bonding (σ) and anti-bonding levels (σ*) with the metals sp band leads to a broadened but filled bonding (σ') and a broadened empty anti-bonding (σ'*) molecule-surface band. The H_2 molecule will be weakly adsorbed on the surface without being dissociated.

When H_2 approaches the surface, both the bonding (σ) and the anti-bonding (σ*) electronic levels of H_2 will start to interact with the metal s and p bands. The effect of the interaction is that both the σ ($1\sigma_g$) and the σ* ($1\sigma_u$) levels of H_2 will shift down and broaden into a bonding (σ') and an anti-bonding (σ'*) H_2 band. The anti-bonding level of H_2 will shift down the most[24,25] (Figure 1.6). The bonding band will be located below the Fermi level whereas the anti-bonding band will be located above the Fermi level. If a metal, for example Al, has an empty d band, only the H_2 bonding band will be filled and the molecule will be weakly bound to the surface without being dissociated. This results

in what is called *weak chemisorption* and a considerable barrier to dissociation is expected to be present for such a system[24,25]. If however the downshift of the bonding hydrogen level is considerably less or the Fermi level is located within the bonding H_2 band, the molecule will be even more weakly bound to the metal. In this case, the H_2 molecule can still be *physisorbed* to the surface[26]. Typical physisorption (or van der Waals interaction) energies of H_2 interacting with a metal surface are a few tenths of an eV: 31 meV for $H_2+Cu(100)$[27] and 55 meV for $H_2+Pt(111)$[28].

For the transition metals that do have d electrons, the interaction of the H_2 bonding (σ') and anti-bonding (σ'*) bands with the metal d band has to be included in the description[24,25]. A considerable amount of overlap between the metal d band and the H_2 σ' and σ'* bands is to be expected because of the valence nature of the d electrons for transition metals. The overlap will result into a further splitting of both the H_2 σ' and the σ'* bands.
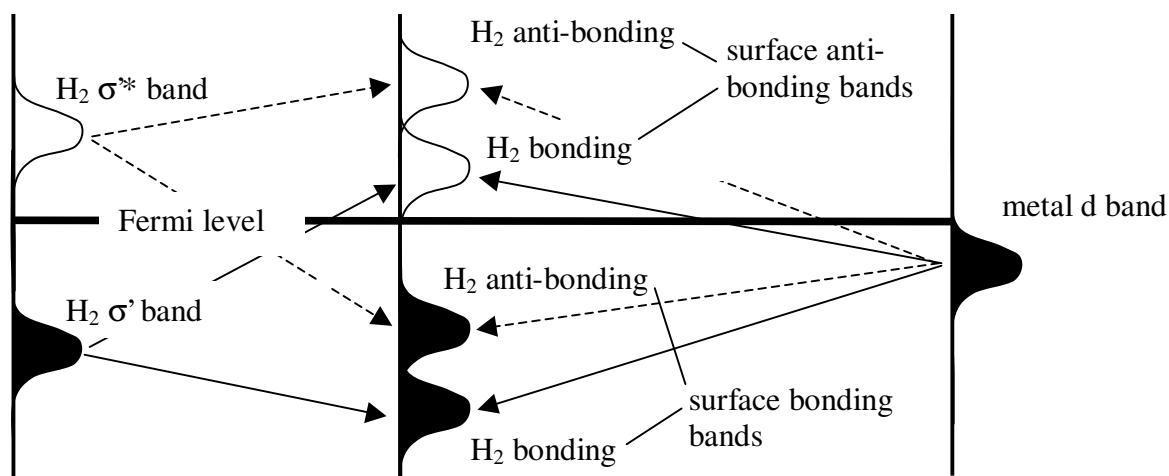
Figure 1.7: The H_2 bonding (σ') and anti-bonding (σ'*) bands are split into four bands if the interaction with the transition metal d band is taken into account. If the Fermi level is above the H_2 anti-bonding - surface bonding band, as is shown here, the molecule can end up dissociated with the hydrogen atoms chemically bound to the surface (dissociative chemisorption).

As is shown in Figure 1.7, four bands are formed that can be divided into two groups: one with two bands of surface bonding character and the other with two bands of surface anti-bonding character. The two bands of each group can be further divided into one of the bands with H_2 bonding character and another with H_2 anti-bonding character. Depending on the coupling strength of the metal d band with the two H_2 bands and the location of the Fermi level, the hydrogen molecule can dissociate with chemical bonds being formed between the H atoms and the surface. The coupling strength of the metal d band with the hydrogen bonding and anti-bonding bands highly depends on how close H_2 is located to the surface and as the molecule approaches the surface, the H_2 anti-bonding - surface bonding band gradually gets filled. This possibility is shown in Figure 1.7 and can lead to *dissociative chemisorption.*

In 1995 Hammer *et al.*[24,25] showed that this picture of hydrogen interacting with metal surfaces can be translated into an approximate quantitative measure explaining the reactivity of transition metals and to which extent the metal d band hybridisation correlates with the barrier height for reaction. More specifically, because the 5d band of Pt(111) is more extended than the 3d band of Cu(111), the coupling matrix element responsible for the splitting is larger for the Pt(111) case causing the H_2 anti-bonding - surface bonding band to be located mostly below the Fermi level and thus to be mostly filled. This results in a lower barrier for reaction of H_2 on Pt(111) than for H_2 on Cu(111). In Figure 1.8, a barrier to dissociative chemisorption is shown by plotting the potential energy surface for the H_2 approaching the Cu(100) surface, as a function of the H-H bond length (r) and the H_2 centre-off-mass distance from the surface (Z). The barrier is indicated with the "**x**". If the molecule has enough energy, the barrier can be crossed and H_2 will end-up dissociated and the atoms bound to the surface.
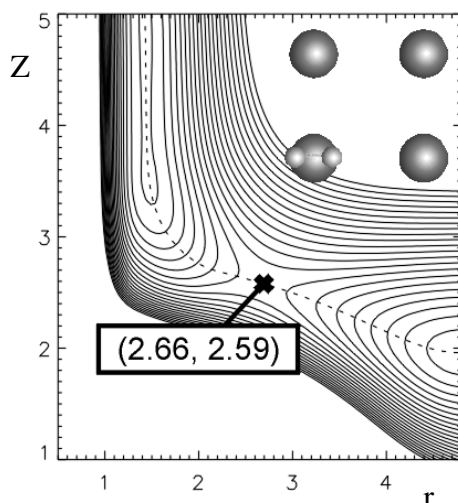
Figure 1.8: The H_2 + Cu(100) interaction potential as a function of Z, the H_2-surface distance and r, the H-H bond distance. All distances are in atomic units (a_0). The barrier to dissociation on top of a Cu atom is indicated with the "**x**". The contours indicate areas of the PES where the potential is increased by 0.1 eV.

Energy transfer to phonons and electron-hole pair excitations

The theory discussed so far was based on H_2 scattering from a static metal surface within the Born-Oppenheimer approximation. The use of a static surface excludes the possibility that the molecule can exchange energy with the surface lattice vibrations during the scattering event. Using the Born-Oppenheimer approximation corresponds to neglecting the possibility of electron-hole pair excitations. In this section, these two approximations are considered in more detail.

Negelect of phonons

If the restriction of freezing the surface atoms is removed, energy exchange with the surface vibrations (phonons) can occur in the scattering event. Recent experiments on rotationally inelastic scattering of H_2 from Pd(111)[29] and Cu(100)[30] showed that a substantial amount of energy can be exchanged with the phonons and that their neglect is,

under some conditions, questionable in the calculation of scattering probabilities. However, the effects of neglecting phonons in the calculation of reaction probabilities are assumed to be less dramatic.

The question of whether the phonons influence the reaction probability has two aspects to it. The first aspect is which influence the presence of phonons has on the computed reaction probability at 0 K. The second aspect is the effect that the phonons have on the reaction probability at elevated surface temperatures. Dohle and Saalfrank[2] have addressed the first question by modelling the phonons as an Einstein oscillator that was coupled to the molecular degrees of freedom in the dissociation of H_2 on copper. They found that the inclusion of phonons in the dynamical model leads to a shift of the reaction probability curve with 0.02 eV. In which direction the shift was, depended on the specific model they used for the molecule-surface interaction. From this it can be concluded that the effects of including phonons in the calculation of reaction probabilities at 0 K is negligible (the 0.02 eV shift is well within the estimated accuracy of the PES based on a DFT/GGA/slab approach[31,32]).

The effects the surface temperature has on the reaction probability can be assessed from experiments on D_2 and H_2 desorbing from Cu(111)[3,4]. These experiments showed that the surface temperature predominantly has a broadening effect on the reaction probability curves for all but the lowest desorption energies. The dynamical barrier height (the energy at which the reaction probability reaches half its asymptotic value) was found not to depend on the surface temperature. Taken together with the previous findings concerning the introduction of phonons at 0K, this suggests that the use of a static surface in a theoretical calculation allows one to determine the dynamical barrier height to reaction to within a few hundredths of an eV, well within the estimated accuracy of a DFT based PES (0.1 to 0.2 eV)[31,32]). The influence of the surface temperature on the reaction probability for non-activated systems (H_2+Pd(100) for example) is expected to be even less because these systems tend to show large reaction probabilities. It is therefore concluded that the neglect of phonons does not pose a serious problem, especially if the goal is to compute reaction probabilities.

Electron-hole pair excitations

Extending the theory beyond the Born-Oppenheimer approximation, while retaining the six molecular degrees of freedom of the hydrogen molecule, is a task not possible yet, for several reasons. First of all, conventional DFT cannot be used anymore, it only allows for the calculation of the ground state PES and other *ab initio* methods have difficulties with slabs or larger clusters of transition metals. The number of electrons in such H_2 -transition metal surface systems is far too large to map out a reasonable PES describing all the important configurations of H_2 dissociation on the metal surface. From the dynamical point of view, going beyond the Born-Oppenheimer approximation entails the use of matrix elements of the electronic wave functions with the Laplacian associated with the nuclear degrees of freedom. These integrals are hard to evaluate, especially if six nuclear degrees of freedom are present, even if the electronic wave functions are known accurately. Theoretical studies, both quantum dynamical and classical, on H_2 dissociating on Cu(100)[33-37] have already shown that all six molecular degrees of freedom are of importance and therefore, at the moment, the Born-Oppenheimer approximation is a necessity. At present it is only possible to estimate the possible errors the neglect of electron-hole pair excitations introduces into the theoretical treatment of H_2 dissociating on metal surfaces.

Recent experiments on atomic and molecular chemisorption[38] found that the probability of excitation of an electron-hole pair decreases with decreasing adsorption energy. The experimentalists estimated an excitation probability of only 6% for an adsorption energy of 0.2 eV. For these findings, one would not expect the reaction to be affected dramatically for low barrier systems like H_2+Pt(111). One would also suspect that the effects are small for medium barrier systems like H_2+Cu(100). From the theoretical point of view, Darling and Holloway[39] argued that the problem of whether electron-hole pairs may have an important effect on the reaction is, at present, unresolved. As is noted by Darling and Holloway, the models employed to treat electron-hole pair excitations have been approximate and the conclusions are hard to evaluate. Moreover, recent six-dimensional quantum dynamical studies on H_2 reacting on Pd(100) and Cu(100), which

employed the Born-Oppenheimer approximation, showed that, in comparison to molecular beam experiments, a good quantitative agreement can be obtained for dissociative chemisorption probabilities[40]. This leads us to conclude that, considering the computation of reaction probabilities, the neglect of electron-hole pair excitations in the model is justified.

1.3. Scope and aim of the thesis

The aim of this thesis was twofold. On the one hand knowledge is wanted on how molecules like H_2, D_2 and HD react on and scatter from transition metal surfaces like Cu(100), Cu(111) and Pt(111). To this end six dimensional quantum wave packet calculations have been performed on H_2 scattering from Cu(100), H_2 and D_2 scattering from Cu(111) and HD scattering from Pt(111). With studies like these, the quality of DFT in describing the molecule-surface interaction is assessed by directly comparing calculated probabilities to experiments. At the same time, explanations are sought for trends observed in experiments on the reaction and scattering of hydrogen from transition metal surfaces, by unravelling the mechanisms found in the dynamical calculations. Moreover, to push the ball even more forwards, trends on the reaction of hydrogen on these surfaces are predicted that reveal important features of the reaction mechanism and which will hopefully be confirmed in experiments yet to be done.

The calculations on Cu(100), a surface with a square shaped unit cell, were performed using a symmetry adapted wave packet (SAWP) method, whereas the calculations on the hexagonal shaped surface unit cells of Pt(111) and Cu(111) were performed using a pseudo-spectral (PS) method, based on the Gauss-Legendre transforms of Lemoine *et al*[41-43]. The pseudo-spectral methods, in general, show better computational scaling but do not make use of the symmetry of the square unit cell. The use of symmetry makes the SAWP method a very efficient method for appropriately fitted PESs, but not for PESs of general form. The second goal of the thesis was therefore to develop a new symmetry

adapted pseudo-spectral (SAPS) wave packet method that combines the advantageous computational scaling of pseudo-spectral methods with those of using the symmetry of square shaped surface unit cells, for the scattering of normally incident diatomic molecules, and employing a general PES.

In **Chapter 2** the general quantum dynamical theory of molecule-surface scattering is presented, based on the time dependent wave packet technique. Also presented is a general introduction to DFT and the fitting methods used to obtain the various PESs employed in the remaining chapters of this thesis.

In **Chapter 3** the reaction of H_2 on Cu(100) is studied using the SAWP method for a range of initial rotational levels (j=0-5) for both the vibrational ground (v=0) state and first excited (v=1) state of H_2. To this end, a PES, in this thesis referred to as PES 4, is used that was fitted to a limited number of symmetry adapted basis functions. This specific fit form of the PES is a restriction of the SAWP method. Previous studies of this system had revealed that (v=0,j=0/4) initial H_2 prefers to react at the bridge site whereas (v=1,j=0/4) prefers to react at the top site for low incidence energies[44-46]. At the same time, it was shown that the rotational quadrupole alignment of the molecules that react was higher for (v=1,j=4) H_2 than for (v=0,j=4) H_2. This was explained by orientational and rotational hindering mechanisms that play a role in the reaction on both sites and it was predicted that the difference in the rotational quadrupole alignment could be used by experimentalists to measure, in an indirect way, where H_2 prefers to react on the surface. The question addressed here is whether the difference in the preferred reaction site between initially (v=0) and (v=1) H_2 previously found for (j=0) and (j=4) is general for low j (j=0-5). We have also investigated whether the experimental signature of the difference in the reaction site (the higher rotational quadrupole alignment of reacting (v=1) H_2) is general for low j (j=0-5). Another aim was to derive an additional experimental signature for the difference between the preferred reaction sites of initial (v=0) and (v=1) H_2.

In **Chapter 4** the newly developed symmetry adapted pseudo-spectral (SAPS) wave packet method is introduced and applied to the scattering and reaction of H_2 on Cu(100). The aim of this study was to combine the better computational scaling laws of the pseudo-spectral (PS) methods with the symmetry techniques that have been used in the SAWP method. The SAWP method only allows for efficient wave packet calculations, for normal incident diatomic molecules scattering from square surfaces, if the six-dimensional PES is fitted to a limited number of symmetry adapted basis functions. With the new SAPS method, which is based on the non-direct product Gauss-Legendre transforms of Lemoine *et al.*[41-43] and the introduction of symmetry associated with the surface unit cell, we hoped to obtain a method, which is far more efficient than the ordinary PS method, without loss of generality in the PES of the system. To this end, two test calculation were performed employing PES 4, developed for the SAWP method, to compare the computational efficiency of the new SAPS method to that of the SAWP method. Two other test calculations, employing a PES based on the corrugation reduction interpolation scheme[47], were performed to compare the computational efficiency of the SAPS method to that of the ordinary PS method.

Chapter 5 addresses the scattering and reaction of initial (v=0,j=0) H_2 and D_2 from Cu(111). To this end we have calculated scattering and reaction probabilities using the two different LEPS PESs[48,49], that are available for this system at the moment, as input. Both LEPS PESs have been fitted to DFT results based on super cell models of the surface-adsorbate system[50]. Although six-dimensional quantum dynamical studies on one of the LEPS PESs have been performed by Dai *et al.*[51,52], who studied the effects of the initial rotational and vibrational state of H_2 on the reaction, a direct comparison to experiments had never been made and no results on the vibrationally inelastic scattering had ever been reported. The aim of this study was thus to compare the computed reaction and vibrationally inelastic scattering probabilities directly to experimental results and thereby assess the quality of both PESs.

The scattering and reaction of initial (v=0,j=0) HD on Pt(111) is the subject of **Chapter 6**. Recent six-dimensional quantum dynamical wave packet calculations by Pijper *et*

al.[53,54] on the H$_2$ + Pt(111) system helped to solve an experimental paradox. In the scattering experiments of HD on Pt(111) by Cowin *et al.*[55] the lack of significant in-plane diffraction suggested that the Pt(111) surface is not corrugated (flat). However, the molecular beam experiments of Luntz *et al.*[56], who studied the dissociative chemisorption of H$_2$ and D$_2$ on Pt(111), suggested that the Pt(111) surface must be rather corrugated since they found the reaction probability to be dependent on the initial parallel momentum of the molecule. The calculations performed by Pijper *et al.* supported the findings of non-normal energy scaling of the reaction probability found by Luntz *et al.* and at the same time suggested that the experiments of Cowin *et al.* failed to find proof of the corrugation because only in-plane diffraction was measured. The calculations suggested that the corrugation of the PES should manifest itself in a large probabilities for out-of-plane diffraction for the H$_2$ + Pt(111) system. However, the same calculations still found more in-plane diffraction compared to non-diffractive reflection than was found in the experiments of HD on Pt(111) of Cowin *et al.*

Here, the question is addressed of whether more in-plane diffraction was found in the calculations because H$_2$ was modelled, whereas the experiments were performed for HD. For HD it was expected that rotationally inelastic scattering would be especially efficient, and that the competition between rotationally inelastic scattering and in-plane diffraction could lower the in-plane diffraction probability. To see whether this expectation holds, six-dimensional quantum dynamical calculations have been performed on the scattering and reaction of HD on Pt(111) at off-normal angles of incidence, for incidence along the $<10\bar{1}>$ and $<11\bar{2}>$ directions, using the same pseudo-spectral wave packet (PS) method as was used by Pijper *et al.* in their study of H$_2$ + Pt(111). Moreover, the PES employed in these calculations is based on the corrugation reduction interpolation method[47] for the H$_2$+Pt(111) system, as was the case in the study of Pijper *et al*[53,54]. The PES was converted into a PES for HD+Pt(111) by a centre-off-mass transform. From the computational point of view, these calculations can be considered to be a significant step forwards in the molecule-surface quantum dynamical community, for they are the first wave packet calculations on a heteronuclear diatomic molecule scattering from a metal surface, treating all the six molecular degrees of freedom quantum dynamically.

1.4. Main results

In this section the main results of the thesis are discussed.

*1.4.1. - **Chapter 3** - Signatures of site specific reaction of H_2 on Cu(100).*

The calculations of H_2 reacting on Cu(100) at normal incidence, for H_2 initially in the (j=0-5) rotational levels and in the (v=0,1) states, predict that at low energies (near threshold) initial (v=0) H_2 prefers to react at the bridge site. The initial (v=1) H_2 molecules where found to react preferably at the top site. At the same time, the molecules, whether they are initially (v=0) or (v=1) H_2, that react at the top site, showed a clear rotational enhancement effect: the higher the j level of the initial molecule, the higher the reaction probability at low incidence energies was found to be. These observations have been explained by the unique features of the PES at the top site: at this site, the barrier is later (occurs at a larger value of the H-H inter-nuclear distance) than at all the other sites and shows a large curvature in the reaction path towards the barrier. The strong curvature and late barrier allows for initial (v=1) H_2 to release most of its excess vibrational energy to motion along the reaction path, thereby promoting reaction at the top site. At the same time, the late barrier allows the release of rotational energy through the lowering of the rotational constant associated with the molecule. The released rotational energy can also be used to overcome the barrier to reaction. It was therefore concluded that the presence of rotational enhancement is a clear indication of top site reactivity of initial (v=1) H_2 in this system.

The originally proposed rotational quadrupole alignment signature was found not to hold for all the initial rotational levels considered. The rotational quadrupole alignment of the molecules about to react, for the (v=1) incident molecules was found not to be always larger than for the initial (v=0) molecules. To be more specific, for the initial (j=2) H_2, the (v=0) alignment was found to be higher than the (v=1) alignment and for initial (j=3)

H_2, the (v=1) and (v=0) alignments were found to be comparable. For the initial (j=0,1,4 and 5) H_2, the (v=1) alignments were found to be higher than for the initial (v=0) H_2. These observations could not be explained by the rotational and orientational hindering mechanisms considered so far in explaining the results found in previous studies of initial (j=4) H_2[44-46]. An explanation for these observations was found in the inclusion of rotational enhancement mechanism effects into the picture and a distinction between two types of rotational enhancement mechanisms has been made: the *elastic rotational enhancement* and the *inelastic rotational enhancement* mechanism. The latter mechanism was found to enhance reaction of initial (j=2,m_j=0) H_2 at the top site barrier, which could be related to the high polar (θ) and low azimuthal (ϕ) anisotropy of the PES at the top site barrier geometry.

*1.4.2. - **Chapter 4** - Symmetry adapted pseudo-spectral method for diatomics scattering from a square surface: H_2+Cu(100).*

A new symmetry adapted pseudo-spectral method (SAPS) has been developed and tested on the scattering and reaction of normally incident H_2 on Cu(100). The test consisted of four calculations using two different PESs for this system that has a square shaped surface unit cell. Two calculations, for H_2 initially in the (v=0,j=4,m_j=0) state for the incidence energy range 0.3 to 0.9 eV, were performed on a PES suitable for the symmetry adapted close-coupling wave packet method (SAWP) and a comparison of the computational efficiency was made between the SAPS and the SAWP method. The results of the SAPS versus SAWP test indicate that the SAPS method is competitive with the SAWP method even for PESs especially developed to be efficiently used in the SAWP method. The other two test calculations, for initially (v=0,j=0,m_j=0) H_2 for the normal incidence energy range of 0.3 to 1.15 eV, have been performed on a more general PES[47] and the computational efficiency of the SAPS method was compared to that of the general pseudo-spectral (PS) approach based on the Gauss-Legendre non-direct product spherical harmonics transforms of Lemoine *et al*[41-43]. The test calculations performed

with the SAPS and the PS methods on the more general PES show that the SAPS method is, in general, superior to the PS method by a factor of three in use of memory and in computational efficiency. At the same time, the latter test calculations represent new results on the dynamics of H_2 scattering from Cu(100) using the more general corrugation reduction scheme based PES[47].

*1.4.3. - **Chapter 5** - H_2 and D_2 scattering from Cu(111): two LEPS PESs.*

The calculations of (v=0,j=0) H_2 scattering from and reacting on the LEPS PES constructed by Dai *et al.*[48], denoted by DZ-PES, showed that, comparing to the molecular beam experiments of H_2 and D_2 from Cu(111) of Rettner *et al.*[19,57,58], for large collision energies (> 0.6 eV) the reaction probabilities obtained from the DZ-PES are probably too high. At the same time, the comparison also showed that for the DZ-PES, the barriers to dissociation are too high by at least 0.1 eV. Calculations performed on the scattering and reaction of (v=0,j=0) H_2 from Cu(111) using the LEPS PES constructed by Persson *et al.*[49], denoted by ER-PES, showed a better agreement with the experiments of Rettner *et al.* at the threshold for reaction. The reason for this is that the lowest barrier to reaction in the ER-PES is more realistic, being in better agreement with converged DFT results of Hammer *et al*[50]. However, the results based on the ER-PES also show a too high reaction probability at large collision energies. Because the molecular beam experiments on H_2 + Cu(111) of Rettner *et al.* were based on collision energies of at most 0.5 eV, whereas in seeded beam experiments on D_2 + Cu(111) collision energies of 0.83 eV could be reached[19,57,58], a separate calculation on (v=0,j=0) D_2 scattering from and reacting on Cu(111), using the ER-PES, was performed. The results of the (v=0,j=0) D_2 calculation also showed a reaction probability too high at large collision energies, when comparing to the experimental data[19,57,58]. An explanation for these observations was found in the lack of vibrationally inelastic scattering in the calculations performed on either LEPS PES, when compared to the experimental data. The vibrationally inelastic scattering process competes with the reaction and a lack of vibrationally inelastic scattering would enhance the reaction probability. The fact that both LEPS PESs give rise to almost no

vibrationally inelastic scattering has been attributed to the LEPS form not being able to reproduce the curvature in the reaction path and the late barrier location which together allow for efficient vibrationally inelastic scattering.

*1.4.4. - **Chapter 6** - HD reacting and scattering from Pt(111).*

The calculations of (v=0,j=0) HD scattering from Pt(111), for incidence along the directions $<10\overline{1}>$ and $<11\overline{2}>$, with an initial parallel translational energy of HD of 55 meV for the normal incidence energy range of 0.05 to 0.16 eV, showed that the probability of out-of-plane diffraction is larger than the in-plane diffraction of HD. The latter observation supports the findings of Pijper *et al.*[53,54] in the study of H_2 scattering from Pt(111) and underline that experiments attempting to find proof of corrugation of the surface by merely measuring in-plane diffraction can be inconclusive. Comparing the calculated reaction probabilities of HD to those of H_2 on Pt(111) shows that the HD molecule, independent of the incidence direction, has a lower reaction probability due to the increased competition with rotationally inelastic scattering for HD. The higher probabilities for rotationally inelastic scattering of HD have been attributed to the following effects: (i) HD is a heteronuclear molecule allowing the occupation of odd and even valued j levels, (ii) HD has a larger mass such that the rotational energy levels are more closely spaced, and (iii) HD has no inversion symmetry making the molecule-surface potential more anisotropic. The rotationally inelastic scattering probabilities of HD scattering from Pt(111) were found to be almost identical for the two different incidence directions, for the initial parallel momentum of 55 meV. Cowin *et al.*[55] obtained the same qualitative finding in the experiment and considered this to be proof of a lack of corrugation of the surface. However, as was shown by Pijper *et al.*, rotationally inelastic scattering is expected to be different for the two different incidence directions for higher initial parallel translational energies, due to the corrugation of the surface.

The quantitative comparison of the calculated and measured in-plane rotationally inelastic scattering probabilities of HD showed that in the calculation the majority of the

molecules scatter back into the (j'=1) level whereas in the experiments of Cowin *et al.* both the (j'=1) and the (j'=2) levels are highly populated. This discrepancy between theory and experiment has been attributed to two possible causes: (i) the neglect of phonons in the dynamical model, and (ii) the incapability of the DFT functionals, used in constructing the PES[59,60], to reproduce the attractive long range van der Waals physisorption well, which has an estimated well-depth of 55 meV[28]. Although the calculations on HD showed that the computed inelastic rotational scattering probabilities are indeed higher for HD than those computed for H_2, the ratio of specular reflection / in-plane diffraction, for each incidence direction, were also shown to be unexpectedly lower for HD than those computed for H_2 by Pijper *et al.* This was attributed to the fact that for HD the energy gaps between the diffraction states are smaller than for H_2, leading to larger probabilities for diffractive scattering in the calculations. The apparent discrepancy between theory and experiment in the ratio of specular reflection / in-plane diffraction can likewise be caused by the neglect of phonons in the dynamical method and the absence of the physisorption well in the PES.

1.5. Outlook

In science it has always been the case that in the attempt to answer one question, new questions tend to appear that leave us humble human beings bewildered if not more confused than when we started out. The research presented in this thesis is by no means an exception to that rule and therefore the reader is given an outlook in this section, summarising the new questions that have arisen.

1.5.1. Hydrogen on Copper

H_2 and D_2 + Cu(111)

The research done on H_2 and D_2 + Cu(111) has shown that the LEPS PESs used can show some serious flaws. The suggestion given in chapter 5 to improve the LEPS PESs, by making the Sato-parameters site dependent, is believed to be a significant step forwards. The site dependent Sato-parameters could allow for a better description of the individual barriers found at the different sites. This, in turn, could allow for more curvature in the reaction path and a later barrier location for the top site and thereby for increased vibrationally inelastic scattering as needed. However, further research is needed to determine to what extent these improvements help, or whether the LEPS based approach to fit the PESs should be abandoned altogether.

H_2 + Cu(100)

In the study of H_2 reacting and scattering from Cu(100) of chapter 3, an experimental signature of site reactivity was predicted. It was found that the initial (v=0) hydrogen molecules prefer to react at the bridge site, whereas the initial (v=1) H_2 molecules prefer to react at the top site, for low incidence energies. Moreover, the initial (v=1) molecules showed a clear j-dependence in the reaction probability that could be correlated to top site reactivity: the higher the initial j level of H_2, the higher the reaction probability was found to be, for j=0-5. At the same time, it was predicted that the rotational quadrupole alignment for reacting molecules, for initial (v=1,j=0,4 and 5) H_2 is higher than for the corresponding (v=0) initial molecules. For the initial (v=1,j=2) molecule the rotational quadrupole alignment was found to be lower than for the initial (v=0,j=2) H_2.

Assuming the validity of detailed balance, associative desorption experiments using state-selective detection in combination with time-of-flight techniques, are able to obtain

vibrationally (v), rotationally (j) and energy resolved relative reaction probabilities[58,61,62]. At the same time, these types of experiments are also able to measure the rotational quadrupole alignment of the angular momentum of the desorbing molecules[19,58,63-66]. Experiments on the desorption of H_2 from Cu(100) could test our predictions and at the same time could find evidence for the predicted difference in reaction site of (v=0) and (v=1) H_2.

Apart from our suggestion to perform these associative desorption experiments, a recent comparison on the reactive scattering of initial (v=1,j=1) H_2 from Cu(100) to molecular beam experiments by Watts *et al.*[67], showed that, although a good agreement was obtained for the rovibrationally elastic scattering probability, the computed rotationally inelastic scattering probabilities were too large. It was noted by Watts *et al.* that this disagreement between the experimentally observed and theoretically calculated rotationally inelastic scattering probabilities, could originate from the fitting procedure employed to obtain the PES, i.e. PES 4. As noted before, PES 4 has been fitted to a limited number of symmetry adapted basis functions, which included only up to the 4th order spherical harmonic (see chapters 3 and 4). It was suggested that the anisotropy in the polar degree of freedom of H_2 could be overestimated in PES 4 and that a PES based on the corrugation reduction interpolation method should be employed instead. Recently such a PES has been constructed by Olsen *et al.*[47] and has already been successfully used to test the new SAPS method in chapter 4 (PES 5). Moreover, preliminary studies on the anisotropies at the three high-symmetry sites indicate that PES 5 indeed shows a different dependence on θ and ϕ at the barriers than PES 4. With the new SAPS method now available, the calculations on initial (v=1,j=1) H_2 employing the new PES 5 can be completed in the near future.

1.5.2. Hydrogen on Platinum

Although the calculations performed on the scattering of (v=0,j=0) HD from Pt(111) showed that indeed the rotationally inelastic scattering probabilities for HD are higher

than for H_2, this did not lead to the expected lowering of the ratio of specular reflection / in-plane diffraction by the competition of the rotationally inelastic scattering with diffraction. It was also shown, for in-plane rotationally inelastic scattering, that the majority of the HD molecules scattered back into the (j'=1) final level, rather than in the (j'=1) and (j'=2) levels. Both results reflect a lack of agreement with the in-plane scattering experimental results of Cowin *et al.* and it was suggested that this could be caused by the neglect of phonons in the dynamical model or, equally possible, by the imperfections in the PES that was used. The inclusion of phonons in the model, whilst treating the six molecular degrees of freedom fully quantum dynamically, might become possible in the near future (see below). However, it is believed that, at the moment, improvements should be directed at reproducing the physisorption well in the PES by using DFT functionals that include the van der Waals interactions to some extent. The currently used PES lacks this physisorption well of 55 meV[28]. The inclusion of a physisorption well in the PES would shift the barrier to reaction more towards the surface, perhaps resulting in a barrier with more anisotropy, which would increase the rotationally inelastic scattering probabilities especially for scattering to higher j' levels.

Recently new DFT functionals[68-71] have been developed that show promising results in their description of the van der Waals interactions and therefore it would be interesting to compute a PES, using the corrugation reduction scheme, based on DFT data using one of these new functionals. Another approach to include the van der Waals interactions in the PES, that could also be adopted, is based on a density functional plus damped dispersion (DFdD) scheme as proposed by Wu *et al*[72]. In the latter scheme, the gradient corrected Becke's hybrid[73] (B3) functional was used to account for the exchange part, the Vosko-Wilk-Nusair[74] (VWN5) functional to account for the local correlation contribution and a damped multipolar expansion of the dispersion energy to account for the dispersion energy. The multipolar expansion coefficients were obtained mostly semi-empirically. With the DFdD approach, good results were obtained for the water dimer and benzene dimer potentials and for the metal carbonyls dissociation energies[72]. One way of implementing the DFdD scheme to include the van der Waals interaction in our PES for H_2 + Cu(100) and Pt(111) would be to remove the Perdew correction from the Becke-

Perdew DFT data and replace it with damped dispersion. It would be interesting to investigate whether this would lead to improved results.

1.5.3. Symmetry adapted treatment of diatomic molecules scattering from surfaces

Apart from the possibility of performing systematic studies of diatomic molecules scattering from square surfaces at normal incidence, which the SAPS method already offers for any type of PES, as mentioned above, several improvements can still be made from the methodological point of view. As noted in chapter 4, the use of a "diamond shaped" momentum grid for diffraction could allow for a considerable reduction of computational cost in the fast Fourier transforms needed to apply the kinetic energy operators in the r and Z degrees of freedom of the molecule. Moreover, this could also considerably reduce the memory requirements associated with the finite base representation of the wave function. If at the same time a flux based analysis method is implemented, as was done in the SAWP method used in the study of chapter 3, the possibility to calculate site-specific reaction probabilities on any form of a PES arises. This would allow for systematic studies on site reactivity to be carried out on any diatomic molecule + square surface (belonging to the C_{4v} pointgroup) system, employing a general form of the PES at moderate cost.

Extending the symmetry adapted pseudo-spectral method to i.e. the C_{6v} pointgroup, would offer the same possibilities for diatomic molecules scattering from metal surfaces with hexagonal shaped unit cells, i.e. Pt(111), Cu(111) and Pd(111). At the moment, the symmetry adapted associated Legendre transforms do allow for C_{6v} symmetry, but an efficient method for transforming along the C_{6v} symmetry adapted diffractional degrees of freedom has not been developed yet. Another possibility is to extend the current C_{4v} algorithms to the C_{2v} pointgroup. This would allow for a symmetry adapted pseudo-spectral method to be applied to diatomic molecules scattering from surfaces with a rectangular surface unit cell, like Cu(110).

1.5.4. The inclusion of phonons in the model

Although, including phonons in the model, while retaining the six molecular degrees of freedom of the diatomic molecule might seem to be an impossible task, it might very well be possible, in future, to include phonons through the use of the surface oscillator (SO) model[2,75-78]. In the SO model, phonons are modelled by making the molecule-surface interaction potential dependent on a co-ordinate d, associated with the oscillator, in the centre-of-mass co-ordinate Z of the molecule, and by adding a harmonic term in d, as follows: $V(X,Y,Z,r,\theta,\phi,d) = V(X,Y,Z-d,r,\theta,\phi) + Cd^2/2$, with C being a collective model parameter[75,79]. The inclusion of phonons through the SO model essentially transforms the 6D problem into a 7D problem and if the assumption is made that the harmonic term needed to model phonons does not break the symmetry of the PES that is associated with the surface unit cell, the SAPS approach can be used to make the task tangible. If the number of oscillator states needed is rather low (≤ 10), as is expected to be a valid approximation for the H_2+Pt(111) system, the increase in computational cost can be largely offset by the use of symmetry of the surface unit cell. Moreover, if the SAPS method is extended to C_{6v} symmetry, the possibility to model surface temperature dependent dissociation probabilities for the H_2 + Cu(111) system emerges. For the later system, a large amount of experimental data is available[3,4,30]. Including phonons through the SO model might even be possible with the PS method (i.e., not using symmetry), but such calculations would be really at the limit of what is currently feasible.

1.6. References

1   G. A. Somorjai, Introduction to surface chemistry and catalysis (Wiley, New York, 1994).
2   M. Dohle and P. Saalfrank, Surf. Sci. 373, 95 (1997).
3   H. A. Michelsen, C. T. Rettner, and D. J. Auerbach, Surf. Sci. 272, 65 (1992).
4   M. J. Murphy and A. Hodgson, J. Chem. Phys. 108, 4199 (1998).
5   M. F. Bertino and D. Farias, J. Phys.-Condens. Mat. 14, 6037 (2002).
6   G. J. Kroes, Prog. Surf. Sci. 60, 1-85 (1999).
7   G. R. Darling and S. Holloway, Surf. Sci. 268, l305 (1992).

8   G. R. Darling and S. Holloway, J. Chem. Phys. 97, 734 (1992).
9   G. R. Darling and S. Holloway, J. Electron Spectrosc. Relat. Phenom. 64-65, 517 (1993).
10   G. R. Darling and S. Holloway, Surf. Sci. 307-409, 153. (1994).
11   J. M. Jackson and A. Howarth, Proc. R. Soc. London Ser. A 152, 515 (1935).
12   G. Boato, P. Cantini, and L. Mattera, J. Chem. Phys. 65, 544 (1976).
13   G. Boato, P. Cantini, and A. Howarth, Jpn. J. Appl. Phys. Suppl. 2, 553 (1974).
14   R. G. Rowe and G. J. Ehrlich, J. Chem. Phys. 62, 735 (1975).
15   R. G. Rowe and G. J. Ehrlich, J. Chem. Phys. 63, 4648 (1975).
16   C. T. Rettner, F. Fabre, J. Kimman, and D. J. Auerbach, J. Phys. Rev. Lett. 55, 1904 (1985).
17   B. D. Kay, T. D. Raymond, and M. E. Coltrin, Phys. Rev. Lett. 59, 2792 (1987).
18   A. Hodgson, J. Moryl, P. Traversaro, and H. Zhao, Nature 356, 501 (1992).
19   C. T. Rettner, D. J. Auerbach, and H. A. Michelsen, Phys. Rev. Lett. 68, 2547 (1992).
20   F. Bloch, Z. Physik 52, 555 (1928).
21   N. W. Ashcroft and N. D. Mermin, Solid state physics (Saunders College, Philadephia, 1976).
22   C. Kittel, Introduction to solid state physics (John Wiley & Sons inc., New York, Chichester, 1986).
23   I. Estermann and O. Stern, Z. Phys. 63, 95 (1930).
24   B. Hammer and J. K. Norskov, Nature 376, 238 (1995).
25   B. Hammer and J. K. Norskov, Surf. Sci. 343, 211 (1995).
26   G. Burns, Solid state physics (Academic press, inc., San Diego, 1990).
27   S. Andersson, L. Wilzen, and M. Persson, Phys. Rev. B 38, 2967 (1988).
28   J. P. Cowin, C. F. Yu, and L. Wharton, Surf. Sci. 161, 221 (1985).
29   E. Watts and G. O. Sitz, J. Chem. Phys. 111, 9791 (1999).
30   E. Watts and G. O. Sitz, J. Chem. Phys. 114, 4171 (2001).
31   M. T. Nguysen, S. Crene, and L. G. Vanquickenborne, J. Chem. Phys. 100, 18422 (1996).
32   J. Baker, M. Muir, and J. Andzelm, J. Chem. Phys. 102, 2063 (1995).
33   G. R. Darling and S. Holloway, J. Chem. Phys. 101, 3268 (1994).
34   C. Engdahl, B. I. Lundqvist, U. Nielsen, and J. K. Nørskov, Phys. Rev. B 45, 11362 (1992).
35   C. Engdahl and U. Nielsen, J. Chem. Phys. 98, 4223 (1993).
36   G. J. Kroes, E. J. Baerends, and R. C. Mowrey, J. Chem. Phys. 107, 3309 (1997).
37   D. A. McCormack, G. J. Kroes, E. J. Baerends, and R. C. Mowrey, Faraday Discuss. 110, 267 (1998).
38   B. Gergen, H. Niehaus, W. H. Weinber, and W. W. McFarland, Science 294, 2521 (2001).
39   G. R. Darling and S. Holloway, Rep. Prog. Phys. 58, 1595 (1995).
40   G. J. Kroes, A. Gross, E. J. Baerends, M. Scheffler, and D. A. McCormack, Acc. Chem. Res. 35, 193 (2002).
41   D. Lemoine and G. C. Corey, J. Chem. Phys. 92, 6175 (1990).

42 G. C. Corey, J. W. Tromp, and D. Lemoine, in Numerical grid methods and their applications to Schrodinger equation, Vol. 412, edited by C. Cerjan (Kluwer Academic, Dordrecht, 1993), pp. 1-23.

43 G. C. Corey and D. Lemoine, J. Chem. Phys. 97, 4115 (1992).

44 D. A. McCormack, G. J. Kroes, R. A. Olsen, J. A. Groeneveld, J. N. P. v. Stralen, E. J. Baerends, and R. C. Mowrey, Chem. Phys. Lett. 328, 317-324 (2000).

45 D. A. McCormack, G. J. Kroes, R. A. Olsen, J. A. Groeneveld, J. N. P. v. Stralen, E. J. Baerends, and R. C. Mowrey, Faraday Discuss. 117, 109 (2000).

46 D. A. McCormack, G. J. Kroes, R. A. Olsen, J. A. Groeneveld, J. N. P. v. Stralen, E. J. Baerends, and R. C. Mowrey, Chem. Phys. Lett. 346, 347-348 (2001).

47 R. A. Olsen, H. F. Busnengo, A. Salin, M. F. Somers, G. J. Kroes, and E. J. Baerends, J. Chem. Phys. 116, 3841 (2002).

48 J. Q. Dai and J. Z. H. Zhang, J. Chem. Phys. 102, 6280 (1995).

49 M. Persson, J. Stromquist, L.Bengtsson, B. Jackson, D. V. Shalashilin, and B. Hammer, J. Chem. Phys. 110, 2240 (1999).

50 B. Hammer, M. Scheffler, K. W. Jacobsen, and J. K. Norskov, Phys. Rev. Lett. 73, 1400 (1994).

51 J. Q. Dai and J. C. Light, J. Chem. Phys. 107, 1676 (1997).

52 J. Q. Dai and J. C. Light, J. Chem. Phys. 108, 7816 (1998).

53 E. Pijper, G. J. Kroes, R. A. Olsen, and E. J. Baerends, J. Chem. Phys. 117, 5885 (2002).

54 E. Pijper, M. F. Somers, G. J. Kroes, R. A. Olsen, E. J. Baerends, H. F. Busnengo, A. Salin, and D. Lemoine, Chem. Phys. Lett. 347, 277 (2001).

55 J. P. Cowin, C. F. Yu, S. J. Sibener, and J. E. Hurst, J. Chem. Phys. 79, 3537 (1983).

56 A. C. Luntz, J. K. Brown, and M. D. Williams, J. Chem. Phys. 93, 5240 (1990).

57 H. A. Michelsen, C. T. Rettner, D. J. Auerbach, and R. N. Zare, J. Chem. Phys. 98, 8294-8307 (1993).

58 C. T. Rettner, H. A. Michelsen, and D. J. Auerbach, J. Chem. Phys. 102, 4625 (1995).

59 A. D. Becke, Phys. Rev. A 38, 3098 (1988).

60 J. P. Perdew, Phys. Rev. B 33, 8822 (1986).

61 G. Comsa and R. David, Surf. Sci. 117, 77 (1982).

62 H. A. Michelsen and D. J. Auerbach, J. Chem. Phys. 94, 7502 (1991).

63 H. Hou, S. J. Gulding, C. T. Rettner, A. M. Wodtke, and D. J. Auerbach, Science 277, 80 (1997).

64 D. Wetzig, M. Rutkowski, R. David, and H. Zacharias, Europhys. Lett. 36, 31 (1996).

65 D. Wetzig, R. Dopheide, M. Rutkowski, R. David, and H. Zacharias, Phys. Rev. Lett. 76, 463 (1996).

66 S. J. Gulding, A. M. Wodtke, H. Hou, C. T. Rettner, H. A. Michelsen, and D. J. Auerbach, J. Chem. Phys. 105, 9702 (1996).

67 E. Watts, G. O. Sitz, D. A. McCormack, G. J. Kroes, R. A. Olsen, J. A. Groeneveld, J. N. P. v. Stralen, E. J. Baerends, and R. C. Mowrey, J. Chem. Phys. 114, 495-503 (2001).

68 Y. Andersson, D. C. Langreth, and B. I. Lundqvist, Phys. Rev. Lett. 76, 102 (1996).

69 T. A. Wesolowski, Y. Ellinger, and J. Weber, J. Chem. Phys. 108, 6078 (1998).

70   J. F. Dobson and J. Wang, Phys. Rev. Lett. 82, 2123 (1999).
71   E. Hult, Ph. D Thesis, Chalmers University of Technology and Goteborg University, (2001).
72   X. Wu, M. C. Vargas, S. Nayak, V. Lotrich, and G. Scoles, J. Chem. Phys. 115, 8748 (2001).
73   A. D. Becke, J. Chem. Phys. 98, 5648 (1993).
74   S. H. Vosko, L. Wilk, and M. Nusair, Can. J. Phys. 58, 1200 (1980).
75   M. Hand and J. Harris, J. Chem. Phys. 92, 7610 (1990).
76   G. R. Darling and S. Holloway, Surf. Sci. 321, L189 (1994).
77   G. R. Darling and S. Holloway, Surf. Sci. 336, L771 (1995).
78   Z. S. Wang, G. R. Darling, B. Jackson, and S. Holloway, J. Phys. Chem. B 106, 8422 (2002).
79   A. C. Luntz and J. Harris, Surf. Sci. 258, 397 (1991).

Chapter 2

Theory of molecule-surface scattering

In this chapter the general theory of molecule-surface scattering is presented, as it will be used in subsequent chapters. In section (2.1) the rigid surface model is treated. Section (2.2) describes how the molecule-surface interaction is obtained using density functional theory (DFT), and how the DFT data are subsequently fitted to obtain potential energy surfaces (PESs). Section (2.3) will introduce the time-dependent wave packet approach and, finally, in section (2.4) different representations of the wave function are explained.

2.1. Rigid surface model of electronically adiabatic molecule-surface scattering

The Schrödinger equation for a molecule interacting with a surface, can be written as:

$$\hat{H}_{tot}\Psi(\vec{Q},\vec{q}) = E_{tot}\Psi(\vec{Q},\vec{q}) \tag{2.1}$$

in which E_{tot} is the total energy and $\Psi(\vec{Q},\vec{q})$ is the wave function, depending on all the electronic co-ordinates $\vec{q}$ and all the nuclear co-ordinates $\vec{Q}$, both for the complete system. $\hat{H}_{tot}$ is the Hamiltonian describing both the electronic and nuclear motions and can be written as:

$$\hat{H}_{tot} = \hat{H}_e(\vec{Q},\vec{q}) + \sum_n \frac{-1}{2m_n}\nabla^2_{\vec{Q}_n} \tag{2.2}$$

in which $\vec{Q}_n$ are now the co-ordinates for a single nucleus n with mass m_n and $\hat{H}_e(\vec{Q},\vec{q})$ corresponds to the electronic Hamiltonian, which depends on the electronic and nuclear co-ordinates. In equation (2.2), and below, atomic units are used. The electronic Hamiltonian can be written as:

$$\hat{H}_e(\vec{Q},\vec{q}) = \hat{K}_e(\vec{q}) + \hat{V}_{ee}(\vec{q}) + \hat{V}_{nn}(\vec{Q}) + \hat{V}_{en}(\vec{Q},\vec{q}) \tag{2.3}$$

in which $\hat{K}_e(\vec{q})$ is the kinetic energy operator associated with the electrons, $\hat{V}_{ee}(\vec{q})$ the electron-electron interaction potential operator, $\hat{V}_{nn}(\vec{Q})$ the nuclear-nuclear interaction potential operator and $\hat{V}_{en}(\vec{Q},\vec{q})$ the electron-nuclear interaction potential operator.

To solve (2.1), the *adiabatic approach* is taken and the *electronic Schrödinger equation* is solved first:

$$\hat{H}_e(\vec{Q},\vec{q})\zeta_k(\vec{Q};\vec{q}) = V_k(\vec{Q})\zeta_k(\vec{Q};\vec{q}) . \tag{2.4}$$

In (2.4), $\zeta_k(\vec{Q};\vec{q})$ is the electronic eigen function of state k and $V_k(\vec{Q})$ the corresponding eigen energy, both depending parametrically on all the nuclear co-ordinates $\vec{Q}$. $V_k(\vec{Q})$ will be referred to as the potential energy surface (PES) for electronic state k. The approximate solution of (2.4) with density functional theory (DFT) will be the subject of the next section in this chapter and is referred to as solving the *electronic structure problem*.

$\Psi(\vec{Q},\vec{q})$ can now be expanded, without loss of generality, as:

$$\Psi(\vec{Q},\vec{q}) = \sum_k \chi_k(\vec{Q})\zeta_k(\vec{Q};\vec{q}) . \tag{2.5}$$

If (2.5) is used in (2.1), a set of coupled equations appears for $\chi_k(\vec{Q})$, the part of the full wave function describing the nuclear motion corresponding to the kth electronic state. The set of coupled equations can be de-coupled if it is assumed that:

$$\nabla_{\vec{Q}_n} \zeta_k(\vec{Q};\vec{q}) = 0 \text{ and } \nabla^2_{\vec{Q}_n} \zeta_k(\vec{Q};\vec{q}) = 0 \tag{2.6}$$

for all nuclei n and electronic states k of (2.4). The assumptions of (2.6) introduce an approximation, which is known as the Born-Oppenheimer approximation, in solving (2.1).

The use of (2.6), (2.5) and (2.4) in (2.1) leads to the following equation to be solved for $\chi_k(\vec{Q})$ and E_{tot}:

$$\left\{ \sum_n \frac{-1}{2m_n} \nabla^2_{\vec{Q}_n} + V_k(\vec{Q}) \right\} \cdot \chi_k(\vec{Q}) = E_{tot} \cdot \chi_k(\vec{Q}) . \tag{2.7}$$

Equation (2.7) is referred to as the *nuclear Schrödinger equation* describing the motion of all the nuclei of the system in the kth electronic state described by $V_k(\vec{Q})$. Assuming the surface atoms to be fixed and considering the ground state PES only, (2.7) is reduced to

$$\left\{ \sum_n \frac{-1}{2m_n} \nabla^2_{\vec{\rho}_n} + V(\vec{\rho}) \right\} \cdot \chi(\vec{\rho}) = \hat{H}_{nuc}(\vec{\rho}) \cdot \chi(\vec{\rho}) = E_{tot} \cdot \chi(\vec{\rho}) , \tag{2.8}$$

in which $\vec{\rho}$ represent the molecule's nuclear co-ordinates, $\chi(\vec{\rho})$ the nuclear part of the full wave function, $\Psi(\vec{\rho},\vec{q}) = \chi(\vec{\rho})\zeta(\vec{\rho};\vec{q})$, $V(\vec{\rho})$ the ground state PES and $\hat{H}_{nuc}(\vec{\rho})$ the Hamiltonian describing the nuclear motion of the molecule.

Solving (2.8) is usually referred to as *solving the dynamics problem.* After transforming the molecule's nuclear co-ordinates $\vec{\rho}$ into a centre-of-mass $\vec{R} = (X, Y, Z)$ co-ordinate system with $\vec{r}$ representing the molecules internal co-ordinates, $\hat{H}_{nuc}(\vec{\rho})$ can be written as:

$$\hat{H}_{nuc}(\vec{\rho}) = \hat{H}_{nuc}(\vec{R}, \vec{r}) = \frac{-1}{2M}\nabla_{\vec{R}}^2 - \frac{1}{2\mu}\nabla_{\vec{r}}^2 + V(\vec{R}, \vec{r}) . \qquad (2.9)$$

In (2.9), M corresponds to the total mass and μ to the reduced mass of the molecule. Moreover, the Laplacian corresponding to the molecule's internal co-ordinates can be partitioned into a vibrational and a rotational contribution and (2.9) can be written as:

$$\hat{H}_{nuc}(\vec{R}, \vec{r}) = \frac{-1}{2M}\nabla_{\vec{R}}^2 + \hat{H}_{vib}(\vec{r}) + \hat{H}_{rot}(\vec{r}) + V(\vec{R}, \vec{r}) . \qquad (2.10)$$

For a diatomic molecule, like H_2, scattering from a static surface, $\vec{r} = (r, \theta, \varphi)$ can be taken with r corresponding to the H-H distance and (θ, φ) to the H-H bond orientation with respect to the surface and its normal (see for instance Figure 3.1). Moreover, for diatomic molecules, rather simple expressions for $\hat{H}_{vib}(\vec{r})$ and $\hat{H}_{rot}(\vec{r})$ can be formulated:

$$\hat{H}_{vib}(\vec{r}) = -\frac{1}{2\mu} \cdot \frac{\partial^2}{\partial r^2} , \qquad (2.11)$$

$$\hat{H}_{rot}(\vec{r}) = \frac{\hat{j}^2}{2\mu r^2} . \qquad (2.12)$$

In (2.12), $\hat{j}$ is the angular momentum operator associated with the angular momentum of the molecule. With the use of expression (2.11) for $\hat{H}_{vib}(\vec{r})$, the transformation of the nuclear part of the wave function, $\chi'(\vec{R}, \vec{r}) = r \cdot \chi(\vec{R}, \vec{r})$, has been used and therefore the dot-product needs to be redefined to $\left\langle \chi'(\vec{R}, \vec{r}) \middle| \chi'(\vec{R}, \vec{r}) \right\rangle \equiv$

$\iint \chi^{*}(\vec{R}, \vec{r}) \chi'(\vec{R}, \vec{r}) \sin(\theta) d\vec{R} d\vec{r}$ instead of the usual definition of $\left\langle \chi(\vec{R}, \vec{r}) \middle| \chi(\vec{R}, \vec{r}) \right\rangle \equiv$

$\iint \chi^{*}(\vec{R}, \vec{r}) \chi(\vec{R}, \vec{r}) r^{2} \sin(\theta) d\vec{R} d\vec{r}$ when using spherical co-ordinates[1].

2.2. The molecule-surface interaction

The first step in solving the full Schrödinger equation (2.1) was solving the electronic Schrodinger equation (2.4) to obtain the ground state PES, $V(\vec{R}, \vec{r})$. The PESs used in the studies on the dynamics of hydrogen scattering from and reacting on metal surfaces, presented in this thesis, have all been obtained by density functional theory (DFT). Therefore a brief description on the subject of DFT and how the PESs, based on the DFT data, have been fitted, will be presented now.

2.2.1. Density functional theory

In 1964 Hohenberg and Kohn[2] showed that for a system of N interacting electrons in an external field, the many particle wave function of the ground state can be written as a functional of the electron density if the ground state is non-degenerate. In solving the electronic structure problem within the Born-Oppenheimer approximation, the nuclei provide an external field to the many-electron system to be solved (2.4). Kohn and Sham[3] found that, by using the Hohenberg-Kohn variational principle[2], the many-electron problem of (2.4) can be reformulated in a set of N single electron equations:

$$\left\{ -\tfrac{1}{2}\nabla_{\vec{s}}^{2} + \upsilon(\vec{Q}; \vec{s}) + \int \frac{\rho(\vec{Q}; \vec{s}')}{|\vec{s} - \vec{s}'|} d\vec{s}' + \upsilon_{xc}(\vec{Q}; \vec{s}) \right\} \cdot \psi_{i}(\vec{Q}; \vec{s}) = \varepsilon_{i}(\vec{Q})\psi_{i}(\vec{Q}; \vec{s}) . \qquad (2.13)$$

In (2.13), $\vec{s}$ and $\vec{s}'$ are position vectors, $\rho(\vec{Q};\vec{s})$ is the electron density, $\upsilon(\vec{Q};\vec{s})$ the external potential (it can be related to (2.3) by $<\hat{V}_{en}(\vec{Q};\vec{q})> = \int \upsilon(\vec{Q};\vec{s})\rho(\vec{Q};\vec{s})d\vec{s}$), $\upsilon_{xc}(\vec{Q};\vec{s})$ the exchange-correlation potential and $\psi_i(\vec{Q};\vec{s})$ the ith one-electron Kohn-Sham wave function, all for a given configuration $\vec{Q}$ of the nuclei. The exchange-correlation potential, $\upsilon_{xc}(\vec{Q};\vec{s})$, is given by the functional derivative of the exchange-correlation energy, $E_{xc}[\rho(\vec{Q};\vec{s})]$, with respect to the electron density:

$$\upsilon_{xc}(\vec{Q};\vec{s}) = \frac{\delta E_{xc}[\rho(\vec{Q};\vec{s})]}{\delta\rho(\vec{Q};\vec{s})}. \tag{2.14}$$

At the same time, the electron density, $\rho(\vec{Q};\vec{s})$, is given from the one-electron Kohn-Sham wave functions, $\psi_i(\vec{Q};\vec{s})$, by:

$$\rho(\vec{Q};\vec{s}) = \sum_{i=1}^{N} \left|\psi_i(\vec{Q};\vec{s})\right|^2. \tag{2.15}$$

Using some functional expression for the exchange-correlation energy, $E_{xc}[\rho(\vec{Q};\vec{s})]$, (2.15), (2.14) and (2.13) can be used to solve self-consistently for $\rho(\vec{Q};\vec{s})$, resulting in the electronic ground state energy, $V(\vec{Q})$, for nuclear configuration $\vec{Q}$:

$$V(\vec{Q}) = \sum_{i}^{N}\varepsilon_i(\vec{Q}) - \tfrac{1}{2}\int\frac{\rho(\vec{Q};\vec{s})\rho(\vec{Q};\vec{s}')}{\left|\vec{s}-\vec{s}'\right|}d\vec{s}d\vec{s}' + E_{xc}[\rho(\vec{Q};\vec{s})] - \int\upsilon_{xc}(\vec{Q};\vec{s})\rho(\vec{Q};\vec{s})d\vec{s} + V_{nn}(\vec{Q}) \tag{2.16}$$

The method scales favourably with N and this makes DFT a suitable method to obtain the ground state PES for systems with many electrons (such as H_2 + metal surface systems, in which the surface is treated as a slab).

If the exact exchange-correlation functional would be used in the above procedure, (2.16) would yield the exact ground state energy. Unfortunately, the functional $E_{xc}[\rho(\vec{Q};\vec{s})]$ is not known and only approximations to it are available. One of the approximations is the so-called local density approximation[4] (LDA) where the exchange-correlation functional is taken to be:

$$E_{xc}^{LDA}[\rho(\vec{s})] = \int \rho(\vec{s}')\varepsilon_{xc}(\rho(\vec{s}))d\vec{s}'$$ (2.17)

in which $\varepsilon_{xc}(\rho(\vec{s}))$ corresponds to the exchange and correlation energy per electron of a uniform electron gas of density $\rho(\vec{s})$. The LDA approximation, though crude, often gives good results for quantities like bond lengths and vibrational frequencies of molecules and for atoms adsorbed on surfaces. However, in determining molecular binding energies and adsorption energies, the LDA approximation is known to fail and wrongly predict the shape of the PES for systems like $H_2+Cu(100)$[5,6] and $H_2+Cu(111)$[7].

More successful approximating functionals, for obtaining molecule-surface PESs , are based on the generalised gradient approximation[8,9] (GGA). In the GGA, the exchange-correlation energy is written as a functional of the electron density and its gradient:

$$E_{xc}^{GGA}[\rho(\vec{s}),\nabla\rho(\vec{s})] = \int f_{xc}(\rho(\vec{s}),\nabla\rho(\vec{s}))\rho(\vec{s}')d\vec{s}'.$$ (2.18)

A number of different GGAs, such as the combination of the Becke-exchange[10] and Perdew-correlation[11] corrections or the gradient corrected functional of Perdew[12,13], have been successfully applied to systems like $H_2+Pd(100)$[14], $H_2+Cu(100)$[15-17], $H_2+Cu(111)$[18,19] and $H_2+Pt(111)$[16]. The PESs used in the dynamics presented in this thesis are also based on these types of GGA functionals.

In addition to the use of GGA functionals in the DFT calculations, the use of a two-dimensional (2D) slab[20] or a 3D supercell[21] approach is required for obtaining accurate molecule-surface interaction energies. With such periodic models, good convergence of

the molecule-surface interaction energy, with respect to substrate size, can be obtained. If the substrate is modelled with a simple cluster, the interaction energy is known to vary widely with cluster size[20,22,23]. Although this problem can, in principle, also be solved by using embedding techniques[23], the PESs used in the dynamics of this thesis have all been based on a 2D slab approach.

2.2.2. Fitting and interpolating methods

Although DFT is an efficient method for obtaining the electronic ground state energy (PES), the number of points of the PES that is needed in a quantum dynamical wave packet calculation is too large to compute them all with DFT. To this end, a restricted number of DFT calculations is usually performed and a fit or an interpolation method is used to generate the full PES used in the dynamics. In this part three different fitting/interpolation methods will be briefly discussed because they have been used to represent the PESs employed in the studies of this thesis.

LEPS fit

McCreery and Wolken[24], and Sato[25], were the first to adapt the LEPS form for a PES to obtain PESs for molecule-surface reactions. In general, the modified LEPS form, for H_2 + surface systems, reduces to a modified Morse potential for the H_2 molecule if both H atoms are far away from the surface. Moreover, for large H-H distances, the modified LEPS form also reduces to a modified Morse potential for the H atom - surface interaction. As is shown in Figure 2.1, McCreery and Wolken thought of the surface as a source of two electrons used for creating the H_2 - surface bonds and within this picture the modified LEPS PES takes on the form:

$$V = U_{HH} + U_{HM_1} + U_{HM_2} - \sqrt{Q_{HH}^2 + (Q_{HM_1} + Q_{HM_2})^2 - Q_{HH}(Q_{HM_1} + Q_{HM_2})} \qquad (2.19)$$

with

$$U_{AB} = \frac{D_{AB}}{4(1+\Delta_{AB})}\left[(3+\Delta_{AB}) \cdot e^{-2\alpha_{AB}(r_{AB}-r_{AB}^0)} - (2+6\Delta_{AB}) \cdot e^{-\alpha_{AB}(r_{AB}-r_{AB}^0)}\right] \qquad (2.20)$$

and

$$Q_{AB} = \frac{D_{AB}}{4(1+\Delta_{AB})}\left[(1+3\Delta_{AB}) \cdot e^{-2\alpha_{AB}(r_{AB}-r_{AB}^0)} - (6+2\Delta_{AB}) \cdot e^{-\alpha_{AB}(r_{AB}-r_{AB}^0)}\right]. \qquad (2.21)$$

In (2.20) and (2.21), for A and B $\in$ {H,M$_1$,M$_2$}, r_{AB} is the A-B distance, r_{AB}^0 is the A-B equilibrium bond length, α_{AB} is the Morse parameter, Δ_{AB} is the Sato parameter and D_{ab} is the dissociation energy of the AB bond. The in total eight parameters (four for the H-H interaction and four for the H atom - surface interaction, the four parameters being r_{AB}^0, α_{AB}, Δ_{AB} and D_{ab}) are used to obtain a fit of V in (2.19), using the DFT data as input.
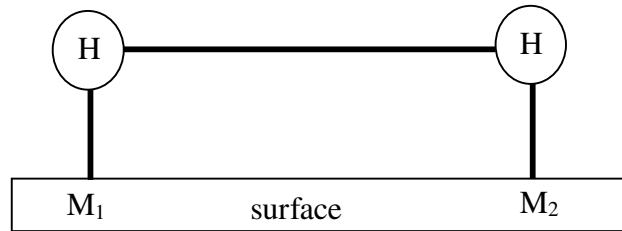
Figure 2.1: The modified LEPS model for two hydrogen atoms interacting with the surface. The three pair interactions are indicated with the thick lines.

A modified LEPS model, in which the H atom - surface interaction was made surface site dependent, has been used by Dai *et al.*[18] to fit a PES to computed DFT points for the H$_2$+Cu(111) system. In chapter 5, the LEPS PES, referred to as the DZ-PES, has been used, together with the modified LEPS PES of Persson *et al.*[19], in calculations on the

reaction of H_2 on and vibrationally inelastic scattering of H_2 from Cu(111). Two-dimensional cuts through both LEPS PESs are shown in Figure 5.2.

Symmetry adapted interpolation

The PES[15] used for H_2 + Cu(100) in the calculations of chapter 3 and also in two test calculations of chapter 4, is based on a direct interpolation method. As explained in these chapters, symmetry adapted basis functions were used to expand the PES:

$$V = \sum_{jm_jp=00,20,40,44e} \sum_{nm=00,10,11} V_{jm_jpnm}(r,Z)\mathbf{Y}_{jm_jp}(\theta,\varphi)H_{nm}(X,Y) + \sum_{jm_jp=22e,42e} V_{jm_jpB_110}(r,Z)\mathbf{Y}_{jm_jp}(\theta,\varphi)H_{B_110}(X,Y)$$

(2.22)

with $H_{nm}(X,Y)$, $H_{B_110}(X,Y)$ and $\mathbf{Y}_{jm_jp}(\theta,\varphi)$ defined as in (4.37) and (4.38) of chapter 4, respectively. The interpolation coefficients, $V_{jm_jpnm}(r,Z)$ and $V_{jm_jpB_110}(r,Z)$ in (2.22), have been determined through a two step procedure as explained in references 15, 17 and, in less detail, in section 2 of chapter 4. In Figure 3.3, two-dimensional cuts of the PES, which in this thesis is referred to as PES 4, are shown for three different high-symmetry sites. Table 3.2 gives the barrier positions, the barrier heights and a measure of the anisotropies in the polar and azimuthal degrees of freedom found for the individual barriers at the top, hollow and bridge sites (see Figure 3.1).

Corrugation reduction interpolation method

Recently PESs have been constructed for the H_2+Pt(111) and the H_2+Cu(100) systems by Olsen *et al.*[16], using the corrugation reduction interpolation method as proposed by Busnengo *et al*[26]. At the heart of the corrugation reduction method lies the separation of

the full six-dimensional potential, of a diatomic molecule AB interacting with a static surface, into two atom-surface parts and an interpolation function:

$$V(\vec{R},\vec{r}) = I(\vec{R},\vec{r}) + V_A(X_A,Y_A,Z_A) + V_B(X_B,Y_B,Z_B) .$$ (2.23)

In (2.23), $I(\vec{R},\vec{r})$ is the interpolation function, which depends on the AB molecule's centre-of-mass co-ordinates $\vec{R}$ and internal co-ordinates, $\vec{r}$. $V_A(X_A,Y_A,Z_A)$ is the atom-surface contribution of atom A situated at location (X_A,Y_A,Z_A). $V_B(X_B,Y_B,Z_B)$ is a similar term, but for atom B. With the separation of (2.23), the corrugation is reduced in $I(\vec{R},\vec{r})$, making the interpolation of $I(\vec{R},\vec{r})$ easier[16,26]. Once the smoother function $I(\vec{R},\vec{r})$ has been interpolated, the true potential can be retrieved by adding the V_A and V_B terms to it. To obtain the A atom-surface contribution, V_A, the corrugation reduction method is used once more:

$$V_A(X_A,Y_A,Z_A) = I_A(X_A,Y_A,Z_A) + \sum_{i=0}^{N} Q(\rho_i) .$$ (2.24)

In (2.24), $Q(\rho_i)$ is a one-dimensional reference function, which depends on the distance between atom A and surface atom i (ρ_i), N is the number of surface atoms used in the pair sum and $I_A(X_A,Y_A,Z_A)$ is a three-dimensional interpolation function. The one-dimensional reference function, $Q(\rho_i)$, and the set of N surface atoms are chosen in such a way that $I_A(X_A,Y_A,Z_A)$ again becomes a smooth function which is easily interpolated. A similar scheme is used to obtain V_B of (2.23). For homo-nuclear diatomic molecules, V_B is taken equal to V_A.

The corrugation reduction method for interpolation has been successfully applied to obtain PESs for H_2 interacting with Ni(111), Ni(110) and Ni(100)[27], for H_2+Pd(111)[26], for H_2+Pt(111)[16] and for H_2+Cu(100)[16]. The PES used in the calculations of HD scattering from and reacting on Pt(111) in chapter 6 of this thesis, and also PES 5 of

chapter 4, which was used to test the SAPS wave packet method on the H_2+Cu(100) system, have both been constructed using the corrugation reduction interpolation method.

2.3. The time-dependent wave packet method

In the second step of solving the full Schrödinger equation (2.1) within the Born-Oppenheimer approximation (2.6), the nuclear Schrodinger equation (2.8) for a static surface is solved, with the Hamiltonian given by (2.10). In the time-dependent wave packet (TDWP) method, the starting point is the time-dependent Schrödinger equation, which is:

$$i\frac{\partial \Psi(t;\vec{R},\vec{r})}{\partial t} = \hat{H}_{nuc}(\vec{R},\vec{r})\Psi(t;\vec{R},\vec{r}) . \qquad (2.25)$$

The formal solution of (2.25), for a time independent Hamiltonian, $\hat{H}_{nuc}(\vec{R},\vec{r})$, is given by:

$$\Psi(t = \Delta t;\vec{R},\vec{r}) = \exp(-i\hat{H}_{nuc}(\vec{R},\vec{r})\Delta t) \cdot \Psi(t = 0;\vec{R},\vec{r}) \qquad (2.26)$$

so that (2.8) is now formulated as an initial value problem rather than a boundary condition problem.

In (2.26), $\exp(-i\hat{H}_{nuc}(\vec{R},\vec{r})\Delta t)$ is called the time-evolution operator and allows for $\Psi(t = \Delta t;\vec{R},\vec{r})$ to be written as a superposition of stationary scattering states, $\chi(E;\vec{R},\vec{r})$, which are solutions of (2.8) with E=E_{tot}:

$$\Psi(t = \Delta t;\vec{R},\vec{r}) = \int_{-\infty}^{\infty}\chi(E;\vec{R},\vec{r}) \cdot e^{-iE\Delta t}dE . \qquad (2.27)$$

The stationary scattering state, $\chi(E;\vec{R},\vec{r})$, can also be written as a Fourier transform of the time-dependent wave function $\Psi(t;\vec{R},\vec{r})$:

$$\chi(E;\vec{R},\vec{r}) = \frac{1}{2\pi} \int_{-\infty}^{\infty} \Psi(t;\vec{R},\vec{r}) \cdot e^{iEt} dt \ . \tag{2.28}$$

2.3.1. The initial wave packet

If the molecule is located in the gas phase, i.e. if the centre-of-mass co-ordinate Z→∞, $V(\vec{R},\vec{r})$ will be independent of $\vec{R}$:

$$\lim_{Z \to \infty} V(\vec{R},\vec{r}) = V_{gas}(\vec{r}) \tag{2.29}$$

and $V(\vec{R},\vec{r})$ can therefore be split into an interaction potential, V_{int}, and a gas phase potential, V_{gas}:

$$V(\vec{R},\vec{r}) = V_{gas}(\vec{r}) + V_{int}(\vec{R},\vec{r}) \ . \tag{2.30}$$

Moreover, within the same limit of Z→∞ and making use of (2.30), $\hat{H}_{nuc}(\vec{R},\vec{r})$ becomes:

$$\lim_{Z \to \infty} \hat{H}_{nuc}(\vec{R},\vec{r}) = \hat{H}_{gas}(\vec{R},\vec{r}) = \frac{-1}{2M} \nabla_{\vec{R}}^2 + \hat{H}_{vib}(\vec{r}) + \hat{H}_{rot}(\vec{r}) + V_{gas}(\vec{r}) \ . \tag{2.31}$$

The eigen functions of $\hat{H}_{gas}(\vec{R},\vec{r})$ thus can be taken as a direct product of a plane-wave function in $\vec{R}$ and the molecule's nuclear eigen function corresponding to the rovibrational state κ, $\Phi_\kappa(\vec{r})$:

$$\hat{H}_{gas}(\vec{R},\vec{r})\left\{e^{i\vec{k}_0\cdot\vec{R}}\cdot\Phi_\kappa(\vec{r})\right\} = \left(E_{kin}(\vec{k}_0)+E_\kappa\right)\cdot\left\{e^{i\vec{k}_0\cdot\vec{R}}\cdot\Phi_\kappa(\vec{r})\right\}. \tag{2.32}$$

Here, $\vec{k}_0 = (k_0^X, k_0^Y, k_0^Z)$ is the momentum vector describing the molecule's translational motion corresponding to the molecule's centre-of-mass translational energy $E_{kin}(\vec{k}_0)$. Moreover, E_κ corresponds to the molecule's rovibrational eigen energy for state κ. With (2.32), $\Psi(t=0;\vec{R},\vec{r})$ of (2.26), can now be taken as a linear superposition of plane-waves $\exp(ik_0^Z Z)$ multiplied with a plane-wave function for initial parallel translational motion and the wave function describing the initial rovibrational state κ, $\Phi_\kappa(\vec{r})$:

$$\Psi(t=0;\vec{R},\vec{r}) = \Phi_\kappa(\vec{r})\cdot e^{ik_0^X X + ik_0^Y Y}\cdot\int_{-\infty}^{\infty} b(k_0^Z)\cdot e^{ik_0^Z Z}dk_0^Z. \tag{2.33}$$

Here, $b(k_0^Z)$ can be taken to be a Gaussian shaped momentum distribution with average momentum $\bar{k}$ and centred on $Z=Z_0$ with a half-width parameter σ:

$$b(k_0^Z) = \left(\frac{2\sigma^2}{\pi}\right)^{1/4}\cdot e^{-\sigma^2(\bar{k}-k_0^Z)^2}\cdot e^{i(\bar{k}-k_0^Z)Z_0}. \tag{2.34}$$

With (2.33) and (2.34), $\Psi(t=0;\vec{R},\vec{r})$ is taken to be a Gaussian wave packet corresponding to initial rovibrational state κ of the molecule and if $\bar{k}$ is taken to be negative, the wave packet will describe molecules moving towards the surface with a range of translational energies. However, sometimes it is advantageous to divert from this general complex form of a Gaussian wave packet. In chapter 4, section 2.3, an initial real

wave packet is constructed to ensure the use of real algebra in the computationally expensive parts of the calculations in the SAPS and the SAWP methods.

2.3.2. Time propagation

Having constructed $\Psi(t = 0; \vec{R}, \vec{r})$ according to (2.33), the time evolution operator of (2.26) can be used to propagate the time-dependent wave function forwards in time. Two propagation methods have been used in this thesis, which are both described in detail in chapter 4, section 2.3.

In the PS method, of chapters 4 to 6, use is made of the split operator formalism[28] (SPO):

$$
\begin{aligned}
\exp(-i\hat{H}_{nuc}(\vec{R}, \vec{r})\Delta t) = {} & \exp(-i\hat{K}(\vec{R}, \vec{r})\Delta t/2) \cdot \exp(-i\hat{H}_{rot}(\vec{r})\Delta t/2) \cdot \\
& \exp(-i\hat{V}(\vec{R}, \vec{r})\Delta t) \cdot \exp(-i\hat{H}_{rot}(\vec{r})\Delta t/2) \cdot \\
& \exp(-i\hat{K}(\vec{R}, \vec{r})\Delta t/2)
\end{aligned}
\tag{2.35}
$$

in which $\hat{K}(\vec{R}, \vec{r}) = \dfrac{-1}{2M}\nabla_{\vec{R}}^2 + \hat{H}_{vib}(\vec{r})$. With the symmetrical splitting of the potential operator and the kinetic energy operators in (2.35), the split operator propagator is a third order approximation to the time evolution operator[29,30] with an error of order $O(\Delta t^3)$. The time step, Δt, should therefore not be taken too big and the SPO should be considered to be a multiple time step propagator.

The other propagator used in this thesis is the modified Chebyshev propagator incorporating absorbing boundary conditions (ABC)[31]. It has been used in the SAPS and the SAWP methods in chapters 3 and 4. Using the ABC-Chebyshev propagator and symmetry adapted basis functions in the representation of the wave function, it becomes advantageous to take $\Psi(t = 0; \vec{R}, \vec{r})$ real, as explained in chapter 4, section 2.3. In the

ABC-Chebyshev propagation method, the application of the time-evolution operator on $\Psi(t = 0; \vec{R}, \vec{r})$ is expanded as:

$$\exp(-i\hat{H}_{nuc}(\vec{R}, \vec{r})\Delta t) \cdot \Psi(t = 0; \vec{R}, \vec{r}) = \sum_{n} a_n(t = \Delta t) \cdot \hat{Q}_n(\vec{R}, \vec{r}). \qquad (2.36)$$

In (2.36), the time-dependent coefficients $a_n(t = \Delta t)$ are related to Bessel functions of the first kind. The adapted Chebyshev polynomials $\hat{Q}_n(\vec{R}, \vec{r})$ stay real if $\Psi(t = 0; \vec{R}, \vec{r})$ is taken real and a dampened recursion relation exists in generating the $\hat{Q}_n(\vec{R}, \vec{r})$ from $\Psi(t = 0; \vec{R}, \vec{r})$ [31]. With the ABC-Chebyshev method, it is possible to achieve machine's precision for any Δt and the method is more efficient as a single time step propagator. Once the $\hat{Q}_n(\vec{R}, \vec{r})$ have been calculated, $\Psi(t; \vec{R}, \vec{r})$ can be computed using (2.36) by choosing the $a_n(t)$ for any time $0 < t < \Delta t$ for use in the subsequent asymptotic analysis, which is the subject of the next section.

2.3.3. Analysis of wave packet

The solutions to (2.8), $\chi(E; \vec{R}, \vec{r})$, should obey the correct scattering boundary conditions for a large enough Z value, $Z = Z_\infty$:

$$\chi(\vec{R}, \vec{r}, E)\Big|_{Z=Z_\infty} = \frac{1}{\sqrt{2\pi \cdot L_X L_Y}} e^{-ik_0^Z Z_\infty} \cdot e^{ik_0^X X} \cdot e^{ik_0^Y Y} \cdot \Phi_\kappa(\vec{r}) -$$

$$\sum_{\kappa' nm} \left\{ \left(\frac{k_0^Z}{k_{\kappa' nm}^Z}\right)^2 \cdot S_{\kappa \to \kappa' nm}(E) \cdot \Phi_{\kappa'}(\vec{r}) \cdot \right. \qquad (2.37)$$

$$\left. \frac{e^{ik_{\kappa' nm}^Z Z_\infty}}{\sqrt{2\pi \cdot L_X L_Y}} \cdot e^{i(k_0^X + n\frac{2\pi}{L_X})X} \cdot e^{i(k_0^Y + n\frac{2\pi}{L_Y})Y} \right\}$$

in which $k^Z_{\kappa'nm}$ is the final momentum in Z of the molecule, in the final rovibrational state κ' and diffraction state (n,m). Moreover, in (2.37), $S_{\kappa \to \kappa'nm}(E)$ is the total energy dependent scattering matrix, describing the scattering of the molecule initially in rovibrational state κ to the final state (κ',n,m), L_X is the surface unit cell length along X and L_Y along Y. The total energy E is conserved during the scattering event and is related to $k^Z_{\kappa'nm}$, through $\vec{k}_{\kappa'nm} = (k^X_0 + n\frac{2\pi}{L_X}, k^Y_0 + m\frac{2\pi}{L_Y}, k^Z_{\kappa'nm})$, by:

$$E = E_{\kappa'} + E_{kin}(\vec{k}_{\kappa'nm}) = E_{\kappa'} + \frac{\vec{k}_{\kappa'nm} \cdot \vec{k}_{\kappa'nm}}{2M}. \tag{2.38}$$

Using (2.37) and (2.28), the S-matrix elements can be calculated using the scattering matrix amplitude formalism of Balint-Kurti *et al.*[32,33] adapted for molecule-surface scattering[34]:

$$S_{\kappa \to \kappa'nm}(E) = \delta_{n,0}\delta_{m,0}\delta_{\kappa',\kappa} \cdot e^{-2ik^Z_0 Z_\infty} - \frac{e^{-ik^Z_{\kappa'nm}Z_\infty}}{Mb(-k^Z_0)} \cdot \sqrt{\frac{k^Z_0 \cdot k^Z_{\kappa'nm}}{2\pi}} \cdot A^{Z_\infty}_{\kappa'nm}(E) \tag{2.39}$$

with

$$A^{Z_\infty}_{\kappa'nm}(E) = \int_0^{\Delta t} C^{Z_\infty}_{\kappa'nm}(t) \cdot e^{iEt} dt \tag{2.40}$$

and

$$C^{Z_\infty}_{\kappa'nm}(t) = \left\langle \frac{e^{i(k^X_0 + n\frac{2\pi}{L_X})X} \cdot e^{i(k^Y_0 + m\frac{2\pi}{L_Y})Y}}{\sqrt{L_X L_Y}} \cdot \Phi_{\kappa'}(\vec{r}) \middle| \Psi(t;\vec{R},\vec{r}) \middle|_{Z=Z_\infty} \right\rangle. \tag{2.41}$$

Having obtained the S-matrix elements, the scattering probabilities can be obtained through:

$$P_{\kappa \to \kappa'nm}(E) = \left| S_{\kappa \to \kappa'nm}(E) \right|^2 .$$

(2.42)

The initial state selective reaction probability, as a function of the energy, is then obtained by:

$$P_r^\kappa(E) = 1 - \sum_{\kappa'nm} P_{\kappa \to \kappa'nm}(E) .$$

(2.43)

The scattering amplitude formalism is used in all implementations of the wave packet method described in this thesis and allows for the calculation of a column of the S-matrix for the range of energies contained in the initial wave packet.

In the SAWP method another analysis method, based on the calculation of the flux of the stationary scattering state through a surface, is used to obtain site-specific reaction probabilities[15,35]. In general, the flux density, $\mathbf{J}(E;X,Y,\vec{r})$, through a surface at $Z=Z_\infty$ for $\chi(E;\vec{R},\vec{r})$ is defined as[36]:

$$\mathbf{J}(E;X,Y,\vec{r}) = \frac{1}{\mu} \cdot Im\left(\chi^*(E;\vec{R},\vec{r}) \cdot \frac{\partial \chi(E;\vec{R},\vec{r})}{\partial Z} \right)\Bigg|_{Z=Z_\infty} .$$

(2.44)

By using (2.28), the stationary scattering state and its partial derivative with respect to Z can be related to the time-dependent wave function $\Psi(t;\vec{R},\vec{r})$ [15,35].

With these quantities at hand, $\mathbf{J}(E;X,Y,\vec{r})$ can be calculated straightforwardly and the reaction probability is obtained by integrating $\mathbf{J}(E;X,Y,\vec{r})$ over all the remaining degrees of freedom (X, Y and $\vec{r}$):

$$P_r(E) = -\int\int\int \mathbf{J}(E;X,Y,\vec{r})dXdYd\vec{r}. \qquad (2.45)$$

In section 2.2 of chapter 3, details are given on how the flux-based analysis method can be used to obtain site-specific reaction probabilities for H_2 reacting on Cu(100).

2.3.4. Optical potentials

The part of the wave packet that has been analysed is no longer needed and should be absorbed to avoid the storage of the wave function in memory for large Z. The absorption of the wave packet, in methods based on the SPO propagator, is easily achieved by including a purely imaginary potential into the $\exp(-i\hat{V}(\vec{R},\vec{r})\Delta t)$ part of (2.35). By including $V_{opt} = -iV_{quad}(Z)$, with $V_{quad}(Z)$ being a real function of Z, in $\hat{V}(\vec{R},\vec{r})$ in the SPO expansion, a term $\exp(-V_{quad}(Z))$ will appear in (2.35). The latter term will dampen the wave function for $Z_{min} > Z > Z_{max}$ if $V_{quad}(Z)$ is taken to be:

$$V_{quad}(Z) = \begin{cases} A\left(\dfrac{Z-Z_{min}}{Z_{max}-Z_{min}}\right)^2 & \text{for} \quad Z_{min} < Z < Z_{max} \\ 0 & \text{for} \quad Z < Z_{min} \end{cases} \qquad (2.46)$$

in which A is the strength parameter. Vibok *et al.*[37] have investigated several optical potentials of the form Ax^n and determined optimal strength parameters for them so that the sum of reflection from and transmission through the optical potential is minimal. In the calculations performed in this thesis, only the quadratic form of (2.46) has been used because it gives good results for a range of absorption energies. The higher order optical

potentials tend to absorb better for a single energy but not that well over the large range of energies typically contained in a wave packet.

With the ABC-Chebyshev propagator, the absorption of the wave packet at large Z values is achieved by the damped recursion relation of the polynomials, $\mathbf{Q}_n(\vec{R}, \vec{r})$, of (2.36)[31]. As explained in section 2.3 of chapter 4, the use of a damping operator $\hat{\gamma}$ in (4.34) not only leads to optical potential equal to

$$V_{opt} = \Delta H \left[\cos\varphi\{1 - \cosh\hat{\gamma}\} - i\sin\varphi\sinh\hat{\gamma}\right] \text{ with } \varphi = \arccos\left(\frac{E - \overline{H}}{\Delta H}\right), \qquad (2.47)$$

it also ensures that the $\mathbf{Q}_n(\vec{R}, \vec{r})$ stay real. In (2.47), ΔH and $\overline{H}$ are related to the highest and lowest eigen values of the Hamiltonian. The rather complex and energy dependent V_{opt} that is effectively used in the ABC-Chebyshev propagator is equal to, within a first order Taylor expansion, a negative imaginary optical potential of the form:

$$V_{opt} \approx -i\sin\varphi\Delta H\hat{\gamma}, \qquad (2.48)$$

which means that for $\hat{\gamma}$ a similar form to that of (2.46) can be used. Moreover, the optimal strength parameters A of (2.46), found by Vibok *et al.*[37], can be converted, taking (2.48) into account, to obtain approximate strength parameters for the $\hat{\gamma}$ operator. In the conversion, using (2.47), a rather low target energy E is taken because the choice of V_{opt} is especially important for the lower energy range, in which the wavelength associated with the translational motion is large, making the absorption hard.

2.4. Representations of the wave function

Within the time-dependent wave packet method, the propagation of the wave function corresponds to repeatedly applying the Hamiltonian, or parts of it, to the wave function. The way the application of the various operators on the wave function is performed is closely related to the representation used for the wave function. The representation of the wave function therefore determines the efficiency of the implementation of the time-dependent wave packet method on a computer. Several different representations can be taken for the wave function and this will be the subject of the current section.

2.4.1. Collocation method

A given wave function, $\Psi(\vec{r})$, can be approximated by an expansion in a set of N linearly independent basis functions $f_n(\vec{r})$:

$$\Psi(\vec{r}) \approx \sum_{n=1}^{N} C_n f_n(\vec{r}). \tag{2.49}$$

In the collocation method[29], the N coefficients C_n of (2.49) are found by relating the wave function at N points in $\vec{r}$ to the expansion and solving the N linear equations by a matrix inversion:

$$\Psi(\vec{r}_i) = \sum_{n=1}^{N} C_n f_n(\vec{r}_i) \quad \hat{=} \quad \vec{\Psi} = \mathbf{f}\vec{C}. \tag{2.50}$$

In (2.50), $\mathbf{f}$ is an N dimensional square matrix transforming the coefficient vector $\vec{C}$ into the wave function vector $\vec{\Psi}$. The inverse of the matrix $\mathbf{f}$, $\mathbf{f}^{-1}$, can be used to obtain the vector $\vec{C}$ from the vector $\vec{\Psi}$ by $\vec{C} = \mathbf{f}^{-1}\vec{\Psi}$. Once $\vec{C}$ has been obtained, the action of a

non-local operator in $\vec{r}$ on $\Psi(\vec{r})$, $\hat{O}(\vec{r})$ with $\hat{O}(\vec{r})f_n(\vec{r}) = f_n^{'}(\vec{r})$, can be approximated by applying $\hat{O}(\vec{r})$ to (2.49):

$$\hat{O}(\vec{r})\Psi(\vec{r}) \approx \sum_{n=1}^{N} C_n \hat{O}(\vec{r})f_n(\vec{r}) \approx \sum_{n=1}^{N} C_n f_n^{'}(\vec{r}). \qquad (2.51)$$

The basis of the collocation method is thus the construction and inversion of matrix **f** to be able to find the vector $\vec{C}$ so that the effect of $\hat{O}(\vec{r})$ on $\Psi(\vec{r})$ can be computed according to (2.51). The advantage of the collocation method lies in the freedom of choice in $f_n(\vec{r})$ so that the calculation of $\hat{O}(\vec{r})f_n(\vec{r}) = f_n^{'}(\vec{r})$ is easier than calculating $\hat{O}(\vec{r})\Psi(\vec{r})$ directly.

2.4.2. Finite Basis Representations and Discrete Variable Representations

In the collocation method the matrix $\mathbf{f}^{-1}$, the inverse of **f** in (2.50), effectively transforms the wave function at the N points $\vec{r}_i$ into the N coefficients C_n. However, if the linearly independent basis functions $f_n(\vec{r})$ of (2.49) are chosen to be eigen functions of the operator $\hat{O}(\vec{r})$ and are taken to be mutually orthogonal over the N discrete points $\vec{r}_i$:

$$\sum_{k=1}^{N} f_n^{*}(\vec{r}_k)f_m(\vec{r}_k) = \delta_{n,m}, \qquad (2.52)$$

the collocation scheme can be significantly simplified. The matrix **f** does not have to be inverted anymore because with (2.52) the following holds for (2.50):

$$\sum_{k=1}^{N} f_m^{*}(\vec{r}_k)\Psi(\vec{r}_k) = \sum_{n=1}^{N}\sum_{k=1}^{N} C_n f_n(\vec{r}_k)f_m^{*}(\vec{r}_k) = \sum_{n=1}^{N} C_n \delta_{n,m} = C_m. \qquad (2.53)$$

If at the same time $\hat{O}(\vec{r})f_n(\vec{r})=o_nf_n(\vec{r})$ holds, (2.51) reduces to

$$\hat{O}(\vec{r})\Psi(\vec{r}) \approx \sum_{n=1}^{N}C_n\hat{O}(\vec{r})f_n(\vec{r}) \approx \sum_{n=1}^{N}C_no_nf_n(\vec{r}) \approx \sum_{n=1}^{N}C_n'f_n(\vec{r}) \qquad (2.54)$$

and the operator $\hat{O}(\vec{r})$ is considered to be diagonal in the $\vec{C}$ representation. The effect of $\hat{O}(\vec{r})$ on $\Psi(\vec{r})$ can now be computed in three steps:

1) Transforming the discrete variable representation[38-41] (DVR) of $\Psi(\vec{r})$, $\vec{\Psi}$, into the finite basis representation[38-41] (FBR) of $\Psi(\vec{r})$, $\vec{C}$, by using $\mathbf{f}^{-1}=\mathbf{f}^{\dagger}$ because of (2.52).

2) Applying the operator $\hat{O}(\vec{r})$ on the FBR of $\Psi(\vec{r})$ to get the result $\vec{C}'$, which is an FBR of $\hat{O}(\vec{r})\Psi(\vec{r})$. The operator $\hat{O}(\vec{r})$ can be represented by a diagonal matrix $\mathbf{O}_{nm}=\delta_{nm}o_n$ in the FBR because only a vector-vector dot product is needed to apply $\hat{O}(\vec{r})$ on $\vec{C}$.

3) Transforming $\vec{C}'$, the FBR of $\hat{O}(\vec{r})\Psi(\vec{r})$, back to the DVR of $\hat{O}(\vec{r})\Psi(\vec{r})$, $\vec{\Psi}'$, by using $\mathbf{f}$.

The matrices $\mathbf{f}$ and $\mathbf{f}^{-1}$ are used to switch between the DVR and the FBR of the wave function and the two representations can be considered to be conjugate to each other[38-41]. Moreover, the complete procedure of applying $\hat{O}(\vec{r})$ on $\Psi(\vec{r})$ can now be expressed in matrix vector notation as: $\vec{\Psi}' = \mathbf{fOf}^{-1}\vec{\Psi}$. This method of applying an operator to a wave function is called a pseudo-spectral (PS) method because use of a discrete co-ordinate space and its conjugate space is made in the procedure[38-41]. In this thesis, several representations of the wave function have been based on this general pseudo-spectral scheme. Two of them will be briefly discussed here.

The Fourier representation

The plane-wave functions, $e^{ik\cdot r}$, have three remarkable properties. Firstly, they are eigen functions of the Laplacian, $\nabla_r^2 e^{ik\cdot r} = -k^2 e^{ik\cdot r}$, secondly they are mutually orthogonal for a series of N equally spaced discrete points $r_n = nL/N$ over the range [0,L]:

$$\sum_{n=0}^{N-1} e^{\frac{-2\pi ip\cdot r_n}{L}} e^{\frac{2\pi iq\cdot r_n}{L}} = N\delta_{p,q} \tag{2.55}$$

where p and q are integers and thirdly, they form a complete set for periodic or bandwidth limited functions of $r^{42,43}$. According to (2.55), the discrete space conjugate to r_n, often referred to as momentum space, is given by $k_m = \dfrac{2\pi m}{L}$ with 0≤m≤N-1 so that Δk=2π/L. The unitary change-of-basis matrix $\mathbf{f}$ of (2.50) for plane-waves has the elements $\mathbf{f}_{mn} = e^{2\pi imn/N}$. Plane-waves are often used to represent the wave function in translational or vibrational degrees of freedoms, especially if there is periodicity associated with these degrees of freedom, like for diffraction[44-47], because the plane-waves are eigen functions of the Laplacian and form a complete set for periodic functions. Moreover, transforms based on plane-waves are called Fourier transforms and efficient algorithms are available to compute them: whereas the normal discrete Fourier transform, scales as N^2, the Fast Fourier Transform (FFT) method scales approximately as $N\log_2 N$ for suitably chosen values of $N^{42,48}$.

Gaussian Quadratures

In order to achieve the discrete orthogonality of $f_n(\vec{r}_k)$ over the N points $\vec{r}_k$ in (2.52), use can also be made of continuous polynomials $p_n(\vec{r})$ mutually orthogonal with respect to a weighting function $\omega(\vec{r})$ over the range [a,b]:

$$\int_a^b \omega(\vec{r}) p_n^*(\vec{r}) p_m(\vec{r}) d\vec{r} = \delta_{n,m} .$$
(2.56)

In (2.56), assuming $p_n(\vec{r})$ to be an nth order polynomial, $p_n^*(\vec{r}) p_m(\vec{r})$ is a polynomial of degree n+m and the above orthogonality integral can be written as:

$$\int_a^b \omega(\vec{r}) P_{n+m}(\vec{r}) d\vec{r} = \delta_{n,m} .$$
(2.57)

According to the Gaussian quadrature theorem[38-43,49,50], the integral of (2.57) can be numerically calculated by:

$$\int_a^b \omega(\vec{r}) P_{n+m}(\vec{r}) d\vec{r} = \sum_{k=1}^N A_k P_{n+m}(\vec{r}_k)$$
(2.58)

with

$$A_k = \int_a^b \frac{\omega(\vec{r}) \cdot p_N(\vec{r})}{(\vec{r} - \vec{r}_k) \cdot \left. \dfrac{\partial p_N(\vec{r})}{\partial \vec{r}} \right|_{\vec{r} = \vec{r}_k}} d\vec{r}$$
(2.59)

and $\vec{r}_k$ being the N roots of the Nth order polynomial $p_N(\vec{r})$ which obeys (2.56). The numerical calculation of (2.58) is exact if n+m≤2N-1.

With these formulas, (2.56) can be rewritten as

$$\delta_{n,m} = \int_a^b \omega(\vec{r})p_n^*(\vec{r})p_m(\vec{r})d\vec{r} = \sum_{k=1}^N \left(\sqrt{A_k}\,p_n^*(\vec{r}_k)\right)\left(\sqrt{A_k}\,p_m(\vec{r}_k)\right) \qquad (2.60)$$

and (2.52) can be obtained by setting $f_n(\vec{r}_k)=\sqrt{A_k}\,p_n(\vec{r}_k)$. With this choice, the transformation matrix $\mathbf{f}$ of (2.50) will have the elements $\mathbf{f}_{kn}=\sqrt{A_k}\,p_n(\vec{r}_k)$ and can be shown to be an orthogonal matrix ($\mathbf{f}^{-1}=\mathbf{f}^T$) from (2.60) for real polynomials $p_n(\vec{r})$.

Gauss-Legendre representation

Whereas the plane-waves form a suitable basis set for degrees of freedom for which the wave function exhibits periodicity, or for evaluating the action of operators like the Laplacian, the rotational kinetic energy operator of the Hamiltonian and the angular parts of the wave function, suggest a different representation. The eigen functions of the rotational kinetic energy operator $\hat{H}_{rot}(\vec{r})$ of the Hamiltonian for a diatomic molecule, (2.12), are given by the spherical harmonics:

$$\frac{\hat{j}^2}{2\mu r^2}\mathbf{Y}_{jm_j}(\theta,\varphi) = \frac{j(j+1)}{2\mu r^2}\mathbf{Y}_{jm_j}(\theta,\varphi)\,. \qquad (2.61)$$

A representation of the angular part of the wave function based on spherical harmonics would therefore be advantageous. Moreover, because the spherical harmonics can be written as

$$\mathbf{Y}_{jm_j}(\theta,\varphi) = \frac{1}{\sqrt{2\pi}}L_{m_j}^j(\cos\theta)\cdot e^{im_j\varphi} \qquad (2.62)$$

with $L^j_{m_j}(x)$ being the normalised associated Legendre polynomials[39,42,43,49], an orthogonality relation for the $\mathbf{Y}_{jm_j}(\theta,\varphi)$ exists:

$$\left\langle \mathbf{Y}_{jm_j}(\theta,\varphi) \middle| \mathbf{Y}_{j'm_j'}(\theta,\varphi) \right\rangle = \delta_{j',j}\delta_{m_j,m_j'}. \tag{2.63}$$

Because of (2.63), an orthogonal transform from the (j,m_j) FBR to the (θ,φ) DVR, based on Gaussian quadratures for θ and FFTs for φ, can be formulated[39,49-52] as is explained in section 2.2 of chapter 4, where it has been used in the PS method. Also explained, in that same section, is the adaptation of this transform, originally developed by Lemoine *et al.*[39,49-52], to the C_{4v} symmetry case for square surfaces so that it can be used in the SAPS method.

2.4.3. Mixed representation

In the representations discussed above, the wave function was either defined on specific grid points in co-ordinate space (DVR), or equivalently, as a set of expansion coefficients corresponding to a suitable basis set in conjugate space (FBR). In general a matrix transform was used to switch between the DVR and the FBR and the action of an operator was taken to be diagonal in one of the two representations. Besides these pseudo-spectral schemes, other methods exist that do not need the wave function to be transformed back and forth by a matrix to apply an operator. The Close-Coupling Wave Packet[53-55] (CCWP) method represents the operator itself, which corresponds to specific degrees of freedom of the wave function, as a matrix. This is easily understood by considering the following hybrid representation of the wave function:

$$\Psi(t;\vec{R},\vec{r}) = \sum_n C_n(t;\vec{R})p_n(\vec{r}). \tag{2.64}$$

In (2.64), $\vec{r}$ represents one or more of the molecule's internal co-ordinates, $\vec{R}$ the other degrees of freedom and the $C_n(t;\vec{R})$ the expansion coefficients corresponding to the basis functions $p_n(\vec{r})$. If the basis functions $p_n(\vec{r})$ are taken to be mutually orthogonal,

$$\langle p_n(\vec{r}) | p_m(\vec{r}) \rangle = \delta_{n,m}, \tag{2.65}$$

the equations of motion for the coefficients $C_n(t;\vec{R})$ can be found by inserting (2.64) into the time dependent nuclear Schrödinger equation with Hamiltonian (2.10) and making use of (2.65):

$$\left\langle p_m(\vec{r}) \middle| \hat{H}_{nuc}(\vec{R},\vec{r}) \left\{ \sum_n C_n(t;\vec{R}) p_n(\vec{r}) \right\} \right\rangle = i \frac{\partial C_m(t;\vec{R})}{\partial t}. \tag{2.66}$$

The left-hand side of (2.66) can be rewritten as:

$$\frac{-1}{2M} \nabla_{\vec{R}}^2 C_m(t;\vec{R}) + \sum_n C_n(t;\vec{R}) \langle p_m(\vec{r}) | \left(\hat{H}_{vib}(\vec{r}) + \hat{H}_{rot}(\vec{r}) + V(\vec{R},\vec{r}) \right) | p_n(\vec{r}) \rangle \tag{2.67}$$

and the matrix corresponding to the operator $\hat{O}(\vec{R},\vec{r}) = \left(\hat{H}_{vib}(\vec{r}) + \hat{H}_{rot}(\vec{r}) + V(\vec{R},\vec{r}) \right)$ starts to appear. The equation of motion for the $C_m(t;\vec{R})$ is rewritten to

$$i \frac{\partial C_m(t;\vec{R})}{\partial t} = \frac{-1}{2M} \nabla_{\vec{R}}^2 C_m(t;\vec{R}) + \sum_n C_n(t;\vec{R}) \langle p_m(\vec{r}) | \hat{O}(\vec{R},\vec{r}) | p_n(\vec{r}) \rangle \tag{2.68}$$

and as is clear from (2.68), the set of second order differential equations for $C_m(t;\vec{R})$ is coupled by the operator matrix $\mathbf{O}_{mn}(\vec{R}) = \langle p_m(\vec{r}) | \hat{O}(\vec{R},\vec{r}) | p_n(\vec{r}) \rangle$. To solve (2.68) a pseudo-spectral technique can be used by employing DVR/FBR transforms for the

$C_m(t;\vec{R})$ in order to evaluate the Laplacian in $\vec{R}$. The representation of the full wave function in (2.64) is therefore called a mixed or hybrid representation.

Although a clear distinction between the CCWP and the general PS approach is made based on how the action of an operator on the wave function is calculated, a correspondence can be found in the computation of the matrices that represent the operators in either method[38,40,41]. To understand this and relate the CCWP approach to the PS approach, one extra assumption has to be made about the basis functions $p_n(\vec{r})$ used in (2.64). If the $p_n(\vec{r})$ are, apart from being mutually orthogonal, also assumed to be eigen functions of the $\hat{H}_{rot}(\vec{r})$ and $\hat{H}_{vib}(\vec{r})$ operators, $\left(\hat{H}_{rot}(\vec{r}) + \hat{H}_{rot}(\vec{r})\right)p_n(\vec{r}) = \varepsilon_n p_n(\vec{r})$, the equation of motion of $C_m(t;\vec{R})$, (2.68), can be rewritten as:

$$
i\frac{\partial\, C_m(t;\vec{R})}{\partial\, t} = \frac{-1}{2M}\nabla_{\vec{R}}^2 C_m(t;\vec{R}) + \varepsilon_m C_m(t;\vec{R}) +
$$
$$
\sum_n C_n(t;\vec{R})\langle p_m(\vec{r})|\, V(\vec{R},\vec{r})\, |p_n(\vec{r})\rangle.
$$

(2.69)

The original coupling matrix $\mathbf{O}_{nm}(\vec{R})$ corresponding to the operator $\hat{O}(\vec{R},\vec{r})$ has been replaced by a potential coupling-matrix $\mathbf{V}_{nm}(\vec{R}) = \langle p_m(\vec{r})|V(\vec{R},\vec{r})|p_n(\vec{r})\rangle$, corresponding to the potential operator $V(\vec{R},\vec{r})$ which is diagonal in co-ordinate space.

In the PS method the action of an operator, that is diagonal in conjugate space, on the wave function in co-ordinate space was found to be $\vec{\Psi}' = \mathbf{f}\mathbf{O}\mathbf{f}^{-1}\vec{\Psi}$ with $\mathbf{O}$ being a diagonal matrix. For an operator that is local in co-ordinate space, $\vec{\Psi}' = \mathbf{V}\vec{\Psi}$ with $\mathbf{V}$ being diagonal, the corresponding expression of such an operator acting on the wave function in conjugate space would be $\vec{C}' = \mathbf{f}^{-1}\mathbf{V}\mathbf{f}\vec{C}$.

The matrix elements of the similarity-transformed matrix, $\mathbf{f}^{-1}\mathbf{V}\mathbf{f}$, can be found by the expansion of the individual matrices into their elements:

$$\sum_{i,j}\mathbf{f}_{ni}^{-1}\mathbf{V}_{ij}\delta_{ij}\mathbf{f}_{jm} = \sum_{i}\mathbf{f}_{ni}^{*T}V(\vec{R},\vec{r}_i)\mathbf{f}_{im} = \sum_{i}f_n^{*}(\vec{r}_i)V(\vec{R},\vec{r}_i)f_m(\vec{r}_i) \approx \mathbf{V}_{nm}(\vec{R}). \qquad (2.70)$$

If the basis set $f_n(\vec{r})$ and the discrete points $\vec{r}_i$, in the PS approach, are chosen according to the Gaussian quadrature theory of the previous section, $f_n(\vec{r}_i)=\sqrt{A_i}\,p_n(\vec{r}_i)$, the right-hand side of (2.70) corresponds to the CCWPs potential coupling-matrix, $\mathbf{V}_{nm}(\vec{R})$, being calculated numerically with Gaussian accuracy rather than analytically.

A version of the CCWP method that is based on the expansion of the wave function in spherical harmonics is described in section 2.2 of chapter 4. It has been used in the first non-reactive rotationally inelastic molecule-surface scattering calculations[53-55] and can easily be extended to the use of a symmetry-adapted basis set[56-58].

2.4.4. Symmetry Adapted representations

As explained in section 2.2 of chapter 4, the introduction of the use of a symmetry-adapted basis set into the CCWP method, is rather straightforward. The symmetry-adapted wave packet[56-58] (SAWP) method does precisely this by defining a potential coupling matrix given by (4.21). Details on obtaining the symmetry-adapted basis set for diatomic molecules scattering at normal incidence from a square and static surface are presented in chapter 4 and the reader is referred to that part of the thesis. The incorporation of symmetry in the general pseudo-spectral scheme for the rotational degrees of freedom of Lemoine *et al.*[39,49-52], to obtain the symmetry-adapted pseudo-spectral (SAPS) method, is also explained in that chapter.

2.5. References

1   A. Messiah, Quantum Mechanics (John Wiley & sons, New York, Chichester, Brisbane, Toronto, 1958).
2   P. Hohenberg and W. Kohn, Phys. Rev. B 136, 864 (1964).
3   W. Kohn and L. J. Sham, Phys. Rev. A 140, 1133 (1965).
4   S. H. Vosko, L. Wilk, and M. Nusair, Can. J. Phys. 58, 1200 (1980).
5   J. A. White, D. M. Bird, M. C. Payne, and I. Stich, Phys. Rev. Lett. 73, 7344 (1994).
6   G. Wiesenekker, G. J. Kroes, E. J. Baerends, and R. C. Mowrey, J. Chem. Phys. 102, 3873 (1995).
7   B. Hammer, M. Scheffler, K. W. Jacobsen, and J. K. Norskov, Phys. Rev. Lett. 73, 1400 (1994).
8   D. J. W. Geldart and M. Rasolt, Phys. Rev. B 13, 1477 (1976).
9   J. P. Perdew, Physica B 172, 1 (1991).
10   A. D. Becke, Phys. Rev. A 38, 3098 (1988).
11   J. P. Perdew, Phys. Rev. B 33, 8822 (1986).
12   J. P. Perdew, Electronic structure of Solids '91 (Akademie Verslag, Berlin, 1991).
13   J. P. Perdew, J. A. Chevary, S. H. Vosko, K. A. Jackson, M. R. Pederson, D. J. Singh, and C. Fiolhais, Phys. Rev. B 46, 6671 (1992).
14   S. Wilke and M. Scheffler, Phys. Rev. B 53, 4926-4932 (1996).
15   D. A. McCormack, G. J. Kroes, R. A. Olsen, J. A. Groeneveld, J. N. P. v. Stralen, E. J. Baerends, and R. C. Mowrey, Faraday Discuss. 117, 109 (2000).
16   R. A. Olsen, H. F. Busnengo, A. Salin, M. F. Somers, G. J. Kroes, and E. J. Baerends, J. Chem. Phys. 116, 3841 (2002).
17   G. Wiesenekker, G. J. Kroes, and E. J. Baerends, J. Chem. Phys. 104, 157 (1996).
18   J. Q. Dai and J. Z. H. Zhang, J. Chem. Phys. 102, 6280 (1995).
19   M. Persson, J. Stromquist, L.Bengtsson, B. Jackson, D. V. Shalashilin, and B. Hammer, J. Chem. Phys. 110, 2240 (1999).
20   G. T. Velde and E. J. Baerends, Chem. Phys. 177, 399 (1993).
21   J. Neugebauer and M. Scheffler, Phys. Rev. B 46, 16067 (1992).
22   D. Post and E. J. Baerends, J. Chem. Phys. 78, 5663 (1983).
23   J. L. Whittem and H. Yang, Surf. Sci. Repts. 24, 55 (1996).
24   J. McCreery and G. Wolken, J. Chem. Phys. 63, 2340 (1975).
25   S. Sato, J. Chem. Phys. 23, 592 (1955).
26   H. F. Busnengo, A. Salin, and W. Dong, J. Chem. Phys. 112, 7641 (2000).
27   G. Kresse, Phys. Rev. B 62, 8295 (2000).
28   M. D. Feit, J. A. Fleck, and A. Steiger, J. Comput. Phys. 47, 412 (1982).
29   R. Kosloff, J. Phys. Chem. 92, 2087 (1988).
30   L. L. Halcomb and D. J. Diestler, J. Chem. Phys. 84, 3130 (1986).
31   V. A. Mandelshtam and H. S. Taylor, J. Chem. Phys. 103, 2903 (1995).
32   G. G. Balint-Kurti, R. N. Dixon, and C. C. Marston, J. Chem. Soc. 86, 1741 (1990).
33   G. G. Balint-Kurti, R. N. Dixon, and C. C. Marston, Int. Rev. Phys. Chem. 11, 317 (1992).
34   R. C. Mowrey and G. J. Kroes, J. Chem. Phys. 103, 1216 (1995).

35   D. A. McCormack, G. J. Kroes, R. A. Olsen, J. A. Groeneveld, J. N. P. v. Stralen, E. J. Baerends, and R. C. Mowrey, Chem. Phys. Lett. 328, 317-324 (2000).

36   R. A. Olsen, P. H. T. Philipsen, E. J. Baerends, G. J. Kroes, and O. M. Lovvik, J. Chem. Phys. 106, 9286 (1997).

37   A. Vibok and G. G. Balint-Kurti, J. Phys. Chem. 96, 8712 (1992).

38   J. V. Lill, G. A. Parker, and J. C. Light, Chem. Phys. Lett. 89, 483 (1982).

39   G. C. Corey, J. W. Tromp, and D. Lemoine, in Numerical grid methods and their applications to Schrodinger equation, Vol. 412, edited by C. Cerjan (Kluwer Academic, Dordrecht, 1993), pp. 1-23.

40   A. S. Dickinson and P. R. Certain, J. Chem. Phys. 49, 4209 (1968).

41   J. P. Hamilton and J. C. Light, J. Chem. Phys. 84, 306 (1986).

42   Numerical Recipes in FORTRAN 77 (Cambridge University Press, 1992).

43   G. B. Arfken and H. J. Weber, Mathematical methods for physicists, 4 ed. (Acedemic press, San Diego, California, 1995).

44   A. Gross, S. Wilke, and M. Scheffler, Phys. Rev. Lett. 75, 2718 (1995).

45   G. J. Kroes, E. J. Baerends, and R. C. Mowrey, Phys. Rev. Lett. 78, 3583 (1997).

46   J. Q. Dai and J. C. Light, J. Chem. Phys. 107, 1676 (1997).

47   J. Q. Dai and J. C. Light, J. Chem. Phys. 108, 7816 (1998).

48   A. Besprozvannaya and D. J. Tannor, Comput. Phys. Commun. 63, 569 (1991).

49   G. C. Corey and D. Lemoine, J. Chem. Phys. 97, 4115 (1992).

50   D. Lemoine and G. C. Corey, J. Chem. Phys. 92, 6175 (1990).

51   D. Lemoine, Comput. Phys. Commun. 97, 331 (1996).

52   D. Lemoine and G. C. Corey, J. Chem. Phys. 94, 767 (1991).

53   R. C. Mowrey and D. J. Kouri, Chem. Phys. Lett. 119, 285 (1985).

54   R. C. Mowrey and D. J. Kouri, J. Chem. Phys. 84, 6466 (1986).

55   R. C. Mowrey and D. J. Kouri, J. Chem. Phys. 86, 6140 (1987).

56   G. J. Kroes, J. G. Snijders, and R. C. Mowrey, J. Chem. Phys. 103, 5121 (1995).

57   G. J. Kroes, E. J. Baerends, and R. C. Mowrey, J. Chem. Phys. 107, 3309 (1997).

58   G. J. Kroes, J. G. Snijders, and R. C. Mowrey, J. Chem. Phys. 102, 5512-5524 (1994).

Chapter 3

Signatures of site-specific reaction of H_2 on Cu(100)

Abstract

Six-dimensional quantum dynamical calculations are presented for the reaction of (v,j) H_2 on Cu(100), at normal incidence, for v=0-1 and (j=0-5. The dynamical calculations employed a potential energy surface computed with density functional theory, using the generalised gradient approximation and a slab representation for the adsorbate-substrate system. The aim of the calculations was to establish signatures from which experiments could determine the dominant reaction site of H_2 on the surface and the dependence of the reaction site on the initial rovibrational state of H_2. Two types of signatures were found. First, we predict that, at energies near threshold, reaction of (v=1) H_2 is rotationally enhanced, because it takes place at the top site, which has an especially late barrier and a reaction path with a high curvature. On the other hand, we predict reaction to be almost independent of j for (v=0) H_2, which reacts at the bridge site. Second, we predict that, at collision energies slightly above threshold for which the reaction probabilities of the (v=0) and (v=1) states are comparable, the rotational quadrupole alignment of (v=1) reacting molecules should be larger than that of (v=0) reacting molecules, for j=1, 4 and 5. For (j=2) H_2, the opposite should be true and for (j=3) H_2, the rotational quadrupole alignment should be approximately equal for (v=1) and (v=0) H_2. These differences can all be explained by the difference in the predicted reaction site for (v=1) and (v=0) H_2 (top and bridge) and by the differences in the anisotropy of the potential at the reaction barrier geometries associated with these sites. Our predictions can be tested in associative desorption experiments, using currently available experimental techniques.

3.1. Introduction

The dissociation of H_2 on Cu is a benchmark system for activated surface reactions[1] and has been labelled a "springboard for new ideas on molecule-surface reactions"[2]. Many experimental[3-24] and theoretical[24-56] studies have been performed on this system, but much remains to be learnt.

In the past two decades, progress in the unravelling of H_2+metal-surface reactions has been enormous both for theory[24-73] and experiments[3-24]. Molecular beam experiments yield reaction probabilities[11,12,21] and inelastic scattering probabilities[17,18,24] that are resolved with respect to the collision energy. With the use of stimulated Raman pumping in molecular-beam-experiments, the scattering of H_2 from a specified initial (v=1,j) level can now be investigated for reactive surfaces[17,18,24]. Invoking detailed balance, relative reaction probabilities can be obtained from associative desorption experiments[12,22,23]. Using state-selective detection in combination with time-of-flight techniques, such experiments[12] can now determine energy-resolved relative reaction probabilities which are initial-state selected with respect to both the vibrational state (v) and rotational level (j). Associative desorption experiments can also determine the influence on reaction of the molecule's alignment with respect to the surface, by measuring the rotational quadrupole alignment, $A_0^{(2)}(v,j)$, of the angular momentum of the desorbing molecules[13-16].

Theory can now also make important contributions. Reduced-dimensionality theoretical studies on similar systems and models[25,34,37-39,42-52,55-58,69,72] have revealed interesting effects like vibrational enhancement of reaction[40,41,46,52], the effect on reaction of the corrugation of the potential energy surface (PES)[47] and effects of the alignment of the incident H_2 molecule[34,39,42-44,47,48]. These calculations and classical trajectory studies[74,75], suggested that in order to obtain quantitatively accurate reaction probabilities, a six-dimensional (6D) quantum dynamical study would be needed. This was confirmed in one

of the first 6D quantum studies[31]. In such 6D calculations, the motion in all six degrees of freedom of the incident molecule is modelled without approximation.

Thanks to the improved accuracy of density functional theory (DFT[76,77]) for determining potential energy surfaces (PESs) for H_2 + metal systems[26,78-80], six-dimensional quantum dynamical calculations now yield quantitatively accurate results[26,67,81-83] and are starting to offer a structured procedure for obtaining predictions for experiments[26,35,59,66,83]. In one case, the calculations[66] actually challenged older experiments[8,10], with newer experiments confirming the validity of the theoretical results[59]. Although 6D calculations have been performed for H_2+Pd(100)[60-67], using a time-independent method, and for H_2+Cu(100)[26,28-31,35] and H_2+Cu(111)[32,33], using time-dependent methods, six dimensional quantum dynamical calculations still represent a formidable task requiring the use of super-computers and specialised codes.

In recent 6D quantum dynamical studies of the H_2+Cu(100) system, a new flux-based method was used to obtain site-specific reaction probabilities for a range of initial rovibrational states of H_2 (v=0 and 1, j=0,1,4 with m_j=0-j)[26,27]. These studies showed that for low incidence energies the reaction does not always occur at the site with the minimum barrier height. Depending on the initial rovibrational state of the H_2 molecule, the dissociation can take place almost exclusively on sites with higher barriers, with total reaction probabilities of the order of 5%. Furthermore, both studies also suggested an experimental signature of the dependence of the preferred reaction site on the initial vibrational state of the molecule. Specifically, it was noted that the rotational quadrupole alignment, $A_0^{(2)}(E;v,j)$, of (v=1,j=4) H_2 should be fairly high compared to the alignment of (v=0,j=4) H_2 at low translational energies where the total reaction probability is around 5%. The measurement of this effect would confirm our prediction and therefore support our finding that (v=1) H_2 reacts at the top site and (v=0) H_2 at the bridge site[26,27].

The aims of the present study are to see whether the alignment signature for the reaction site previously found for (j=4) also holds for other low j values and to find additional signatures for site-specific reaction. To achieve these goals, calculations were performed

on the scattering of (v,j,m_j) H_2 from Cu(100), for v=0-1 and j=0-5. Our calculations will show that the alignment signature previously found for (j=4) H_2 also holds for (j=1) and (j=5) H_2, but that the differences between the rotational quadrupole alignment of (v=1) and (v=0) reacting H_2 are related to the preferred reaction sites of (v=1) and (v=0) H_2 in a different way for (j=2) and (j=3). We will show that the trends in the alignment of the reacting molecules can be explained by steric hindering effects and an inelastic rotational enhancement effect, in which the molecule transfers energy from its rotation to motion along the reaction path via a rotationally-inelastic mechanism.

Our calculations will also show a second signature for site-specific reaction. This is related to the j-dependence of the degeneracy-averaged reaction probabilities, which differs for (v=1) and (v=0) H_2. We will show that another rotational enhancement mechanism (elastic rotational enhancement, in which the energy transfer from rotation to motion along the reaction path occurs because the molecule's rotational constant is lower at the barrier than in the gas phase) is largely responsible for this.

Section (3.2) discusses the system and the dynamical methods we use. In section (3.3) the PES is discussed and computational details are given in section (3.4). Degeneracy-averaged and site-specific degeneracy-averaged reaction probabilities will be presented and discussed in section (3.5.1). The question of whether the previously found rotational quadrupole alignment signature holds for all low j (j=1-5) will be discussed in section (3.5.2). Results for the two experimental signatures found are summarised in section (3.6).

3.2. Dynamical method

3.2.1. Model

The results of this study were obtained with a six-dimensional symmetry-adapted close-coupling time-dependent wave-packet method (SAWP)[31]. In this method, all degrees of freedom of the H_2 molecule are treated quantum mechanically using two approximations, the Born-Oppenheimer approximation and neglect of phonons.

The use of the Born-Oppenheimer approximation corresponds to the neglect of electron-hole pair excitations and the use of a single PES, in this case the PES for the electronic ground-state. The validity of this approximation is discussed in references 1, 53 and 84. The neglect of phonons of the Cu(100) surface entails the use of a dynamical model in which the copper atoms are fixed at their ideal lattice positions so that the system, which is in principle of infinite dimensionality, reduces to a six-dimensional problem. Due to the large difference in mass of the hydrogen and copper atoms, the neglect of phonon excitation is thought to be reasonable[85-87]. A more detailed justification of these approximations is given elsewhere[1,53].

3.2.2. Wave packet method

Within the Born-Oppenheimer approximation and the static representation of the metal surface, the Hamiltonian of the system can be written in atomic units:

$$\hat{H}_{6D} = -\frac{1}{2M}\left(\frac{\partial^2}{\partial X^2} + \frac{\partial^2}{\partial Y^2} + \frac{\partial^2}{\partial Z^2}\right) - \frac{1}{2\mu}\frac{\partial^2}{\partial r^2} + \frac{\hat{j}^2}{2\mu r^2} + V(Z,X,Y,r,\theta,\varphi) \qquad (3.1)$$

Here, X, Y and Z describe the motion of the centre of mass of H_2 and M and μ are the total and reduced masses of the H_2 molecule respectively. Furthermore, $V(Z,X,Y,r,\theta,\phi)$ is the 6D PES, which depends on the distance of the molecule to the surface, Z, the molecule's centre-of-mass co-ordinates for motion along the surface, X and Y, the H-H distance r and the angles representing the orientation of the molecule, θ and ϕ (see Figure 3.1).
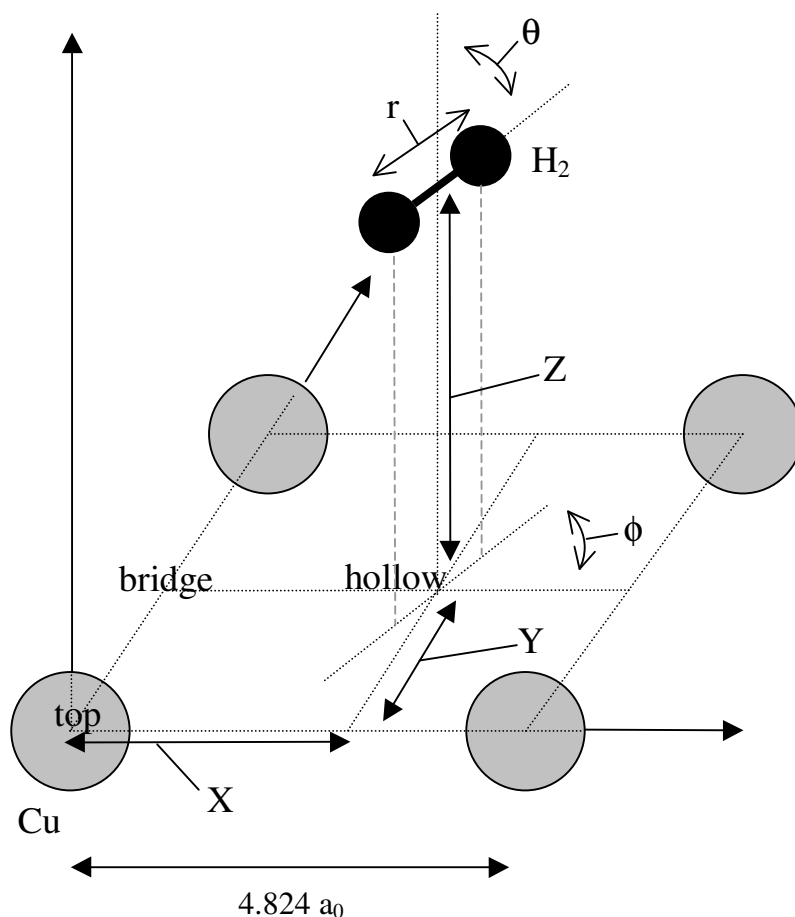
Figure 3.1: The co-ordinate system for H_2 + Cu(100). Here X,Y and Z give the position of the molecule's centre-of-mass, r is the H-H distance, ϕ the azimuthal angle and θ the polar angle of orientation of the molecule. The high-symmetry surface sites are also shown.

When considering normal incidence only, the symmetry of the metal surface can be used to reduce the computational costs[31,68,73]. The non-symmetry-adapted wave function can be projected onto a symmetry-adapted basis set, with functions belonging to different irreducible representations. For each of these representations, a separate calculation must be performed. The number of calculations needed (one or two) and the relevant species, depend on the initial value of the magnetic rotational quantum number of the molecule, m_j. Having completed the calculations for the separate irreducible representations, state-to-state probabilities for scattering and reaction probabilities can be obtained by performing a unitary transformation of the blocked symmetry-adapted scattering matrix[68,73].

Within the SAWP method, the wave packet at time t for species Γ of the C_{4v} point group is represented as an expansion of real symmetry-adapted basisfunctions χ, dependent on X, Y, θ and ϕ for species Γ[29,30,38]. A grid representation is used for the r and Z degrees of freedom:

$$\Psi_{6D}^{\Gamma}(Z_i, r_j, X, Y, \theta, \phi; t) = \sum_{\ell} f_{\ell}^{\Gamma}(Z_i, r_j; t)\chi_{\ell}^{\Gamma}(X, Y, \theta, \phi) \qquad (3.2)$$

with ℓ being a collective index for the quantum numbers j and m_j associated with the rotational state and n and m associated with the diffractional state of the molecule.

The initial symmetry-adapted wave packet for species Γ is propagated in time using the absorbing boundary condition (ABC)[88] evolution operator:

$$\exp(-i\hat{H}t) = \sum_{n=0}^{} (2-\delta_{n0}) \cdot \exp(-i\overline{H}t) \cdot (-i)^n \cdot J_n(\Delta Ht) \cdot \hat{Q}_n \qquad (3.3)$$

with $\overline{H}$ and ΔH being estimates of the midpoint and the halfwidth of the spectrum of $\hat{H}$. The J_n are Bessel functions and the $\hat{Q}_n$ are modified Chebyshev polynomials[88]. The ABC

propagator incorporates the use of an optical potential to absorb the wave packets at the edges of the grid[88].

The initial symmetry-adapted wave packets are chosen to be real and of the form of superimposed Gaussians in Z. The two Gaussian components of the initial wave packet describe a wave packet going towards the surface and its complex conjugate which moves away from the surface[31]. This choice of form of the initial wave packet and the use of the ABC propagator allows the use of real algebra throughout the propagation part of the calculations.

From the propagated wave packet, the column of the symmetry-adapted S-matrix that corresponds to the initial state of the system for which the calculation was performed is obtained by projecting the wave packet onto the symmetry-adapted asymptotic gas-phase wave functions and using the scattering amplitude formalism[68,73,89,90]. After obtaining the scattering information for each symmetry species Γ, the desired column of the non-symmetry-adapted scattering matrix can be computed.

3.2.2. Site-specific reaction probabilities

To obtain site-specific reaction probabilities, a flux-based method was used. From the time-dependence of the wave-packet, the stationary scattering state $\Phi(E_{tot})$ and its derivative with respect to the bond length r can be computed[91,92]:

$$\Phi(E_{tot}) = \frac{|k_z|}{2\pi \cdot M \cdot b(-k_z)} \cdot \int_0^\infty e^{iE_{tot}t} \cdot \Psi(t)dt \tag{3.4}$$

$$\frac{\partial \Phi(E_{tot})}{\partial r} = \frac{|k_z|}{2\pi \cdot M \cdot b(-k_z)} \cdot \int_0^\infty e^{iE_{tot}t} \cdot \frac{\partial \Psi(t)}{\partial r}dt \tag{3.5}$$

In these formulas k_z is the momentum conjugate to Z and $b(k_z)$ is the momentum representation conjugate to Z of the initial wave-packet:

$$b(-k_z) = \frac{1}{\sqrt{2\pi}} \cdot \int_{-\infty}^{\infty} \Psi(Z; t = 0) \cdot e^{ik_z t} dt \qquad (3.6)$$

With these three formulas, the flux through a surface at $r = r_{cut}$ can be calculated as a function of the total energy for an initial state (v, j, m_j)[92]:

$$\rho(E_{tot}; v, j, m_j; Z, X, Y, \theta, \phi) = \frac{2\pi M}{|k_z| \cdot \mu} \cdot Im\left(\Phi^*(E_{tot}) \cdot \frac{\partial \Phi(E_{tot})}{\partial r}\bigg|_{r=r_{cut}} \right) \qquad (3.7)$$

If the flux ρ is integrated over the co-ordinates X, Y, Z, θ and ϕ for a large enough value of r, the reaction probability is obtained[91-94].

However, if the flux is only integrated over Z, θ and ϕ and the surface is positioned at a value r_{cut} which is just behind the barrier, a measure of the site reactivity can be obtained as a function of X and Y for a specific energy E_{tot}:

$$P_r(E_{tot}; v, j, m_j; X, Y) = \iiint \rho(E_{tot}; v, j, m_j; Z, X, Y, \theta, \phi) dZ\, d\cos(\theta)\, d\phi \qquad (3.8)$$

The function $P_r(E_{tot}; v, j, m_j; X, Y)$ can be integrated over areas of the surface unit cell that have been pre-assigned to the high symmetry sites on the basis of proximity (see Figure 3.2) to obtain site-specific reaction probabilities, $P_r^{site}(E; v, j, m_j)$. A more detailed description of the application of the flux method in the computation of site-specific reaction probabilities within the SAWP method has been given elsewhere[26].
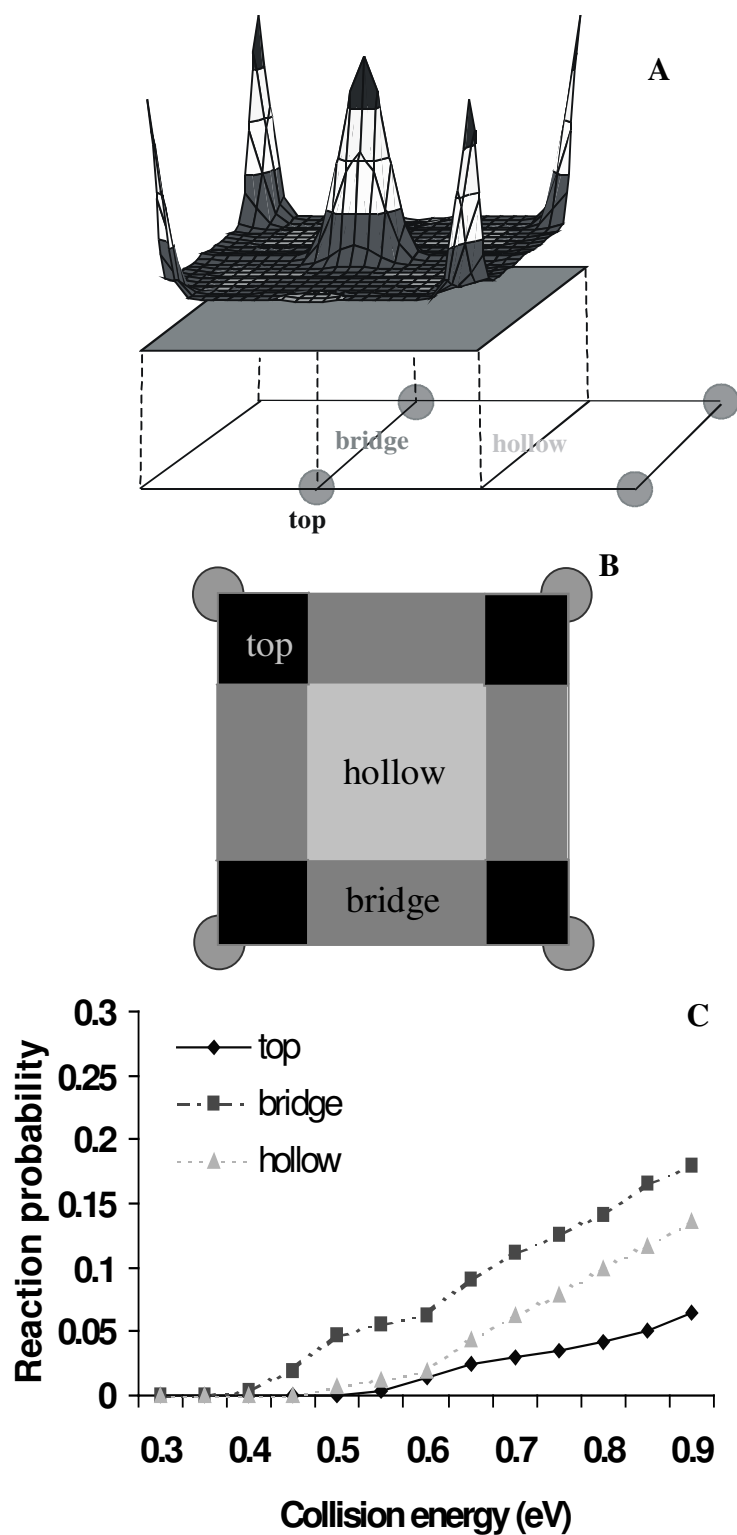
Figure 3.2: A) An example of the reaction probability density as a function of position X and Y as obtained for a specific incidence energy (0.45 eV) for H_2 (v=0,j=2,m_j=0). **B)** The designated areas of the surface unit cell over which the reaction probability densities are integrated to obtain site-specific reaction probabilities. **C)** After integration, site-specific reaction probabilities are obtained as a function of the incidence energy, for the high symmetry bridge, top and hollow sites.
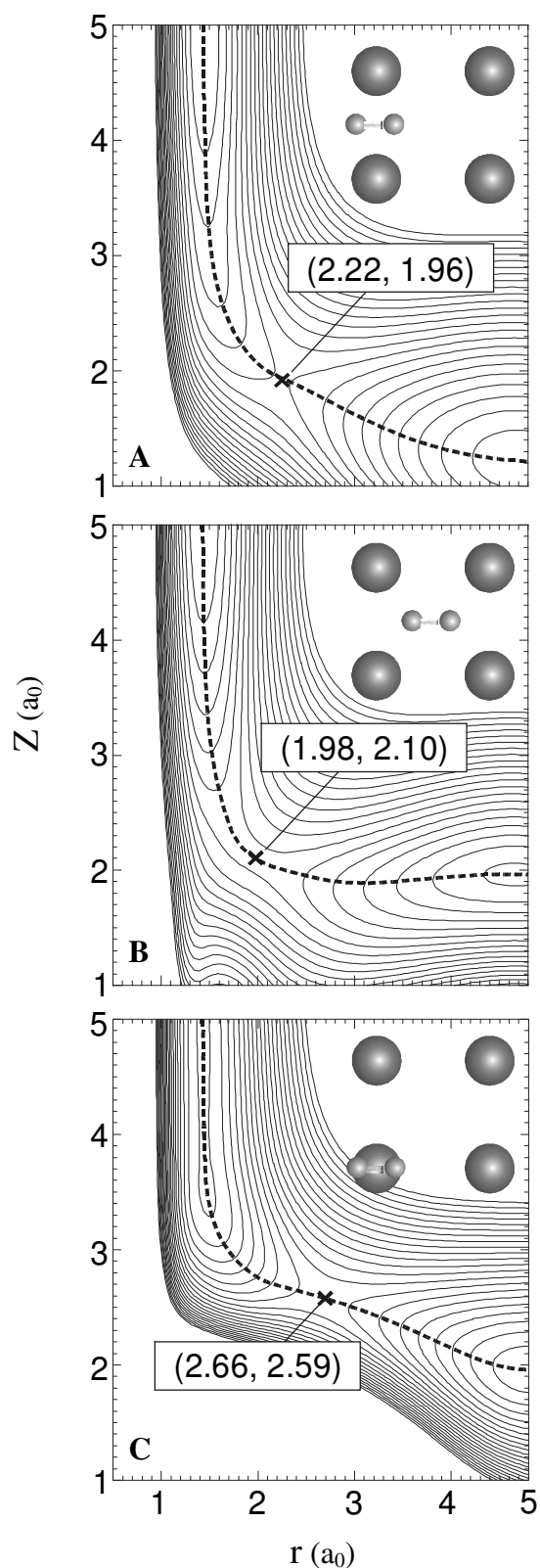
3.3. The Potential energy surface

The 6D PES used in this study is based on 14 two-dimensional cuts in the co-ordinates r and Z with the H$_2$ placed on the high symmetry sites. For each of these cuts, points were calculated with DFT[76,77], using the generalised gradient approximation[95-97] (GGA) and a slab representation of the metal surface. In the representation of the Cu surface, the experimental Cu(100) bulk lattice constant (α_{lat}=4.824 a$_0$) has been used. The convergence of the DFT calculations is believed to be within 0.1 eV of the GGA limit of this system. Details on the DFT calculations for these 2D PESs can be found in reference 26.

The full 6D PES, know as PES 4[26], is expanded in 14 symmetry adapted functions of X, Y, θ and ϕ. In the expansion, the r, Z-dependent expansion coefficients are related to the computed 2D cuts, by the inversion of a set of linear equations[26].

In Figure 3.3 the most essential aspects of the H$_2$+Cu(100) PES are shown. The lowest barrier (0.50 eV) corresponds to dissociation above the bridge site with the H atoms moving towards the hollow sites and H$_2$ oriented parallel to the surface. The highest minimum barrier found above a high symmetry site corresponds to H$_2$, oriented parallel to the surface, dissociating above the top site with the H atoms moving towards the bridge sites (0.63 eV). In Table 3.1, barrier heights found at the high-symmetry sites are collected for different azimuthal angles and for H$_2$ oriented parallel to the surface.

In Table 3.2, barrier locations and two measures of the anisotropy are shown for the high-symmetry sites. The polar anisotropy is defined by the range of potentials experienced by H$_2$ when located at the minimum barrier and rotated out-of-plane, keeping all of the other degrees-of-freedom fixed. The azimuthal anisotropy is defined by rotating the molecule parallel to the surface and keeping all the other degrees-of-freedom fixed at the minimum barrier geometry of a high symmetry-site.

Surface site	θ	φ	Barrier in eV
Bridge (A)	90	0	0.50
Bridge	90	45	0.84
Bridge	90	90	1.19
Top (C)	90	0	0.63
Top	90	45	0.73
Hollow (B)	90	0	0.58
Hollow	90	45	0.65

Table 3.1: Listed are barrier heights for different orientations and surface sites. The labels A, B and C correspond to the labels used in Figure 3.3.

	Bridge (A)	Hollow (B)	Top (C)
Barrier height in eV	0.50	0.58	0.63
Barrier position r in a_0	2.22	1.98	2.66
Barrier position Z in a_0	1.96	2.10	2.59
φ anisotropy in eV	2.39	0.05	0.09
θ anisotropy in eV	1.42	0.56	12.92

Table 3.2: Listed here are the heights and locations of the minimum barriers of the high symmetry sites. Also listed, are the two measures of the potential anisotropy found at these sites (see the text).

Figure 3.3: The H_2+Cu(100) PES. Two-dimensional cuts are shown for three different reaction routes, indicated in the insets: **A)** bridge-to-hollow dissociation **B)** hollow-to-bridge dissociation and **C)** top-to-bridge dissociation. The dotted line represents the reaction-path and the "**x**" marks the barrier location. In each case, H_2 is oriented parallel to the surface.

The top-site barrier is the "latest" (it occurs for the largest value of r) and shows the largest polar anisotropy (12.92 eV), whereas the largest azimuthal anisotropy is found for the bridge site (2.39 eV). The hollow and top sites both show a weak azimuthal anisotropy at the corresponding barrier geometry's, 0.05 eV and 0.09 eV respectively. The site with the lowest polar anisotropy is the hollow site, which displays the earliest barrier of all the high-symmetry sites considered.

3.4. Computational details

Calculations have been performed for all initial states of H_2 with (v=0,j=0-5) and with (v=1,j=0-5). The calculations for the (v=0) states have been performed for the incidence energy range of 0.3 to 0.9 eV. The (v=1) state calculations have been performed for two incidence energy ranges, one from 0.1 to 0.3 eV and one from 0.2 to 0.65 eV, using a smaller rotational basis set for the lower energy range. The overlapping region of incidence energy (0.2 eV - 0.3 eV) has been used to confirm convergence of both calculations of the (v=1) states. (Note: for initially $(v=1,j=1,m_j=1)$ H_2, no site-specific reaction probabilities have been calculated for the energy range 0.1 eV to 0.2 eV.) In all the calculations the initial wave packet was propagated for 60000 a.u. of time.

In all calculations, the diffractional basis employed all functions with $|n|+|m| \leq 11$. For the odd j states, the rotational basis included functions with $j \leq 29$ and for the even j states, $j \leq 28$ was used for all of the (v=0) calculations and the (v=1) calculations for the higher incidence energy range. The rotational basis $j \leq 20$ has been used for the (v=1), even-j-valued initial states in the 0.1 to 0.3 eV incidence energy range. For the odd-j-valued, (v=1) initial states, $j \leq 19$ has been used for the lower energy range. All other parameters have not been changed with respect to earlier studies[26,31]. Tests conducted indicated convergence of reaction and scattering probabilities to within 1% of their absolute values, with respect to basis sizes and propagation time.

3.5. Results and discussion

3.5.1 Degeneracy-averaged reaction probabilities

In Figure 3.4 degeneracy-averaged reaction probabilities, $P_{deg}(E; v, j)$, are shown for (v=0,j=0-5) and (v=1,j=0-5). These $P_{deg}(E; v, j)$ have been calculated from the initial-state-resolved reaction probabilities, $P_r(E; v, j, m_j)$, using:

$$P_{deg}(E; v, j) = \frac{1}{2j+1} \cdot \sum_{m_j=0}^{m_j=j} (2 - \delta_{m_j 0}) \cdot P_r(E; v, j, m_j) \qquad (3.9)$$

The molecules incident in the vibrationally excited (v=1) state (Figure 3.4B) react at much lower energies than molecules initially in the vibrational ground state (v=0) (Figure 3.4A), an effect called vibrational enhancement[36,46,51]. Here we focus on the dependence of reaction on the rotational quantum level j of the incident molecule. A striking difference between (v=0) and (v=1) is that, at low incidence energies where the reaction probability is low (near the reaction threshold), the $P_{deg}(E; v, j)$ clearly increases with j for (v=1) (rotational enhancement) whereas $P_{deg}(E; v, j)$ is almost independent of j for (v=0).

Such a behaviour has not been observed in experimental studies on the analogous systems D_2(v=0,1,2) + Cu(111)[3,4] and H_2(v=0,1) + Cu(111)[12]. In the fits to the experimentally-measured associative-desorption probabilities for Cu(111), $P_{deg}(E; v, j)$ first decreases with j for j=0 up to about 5 (rotational hindering) and then increases with j (rotational enhancement) for both (v=0) and (v=1). The explanation offered for rotational hindering is that rotating molecules are less likely to pass the entire barrier region in an orientation that remains favourable for reaction[3,4,12,33,39,48]. Rotational enhancement can be explained by the presence of a late barrier: at the barrier, the rotational constant of the

molecule is lower than in the gas phase, allowing conversion of energy from rotation to motion along the reaction path, thereby helping the molecule to overcome the barrier[3,4,33,48]. The higher j, the stronger this effect; eventually this dominates the hindering effect.
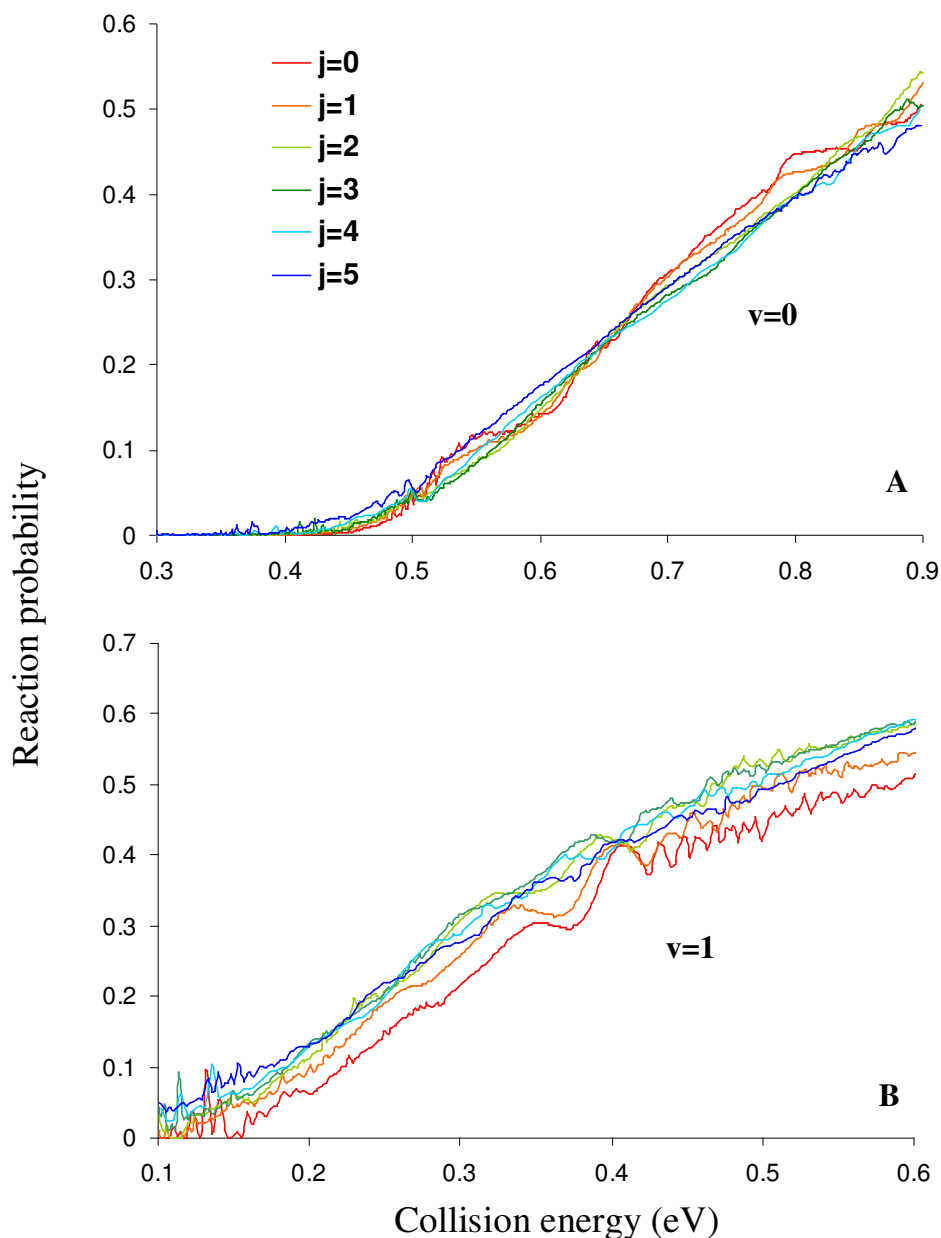
Figure 3.4: The degeneracy-averaged reaction probability as a function of normal incidence energy, for different rotational states j, for (v=0) **(A)** and (v=1) **(B)** H₂.

To explain the difference in the dependence of $P_{deg}(E; v, j)$ on j between (v=0) and (v=1) for H_2 + Cu(100) near threshold and the difference with the experimental results for H_2, D_2 + Cu(111), we will first consider where on the surface unit cell the molecule dissociates for (v=0) and (v=1). Next, we will discuss how the degeneracy-averaged site-specific reaction probabilities, $P_{deg}^{site}(E; v, j)$, depend on j for both the (v=0) and (v=1) molecules. We will show that the j-dependence of $P_{deg}^{site}(E; v, j)$ can be explained on the basis of previous fixed-site[25,39] and flat-surface[44,48] calculations, by relating the computed j-dependence to the anisotropy of the PES at different sites. We end this section by showing how experimental measurement of the j-dependence of $P_{deg}(E; v, j)$ might confirm our predictions concerning the preferred reaction site of H_2(v=0) and H_2(v=1) on Cu(100).

Results of a previous study[26,27] showed that for the (v=0,j=0) and (v=0,j=4) states, reaction takes place predominantly at the bridge site. The (v=1,j=0) and the (v=1,j=4) states, however, react preferably at the top site at near threshold incidence energies. In Figure 3.5 and Figure 3.6 the degeneracy-averaged site-specific reaction probabilities ($P_{deg}^{site}(E; v, j)$) are shown for the states (v=0,j=1-3,5) and (v=1,j=1-3,5) respectively. The $P_{deg}^{site}(E; v, j)$ have been calculated from the $P_r^{site}(E; v, j, m_j)$ using an expression analogous to equation (3.9). Figure 3.5 and Figure 3.6 clearly show that the previous theoretical result that, on Cu(100), (v=0) H_2 preferentially reacts at the bridge site whereas (v=1) H_2 preferentially reacts at the top site for incidence energies just above threshold, is general for low initial j (j=0-5).
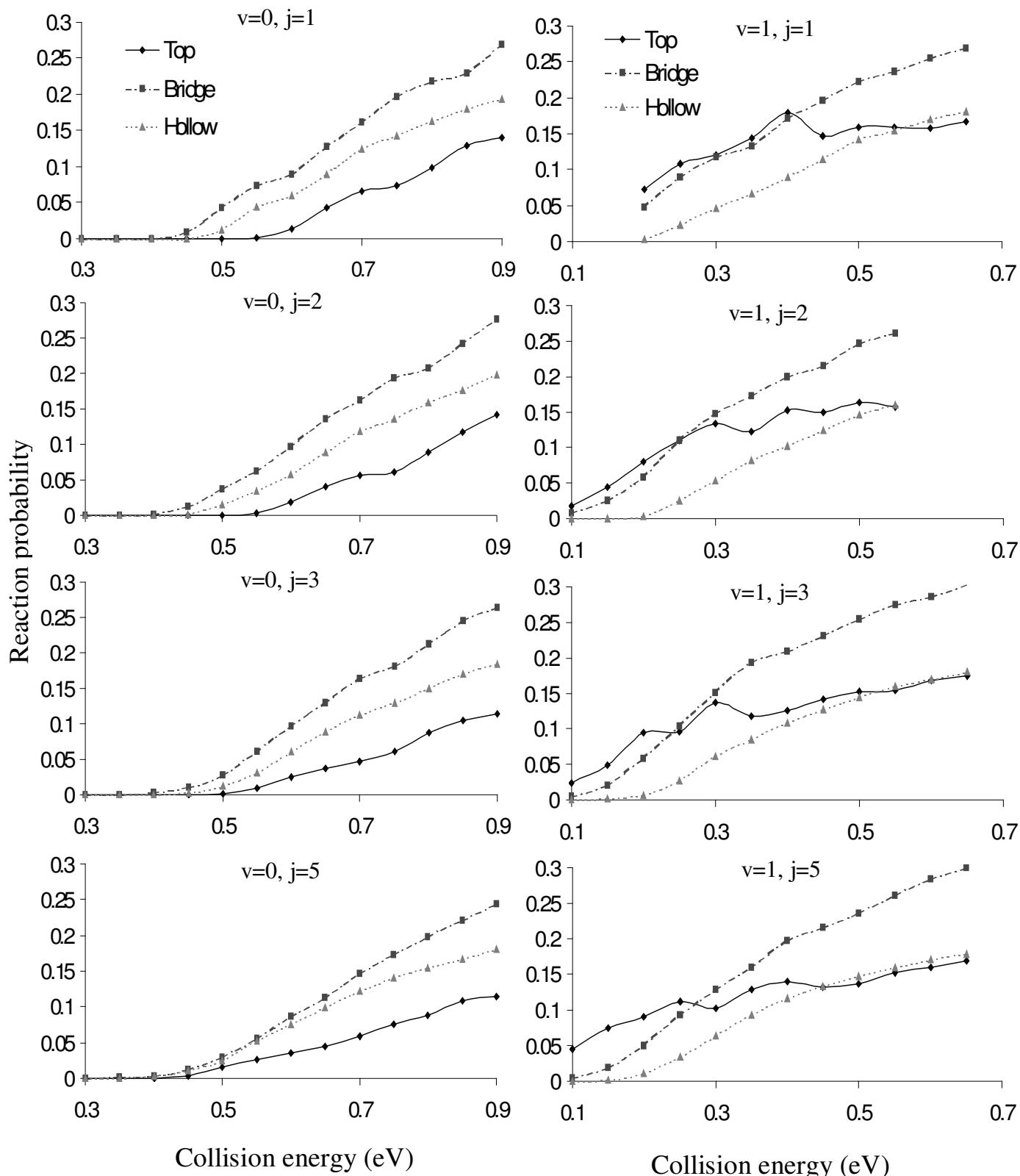
Figure 3.5: The site-specific degeneracy-averaged reaction probability for the (v=0) state as a function of the incidence energy, for specific rotational levels.
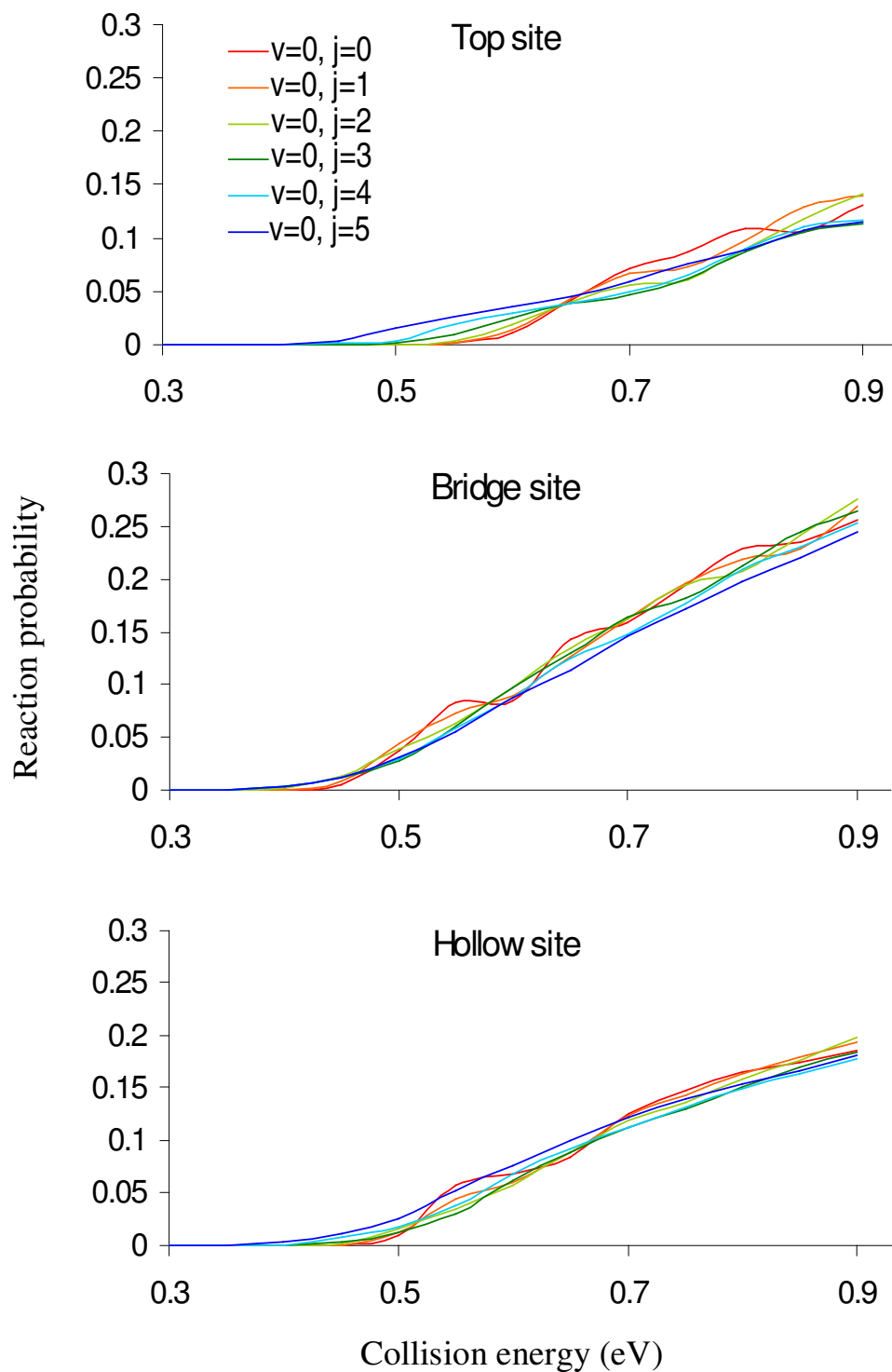
Figure 3.6: The site-specific degeneracy-averaged reaction probability for the (v=1) state as a function of the incidence energy, for specific rotational levels.

As explained before[26,27], (v=0) H_2 preferentially reacts at the bridge site because the barrier to reaction is lowest at this site (see Table 3.2). At relatively low energies, (v=1) H_2 reacts preferentially at the top site because H_2 can convert all of its vibrational energy (in excess of the zero point vibrational energy) to energy of motion along the reaction path, to overcome the higher barrier at this site. This is possible due to special features of the top site PES, which has a reaction path with an especially late barrier (see Table 3.2) and a high curvature in front of the barrier (see Figure 3.3C)[26,27,98].

It is worthwhile to consider whether the different j-dependence of $P_{deg}(E; v, j)$ of (v=0) and (v=1) H_2 at energies just above threshold (Figure 3.4) can be explained from the difference in preferred reaction site of these vibrational states (Figure 3.5 and Figure 3.6). For this purpose, $P_{deg}^{site}(E; v, j)$ for (j=0-5) are plotted separately for each site, for both (v=0) (Figure 3.7) and (v=1) (Figure 3.8). Just above the threshold, the reaction at the top site shows clear rotational enhancement, not just for (v=1) (as in $P_{deg}(E; v, j)$, Figure 3.4B), but also for (v=0). In contrast, the reaction above the bridge site appears to be almost independent of j, not just for (v=0) (as in $P_{deg}(E; v, j)$, Figure 3.4A) but also for (v=1).

The difference in the j-dependence of reaction between the bridge and the top site can be explained by differences in the topology of the PES at these sites. The barrier at the top site shows little azimuthal anisotropy (see Table 3.2). Previous reduced dimensionality studies of H_2 + Cu which employed the flat-surface approximation - so that the potential contains no azimuthal anisotropy - also showed reaction to be rotationally-enhanced for low j, for energies just above the threshold[44,48]. Similar results were obtained in fixed-site studies on H_2 + Cu, for sites at which the potential has little azimuthal anisotropy at the reaction barrier geometry (see for example figure 7 of reference 39 for reaction above the top site of Cu(111) and figure 9 of reference 25 for reaction above the hollow site for Cu(100)). The reason for this trend is that helicoptering molecules, which have $|m_j|=j$ and are the ones first to react just above threshold[13,29,33,35,48], can react without (or with little) rotational hindering in the absence of (a large) azimuthal anisotropy.

Figure 3.7: The site-specific degeneracy-averaged reaction probability as a function of the incidence energy, for different rotational levels of the (v=0) state. These spline-curves where based on the same data points shown in Figure 3.5.
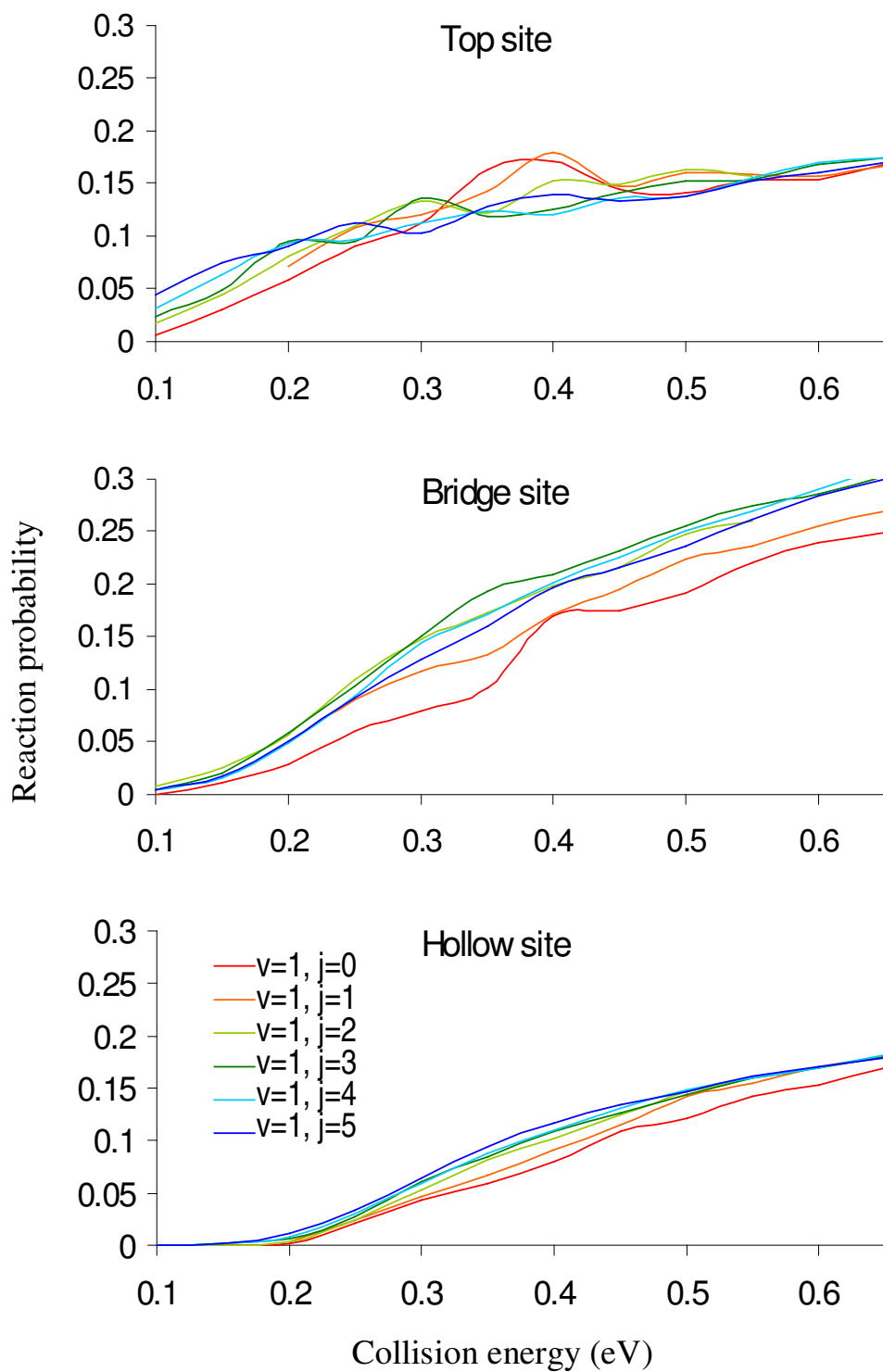
Figure 3.8: The site-specific degeneracy-averaged reaction probability as a function of the incidence energy, for different rotational levels of the (v=1) state. These spline-curves where based on the same data points shown in Figure 3.6.

The reaction will then be rotationally enhanced due to the lateness of the barrier, which leads to a reduction of the molecule's rotational constant at the barrier. In Figure 3.7 and Figure 3.8, the reaction at the hollow site is less rotationally enhanced than reaction at the top site because the barrier is earlier at the hollow site (see Table 3.2).

In flat-surface calculations modelling dissociation of H_2 on Cu(111), Darling and Holloway showed that they could recover the experimentally-found trend that reaction is rotationally hindered for low j[3,4] by introducing azimuthal anisotropy in their potential[48]. Employing a fixed-site LEPS potential based on DFT calculations[79], Dai and Zhang likewise recovered the experimental trend that reaction is hindered, in calculations for reaction on the lowest barrier bridge site, above which the barrier has a high azimuthal anisotropy[39]. Similarly, we find that reaction above the bridge site of Cu(100) is not rotationally enhanced at low j. The reason, again, is that the potential barrier has a high azimuthal anisotropy above the bridge site (see Table 3.2), so that the rotational motion also hinders the reaction of helicoptering molecules. For Cu(100), this compensates the enhancement effect due to the late barrier, so that no clear dependence of reaction on j is found. The increased lateness of the barrier at the top site also contributes to the rotational enhancement of reaction of (v=1) H_2 + Cu(100) in addition to the absence of azimuthal anisotropy discussed above.

Our 6D calculations predict reaction of H_2 on Cu(100) to be nearly independent of j for (v=0) and to be clearly rotationally enhanced for (v=1), at low j and incidence energies. This result differs from experimental[3,4,12] and theoretical[33] (v=0) results for H_2, D_2 + Cu(111), which show a net rotational hindering effect for low j. This difference could be due to a difference in the location of the minimum reaction barrier for Cu(100) and Cu(111). On Cu(100), the barrier occurs at a value of the H-H distance which is 0.1 Å larger than on Cu(111)[99]. Therefore, rotational enhancement should be more important for Cu(100) and is here predicted to offset rotational hindering for (v=0) and to dominate for (v=1). This prediction can be easily tested by performing energy-resolved associative-desorption experiments in which the desorbing H_2 is detected state-selectively with respect to v and j, as have already been performed for H_2, D_2 + Cu(111)[12,20].

The associative-desorption experiments we propose are usually done using high surface temperatures T_s ($T_s \geq 370$ K)[86,87], whereas our calculations are done for a 0 K surface. However, increasing T_s is not expected to change the j-dependence of the reaction probability at low collision energies. It is known from associative desorption experiments that, for H_2 and D_2 on Cu(111), the dependence of the sticking probability on the surface temperature can be modelled easily by assigning larger width-parameters to the fitted, S-shaped reaction probability curves when considering higher surface temperatures[86,87]. Furthermore, for (v=0) H_2 and D_2 the increase of the width with T_s was found to be independent of j[86]. If we assume the same to be true for (v=0,1) H_2 + Cu(100), the effect of increasing T_s would be to increase all $P_{deg}(E;v,j)$ by a similar amount for low E. Then, $P_{deg}(E;v,j)$ would still be approximately independent of j for v=0, and increase with j for v=1.

Our most important result is that, just above threshold, the site-specific degeneracy-averaged reaction probability increases with j for the top site and is nearly independent of j above the bridge site. Because this difference can also be explained by differences in the topology of the PES at these sites, we predict that the j-dependence of the total reaction probability, which is an experimentally-measurable quantity, can be used as a signature for the preferred reaction site. Confirmation of our prediction of no j-dependence of reaction for (v=0) and rotational enhancement for (v=1) would strongly support our finding that (v=0) and (v=1) H_2 react at different sites on Cu(100), i.e. on the bridge and the top sites, respectively.
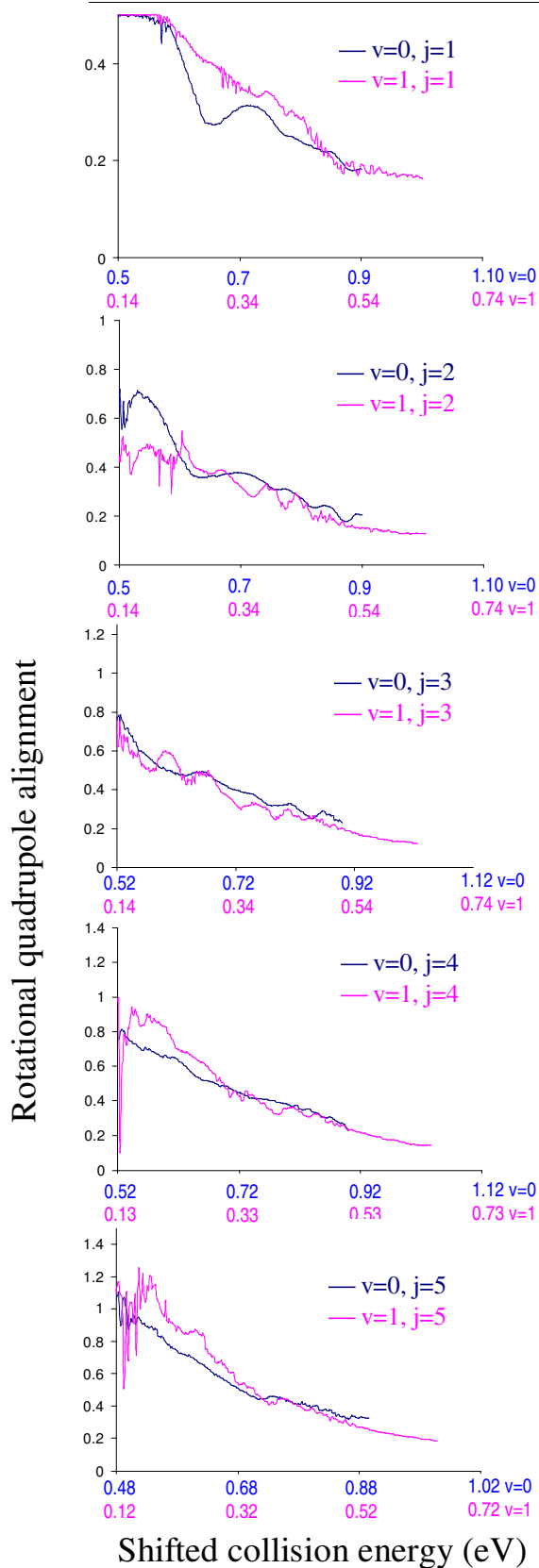
Figure 3.9: A comparison of the rotational quadrupole alignment of reacting (v,j) molecules is shown between the (v=0) and (v=1) state for different rotational levels. The energy scales have been shifted to an offset for which the total reaction probability is 5% for each (v,j) state.
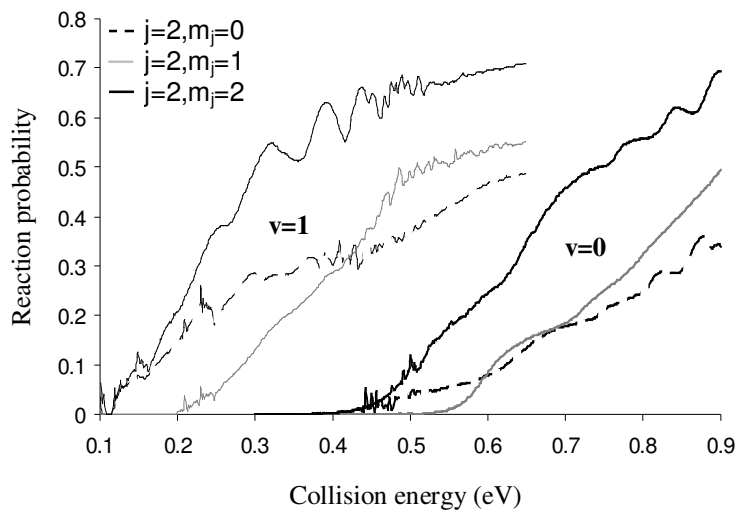
Figure 3.10: The initial state (v,j,m$_j$) resolved reaction probabilities are shown versus normal incidence energy for (v,j=2,m$_j$) H₂ for (v=0 and 1 and m$_j$=0-2).
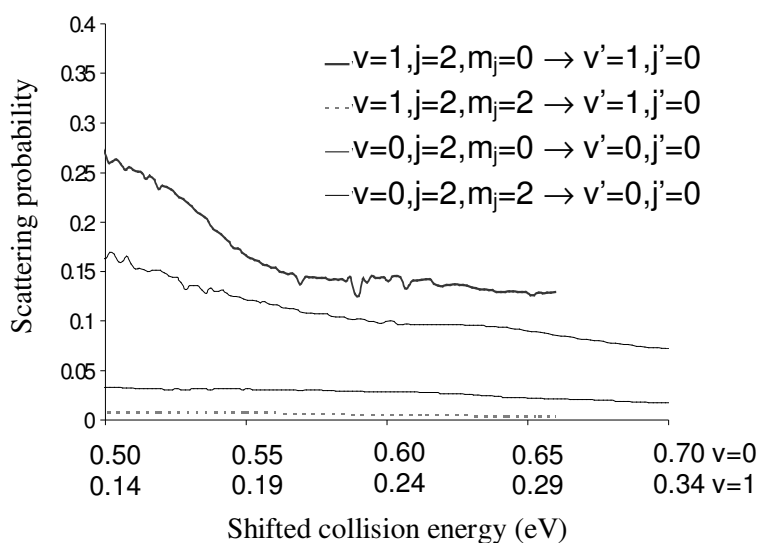
Figure 3.11: The probability for rotational de-excitation, P(v,j=2,m$_j$ → v',j'=0), is shown for v=0 and 1 and m$_j$=0 and 2. The (v=0) and (v=1) energy scales have been shifted to an offset corresponding to the energy for which (v,j=2) H₂ shows a degeneracy-averaged reaction probability of 5%.

3.5.2 Experimental signatures based on the comparison of alignments

The rotational quadrupole alignment, $A_0^{(2)}(E; v, j)$, of the molecules that react can be calculated from initial state (v, j, m_j) resolved reaction probabilities using the following expression[100]:

$$A_0^{(2)}(E; v, j) = \frac{\sum\limits_{m_j} P_r(E; v, j, m_j) \cdot \left(\left\{ \dfrac{3m_j^2}{j(j+1)} \right\} - 1 \right)}{\sum\limits_{m_j} P_r(E; v, j, m_j)} \qquad (3.10)$$

$A_0^{(2)}(E; v, j)$ is a quantity revealing information on the $|m_j|$ distribution of molecules, initially in level (v, j), that go on to react. The maximum value of the alignment for a given j level, $3j/(j+1)-1$, corresponds to the situation where only helicoptering molecules react ($|m_j|=j$). The minimum value, -1.0, corresponds to the situation where only cartwheeling molecules react ($m_j=0$) and an alignment of zero corresponds to helicoptering and cartwheeling molecules reacting with equal probability[26]. Assuming the validity of detailed balance, desorption probabilities, as measured in associative desorption experiments, are equal to reaction probabilities, as measured in adsorption experiments, for desorption normal to the surface. Therefore $A_0^{(2)}(E; v, j)$ is an experimentally-measurable quantity[13].

In a previous study[26], it was noted that $A_0^{(2)}(E; v = 1, j = 4)$ is higher than $A_0^{(2)}(E; v = 0, j = 4)$ for near threshold incidence energies. It was suggested that this behaviour could be correlated to reaction taking place predominantly at the top site for (v=1) H_2 and at the bridge site for (v=0) H_2. Here we address the question of whether this signature for the difference in reaction site between (v=0) and (v=1) H_2 is also valid for the j levels 1-3 and 5.

In Figure 3.9, $A_0^{(2)}(E;v,j)$ is plotted as a function of *shifted* incidence energies. The energies have been shifted to an offset corresponding to a total reaction probability of 5%, for which we know the reaction will take place at either the top site (for v=1) or the bridge site (for v=0), to enable a better comparison between reaction of H₂ in these two initial vibrational levels.

Clearly, at or just above the energy offset reacting (v=1,j=2) and (v=1,j=3) H₂ do not have a higher $A_0^{(2)}(E;v,j)$ than (v=0, j=2) and (v=0,j=3) H₂, respectively (Figure 3.9). In particular, close to threshold, $A_0^{(2)}(E;v=0,j=2)$ is even higher than $A_0^{(2)}(E;v=1,j=2)$. For (v=1,j=4) and (v=1,j=5) H₂ has a higher $A_0^{(2)}(E;v,j)$ than (v=0) H₂ for j=4 and 5 at incidence energies slightly larger than the energy offset. The (j=1) level shows a behaviour similar to that of the (j=4) and (j=5) levels, with the exception that both $A_0^{(2)}(E;v=1,j=1)$ and $A_0^{(2)}(E;v=0,j=1)$ have reached their maximum value of 0.5 at the energy offset. In previous publications[26,27], $A_0^{(2)}(E;v=1,j=4)$ was plotted significantly higher than $A_0^{(2)}(E;v=0,j=4)$ at the energy offset. This was due to an error in the program used to compute the alignments[82]. Here we present the correct plots.

Figure 3.9 clearly shows that the result previously obtained for (j=4), that $A_0^{(2)}(E;v,j)$ is higher for (v=1) somewhat above the energy for which the reaction probability exceeds 5%, is not general for low j. The explanation offered for the greater alignment of (j=4) reacting molecules, for (v=1) compared to (v=0), was based on steric hindering[26]. Vibrationally-excited H₂ reacts preferentially at the top site. At the barrier of this site, the anisotropy in θ is higher than at the bridge site barrier, where (v=0) H₂ prefers to react. This by itself should lead to a greater preference for helicopter reaction at the top site. In addition, reaction of helicoptering H₂ can proceed almost without rotational hindering at the top site, due to the low potential anisotropy in φ at this site's barrier. In contrast, the reaction at the bridge site, which exhibits a strong φ anisotropy, should be rotationally hindered for helicopters (see Table 3.2). These two factors were the key elements in the

explanation of the difference between the alignments of (v=0) and (v=1) for (j=4) H_2 at and slightly beyond threshold.

However, this reasoning predicts that $A_0^{(2)}(E; v = 1, j)$ should also be higher than $A_0^{(2)}(E; v = 0, j)$ for j=1-3 and j=5, for incidence energies at and slightly beyond threshold, because the top site is the preferred reaction site for (v=1) H_2 and the bridge site for (v=0) H_2. As already stated, $A_0^{(2)}(E; v = 1, j)$ is not always higher than $A_0^{(2)}(E; v = 0, j)$ for each j, especially at the energy offset (Figure 3.9). An explanation for this can be found by not only considering the steric hindering effects, but by also including rotational enhancement effects into the picture, as will be discussed below.

The steric hindering effects, mentioned above, can be divided into two separate mechanisms[26]. The first is *orientational hindering* and the second *rotational hindering*. Rotational hindering originates from the fact that molecules rotating fast enough may encounter an unfavourable orientation whilst travelling along the reaction path, regardless of the initial orientation of the molecule. If a high anisotropy is present in the neighbourhood of the barrier, this may of course lead to reflection. In contrast, orientational hindering refers to a static effect: non- or slow-rotating molecules will be reflected from an anisotropic barrier if their initial orientation is unfavourable for reaction.

Rotation may hinder reaction, but it can also help molecules to react. Rotational enhancement effects can also occur by two different mechanisms. In the first mechanism, rotation enhances the reaction due to the decrease of the molecule's rotational constant, as it approaches a late barrier[36]. For this mechanism, which will be called *elastic rotational enhancement*, the higher the j level is, the more rotational energy can be transferred into motion along the reaction path. Elastic rotational enhancement will enhance cartwheels and helicopters, of a given j level, equally well and it should therefore have a less direct influence on the rotational quadrupole alignment of the reacting molecules. (Equation

(3.10) shows that increasing $P_r(E; v, j, m_j)$ for all m_j should lead to a lowering of the absolute value of the alignment.)

The second mechanism of enhancement is closely related to the potential anisotropy (in θ) near the barrier. Not only will a high anisotropy induce hindering effects, as explained above, it may also allow the molecule to *rotationally de-excite* on its way to the barrier and thereby help reaction. The energy gained from this de-excitation can be transferred into motion along the reaction path and thereby help the molecule to cross the barrier[101]. Due to the inversion symmetry of H$_2$, this mechanism can only be effective for molecules with $j \geq 2$. In addition we will show that its effectiveness is very dependent on the specific (j, m_j) level of H$_2$. This mechanism of rotational enhancement is referred to as *inelastic rotational enhancement*. It is expected to be especially important near threshold, where reaction may only be possible through this mechanism.

	Mechanism	PES feature responsible	Site(s) at which most important	Effect on reaction near threshold	Effect on $A_0^{(2)}(E;v,j)$
Enhancement mechanisms	elastic rotational enhancement	small rotational constant at a late barrier	top site	$P_{deg}(E; v, j)$ increases with j	none
	inelastic rotational enhancement	θ anisotropy of the PES at barrier	top site	$P_r(E; v, j, m_j)$ is enhanced for low $|m_j|$ and $j \geq 2$	$A_0^{(2)}(E;v,j)$ decreases
Steric hindering mechanisms	orientational hindering	θ anisotropy of the PES at barrier	top site	$P_r(E; v, j, m_j)$ is reduced for small $|m_j|$	$A_0^{(2)}(E;v,j)$ increases
	rotational hindering	anisotropy of the PES at barrier	bridge site (ϕ) top site (θ)	$P_{deg}(E; v, j)$ decreases with j	$A_0^{(2)}(E;v,j)$ increases with θ-anisotropy and decreases with ϕ-anisotropy

Table 3.3: Mechanisms that affect the reaction probabilities and the rotational quadrupole alignment of reacting molecules. Also presented are the features in the PES which are the most relevant to the mechanism, the surface site for which the mechanism is most important, the effect each mechanism has on the reaction probability and the rotational quadrupole alignment for the different rotational states of the incident H$_2$ molecule.

Having identified these four mechanisms (which are summarised in Table 3.3 and are further discussed below), the observed j dependence of the relative (v=0) and (v=1) H_2 rotational quadrupole alignments can now be understood. For the (j=1) case, both $A_0^{(2)}(E; v = 1, j = 1)$ and $A_0^{(2)}(E; v = 0, j = 1)$ reach the value of 0.5 at the energy offset. This corresponds to *only* helicopters being reactive. The (j=1) helicopters are oriented favourably for reaction on both the bridge ((v=0) H_2) and the top site ((v=1) H_2) compared to the (j=1) cartwheels. At slightly higher incidence energies the (j=1) cartwheels will start to react as well so both $A_0^{(2)}(E; v = 1, j = 1)$ and $A_0^{(2)}(E; v = 0, j = 1)$ will decrease with energy.

However, $A_0^{(2)}(E; v = 0, j = 1)$ will decrease more rapidly than $A_0^{(2)}(E; v = 1, j = 1)$ due to the fact that the higher θ anisotropy of the top site induces a greater *orientational hindering* of the reaction of the (v=1) cartwheels compared to the (v=0) cartwheels reacting at the bridge site. On top of that, the (v=0) helicopters experience more rotational hindering due to the ϕ anisotropy of the reaction barrier being higher at the (v=0) H_2 reaction site (bridge) than at the (v=1) H_2 reaction site (top). Effects of rotational enhancement on the alignment of the reacting molecules can be ruled out for the (j=1) case. No rotational de-excitations are possible because for H_2 the change in j must be even and the energy released by elastic rotational enhancement, although present, is believed to have no direct influence on the alignment.

This changes when considering the differences between the (v=0) and (v=1) H_2 rotational quadrupole alignments for (j=2) incident molecules. $A_0^{(2)}(E; v = 0, j = 2)$ is higher than $A_0^{(2)}(E; v = 1, j = 2)$ at the energy offset. Based on hindering arguments alone, this cannot be understood, because (v=1) H_2 reacts preferably at the top site and (v=0) H_2 at the bridge site. The top site, having the most anisotropy in θ and the least anisotropy in ϕ, should give rise to greater preference for helicopter reaction than the bridge site. The explanation can be found by considering the inelastic rotational enhancement mechanism.

For (v=1,j=2) H$_2$ reacting at the top site, considerable θ anisotropy exists, which not only leads to hindering but also enables H$_2$ to de-excite into the (v'=1,j'=0) state before dissociating (or into the librational state that corresponds adiabatically[102] to the (v'=1,j'=0) state). Because the top site shows a nearly isotropic barrier in ϕ, m$_j$ will be almost conserved[42,43] in collisions with the top site. The only possible rotational de-excitation from the (v=1,j=2) level of H$_2$, with $\Delta j=2$ and $\Delta m_j=0$, is the (v=1,j=2,m$_j$=0) $\rightarrow$ (v'=1,j'=0,m$_j$'=0) transition. The energy released through the rotationally-inelastic mechanism will therefore mostly enhance the reaction of the (j=2) cartwheels, resulting in a decreased alignment of the reacting (j=2) molecules. (v=0) H$_2$, which reacts at the bridge site, encounters less anisotropy in θ. It is therefore believed that inelastic rotational enhancement is more important for (v=1) H$_2$ than it is for (v=0) H$_2$. The greater increase of reactivity of (v=1,j=2,m$_j$=0) H$_2$ is expected to lower the rotational quadrupole alignment of reacting (v=1,j=2) H$_2$ more than for (v=0,j=2) H$_2$, as is seen in Figure 3.9 for energies close to the energy offset.

Support for the importance of rotationally-inelastic enhancement of the reaction of (v=1,j=2) cartwheels comes from Figure 3.10. In this figure the m$_j$-resolved reaction probabilities for (v=1,j=2) and (v=0,j=2) H$_2$ are shown as a function of the incidence energy. The effect of the sudden allowance of (v=1,j=2,m$_j$=0) $\rightarrow$ (v'=1,j'=0,m$_j$'=0) de-excitation near threshold energies is clear. Apparently energy released by the (v=1,j=2,m$_j$=0) $\rightarrow$ (v'=1,j'=0,m$_j$'=0) H$_2$ de-excitation enhances the reaction of (v=1,j=2,m$_j$=0) H$_2$ considerably compared to (v=0,j=2,m$_j$=0) H$_2$ (the reaction probability of the (v=1,j=2) cartwheel is almost as large as that of the (v=1,j=2) helicopter and this is clearly not the case for (v=0,j=2) H$_2$). Based on steric arguments, we would instead expect cartwheel reaction to be much less effective for (v=1) H$_2$, which reacts at the site with the greater θ anisotropy.

Additional support can be found in the state-to-state scattering probabilities of H_2 from different initial j=2 states. In Figure 3.11 the absolute scattering probabilities $P(v,j=2,m_j \rightarrow v',j'=0)$ are shown for (v=0) and (v=1), for $(m_j=0)$ and $(m_j=2)$ (transitions with $\Delta m_j=1$ are forbidden for the PES used[26]). Again, in this figure, the energy scale has been shifted to an offset where the total reaction probability is 5% for each initial vibrational state. Clearly, at the energy offset, initial $(v=1,j=2,m_j=0)$ H_2 shows a higher probability for vibrationally elastic and rotationally-inelastic scattering into the (j=0) state than initial $(v=0,j=2,m_j=0)$ H_2. This suggests a higher probability for rotational de-excitation for the molecule on its way to the barrier and this would also be expected to lead to greater enhancement of (v=1) reaction of cartwheels near threshold through the rotationally-inelastic enhancement mechanism discussed above. On the other hand, initial $(v=1,j=2,m_j=2)$ H_2 shows nearly no inelastic scattering into the $(v'=1,j'=0)$ state. The rotational de-excitation probabilities for (v=1,j=2) cartwheels (high) and helicopters (low) are consistent with scattering from a site with a high θ anisotropy and a low ϕ anisotropy, i.e. the top site (see Table 3.2). Furthermore, initial $(v=0,j=2,m_j=2)$ H_2 shows a higher probability of rotationally-inelastic scattering into the (j'=0) state than initial $(v=1,j=2,m_j=2)$ H_2. This is consistent with $(v=0,j=2,m_j=2)$ H_2 scattering from a site with a higher ϕ anisotropy, i.e. the bridge site (see Table 3.2). It is clear that rotational de-excitation and reaction near threshold are intimately related processes, which occur at similar sites. These processes are related through the anisotropy of the potential at the barrier associated with the reaction site. As a result, the rotationally-inelastic scattering results can be used to help identify reaction sites and to make inferences regarding the reaction mechanisms.

For (v=1,j=2) H_2, the mechanism of inelastic rotational enhancement is clearly present. A similar reasoning can be applied to the comparison between $A_0^{(2)}(E; v = 0, j = 3,4,5)$ and $A_0^{(2)}(E; v = 1, j = 3,4,5)$ at the energy offset. For these j levels several transitions with $\Delta j=2$ and $\Delta m_j=0$ are allowed. For (v=1,j=3) H_2, both $(m_j=1)$ and $(m_j=0)$ are allowed to de-excite into $(v'=1,j'=1,m_j'=1)$ and $(v'=1,j'=1,m_j'=0)$ respectively. (For v=1, j=4) and (v=1,j=5) even more transitions are possible, causing the lowering of the alignment,

resulting from enhancement of non-helicopter state reaction, to be less dramatic. On top of that, the energy gap associated with these transitions increases with increasing j. The associated energy gap for the transition (v=1,j=3) $\rightarrow$ (v'=1,j'=1) H$_2$ ($\approx$0.068 eV) is much larger than that for the transition (v=1,j=2) $\rightarrow$ (v'=1,j'=0) H$_2$ ($\approx$0.041 eV) making inelastic rotational enhancement for (j=3) H$_2$ less probable. It is therefore believed that the importance of inelastic rotational enhancement decreases with increasing j. For (j=4) and (j=5), the inelastic enhancement effect is expected only to be visible at the energy offset, if at all. Beyond the energy offset, steric hindering becomes the dominating factor in determining the ratio of (v=1) H$_2$ alignment and (v=0) H$_2$ alignment. For the reaction of (j=4) and (j=5) H$_2$, orientational and rotational hindering are expected to be most important, for both the reaction of initial (v=0) and (v=1) H$_2$. Both hindering mechanisms will ensure that, beyond the energy offset, $A_0^{(2)}(E; v = 1, j = 4,5)$ will be higher than $A_0^{(2)}(E; v = 0, j = 4,5)$. The (j=3) H$_2$ case can, in this picture, be regarded as the intermediate case, in which the inelastic rotational enhancement and hindering effects on reaction cancel in the influence exerted on the alignment of the reacting molecules. The above explanation accounts for all the trends seen in Figure 3.9.

For j>1 H$_2$, the rotational quadrupole alignments do not reach their maximum limiting values at the energy offset. Previous calculations on H$_2$+Cu(100)[35] and H$_2$+Cu(111)[33] showed a downturn of the alignment of the reacting molecules at low collision energies. It is not completely clear whether the effect that the alignment does not reach its maximum limiting value can be completely attributed to the rotationally-inelastic enhancement mechanism. As noted before, we expect this mechanism to become less important for high j, because the energy gap associated with rotational de-excitation increases with initial j. It is possible that the effect is partly due to steering (m$_j$-scrambling) becoming important at low collision energies[53]. Finally, it should be noted that the quantum mechanical cartwheel states also have a finite probability of being oriented exactly parallel (j is even) or almost parallel (any j) to the surface. In a picture in which rotation is not considered to take place in a "classical" sense, this may still lead to reaction of those cartwheel molecules which happen to be in the right "window of

orientation" when they get to the barrier and this may also contribute to the lowering of the alignment of reacting molecules for higher j near threshold energies.

Despite the fact that the signature for the reaction site, of $A_0^{(2)}(E; v = 1, j)$ > $A_0^{(2)}(E; v = 0, j)$ at and beyond the energy offset, is not as general as one might hope[26], the difference between $A_0^{(2)}(E; v = 1, j)$ and $A_0^{(2)}(E; v = 0, j)$, for j=1, 4 and 5, can still be used to identify top-site-reactivity through experimental measurement. The mechanisms causing the differences between $A_0^{(2)}(E; v = 1, j)$ and $A_0^{(2)}(E; v = 0, j)$, somewhat above threshold, can be related to specific features of the PES at both the top and bridge sites. Specifically, for j=1,4 and 5, $A_0^{(2)}(E; v = 1, j)$ is expected to be higher than $A_0^{(2)}(E; v = 0, j)$ at energies slightly beyond threshold and this difference is clearly related to top-site-reactivity of (v=1) H_2: the reaction barrier at the top site has a greater θ anisotropy, causing more orientational hindering of cartwheel reaction. Measurement of this would confirm our prediction of the difference in preferred reaction site between (v=0) and (v=1) H_2 on Cu(100). Whereas the measurement of $A_0^{(2)}(E; v = 1, j = 2)$ being lower than $A_0^{(2)}(E; v = 0, j = 2)$, together with a high inelastic scattering probability, P(v=1,j=2 H_2 → v'=1,j'=0), of H_2 at threshold energies, would not only confirm top-site-reactivity, but also the importance of inelastic rotational enhancement for the reaction of (v=1,j=2,m_j=0) incident H_2.

The differences we predict between $A_0^{(2)}(E; v = 0, j)$ and $A_0^{(2)}(E; v = 1, j)$ can be confirmed experimentally using currently available techniques, but once again the measurements would have to be performed at high T_s (approximately 900 K)[13], whereas our prediction was derived for a 0 K surface. The effect an elevated surface temperature will have on the alignment signature is not completely clear to us. As mentioned before, associative-desorption experiments on D_2 and H_2 + Cu(111)[86] suggest that the width of the S-shaped degeneracy-averaged reaction probability curves $P_{deg}(E;v,j)$ will increase with T_s for H_2 on Cu(100). One might expect the same to be true for the $P_r(E;v,j,m_j)$. If, at

low E, the $P_r(E;v,j,m_j)$ were to increase by the same amount for all m_j, application of equation (3.10) would lead to a lower value of the alignment. However, the midpoint of the S-shaped reaction probability curve generally shifts to higher E with decreasing $|m_j|$ and the saturation value of the reaction probability decreases with decreasing $|m_j|$ (see for instance figure 3 of reference 35). This suggests that, at low E, the temperature induced broadening of the reaction probability curve would increase $P_r(E;v,j,m_j)$ more for large $|m_j|$ than for small $|m_j|$ and that the measured alignment could be more or less independent of T_s. We therefore expect that the requirement of a high T_s in the experiment should not really hamper the experimental confirmation of our predictions regarding alignment.

3.6. Summary

In this study we have calculated initial-state-resolved reaction probabilities for H₂+Cu(100), for the (v=0, j=0-5) and the (v=1, j=0-5) states of H₂, for normal incidence only, modelling motion in all six degrees of freedom of H₂. In the quantum dynamical calculations, the symmetry-adapted wave packet (SAWP[31]) method was used. The ground-state potential energy surface used in this study (PES 4) was taken from density functional theory calculations, with the Cu(100) surface being represented by a slab with application of periodic boundary conditions and using the generalised gradient approximation (GGA)[26]. We used the recently implemented flux analysis method to obtain initial-state-selective site-specific reaction probabilities for the bridge, hollow and top sites[26].

Analysis of the site-specific degeneracy-averaged reaction probabilities showed that, for all j levels studied, initial (v=1) H₂ prefers to react at the top site and initial (v=0) H₂ at the bridge site, near threshold energies. The mechanism behind the greater reactivity of (v=1) H₂ at the top site derives from special features of the PES at the top site, i.e., a reaction path with a large curvature in front of an especially late barrier[26,27,98]. Initially vibrationally excited H₂ molecules can be vibrationally de-excited on the way to the

barrier, converting their excess vibrational energy into energy of motion along the reaction path, thus reacting at low incidence energies better at the top site. For the initial ($v=0$) H_2 molecules, the preferred reaction site could be understood solely on the basis of the relative barrier heights (the ($v=0$) H_2 reaction site has the lowest barrier to reaction).

Site-specific degeneracy-averaged reaction probabilities also showed that, in general, the lateness of the top site barrier induces a clear elastic rotational enhancement effect: rotational energy can be used to overcome the barrier because the rotational constant is lowered at the barrier, due to the H-H distance being longer. For reaction at the top site, this was found to be the case for both initial ($v=1$) H_2 and initial ($v=0$) H_2. The absence of azimuthal anisotropy at the top site barrier also plays a large role allowing molecules in helicopter states to react without rotational hindering above that site. The bridge site, having an earlier barrier, which is more anisotropic in ϕ than the top site barrier, showed no such behaviour. This finding was related to other theoretical studies of reduced dimensionality on the same or similar systems. Because initial ($v=1$) H_2 tends to react at the top site at near threshold energies, the total reaction probabilities show a clear elastic rotational enhancement near threshold for ($v=1$) H_2. This, by itself, is a signature for top site reaction of $v=1$ H_2 that could be measured in associative desorption experiments. On the other hand, near threshold the reaction of ($v=0$) H_2 shows no rotational enhancement because it reacts at the bridge site. If experimentally measured reaction probabilities would show a clear elastic rotational enhancement effect near threshold for initial ($v=1$) H_2 and not for ($v=0$) H_2, this would strongly support our theoretical finding that ($v=1$) H_2 reacts at the top site and ($v=0$) H_2 at the lowest barrier bridge site.

The dependence of reaction of ($v=0$) and ($v=1$) H_2 on j that is here predicted for Cu(100) (no dependence for ($v=0$), rotational enhancement at low j for ($v=1$)) differs from that measured for H_2+Cu(111)[12]. Specifically, on Cu(111) the reaction of H_2 is hindered for low j and rotationally enhanced for j > 4, for both ($v=0$) and ($v=1$). The difference between the j dependence of reaction of H_2 on Cu(100) and Cu(111) was attributed to differences in barrier locations, reaction barriers being later for the Cu(100) surface.

A detailed analysis of the previously found experimental signature[26,27], based on the comparison of the (v=0) and (v=1) rotational quadrupole alignments of reacting H$_2$, has been presented for all j levels considered. The observed trends could not be explained by steric hindering arguments alone, as was possible for initial (j=4) H$_2$. These arguments are only sufficient to explain the alignment of initial j=1, 4 and 5 reacting H$_2$. The alignment of reacting (j=2) and (j=3) H$_2$ is also strongly affected by inelastic rotational enhancement near threshold energies. Near threshold, a mechanism in which the molecule converts its rotational energy into energy in motion along the reaction path may be the only mechanism through which it can react. For (v=1) H$_2$, which reacts at a site (top) which has a very large polar anisotropy, the rotational de-excitation mechanism is especially effective for cartwheel states, lowering the alignment of reacting H$_2$ near threshold. The inelastic rotational enhancement mechanism is most effective for (j=2) and (j=3) H$_2$ because rotational de-excitation may occur with small energy gaps for these low j levels.

All observed trends in the relative heights of the rotational quadrupole alignments of (v=1) and (v=0) reacting H$_2$ molecules close to threshold have been shown to correlate to specific features of the PES at the preferred reaction site. This makes the measurement of the relative alignments of (v=0) and (v=1) reacting molecules suitable for identifying the reaction site, although the interpretation is more complicated than could have been anticipated from previous results for (j=4) H$_2$ only. Specifically: if the rotational quadrupole alignment of initial (v=1,j=1,4 and 5) H$_2$ is measured to be higher than the rotational quadrupole alignment of initial (v=0,j=1,4 and 5) H$_2$ at energies close to threshold, this indicates that (v=1) H$_2$ reacts at the top site and (v=0) H$_2$ at the bridge site. If at the same time the rotational quadrupole alignment of reacting (v=1,j=2) molecules were measured to be lower than for (v=0,j=2) near threshold, this would support our finding that the reaction of (j=2) cartwheels can be enhanced through a rotationally-inelastic mechanism. It would also give further support to our theoretical finding that (v=1) H$_2$ reacts at the top site and (v=0) H$_2$ at the bridge site. Our predictions can be confirmed in experiments using currently available techniques, provided that detailed balance holds so that reaction probabilities can be inferred from associative desorption

probabilities. Specifically, the rotational enhancement signature can be confirmed in associative desorption experiments using TOF techniques and laser detection (for instance, REMPI) to obtain reaction (desorption) probabilities that are resolved with respect to the collision (desorption) energy and the (v,j) level of H_2[12]. The rotational quadrupole alignment of reacting (desorbing) H_2 can be measured by performing two different experiments with linearly polarised laser light, taking the polarisation normal to the surface in the one experiment and parallel in the other[13]. Confirmation of our predictions for Cu(100) would add significant weight to our belief in the predicting power of present day functionals (based on the generalised gradient approximation) of DFT: it would show that DFT can predict the location of the lowest reaction barrier, as well as relative barrier heights and the detailed features of the potential at barrier geometries that determine reactivities for specific initial (v,j,m_j) states of H_2.

3.7. References

1   G. R. Darling and S. Holloway, Rep. Prog. Phys. 58, 1595 (1995).
2   B. E. Hayden, in Dynamics of Gas-Surface Interactions, edited by C. T. Rettner and M. N. R. Ashfold (The Royal Society of Chemistry, Letchworth, 1991), pp. 137-170.
3   H. A. Michelsen, C. T. Rettner, and D. J. Auerbach, Phys. Rev. Lett. 69, 2678 (1992).
4   H. A. Michelsen, C. T. Rettner, D. J. Auerbach, and R. N. Zare, J. Chem. Phys. 98, 8294-8307 (1993).
5   L. Schröter, R. David, and H. Zacharias, J. Vac. Sci. Technol. A 9, 1712 (1991).
6   M. Gostein and G. P. Sitz, J. Chem. Phys. 106, 7378 (1997).
7   B. E. Hayden and C. L. A. Lamont, Phys. Rev. Lett. 63, 1823 (1989).
8   L. Schröter, H. Zacharias, and R. David, Phys. Rev. Lett. 62, 571 (1989).
9   G. D. Kubiak, G. O. Sitz, and R. N. Zare, J. Chem. Phys. 83, 2538 (1985).
10   L. Schröter, R. David, and H. Zacharias, Surf. Sci. 258, 259 (1991).
11   K. D. Rendulic and A. Winkler, Surf. Sci. 299-300, 261 (1994).
12   C. T. Rettner, H. A. Michelsen, and D. J. Auerbach, J. Chem. Phys. 102, 4625 (1995).
13   H. Hou, S. J. Gulding, C. T. Rettner, A. M. Wodtke, and D. J. Auerbach, Science 277, 80 (1997).
14   D. Wetzig, R. Dopheide, M. Rutkowski, R. David, and H. Zacharias, Phys. Rev. Lett. 76, 463 (1996).
15   D. Wetzig, M. Rutkowski, R. David, and H. Zacharias, Europhys. Lett. 36, 31 (1996).

16   S. J. Gulding, A. M. Wodtke, H. Hou, C. T. Rettner, H. A. Michelsen, and D. J. Auerbach, J. Chem. Phys. 105, 9702 (1996).

17   M. Gostein, H. Parhikhteh, and G. O. Sitz, Phys. Rev. Lett. 75, 342 (1995).

18   A. Hodgson, P. Samson, A. Wights, and C. Cottrell, Phys. Rev. Lett. 78, 963 (1997).

19   A. Hodgson, J. Moryl, P. Traversaro, and H. Zhao, Nature 356, 501 (1992).

20   C. T. Rettner, D. J. Auerbach, and H. A. Michelsen, Phys. Rev. Lett. 68, 2547 (1992).

21   G. Anger, A. Winkler, and K. D. Rendulic, Surf. Sci. 220, 1 (1989).

22   G. Comsa and R. David, Surf. Sci. 117, 77 (1982).

23   H. A. Michelsen and D. J. Auerbach, J. Chem. Phys. 94, 7502 (1991).

24   E. Watts, G. O. Sitz, D. A. McCormack, G. J. Kroes, R. A. Olsen, J. A. Groeneveld, J. N. P. van Stralen, E. J. Baerends, and R. C. Mowrey, J. Chem. Phys. 114, 495-503 (2001).

25   R. C. Mowrey, G. J. Kroes, and E. J. Baerends, J. Chem. Phys. 108, 6906 (1998).

26   D. A. McCormack, G. J. Kroes, R. A. Olsen, J. A. Groeneveld, J. N. P. van Stralen, E. J. Baerends, and R. C. Mowrey, Faraday Discuss. 117, 109 (2000).

27   D. A. McCormack, G. J. Kroes, R. A. Olsen, J. A. Groeneveld, J. N. P. van Stralen, E. J. Baerends, and R. C. Mowrey, Chem. Phys. Lett. 328, 317-324 (2000).

28   G. J. Kroes, E. J. Baerends, and R. C. Mowrey, Phys. Rev. Lett. 78, 3583 (1997).

29   D. A. McCormack, G. J. Kroes, E. J. Baerends, and R. C. Mowrey, Faraday Discuss. 110, 267 (1998).

30   D. A. McCormack, G. J. Kroes, R. A. Olsen, E. J. Baerends, and R. C. Mowrey, Phys. Rev. Lett. 82, 1410 (1999).

31   G. J. Kroes, E. J. Baerends, and R. C. Mowrey, J. Chem. Phys. 107, 3309 (1997).

32   J. Q. Dai and J. C. Light, J. Chem. Phys. 107, 1676 (1997).

33   J. Q. Dai and J. C. Light, J. Chem. Phys. 108, 7816 (1998).

34   R. C. Mowrey, G. J. Kroes, G. Wiesenekker, and E. J. Baerends, J. Chem. Phys. 106, 4248 (1997).

35   D. A. McCormack, G. J. Kroes, R. A. Olsen, E. J. Baerends, and R. C. Mowrey, J. Chem. Phys. 110, 7008 (1999).

36   D. Halstead and S. Holloway, J. Chem. Phys. 93, 2859-2870 (1990).

37   J. Q. Dai and J. Z. H. Zhang, Surf. Sci. 319, 193 (1994).

38   G. J. Kroes, G. Wiesenekker, E. J. Baerends, and R. C. Mowrey, Phys. Rev. B 53, 10397 (1996).

39   J. Q. Dai and J. Z. H. Zhang, J. Chem. Phys. 102, 6280 (1995).

40   J. Harris, Surf. Sci. 221, 335 (1989).

41   G. R. Darling and S. Holloway, Surf. Sci. 268, l305 (1992).

42   J. Sheng and J. Z. H. Zhang, J. Chem. Phys. 97, 6784 (1992).

43   J. Sheng and J. Z. H. Zhang, J. Chem. Phys. 99, 1373 (1993).

44   J. Q. Dai, J. Sheng, and J. Z. H. Zhang, J. Chem. Phys. 101, 1555 (1994).

45   G. R. Darling and S. Holloway, Faraday Discuss. 110, 253 (1998).

46   M. R. Hand and S. Holloway, J. Chem. Phys. 91, 7209 (1989).

47   G. R. Darling and S. Holloway, Surf. Sci. 304, L461 (1994).

48   G. R. Darling and S. Holloway, J. Chem. Phys. 101, 3268 (1994).

49   G. R. Darling, M. Kay, and S. Holloway, Surf. Sci. 400, 314 (1998).

50   T. Burner and W. Brenig, Surf. Sci. 317, 303 (1994).

51   G. R. Darling and S. Holloway, Surf. Sci. 307-409, 153. (1994).
52   M. Hand and S. Holloway, Surf. Sci. 211, 940 (1989).
53   G. J. Kroes, Prog. Surf. Sci. 60, 1-85 (1999).
54   R. C. Mowrey, J. Chem. Phys. 99, 7049 (1993).
55   G. R. Darling and S. Holloway, Faraday Discuss. 96, 43 (1993).
56   G. J. Kroes, G. Wiesenekker, E. J. Baerends, R. C. Mowrey, and D. Neuhauser, J. Chem. Phys. 105, 5979 (1996).
57   G. R. Darling and S. Holloway, Chem. Phys. Lett. 191, 396 (1992).
58   G. R. Darling and S. Holloway, J. Chem. Phys. 97, 5182 (1992).
59   D. Wetzig, M. Rutkowski, H. Zacharias, and A. Gross, Phys. Rev. B 63, 205412 (2000).
60   A. Gross and M. Scheffler, Chem. Phys. Lett. 263, 567 (1996).
61   A. Gross and M. Scheffler, Phys. Rev. Lett. 77, 405 (1996).
62   A. Gross, S. Wilke, and M. Scheffler, Surf. Sci. 358, 614 (1996).
63   A. Gross and M. Scheffler, Phys. Rev. B 57, 2493 (1998).
64   A. Gross, C. M. Wei, and M. Scheffler, Surf. Sci. 416, L1095 (1998).
65   A. Gross and M. Scheffler, Prog. Surf. Sci. 53, 187 (1996).
66   A. Gross and M. Scheffler, Chem. Phys. Lett. 256, 417 (1996).
67   A. Gross, S. Wilke, and M. Scheffler, Phys. Rev. Lett. 75, 2718 (1995).
68   G. J. Kroes, J. G. Snijders, and R. C. Mowrey, J. Chem. Phys. 102, 5512-5524 (1994).
69   G. R. Darling and S. Holloway, J. Electron Spectrosc. Relat. Phenom. 64-65, 517 (1993).
70   H. F. Busnengo, W. Dong, and A. Salin, Chem. Phys. Lett. 320, 328-334 (2000).
71   H. F. Busnengo, C. Crespos, W. Dong, A. Salin, and J. C. Rayez, Phys. Rev. B 63, 041402 (2001).
72   A. Gross, J. Chem. Phys. 110, 8696 (1999).
73   G. J. Kroes, J. G. Snijders, and R. C. Mowrey, J. Chem. Phys. 103, 5121 (1995).
74   C. Engdahl, B. I. Lundqvist, U. Nielsen, and J. K. Nørskov, Phys. Rev. B 45, 11362 (1992).
75   C. Engdahl and U. Nielsen, J. Chem. Phys. 98, 4223 (1993).
76   P. Hohenberg and W. Kohn, Phys. Rev. B 136, 864 (1964).
77   W. Kohn and L. J. Sham, Phys. Rev. A 140, 1133 (1965).
78   G. Wiesenekker, G. J. Kroes, and E. J. Baerends, J. Chem. Phys. 104, 157 (1996).
79   B. Hammer, M. Scheffler, K. W. Jacobsen, and J. K. Nørskov, Phys. Rev. Lett. 73, 1400 (1994).
80   S. Wilke and M. Scheffler, Phys. Rev. B 53, 4926-4932 (1996).
81   A. Eichler, J. Hafner, A.Gross, and M. Scheffler, Phys. Rev. B 59, 13297-13300 (1999).
82   D. A. McCormack, G. J. Kroes, R. A. Olsen, J. A. Groeneveld, J. N. P. van Stralen, E. J. Baerends, and R. C. Mowrey, Chem. Phys. Lett. 346, 347-348 (2001).
83   G. J. Kroes, A. Gross, E. J. Baerends, M. Scheffler, and D. A. McCormack, Acc. Chem. Res. 35, 193 (2002).
84   A. Gross, Surf. Sci. Repts. 32, 291 (1998).
85   M. Dohle and P. Saalfrank, Surf. Sci. 373, 95 (1997).
86   M. J. Murphy and A. Hodgson, J. Chem. Phys. 108, 4199 (1998).

87   H. A. Michelsen, C. T. Rettner, and D. J. Auerbach, Surf. Sci. 272, 65 (1992).
88   V. A. Mandelshtam and H. S. Taylor, J. Chem. Phys. 103, 2903 (1995).
89   G. G. Balint-Kurti, R. N. Dixon, and C. C. Marston, Int. Rev. Phys. Chem. 11, 317 (1992).
90   G. G. Balint-Kurti, R. N. Dixon, and C. C. Marston, J. Chem. Soc. 86, 1741 (1990).
91   A. Messiah, Quantum Mechanics (John Wiley & sons, New York, Chichester, Brisbane, Toronto, 1958).
92   R. A. Olsen, P. H. T. Philipsen, E. J. Baerends, G. J. Kroes, and O. M. Lovvik, J. Chem. Phys. 106, 9286 (1997).
93   D. H. Neuhauser, M. Baer, R. S. Judson, and D. J. Kouri, Comput. Phys. Commun. 63, 460 (1991).
94   D. H. Zhang and J. Z. H. Zhang, J. Chem. Phys. 101, 1146 (1994).
95   J. P. Perdew, Phys. Rev. B 33, 8822 (1986).
96   S. H. Vosko, L. Wilk, and M. Nusair, Can. J. Phys. 58, 1200 (1980).
97   A. D. Becke, Phys. Rev. A 38, 3098 (1988).
98   G. R. Darling and S. Holloway, J. Chem. Phys. 97, 734 (1992).
99   P. Kratzer, B. Hammer, and J. K. Nørskov, Surf. Sci. 359, 45 (1996).
100   R. N. Zare, Angular momentum, Wiley-Interscience, 226-242 (1988).
101   W. A. Dino, H. Kasai, and A. Okiji, J. Phys. Soc. Jpn 67, 1571 (1998).
102   G. R. Darling, M. Kay, and S. Holloway, Phys. Rev. Lett. 78, 1731 (1997).

Chapter 4

Performance and application of a symmetry adapted pseudo-spectral method for scattering of a diatomic molecule from a square surface: H_2+Cu(100)

Abstract

The H_2+Cu(100) system was used to test the performance of a newly developed, symmetry adapted pseudo-spectral (SAPS) wave packet method for performing six dimensional quantum dynamical calculations on reactive scattering of diatomic molecules from square surfaces. Four test calculations have been performed on two different DFT PESs to compare the performance of the new SAPS method with that of the symmetry adapted wave packet (SAWP) method and the ordinary pseudo-spectral (PS) method. The comparison has been made for the $(v=0,j=4,m_j=0)$ and the $(v=0,j=0,m_j=0)$ initial states of H_2, for the normal incidence energy ranges of 0.3 to 0.9 eV and 0.3 to 1.15 eV, respectively. The results for $(v=0,j=4,m_j=0)$ H_2 reacting on PES 4, a PES expanded in a limited number of symmetry adapted functions so that it is suitable for use in the SAWP method, show that the SAPS method is competitive with the SAWP method, even for this PES. The results for $(v=0,j=0,m_j=0)$ H_2 reacting on PES 5, a DFT PES represented using the corrugation reduction scheme, show that for this initial state the SAPS method is superior to the PS method by a factor of 6. It is concluded that, in general, for a given state the SAPS method will be at least three times faster than the PS method, also using at least three times less memory.

4.1. Introduction

Wave packet methods have been proven to be very successful in applications to molecule-surface scattering problems. Examples include studies of scattering of molecules from impure[1-3] or disordered surfaces[2,4,5], the involvement of phonons in atom-surface scattering[2,6], rotationally[7-24] or vibrationally inelastic scattering[23,25-32] of molecules from surfaces, molecule-surface photodesorption[33-35] and reactive molecule-surface scattering[17-19,26,36-47]. In the latter field, the wave packet studies have moved from using model PESs in reduced dimensional simulations into the realm of full dimensional quantum dynamics calculations on realistic DFT PESs[48-53], which treat all the degrees of freedom of the impinging molecule essentially without approximations[44,45,54-67]. Much of this dynamical work has benefited greatly from the large amount of effort spent in the development of wave packet methods[6,15,68-87]. The methods have become more efficient in using memory and computer resources. Besides that, in the last decade, the use of parallel computing also contributed significantly to the progress.

From the methodological point of view, in the time dependent wave packet techniques applied to molecule-surface scattering problems, two main approaches have been pursued: The close-coupling wave packet (CCWP) scheme[7-10,56-62,66,67,76,81,88-93] on the one hand, and pseudo-spectral (PS) methods[11-16,54,55,63-65,77-79,94-101], which employ the discrete variable representation (DVR) or the finite basis representation (FBR) as the primary representation of the wave packet, on the other hand. Both aimed to reduce the computational costs associated with the application of the Hamiltonian operation. The essential difference between the two approaches is that in the CCWP method, the application of the potential operator is performed by a matrix vector product scaling as N_b^2, with N_b being the total number of basis functions in which the wave packet is expanded for some of the degrees of freedom. A potential coupling matrix is defined, calculated analytically and usually stored in central memory. The advantage of this approach is in the costs associated with the kinetic energy operators of the Hamiltonian operator. The latter usually involve only point wise multiplications.

For the pseudo-spectral schemes the potential energy operation is performed by a point wise multiplication, i.e. it is taken to be diagonal in the DVR and use of the dual space nature of quantum mechanics is made[13,94-96,98-102]. Depending on whether the DVR or the FBR is taken as the primary representation, the kinetic energy operation or the potential operation requires a forward and backward transform between co-ordinate and momentum space. In the pseudo-spectral methods, the costs associated with parts of the Hamiltonian operation are thus shifted from matrix vector products to the transforms needed. An important advantage of a direct product PS representation is that it scales quasi linearly with the total number of grid points used, thus avoiding the quadratic scaling with the total number of basis functions treated within a CCWP scheme. In principle the CCWP scheme becomes unfavourable if more than one degree of freedom is treated within the close-coupling scheme, unless the potential coupling matrix is sparse. In the PS method, the potential only needs to be stored on specific grid points, and the PS method can also be viewed as a CCWP method in which the potential coupling matrix is calculated through a quadrature integration scheme[13,98,99,101].

The PS method was extended to the case of a non-direct product representation[13,101]. For a spherical harmonics FBR the potential operation is performed by using a combination of a Gauss Legendre matrix transform and an FFT transform to obtain the wave packet in the angular DVR (θ,ϕ), followed by a point wise multiplication of the wave function with the potential and similar inverse transforms to regain the FBR. The FBR is chosen as the main representation because the corresponding DVR can be twice as large[97] due to the non-direct product nature of the spherical harmonics. Moreover, it was also shown that the potential operation, including the transforms, approximately scales as $2\,N_{jm_j}^{\;3/2}$ for large N_{jm_j}, the number of spherical harmonics in the wave packet expansion[13,101,103]. This method has been successfully applied to six-dimensional reactive scattering of HD and H_2 from Pt(111)[63,64] and H_2 from Pd(111)[54].

Despite the apparently better scaling laws of the direct product pseudo-spectral schemes, the CCWP strategy has also led to successes. The use of the symmetry of the square

surface, in a method known as the SAWP method[56,88,89], made it possible to perform the first six dimensional quantum dynamical wave packet calculation for a fully activated reaction, the $H_2+Cu(100)$ system[57]. In this method, four of the six degrees of freedom were treated using the close coupling representation. However, the SAWP scheme can only be used efficiently if the PES is expanded in a limited number of symmetry adapted functions of these four degrees of freedom, so that a sparse potential coupling matrix is obtained[89]. Note that symmetry adapted basis functions were also used in the first six dimensional quantum dynamics calculations on dissociation of H_2 on a metal surface, in which a time independent method was used to address the non-activated dissociative chemisorption of hydrogen on $Pd(100)$[104].

In this study we have tried to combine the use of symmetry of the square surface unit cell with the pseudo-spectral approach. The aim was to develop a symmetry adapted pseudo-spectral method, which combines the good scaling properties of the PS methods with the advantages of using the symmetry of the surface, for wave packet calculations on diatomic molecules scattering from square surfaces at normal incidence. The reason that the development of an especially efficient computational method for scattering at normal incidence is of special interest, is that many molecule-surface reactions obey normal energy scaling[105], meaning that the reaction probability only depends on the component of the collision energy normal to the surface.

In the presentation of the new method, section (4.2.1) starts of with the general theory of time dependent quantum dynamical wave packet methods. In section (4.2.2) several methods are briefly discussed in order to correctly classify and better understand the new method. Section (4.2.2.1) starts of with the CCWP[7-9,89] and the rotationally and diffractionally close-coupled wave packet[89] (RDWP) methods, which are closely related and based on close coupling representations of the wave packet. Section (4.2.2.2) will briefly describe the PS method and in section (4.2.2.3) the use of symmetry is introduced into the RDWP method, thus obtaining the SAWP method. Finally, in section (4.2.2.4) symmetry is introduced into the PS method to obtain the new symmetry adapted pseudo-spectral (SAPS) method. Section (4.2.3) provides details on the different propagators that

have been used in the PS, the SAWP and the SAPS methods and in section (4.2.4) the two different PESs used in the test calculations are briefly described. Numerical details of the four calculations performed are given in section (4.2.5). Section (4.3.1) presents the comparison of the performance of the SAPS and SAWP methods for the reaction of H_2 on Cu(100) using a PES (PES 4) which is especially suited to the SAWP scheme. The comparison of the PS and the SAPS method, for a PES of general form (PES 5), is done in section (4.3.2). Finally conclusions are given in section (4.4).
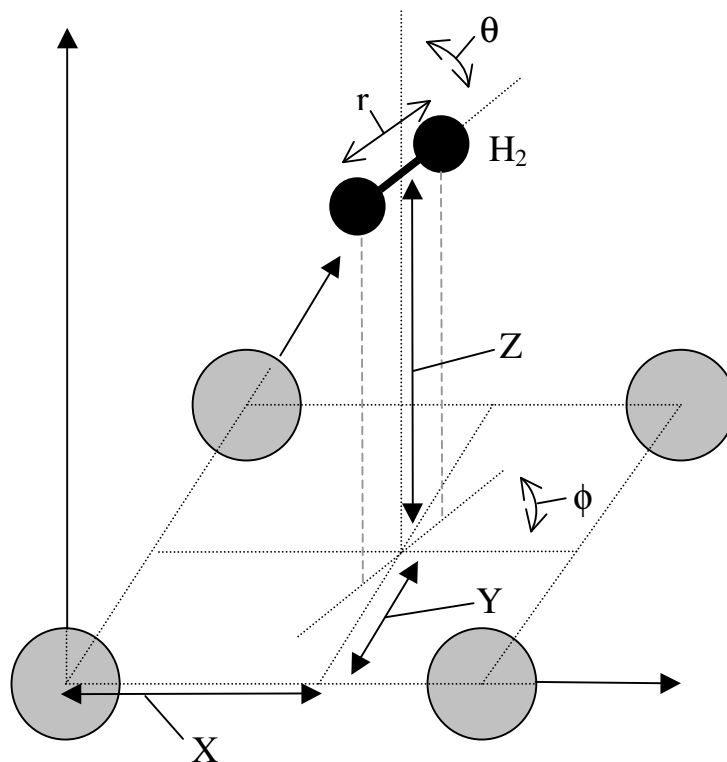
Figure 4.1: The co-ordinate system used. $\vec{R} = (X, Y, Z)$ corresponds to the centre of mass, r to the H-H distance and (θ, ϕ) to the orientation of H_2 with respect to the surface.

4.2. Theory

4.2.1. Outline of wave packet methods for AB surface scattering

The time-independent Hamiltonian describing the dynamics of a diatomic molecule, AB, interacting with a static surface can be written as:

$$\hat{H} = -\tfrac{1}{2M}\nabla_{\vec{R}}^2 - \tfrac{1}{2\mu}\nabla_r^2 + \hat{H}_{rot} + V(\vec{R}, r, \theta, \phi).$$

(4.1)

Atomic units have been used in (4.1) and will be used throughout this paper. Furthermore, $\vec{R} = (X, Y, Z)$ is the vector representing the centre of mass co-ordinate of AB, r the A-B distance, ϕ the azimuthal angle and θ the polar angle of the A-B bond with respect to the surface normal (see Figure 4.1). The term $\hat{H}_{rot}$ is the Hamiltonian describing the rotational energy of AB and V is the potential describing the interactions of the atoms A and B with each other and the surface. Finally, M is the total mass of AB and μ its reduced mass.

The formal scattering solution of the time independent Schrödinger equation obtained from (4.1), the stationary wave function Ψ^+, should obey the scattering boundary conditions, which, for normal incident AB, at a distance Z_∞ far from the surface, can be written as:

$$\Psi^+(E; \vec{R}, r, \theta, \phi)\Big|_{Z=Z_\infty} = \frac{\exp(-ikZ_\infty)}{\sqrt{2\pi}} \cdot \chi_{vj}(r) \cdot \sqrt{1/(L_x L_y)} \cdot Y_{jm_j}(\theta, \phi) -$$

$$\sum_{v'j'm_j'nm}\left[\sqrt{\frac{k}{k_{v'j'm_j'nm}}} \cdot \exp(i \cdot k_{v'j'm_j'nm} Z_\infty)/\sqrt{2\pi} \cdot S_{vjm_j \to v'j'm_j'nm}(E) \cdot\right.$$

$$\left.\chi_{v'j'}(r) \cdot Y_{j'm_j'}(\theta, \phi) \cdot \sqrt{1/(L_x L_y)} \cdot \exp(i \cdot nG_x X + i \cdot mG_y Y)\right].$$

(4.2)

In (4.2), L_x and L_y are the lattice constants in X and Y, $\mathbf{Y}_{jm_j}(\theta,\phi)$ the spherical harmonics, k is the initial momentum of the impinging molecule towards the surface, $k_{v'j'm_j'nm}$ the final momentum of the scattered molecule, $(G_x,G_y) = (\frac{2\pi}{L_x}, \frac{2\pi}{L_y})$ and the $\chi_{vj}(r)$ are the rovibrational eigen functions of the molecule in the gas phase. Also, S(E) is the S-matrix, which depends on the total energy E. Finally, n and m represent the diffractional, j the rotational, m_j the rotational magnetic and v the vibrational quantum numbers of AB.

The probability of scattering from the initial state (v,j,m_j) to the final rovibrational diffraction state (v',j',m_j',n,m) at incidence energy E_k can be obtained through:

$$P_{vjm_j \to v'j'm_j'nm}(E_k) = \left| S_{vjm_j \to v'j'm_j'nm}(E = E_k + E_{vjm_j}) \right|^2 . \tag{4.3}$$

In (4.3), E_{vjm_j} is the internal energy of the incident molecule. The initial state selective reaction probability can be obtained from (4.3) through:

$$P_r^{vjm_j}(E_k) = 1 - \sum_{v'j'm_j'nm} P_{vjm_j \to v'j'm_j'nm}(E_k) . \tag{4.4}$$

Using (4.1) in the time dependent Schrödinger equation, we can formulate the molecule-surface scattering problem as an initial value problem:

$$\psi_{vjm_j}(t = t'; \vec{R}, r, \theta, \phi) = \exp(-i\hat{H}t') \cdot \psi_{vjm_j}(t = 0; \vec{R}, r, \theta, \phi) . \tag{4.5}$$

Defining

$$\Phi_{vjm_j}(k; Z, r, \theta, \phi) = \frac{\exp(-ikZ)}{\sqrt{2\pi}} \cdot \chi_{vj}(r) \cdot \sqrt{1/(L_x L_y)} \cdot \mathbf{Y}_{jm_j}(\theta, \phi) \tag{4.6a}$$

the initial wave packet $\psi_{vjm_j}(t=0)$ can be taken as a linear superposition of stationary scattering states of different energies corresponding to a Gaussian distribution of initial momenta, b(k), centred around $Z=Z_0$ and moving towards the surface:

$$\psi_{vjm_j}(t=0;\vec{R},r,\theta,\phi) = \int_{-\infty}^{\infty} a(E_k)\Phi_{vjm_j}(k;Z,r,\theta,\phi)dE_k \qquad (4.6b)$$

with

$$\begin{aligned} a(E_k)dE_k &= \frac{M}{k}b(k)dk \\ &= \frac{M}{k}\sqrt[4]{\frac{2\zeta 2}{\pi}}\exp\!\left(-(k_{av}-k)^2\zeta^2+i(k_{av}-k)Z_0\right)dk. \end{aligned} \qquad (4.6c)$$

In (4.6b), $\Phi_{vjm_j}(k;Z,r,\theta,\phi)$ is the eigen state of the time independent Hamiltonian (4.1) corresponding to the molecule moving towards the surface at normal incidence in the initial state (v,j,m$_j$) with total energy E before interacting with the potential. Moreover, ζ is the half-width (standard deviation) of the initial Gaussian distribution and k_{av} is the average momentum taken to be negative to represent molecules moving towards the surface.

The initial wave packet (4.6b) can be propagated in time using various approximations to the time evolution operator (4.5), $\exp(-i\hat{H}t')$, such as the Split Operator formalism[100], the short iterative Lanczos[106], the Chebyshev[107] method and the adapted Chebyshev method incorporating ABC[108]. If propagated sufficiently long, t=t$_{tot}$, the stationary scattering state (4.2) can be obtained by Fourier transforming the time dependent wave packet:

$$\int_0^{t_{tot}} \exp(iEt')\cdot\psi_{vjm_j}(t=t';\vec{R},r,\theta,\phi)dt' \approx a(E_k=E-E_{vjm_j})\Psi^+(E;\vec{R},r,\theta,\phi). \qquad (4.7)$$

Finally the scattering matrix can be retrieved from (4.2) and (4.7) in a straightforward way through the Scattering Amplitude formalism[109,110]:

$$S_{vjm_j \to v'j'm_j'nm}(E) = \exp(-2ikZ_\infty) \cdot \delta_{vv'} \cdot \delta_{jj'} \cdot \delta_{m_jm_j'} \cdot \delta_{0n} \cdot \delta_{0m} -$$
$$\frac{1}{M \cdot b(-k)} \cdot \sqrt{k \cdot k_{v'j'm_j'nm}} \cdot \exp(-ik_{v'j'm_j'nm}Z_\infty)/\sqrt{2\pi} \cdot A_{v'j'm_j'nm}(E;Z_\infty)$$
(4.8a)

$$A_{v'j'm_j'nm}(E;Z_\infty) = \int_0^{t_{tot}} \exp(iEt') \cdot C_{v'j'm_j'nm}(t';Z_\infty)dt'$$
(4.8b)

$$C_{v'j'm_j'nm}(t';Z_\infty) = \left\langle \chi_{v'j'}(r) \cdot Y_{j'm_j'}(\theta,\phi) \cdot \sqrt{1/(L_xL_y)} \cdot \exp(i \cdot nG_xX + i \cdot mG_yY) \right|$$
$$\psi_{vjm_j}(t = t';\vec{R},r,\theta,\phi)\Big|_{Z=Z_\infty} \Big\rangle.$$
(4.8c)

In (4.8c), the coefficients $C_{v'j'm_j'nm}(t';Z_\infty)$ are obtained by integration over X, Y, r, θ and ϕ. In a wave packet calculation, S-matrix elements are obtained for the entire range of energies contained in the initial wave packet, though only for the column corresponding to the initial state[96].

4.2.2. Description of individual wave packet methods

The numerical efficiency of a wave packet method depends on the representation of the wave packet used and the manner in which the action of the Hamiltonian is carried out[96]. Various methods[11,13,15,21,56,57,68-89,109,110] have been used for diatomic molecule-surface scattering, of which the most important ones will be briefly described to understand and classify the new SAPS method.

4.2.2.1. CCWP and RDWP methods

The first calculations on *non-reactive* rotationally inelastic molecule-surface scattering were based on a close-coupling wave packet technique and the method was called the CCWP method[7-9]. In the CCWP method the wave packet, for initial state (j,m_j) at time t, is expanded in a set of rotational basis functions and represented by coefficients on equally spaced grids in $\vec{R} = (X, Y, Z)$ of sizes N_x, N_y and N_z:

$$\psi_{jm_j}(t; \vec{R}, \theta, \phi) = \sum_{j'm_j'} C_{j'm_j'}^{jm_j}(\vec{R}, t) \cdot \mathbf{Y}_{j'm_j'}(\theta, \phi).$$
(4.9)

In (4.1), the kinetic energy operations associated with the translational motion can be efficiently performed using FFT's[95,100]. The potential energy operation is performed by multiplying the vector $C_{j'm_j'}^{jm_j}(\vec{R}, t)$ with the potential coupling matrix defined as:

$$\mathbf{V}_{jm_j, j'm_j'}(\vec{R}) = \left\langle \mathbf{Y}_{jm_j}(\theta, \phi) \middle| V(\vec{R}, \theta, \phi) \middle| \mathbf{Y}_{j'm_j'}(\theta, \phi) \right\rangle.$$
(4.10)

If no use is made of the possible sparseness of (4.10), the latter operation scales as $N_z N_x N_y N_{jm_j}^2$, with N_{jm_j} being the number of rotational states included in (4.9). If on the other hand (4.10) is taken to be sparse[88], the scaling is given by $N_z N_x N_y N_{jm_j}^{coup} N_{jm_j}$, in which $N_{jm_j}^{coup}$ is the number of rotational states to which a given rotational state is coupled on average by the potential. Clearly, if the sparseness can be used, the scaling is more favourable and less central memory is needed to store the potential coupling matrix[88]. The total scaling of the Hamiltonian operation in the CCWP method, making use of the sparseness of (4.10), is:

$$N_{jm_j} N_x N_y N_z \left(1 + 2\eta \log(N_x N_y N_z) + N_{jm_j}^{coup}\right).$$
(4.11)

In (4.11), we have used that, once the wave function is in the FBR representation for motion along $\vec{R}$ all the kinetic energy operations (i.e. including the rotational kinetic energy) can be evaluated using a point wise multiplication and the FFT algorithms scale like $\eta NlogN$, in which η is a pre-factor.

Another method very closely related to the CCWP method is the RDWP method[88]. In the latter method not only the rotational, but also the diffractional degrees of freedom of the wave packet are represented by an expansion in a suitable basis set:

$$\psi_{jm_j}(t;\vec{R},\theta,\phi) = \sum_{j'm_j'nm} C^{jm_j}_{j'm_j'nm}(Z,t) \cdot \mathbf{Y}_{j'm_j'}(\theta,\phi) \cdot \frac{\exp(i \cdot nG_xX + i \cdot mG_yY)}{\sqrt{L_xL_y}}. \qquad (4.12)$$

The coefficients $C^{jm_j}_{j'm_j'nm}(Z,t)$ in (4.12) are now defined on an equally spaced grid in Z only.

With the RDWP method, FFT's are no longer needed to evaluate the kinetic operators associated with the motion in X and Y, but the potential coupling matrix needs to be redefined:

$$\begin{aligned}
\mathbf{V}_{jm_jnm,j'm_j'n'm'}(Z) = \frac{1}{L_xL_y} \cdot \Big\langle \mathbf{Y}_{jm_j}(\theta,\phi) \cdot \exp(i \cdot nG_xX + i \cdot mG_yY) \Big| \\
V(\vec{R},\theta,\phi) \Big| \mathbf{Y}_{j'm_j'}(\theta,\phi) \cdot \exp(i \cdot n'G_xX + i \cdot m'G_yY) \Big\rangle.
\end{aligned} \qquad (4.13)$$

Given the definition of (4.13) is seems that, at first glance, the scaling of the RDWP method is worse than that of the CCWP method; the potential energy operation now scales as $N_z \cdot (N_nN_m)^2 \cdot N^2_{jm_j}$ for a general PES. However, the RDWP method also has some advantages. Often one only needs to include diffraction states up to a given order $O = |n| + |m|$, resulting in a total of $N_{nm} = (O+1)(O+2)/2$ diffraction basis functions if a "diamond shaped" grid in momentum space is used, which can in practice be significantly

smaller than the amount of DVR points needed in X and Y with the CCWP scheme[76,88]. On top of that, for suitable potentials, extra use of the sparseness of (4.13) can be made resulting into a potential operator scaling of $N_z N_{nmjm_j}^{coup} N_{nm} N_{jm_j}$, in which $N_{nmjm_j}^{coup}$ is the average number of states to which the potential will couple a given rotation-diffraction state on a given point in Z[88]. The total cost of applying the Hamiltonian operator in the RDWP method scales as:

$$N_z N_{jm_j} N_{nm} \cdot \left(1 + 2\eta \log N_z + N_{nmjm_j}^{coup}\right) \tag{4.14}$$

again taking into account that all the kinetic energy operations can be performed using point wise multiplications.

4.2.2.2. PS method

A spherical harmonics representation first developed for inelastic molecule surface scattering[13,101,103] and recently generalised to *reactive* diatomic molecule surface scattering[54,55,63-65] is based on a Gauss Legendre pseudo-spectral scheme. In this method the wave packet is represented in a non-direct product FBR (Finite Base Representation) of spherical harmonics, $\mathbf{Y}_{jm_j}(\theta,\phi)$, for the angular co-ordinates and Fourier DVR (Discrete Variable Representation) grids in $\vec{R} = (X, Y, Z)$ and r:

$$\psi_{vjm_j}(t;\vec{R},r,\theta,\phi) = \sum_{j'm_j'} C_{j'm_j'}^{vjm_j}(\vec{R},r,t) \cdot \mathbf{Y}_{j'm_j'}(\theta,\phi). \tag{4.15}$$

Again the kinetic energy operations, associated with the translational and reactive degrees of freedom, can be easily evaluated using FFTs[95,100]. To perform the potential operation, the FBR representation, $C_{j'm_j'}^{vjm_j}(\vec{R},r,t)$, is transformed to the DVR, $\psi_{vjm_j}(t;\vec{R},r,\theta_i,\phi_n)$, using a Gauss Legendre transform to switch from the (j',m$_j$') to the (θ_i,m$_j$') representation and FFTs for the (θ_i,m$_j$') to (θ_i,ϕ_n) transforms.

The Gauss Legendre transformation matrix is taken to be[11]:

$$\mathbf{L}_{\theta_i, j'm_{j'}} = \sqrt{\omega(\theta_i)} \cdot L_{j'm_{j'}}(\theta_i).$$

(4.16)

In (4.16), $L_{j'm_{j'}}(\theta_i)$ is the normalised Associated Legendre polynomial, θ_i is the ith root of the $(j_{max}+1)^{th}$ Legendre polynomial, j_{max} being the highest rotational level included in (4.15) and $\omega(\theta_i)$ is the corresponding weight in a Gaussian Quadrature integration scheme.

Having obtained the wave function in the full DVR, $\psi_{vjm_j}(t;\vec{R},r,\theta_i,\phi_n)$, the potential operator is taken to be diagonal and a point wise multiplication of $\psi_{vjm_j}(t;\vec{R},r,\theta_i,\phi_n)$ and $V(\vec{R},r,\theta_i,\phi_n)$ is performed, after which FFTs and the transpose of (4.16) are used again to transform $\psi_{vjm_j}(t;\vec{R},r,\theta_i,\phi_n)$ back to the FBR ($C_{j'm_{j'}}^{vjm_j}(\vec{R},r,t)$).

In the pseudo-spectral scheme, the potential operation can be related to the CCWP method by the way in which the integrals of (4.10) are effectively calculated in the PS scheme, i.e. by using a Gaussian and Fourier quadrature scheme employing a number of points equal to or larger than the number of basis functions[11,98,99,102]. In contrast, in the CCWP method the integrals are done analytically. The total scaling of the potential operation in the PS method is approximately $2N_r N_z N_x N_y N_{jm_j}^{3/2}$, where N_r is the number of points used in the r grid[103]. The total scaling of the Hamiltonian operator in the pseudo-spectral scheme is given by:

$$N_r N_z N_x N_y N_{jm_j} \cdot \left(2N_{jm_j}^{1/2} + 2 + 2\eta \log(N_r N_z N_x N_y)\right)$$

(4.17)

in which $\hat{H}_{rot}$ and the kinetic energy operations for ($\vec{R}$,r) are also accounted for.

4.2.2.3. SAWP method

Although the CCWP and the RDWP methods perform reasonably well for *non-reactive* inelastic scattering problems, which require small basis sets, their application to *reactive* scattering poses problems due to the bad scaling of the potential energy operation. On the other hand, the RDWP method described above allows the straightforward use of symmetry as is now explained[88].

The symmetry of the *surface unit cell* can be used to reduce the computational cost of a scattering calculation: the symmetry operators associated with the surface unit cell act in the individual sub-spaces of the complete Hilbert space of the Hamiltonian operator and leave the Hamiltonian operator invariant. The symmetry operators commute with the Hamiltonian operator and symmetry transformed eigen functions of the Hamiltonian are again eigen functions of the Hamiltonian operator[111]. In general the symmetry of the surface unit cell can therefore be used to reduce computational cost. For normal incidence and square shaped unit cells, the reduction can be significant because only one or two sub spaces (irreps) of the full Hilbert space need to be dealt with[56,58,76,88,89].

C_{4v}, h=8	E	C_{2z}	C_{4z}	C_{4z}^{-1}	σ_y	σ_x	σ_{-xy}	σ_{xy}
E Irrep	$\begin{pmatrix} 1 & 0 \\ 0 & 1 \end{pmatrix}$	$\begin{pmatrix} -1 & 0 \\ 0 & -1 \end{pmatrix}$	$\begin{pmatrix} 0 & -1 \\ 1 & 0 \end{pmatrix}$	$\begin{pmatrix} 0 & 1 \\ -1 & 0 \end{pmatrix}$	$\begin{pmatrix} -1 & 0 \\ 0 & 1 \end{pmatrix}$	$\begin{pmatrix} 1 & 0 \\ 0 & -1 \end{pmatrix}$	$\begin{pmatrix} 0 & -1 \\ -1 & 0 \end{pmatrix}$	$\begin{pmatrix} 0 & 1 \\ 1 & 0 \end{pmatrix}$

Table 4.1: The irrep matrices used to represent the symmetry operations of the two-dimensional E irrep of the C_{4v} point group.

The square surface unit cell belongs to the C_{4v} point group, which is of order 8. The following projection and shifting operators can be defined[111]:

$$\hat{P}_{ij}^{\Gamma} = \frac{d^{\Gamma}}{h} \sum_{\hat{R} \in G} D_{ij}^{\Gamma}(\hat{R}) \cdot \hat{R} . \qquad (4.18)$$

The $D_{ij}^{\Gamma}(\hat{R})$ can be taken from the character table of the C_{4v} point group for the one-dimensional irreps and from Table 4.1 for the two-dimensional irrep[111]. In (4.18), $\hat{R}$ is one of the group symmetry operators, h is the order of the group G and d^{Γ} the dimension of the irrep Γ.

NSA-diffractional basis set	SA-diffractional basis set
$e^{i(|n|Gx + |m|Gy)}$	A_1: $\frac{1}{2}(\cos|n|Gx \cdot \cos|m|Gy + \cos|m|Gx \cdot \cos|n|Gy)$
$e^{i(-|n|Gx + |m|Gy)}$	B_1: $\frac{1}{2}(\cos|n|Gx \cdot \cos|m|Gy - \cos|m|Gx \cdot \cos|n|Gy)$
$e^{i(|n|Gx - |m|Gy)}$	A_2: $-\frac{1}{2}(\sin|n|Gx \cdot \sin|m|Gy - \sin|m|Gx \cdot \sin|n|Gy)$
$e^{i(-|n|Gx - |m|Gy)}$	B_2: $-\frac{1}{2}(\sin|n|Gx \cdot \sin|m|Gy + \sin|m|Gx \cdot \sin|n|Gy)$
$e^{i(|n|Gy + |m|Gx)}$	$E_{1,1}$: $\sin|n|Gx \cdot \cos|m|Gy$
$e^{i(-|n|Gy + |m|Gx)}$	
$e^{i(|n|Gy - |m|Gx)}$	$E_{2,1}$: $\sin|n|Gy \cdot \cos|m|Gx$
$e^{i(-|n|Gy - |m|Gx)}$	

Table 4.2: The non-symmetry-adapted (NSA) diffractional basis functions and the symmetry-adapted (SA) diffractional basis functions for normal incidence as obtained from the NSA plane-wave basis set in X and Y used in (4.19). For the SA basis sets for the 1D irreps we take |n|≥|m|≥0, but for the SA basis set for the E irrep we take |n|≥0,|m|≥0.

NSA-rotational basis set	SA-rotational basis set			
$m_j \in N$	$m_j \in \{0,4,8...\}$	$m_j \in \{2,6,10...\}$	$m_j \in \{1,5,9...\}$	$m_j \in \{3,7,11...\}$
$e^{i|m_j|\phi}$	**A₁:** $\cos|m_j|\phi$	**B₁:** $\cos|m_j|\phi$	**E₂,₁:** $\sin|m_j|\phi$	**E₂,₁:** $-\sin|m_j|\phi$
$e^{-i|m_j|\phi}$	**A₂:** $\sin|m_j|\phi$	**B₂:** $\sin|m_j|\phi$	**E₁,₁:** $\cos|m_j|\phi$	**E₁,₁:** $\cos|m_j|\phi$

Table 4.3: The non-symmetry-adapted (NSA) rotational basis functions and the symmetry-adapted (SA) rotational basis functions obtained from the spherical harmonics as used in (4.19).

Applying (4.18) to the ϕ dependent part of the spherical harmonics and the plane-waves in X and Y of (4.12), the rotational and diffractional non-symmetry adapted (NSA) basis sets respectively, results into the rotational and diffractional symmetry adapted (SA) basis sets. In Table 4.2 the SA diffractional basis functions and in Table 4.3 the SA rotational basis functions are listed. As can be seen from Table 4.2 and Table 4.3, for normal incidence the initial wave packet always transforms as A_1 for the diffractional degrees of freedom ($|n|=|m|=0$) so it can contribute to at most two rotational irreps (contained in $Y_{jm_j}(\theta,\phi)$) for a given initial m_j. For example, if $m_j=0$ the wave packet can only contain the A_1 irrep. For $|m_j| \in \{4,8,12...\}$, the wave packet contains both the A_1 and the A_2 irreps, for $|m_j| \in \{2,6,10...\}$ the B_1 and the B_2 irreps and finally for $|m_j| \in \{1,3,5,7...\}$ the wave packet contains only the E irrep. Moreover, both the rotational and the diffractional SA basis functions are simply linear combinations of NSA rotational and NSA diffractional basis functions, respectively[111].

The total SA basis set is constructed by taking direct products of the SA diffractional and the SA rotational basis sets:

$$g_{j'm_j'nm}^{\Gamma_d\Gamma_r}(X,Y,\theta,\phi) = \chi_{nm}^{\Gamma_d}(X,Y) \cdot \alpha_{j'm_j'}^{\Gamma_r}(\phi) \cdot L_{j'm_j'}(\theta) \tag{4.19}$$

in which $\chi_{nm}^{\Gamma_d}(X,Y)$ is the SA diffractional basis function of irrep Γ_d, $\alpha_{j'm_j'}^{\Gamma_r}(\phi)$ is the SA rotational basis function of irrep Γ_r, $L_{j'm_j'}(\theta)$ the normalised associated Legendre

polynomial and $g^{\Gamma\Gamma_r}_{j'm_j'nm}(X,Y,\theta,\phi)$ is the total SA basis function for irrep Γ composed from the Γ_r rotational irrep. To what total irrep Γ the direct product of the specific partners of the diffractional irrep Γ_d and the Γ_r irrep lead can be determined from the direct product table of the C_{4v} point group[111], shown in Table 4.4. The total SA basis functions can be normalised to unity if needed and only one of the E irrep partners (for Γ_r, Γ_d or Γ) needs to be propagated because the results of the other can be obtained from the one propagated by symmetry[111].

Γ	$\Gamma_d \otimes \Gamma_r$
	$A_1 \otimes A_1$
	$B_1 \otimes B_1$
A_1	$A_2 \otimes A_2$
	$B_2 \otimes B_2$
	$\{E_{1,1} \otimes E_{1,1} + E_{2,1} \otimes E_{2,1}\}/2$
	$A_1 \otimes B_1$
	$B_1 \otimes A_1$
B_1	$A_2 \otimes B_2$
	$B_2 \otimes A_2$
	$\{E_{1,1} \otimes E_{1,1} - E_{2,1} \otimes E_{2,1}\}/2$
	$A_1 \otimes B_2$
	$B_2 \otimes A_1$
B_2	$A_2 \otimes B_1$
	$B_1 \otimes A_2$
	$\{E_{1,1} \otimes E_{2,1} + E_{2,1} \otimes E_{1,1}\}/2$
	$A_1 \otimes A_2$
	$A_2 \otimes A_1$
A_2	$B_1 \otimes B_2$
	$B_2 \otimes B_1$
	$\{E_{1,1} \otimes E_{2,1} - E_{2,1} \otimes E_{1,1}\}/2$
	$A_1 \otimes E_{1,1}$
	$E_{1,1} \otimes A_1$
	$B_1 \otimes E_{1,1}$
	$E_{1,1} \otimes B_1$
E	$A_2 \otimes E_{2,1}$
	$E_{2,1} \otimes A_2$
	$B_2 \otimes E_{2,1}$
	$E_{2,1} \otimes B_2$

Table 4.4: The direct product table of the C_{4v} point group.

Using (4.19), the wave packet for a given total irrep Γ, which is contained in the initial (v,j,m_j) state, can be expanded in the SA basis set:

$$\psi_{vjm_j}^{\Gamma}(t;\vec{R},r,\theta,\phi) = \sum_{j'm_j'nm\Gamma_r} C_{j'm_j'nm}^{\Gamma\Gamma_r,vjm_j}(Z,r,t) \cdot g_{j'm_j'nm}^{\Gamma\Gamma_r}(X,Y,\theta,\phi) \qquad (4.20)$$

in which the expansion coefficients $C_{j'm_j'nm}^{\Gamma\Gamma_r,vjm_j}(Z,r,t)$ are defined on a Fourier grid in Z and r. With (4.20) the potential coupling matrix of (4.13) needs to be redefined:

$$\mathbf{V}_{jm_jnm,j'm_j'n'm'}^{\Gamma\Gamma_r\Gamma_{r'}}(Z,r) = \left\langle g_{jm_jnm}^{\Gamma\Gamma_r}(X,Y,\theta,\phi) \middle| V(\vec{R},r,\theta,\phi) \middle| g_{j'm_j'n'm'}^{\Gamma\Gamma_{r'}}(X,Y,\theta,\phi) \right\rangle \qquad (4.21)$$

in which the diffractional irrep Γ_d or Γ_d' is implied by Γ and Γ_r or Γ_r' respectively (Table 4.4) and a unique matrix is defined for each (Z,r) point. Equation (4.21) expresses that the potential couples combinations of $\Gamma_r \otimes \Gamma_d$ and $\Gamma_r' \otimes \Gamma_d'$ corresponding to the same total Γ irrep which is contained in the initial (v,j,m_j) state ($V(\vec{R},r,\theta,\phi)$ transforms as the total A_1 irrep)[111].

Given (4.21) for a sparse potential coupling matrix and considering the Γ irrep, the potential operation now scales as $N_z N_r \cdot N_{jm_jnm}^{\Gamma} N_{coup}^{\Gamma}$ in which $N_{jm_jnm}^{\Gamma}$ equals the number of total SA basis functions for total irrep Γ. Here, N_{coup}^{Γ} equals the number of SA basis functions a basis function is coupled to on average by the potential. Considering the A_1 total irrep ($m_j=0$ initially), the total number of SA basis functions needed, $N_{jm_jnm}^{A1}$, is between $1/8^{th}$ and $1/6^{th}$ of the amount of basis functions needed in the RDWP method ($N_{jm_j}N_{nm}$ from (4.12) and (4.14))[88].

Besides the better scaling of the potential operation in the SAWP method (compared to the RDWP method) the number of 2D FFTs needed to perform the kinetic energy

operators for the (Z,r) co-ordinates are reduced to $N^{\Gamma}_{jm_jnm}$ for total irrep Γ. The total scaling of the Hamiltonian operator is then given by:

$$N_z N_r N^{\Gamma}_{jm_jnm} \cdot \left(N^{\Gamma}_{coup} + 2\eta \log(N_z N_r) + 2\right) \qquad (4.22)$$

in which the application of $\hat{H}_{rot}$ and the kinetic energy operations are included[88].

In the SAWP method, the individual irreps of the initial wave packet are propagated and use of equations analogous to (4.8a) and (4.8b) with:

$$C^{\Gamma\Gamma_r}_{v'j'm_j'nm}(t';Z_\infty) = \left\langle \chi_{v'j'}(r) \cdot g^{\Gamma\Gamma_r}_{j'm_j'nm}(X,Y,\theta,\phi) \middle| \psi^{\Gamma}_{vjm_j}(t = t'; \vec{R}, r, \theta, \phi) \middle|_{Z=Z_\infty} \right\rangle \qquad (4.23)$$

results into the SA S-matrix[88]. To obtain the S-matrix, a similarity transform needs to be applied:

$$S = T^{-1} \cdot S^{SA} \cdot T \qquad (4.24)$$

in which T is the matrix transforming the SA basis to the NSA basis set. Furthermore, S^{SA} is the S-matrix describing the scattering of initial SA state i=(v,j,m_j,n=0,m=0;Γ,Γ_r) to the final SA state f=(v',j',m_j',n,m;Γ,Γ_r'). After performing the similarity transform, (4.3) and (4.4) can again be used to obtain state to state scattering probabilities or initial state resolved reaction probabilities.

4.2.2.4. SAPS method

The SAWP method, described above, has been extensively used and has proven to work rather well for systems that allow the potential coupling matrix (4.21) to be sparse (for small N_{coup}^{Γ})[56-62,66,67,76,88,89,112]. In the PS method, no such sparseness was needed to get good scaling. Clearly, a scheme based on a pseudo-spectral method but still using the symmetry of the surface unit cell for scattering at normal incidence, as was used in SAWP, could allow for even better scaling and be applicable to general potential expressions. In this section, such a new method is presented.

In the new method, called the SAPS (symmetry adapted pseudo-spectral) method for reasons that will be made clear below, the wave packet for irrep Γ, corresponding to initial state (v,j,m_j,n=m=0), is expanded exactly as was done in the SAWP method (4.20).

The same SA diffractional and SA rotational basis sets of Table 4.2 and Table 4.3, using (4.19) together with Table 4.4, were used. For the sake of brevity, the expansion coefficients of (4.20), $C_{j'm_j'nm}^{\Gamma\Gamma_r,vjm_j}(Z,r,t)$, will be referred to as the SA FBR (symmetry adapted finite base representation) from now onwards, which is taken to be the primary representation. Clearly, the full SA FBR is composed of several SA FBRs, each being indexed with (Γ,Γ_r), with Γ_d implied according to Table 4.4.

The application of the potential is now considered to be a three step procedure; 1) the SA FBRs are transformed to suitable SA DVRs, 2) the potential operator is applied on the SA DVRs and 3) the results are transformed back to the SA FBRs. For this scheme two ingredients are of importance, the forward / backward transforms and the potential operator in the decomposed SA DVR representation.

The transformation of the diffractional part of the SA FBRs can be efficiently implemented using the Fast Cosine (FCT) and Fast Sine (FST) transform algorithms, both derived from the Fast Fourier transform algorithms (FFT)[113,114]. Moreover, the SA

FBRs corresponding to $\Gamma_d=A_1$ and B_1 can be transformed simultaneously by adding them together, applying FCTs along n and m and finally disentangling them, by adding (A_1) or subtracting (B_1) the transformed result reflected in the σ_{xy} mirror plane and dividing by 2. A similar trick can be used for the SA FBRs corresponding to $\Gamma_d=B_2$ and A_2 but by using FSTs instead of FCTs. The reason for this is that the $\Gamma_d=\{A_1,B_2\}$ are both symmetrical with respect to the exchange of X and Y (σ_{xy}), and the $\Gamma_d=\{B_1,A_2\}$ are both anti-symmetrical (see Table 4.2).

In the SA FBR for diffraction with $\Gamma_d=\{A_1,B_1,A_2,B_2\}$, the $C_{j'm_j'nm}^{\Gamma\Gamma_r,vjm_j}(Z,r,t)$ need to be stored only for $n\geq m\geq0$ and effectively one only covers about $1/8^{th}$ of the surface unit cell in their SA DVRs. For the SA FBRs corresponding to $\Gamma_d=\{E_{1,1},E_{2,1}\}$ (or $\Gamma_d=\{E_{1,2},E_{2,2}\}$), both a FST and a FCT is needed and $C_{j'm_j'nm}^{\Gamma\Gamma_r,vjm_j}(Z,r,t)$ needs to be stored for $n\geq0$ and $m\geq0$, effectively covering 1/4 of the surface unit cell in X and Y (see Table 4.2). Moreover, only one of the $\Gamma_d=\{E_{1,1},E_{2,1}\}$ partners (or one of the $\Gamma_d=\{E_{1,2},E_{2,2}\}$), whatever Γ_r it is combined with, needs to be transformed and thus propagated; the other partner can be found by reflection through σ_{xy} as can be seen in Table 4.1[111]. The back transforms of the SA DVRs with respect to X and Y are implemented in exactly the same fashion: the FSTs and FCTs algorithms are, up to a constant, also the inverse FST and FCT algorithms[113,114].

To transform the angular momentum parts of the SA FBRs to the SA DVRs, again use is made of FSTs and FCTs to effect the transforms along ϕ. Furthermore, the Legendre matrix transform of (4.16) is used to transform the SA FBRs from the (j',m_j') to the mixed representations (θ,m_j') whatever Γ_r the $C_{j'm_j'nm}^{\Gamma\Gamma_r,vjm_j}(Z,r,t)$ corresponds to. The transforms of the mixed representations to the full SA DVRs are done separately for each Γ_r by using the frequency shifting and frequency scaling theorems of Fourier analysis[76,113,115]. For example, the $\Gamma_r=A_1$ SA FBR is transformed to its SA DVR by using a FCT with the frequency scaled by a factor of 4 ($|m_j|\in\{0,4,8...\}$, see Table 4.3). The $\Gamma_r=B_2$ SA FBR is transformed using a FST, with a frequency shift of 2 and frequency scaling by 4

($|m_j|\in \{2,6,10\dots\}$, see Table 4.3). The $\Gamma_r=E_{1,1}$ SA FBR is frequency scaled by a factor 2 using a FCT ($|m_j'|\in \{1,3,5\dots\}$, see Table 4.3) and a frequency shift of 1 is applied.

Because of the frequency scaling of the individual Γ_r SA FBRs by a multiple of 2, the corresponding SA DVRs cover at most 1/4 of the space ($0\leq\phi\leq\pi/2$ for the $\Gamma_r=\{E_{1,1},E_{2,1}\}$ and $0\leq\phi\leq\pi/4$ for the others, instead of the usual $0\leq\phi\leq2\pi$)[113]. The back transforms in ϕ are again identical up to a scaling factor[113,114]. Then, to transform the mixed (θ,m_j') representations back to the full angular SA FBRs for each Γ_r, (4.16) is again used in exactly the same way as was done in the PS method.

To act with the potential operator on the individual SA DVR components of total irrep Γ (see Table 4.4), the potential is decomposed using the resolution of identity constructed from the group projection operators (4.18):

$$\hat{I} = \sum_{\Gamma\in G}\sum_i \hat{P}_{ii}^\Gamma .$$

(4.25)

The above resolution of identity clearly states that V can be decomposed into direct product components all transforming as total A_1:

$$\begin{aligned} V &= V_{\Gamma_d=A_1,\Gamma_r=A_1}^{\Gamma=A_1} + V_{\Gamma_d=B_1,\Gamma_r=B_1}^{\Gamma=A_1} + V_{\Gamma_d=A_2,\Gamma_r=A_2}^{\Gamma=A_1} + \\ &\quad V_{\Gamma_d=B_2,\Gamma_r=B_2}^{\Gamma=A_1} + V_{\Gamma_d=E_{1,1},\Gamma_r=E_{1,1}}^{\Gamma=A_1} + V_{\Gamma_d=E_{2,2},\Gamma_r=E_{2,2}}^{\Gamma=A_1} \end{aligned}$$

(4.26)

just by using the group projection operators (4.18) in the DVR. Again, for the E by E part, only $V_{\Gamma_d=E_{1,1},\Gamma_r=E_{1,1}}$ needs to reside in memory: the partner component which also contains a total $\Gamma=A_1$ contribution, $V_{\Gamma_d=E_{2,2},\Gamma_r=E_{2,2}}$, can be derived from the $V_{\Gamma_d=E_{1,1},\Gamma_r=E_{1,1}}$ by using symmetry (the σ_{xy} operator).

With the different potential components, Table 4.4 can be used again to determine to which (Γ,Γ_r) SA DVR component the product of $V_{\Gamma_d=\Gamma_r}$ and the $\psi_{vjm_j}^{\Gamma,\Gamma_r}$ SA DVR will contribute. For example, consider the initial $m_j=0$ case; $\Gamma=A_1$ and the product of $V_{\Gamma_d=B_1,\Gamma_r=B_1}$ and the $\psi_{vjm_j}^{\Gamma=A_1,\Gamma_r=A_2}$ SA DVR will result in a contribution to the $\psi_{vjm_j}^{\Gamma=A_1,\Gamma_r=B_2}$ SA DVR component.

All the products corresponding to any of the one dimensional irreps for $\Gamma_d=\Gamma_r$ of $V_{\Gamma_d=\Gamma_r}$ can be dealt with straightforwardly for any $\psi_{vjm_j}^{\Gamma,\Gamma_r}$ SA DVR. The products concerning $V_{\Gamma_d=E_{1,1},\Gamma_r=E_{1,1}}$ or $V_{\Gamma_d=E_{2,2},\Gamma_r=E_{2,2}}$ need a different approach. According to Table 4.4, the product of $V_{\Gamma_d=E_{1,1},\Gamma_r=E_{1,1}}$ and the $\psi_{vjm_j}^{\Gamma=A_1,\Gamma_r=E_{1,1}}$ SA DVR (taking the initial $m_j=0$ example again) will lead to contributions to the $\psi_{vjm_j}^{\Gamma=A_1,\Gamma_r=A_1}$ and the $\psi_{vjm_j}^{\Gamma=A_1,\Gamma_r=B_1}$ SA DVRs for $\Gamma=A_1$. Similarly, for $\Gamma=B_1$ (initially $m_j=2$ for example), the same product is also needed and will lead to contributions to the $\psi_{vjm_j}^{\Gamma=B_1,\Gamma_r=A_1}$ and the $\psi_{vjm_j}^{\Gamma=B_1,\Gamma_r=B_1}$ SA DVRs.

In general, the products of $V_{\Gamma_d=E_{1,1},\Gamma_r=E_{1,1}}$ and $V_{\Gamma_d=E_{2,2},\Gamma_r=E_{2,2}}$ with the $\psi_{vjm_j}^{\Gamma,\Gamma_r}$ SA DVR, in which Γ_d or Γ_r corresponds to $E_{1,1}$ or $E_{2,1}$, can lead to two components which need to be disentangled. We use that these two components can be disentangled by their behaviour under σ_{xy}, by taking the symmetrical or anti-symmetrical sums and dividing by two.

Although the potential operation in the SAPS method is somewhat more complex, large savings can be made, especially for PESs suitable for the SAWP method. Clearly, the amount of central memory needed to store the various potential components on the grids can be reduced by using the symmetry properties of the individual components, in exactly the same way as was done for the different SA DVRs.

These savings can be made for any potential, but PESs which are suitable for the SAWP method (PESs which do not couple to many states for a given rotational diffractional state

so that N_{coup}^{Γ} is rather small) will often be decomposable in only a few of the six possible components of (4.26)[56,58,76,88,89]. This can lead to extra savings by leaving out the products of $\psi_{vjm_j}^{\Gamma,\Gamma_r}$ and $V_{\Gamma_d=\Gamma_r}$ in the potential operation for those $V_{\Gamma_d=\Gamma_r}$ not present in the PES. Moreover, given an initial value of m_j, Table 4.4 can be used to determine to which Γ_r of $\psi_{vjm_j}^{\Gamma,\Gamma_r}$ the non-zero $V_{\Gamma_d=\Gamma_r}$ components present give rise to. The other Γ_r are not needed in the propagation and can be left out of the calculation.

For example, if the PES only contains the $V_{\Gamma_d=A_1,\Gamma_r=A_1}$ and $V_{\Gamma_d=B_1,\Gamma_r=B_1}$ components, the action of the potential on the initial wave packet of the type $\psi_{vjm_j}^{\Gamma=A_1,\Gamma_r=A_1}$ ($m_j=0$ initially) can only give rise to the $\psi_{vjm_j}^{\Gamma=A_1,\Gamma_r=A_1}$ and the $\psi_{vjm_j}^{\Gamma=A_1,\Gamma_r=B_1}$ SA DVRs. These two components, applying the potential again, again only give rise to the $\psi_{vjm_j}^{\Gamma=A_1,\Gamma_r=A_1}$ and the $\psi_{vjm_j}^{\Gamma=A_1,\Gamma_r=B_1}$ SA DVRs for this specific PES. The other $\psi_{vjm_j}^{\Gamma,\Gamma_r}$ SA DVRs do not need to be included in the calculation, leading to an additional saving by a factor of four[56,58,76,88,89].

In the SAPS method the potential operation is considered to be a three stage process and the transforms described are based on FSTs, FCTs and the Legendre matrix transform. The FSTs and FCTs both approximately scale as $N(\eta'\log(N/2)+3)/2$, in which N is the vector length and η' is the pre-factor[113,114]. The diffractional transform of the SA FBRs of the $\Gamma_d=A_1$ and $\Gamma_d=B_1$ in one step, like described, thus scales approximately as:

$$N_z N_r N_{jm_j}^{\Gamma,<\Gamma_r>} \cdot (nm_{max}+1)^2 \left(\eta'\log\left[\frac{nm_{max}+1}{2}\right]+3 \right) \qquad (4.27)$$

in which nm_{max} is the maximum value of $|n|$ and of $|m|$ included in (4.20). Moreover, $N_{jm_j}^{\Gamma,<\Gamma_r>}$ is the average number of rotational states of all the Γ_r SA FBRs that correspond to $(\Gamma,\Gamma_d\in\{A_1,B_1\})$, which is on average $1/8^{th}$ ($\Gamma_r\in\{A_1,A_2,B_1,B_2\}$) or $1/4^{th}$ ($\Gamma_r\in\{E_{1,1},E_{2,1}\}$) of N_{jm_j} in (4.17). The same applies to the SA FBRs of $\Gamma_d=A_2$ and $\Gamma_d=B_2$, again

transformed together, and to the individual transforms of $\Gamma_d \in \{E_{1,1},E_{2,1}\}$. In case of a $\Gamma \neq E$ calculation, only one $\Gamma_d = E_{1,1}$ SA FBR is needed to retrieve all partners contributing to the total $\Gamma \in \{A_1,B_1,A_2,B_2\}$ irreps in stead of the four $\Gamma_d = E_{1,1}$ SA FBRs that are needed for the $\Gamma = E$ case (see Table 4.4).

Within the SA angular transform, the Legendre matrix transform approximately scales as:

$$N_z N_r N_{xy}^{\Gamma\Gamma_d} \cdot \left(N_{jm_j}^{\Gamma<\Gamma_r>}\right)^{\frac{3}{2}} \tag{4.28}$$

in which $N_{xy}^{\Gamma\Gamma_d}$ is the number of (X,Y) grid points of Γ_d. For $\Gamma_d \in \{A_1,A_2,B_1,B_2\}$ $N_{xy}^{\Gamma\Gamma_d}$ is on average 1/8 of N_xN_y ($N_{xy}^{\Gamma\Gamma_d} = \frac{1}{2}(nm_{max}+1)^2$) as is used in (4.17). For $\Gamma_d \in \{E_{1,1},E_{2,1}\}$, $N_{xy}^{\Gamma\Gamma_d}$ is on average 1/4 of N_xN_y ($N_{xy}^{\Gamma\Gamma_d} = (nm_{max}+1)^2$). The azimuthal SA transforms along ϕ, based on FSTs or FCTs, shifted or non-shifted, scaled or non-scaled, all approximately scale as:

$$N_r N_z N_{xy}^{\Gamma\Gamma_d} N_\theta \cdot \frac{N_\phi^{\Gamma\Gamma_r}}{2}\left(\eta'\log\left[\frac{N_\phi^{\Gamma\Gamma_r}}{2}\right]+3\right) \tag{4.29}$$

in which $N_\phi^{\Gamma\Gamma_r}$ is the number of points on the grid in ϕ, which is on average 1/8 of the N_ϕ in the PS method for $\Gamma_r \in \{A_1,A_2,B_1,B_2\}$. For $\Gamma_r \in \{E_{1,1},E_{2,1}\}$, $N_\phi^{\Gamma\Gamma_r}$ is approximately 1/4 of the N_ϕ in the PS method. N_θ is the number of points in θ which equals ($j_{max}+1$) (or ($j_{max}+1$)/2 for homonuclear molecules) for all Γ_r (see (4.20)) as in the PS method.

The point wise multiplication of the potential operation itself in the SA DVRs scales as:

$$N_r N_z N_\theta \left[\sum_{\Gamma_r^\psi, \Gamma_r^V} N_{xy}^{\Gamma \Gamma_r^\psi} N_\phi^{\Gamma \Gamma_r^\psi} \cdot \left(1 + \delta_{\Gamma_r^V, E} \cdot \delta_{\Gamma_r^\psi, E} + \delta_{\Gamma_r^V, E} \cdot \delta_{\Gamma_d^\psi, E} \right) \right] \tag{4.30}$$

in which Γ_r^V specifies which $V_{\Gamma_d = \Gamma_r}$ component of (4.26) is multiplied with the $\psi_{vjm_j}^{\Gamma, \Gamma_r}$ SA DVR component being indexed with Γ_r^ψ or Γ_d^ψ for the case of a Γ calculation according to Table 4.4. In (4.30) the assumption is made that the disentanglements of the products of $V_{\Gamma_d = E_{1,1}, \Gamma_r = E_{1,1}}$ or $V_{\Gamma_d = E_{2,2}, \Gamma_r = E_{2,2}}$ with the $\psi_{vjm_j}^{\Gamma, \Gamma_r}$ SA DVRs, in which Γ_d^ψ or Γ_r^ψ corresponds to $E_{1,1}$ or $E_{2,1}$, all scale linearly.

4.2.3. Propagators used in the different methods

4.2.3.1. PS method

A wide variety of propagators[100,106-108] can be used to propagate the wave packet in time, of which the split operator (SPO) formalism[100] is the most commonly used due to its simplicity. In the PS method use of this propagator is made by symmetrically splitting the kinetic, the angular momentum and the potential operators:

$$\begin{aligned} \exp(-i\hat{H}\Delta t) = {} & \exp(-i\hat{K}\Delta t/2) \cdot \exp(-i\hat{H}_{rot}\Delta t/2) \cdot \exp(-i\hat{V}\Delta t) \cdot \\ & \exp(-i\hat{H}_{rot}\Delta t/2) \cdot \exp(-i\hat{K}\Delta t/2) \end{aligned} \tag{4.31}$$

Due to the symmetrical splitting of the non-commuting operators, the error in the SPO method is of order Δt^3. Moreover, the SPO method is flexible in that it allows a straightforward application of negative imaginary potentials (NIPs) to absorb the wave packet at the edges of the grids in order to use smaller grids and avoid reflections.

In our calculations with the PS method a quadratic NIP, $-iV_{quad}$, with V_{quad} of the form

$$V_{quad} = \begin{cases} A\left(\dfrac{x - x_{min}}{x_{max} - x_{min}} \right)^2 & \text{for} \quad x_{min} < x < x_{max} \\ 0 & \text{for} \quad x \leq x_{min} \text{ or } x \geq x_{max} \end{cases} \tag{4.32}$$

is used[63,64] to absorb the wave packet from x_{min} to x_{max} ($x = r$ or Z). In (4.32) the strength of V_{quad} is given by A and suitable values can be obtained from reference 116. In our implementation, the $V_{NIP} = -iV_{quad}$ is simply added to the potential in the application of the SPO propagator in the PS method.

4.2.3.2. SAWP and SAPS methods

Although the use of symmetry does not necessarily lead to the use of a specific propagator, certain advantages can be obtained by using a modified Chebyshev propagator incorporating absorbing boundary conditions (ABC)[108].

The SA basis functions in (4.20) are real functions (see Table 4.2 and Table 4.3) and if the initial wave packet in Z is chosen to be real, the initial wave functions in the corresponding SA DVRs are also real. The initial wave packet can be made real by adding the complex conjugate to the initial Gaussian wave packet of (4.6c)[117]. The result is that the initial wave packet corresponds to one Gaussian wave packet moving initially towards the surface and another one moving away from the surface. The latter will just be absorbed by the optical potential and can be safely ignored in the scattering amplitude formalism[109,110] used to obtain the NSA or SA S matrices.

The ABC Chebyshev expansion[108] of the propagated wave function $\psi(\vec{R}; t = 0)$ is:

$$\exp(-i\hat{H}t) \cdot \psi(\vec{R}; t = 0) = \sum_n a_n(t) \cdot \hat{Q}_n(\vec{R}) \tag{4.33}$$

with the recursion relation for the dampened Chebyshev polynomials $\hat{\mathbf{Q}}_n(\vec{R})$:

$$
\begin{aligned}
\hat{\mathbf{Q}}_0(\vec{R}) &= \psi(\vec{R}; t = 0) \\
\hat{\mathbf{Q}}_1(\vec{R}) &= \exp(-\hat{\gamma}) \cdot \hat{H}_{norm} \hat{\mathbf{Q}}_0(\vec{R}) \\
\hat{\mathbf{Q}}_{n+1}(\vec{R}) &= 2\exp(-\hat{\gamma})\hat{H}_{norm}\hat{\mathbf{Q}}_n(\vec{R}) - \exp(-2\hat{\gamma})\hat{\mathbf{Q}}_{n-1}(\vec{R}).
\end{aligned}
\tag{4.34}
$$

The computationally expensive part of the calculation (the recursion of the damped Chebyshev polynomials) can be performed with real algebra. In (4.33), $a_n(t) = (2 - \delta_{n0}) \cdot \exp(-i\overline{H}t) \cdot (-i)^n \cdot J_n(\Delta Ht)$, J_n are the Bessel functions of the first kind, and $\overline{H}$, ΔH and $\hat{H}_{norm}$ are defined as:

$$
\begin{aligned}
\overline{H} &= \tfrac{1}{2}(H_{max} + H_{min}) \\
\Delta H &= \tfrac{1}{2}(H_{max} - H_{min}) \\
\hat{H}_{norm} &= (\hat{H} - \overline{H}) / \Delta H.
\end{aligned}
\tag{4.35}
$$

In (4.35), H_{max} and H_{min} are determined by the highest and lowest eigen values of the Hamiltonian respectively. The ABC are incorporated in (4.34) through the $\hat{\gamma}$ operator and the number of terms needed in (4.33) depends approximately linearly on the spectral range parameter ΔH[108]. For the damping operator $\hat{\gamma}$ a real function of quadratic form similar to that of (4.32) is used and the fact that the adapted Chebyshev polynomials stay real is therefore ensured.

Both the SAWP and the SAPS methods use the ABC Chebyshev propagator but it is believed that the SAPS method can make the most efficient use of this propagator. Having defined the different potential components on the SA DVR grids (see (4.26)), a better cut-off can be implemented on the potential in the SAPS method than in the SAWP method, in which the potential operation is performed employing a potential coupling matrix. The reduced spectral range ensures that the number of terms in (4.33) can be significantly reduced[108], making the ABC-propagator more efficient because less Hamiltonian operations are needed[88].

4.2.4. The potentials used

4.2.4.1. PES 4

To compare the SAPS method with the SAWP method, a PES[61] suitable for SAWP has been used. This H_2+Cu(100) PES is known as PES 4. To make the PES suitable for SAWP, the PES was fitted to SA basis functions[52,61]:

$$
\begin{aligned}
V = \sum_{jm_jp=00,20,40,44e} \sum_{nm=00,10,11} V_{jm_jpnm}(r,Z)\mathbf{Y}_{jm_jp}(\theta,\phi)H_{nm}(X,Y) + \\
\sum_{jm_jp=22e,42e} V_{jm_jpB_l10}(r,Z)\mathbf{Y}_{jm_jp}(\theta,\phi)H_{B_l10}(X,Y)
\end{aligned}
\tag{4.36}
$$

with

$$
\begin{aligned}
H_{00}(X,Y) &= \sqrt{1/A} \\
H_{10}(X,Y) &= \sqrt{1/A}\cdot\left(\cos GX + \cos GY\right) \\
H_{11}(X,Y) &= 2\sqrt{1/A}\cdot\left(\cos GX\cos GY\right) \\
H_{B_l10}(X,Y) &= \sqrt{1/A}\cdot\left(\cos GX - \cos GY\right)
\end{aligned}
\tag{4.37}
$$

where A is the area of the surface unit cell, $G=2\pi/L$ and

$$
\mathbf{Y}_{jm_je}(\theta,\phi) = \sqrt{\tfrac{1}{2}}\left(\mathbf{Y}_{jm_j}(\theta,\phi) + \mathbf{Y}_{j-m_j}(\theta,\phi)\right).
\tag{4.38}
$$

The $V_{jm_jpnm}(r,Z)$ in (4.36) were obtained through a two step procedure explained in reference 61. With this specific form of the PES, the potential coupling matrix (4.21) can be calculated analytically and contains only the $V_{\Gamma_d=A_1,\Gamma_r=A_1}$ and the $V_{\Gamma_d=B_1,\Gamma_r=B_1}$ components. Moreover, N_{coup}^Γ is small (of the order of 100). The latter property makes this PES very suitable for the SAWP method[88].

4.2.4.2. PES 5

In the comparison of the SAPS with the PS method, a recently developed H_2+Cu(100) PES[50] was used. The PES will be referred to as PES 5 throughout the rest of the article. PES 5 is based on the interpolation of DFT data using the accurate corrugation reduction scheme[50] and contains all the possible components of (4.26). Because PES 5 cannot be expressed in a small number of SA basis functions, it is believed that the SAWP method would be inefficient for PES 5. Therefore we compare the SAPS results for PES 5 with the PS results for this PES.

4.2.5. Numerical details

Two sets of calculations have been performed to test the new SAPS method against both the SAWP and the PS methods. In the comparison between the SAPS and the SAWP methods, the initial H_2 state ($v=0, j=4, m_j=0$) was chosen for a normal incidence range of 0.3 to 0.9 eV. The diffraction basis in the SAWP calculation was taken to include all states with $|n|+|m| \leq 11$, whereas for the SAPS method $|n| \leq 11$ and $|m| \leq 11$ was used. In both cases the maximum rotational level included in the basis set was set to $j_{max}=28$. The spectral range parameter in the SAWP method was determined to be $\Delta H = 13.85$ eV whereas in the SAPS method ΔH was 8.85 eV. The difference is due to a different cut-off on the potential: with the SAWP method the maximum eigen value of the potential coupling matrix was estimated to be 16 eV compared to the imposed cut-off of 6 eV in the SAPS calculation. The reaction is slightly exothermic and both PESs, with the H_2 gas phase minima defined to be zero, were assumed not to drop below -0.7 eV in the calculation of ΔH for all test calculations. In the SAPS method, the combined kinetic energy operations of the X, Y and r degrees of freedom and the combined rotational energy and kinetic energy operator for the Z degree of freedom were each set to a maximum of 5.5 eV. For the SAWP method, the combined rotational energy and kinetic energy operators for the X and Y degrees of freedom and the combined kinetic energy operators for the Z and r degrees of freedom have likewise each been set to a maximum

of 5.5 eV. In Table 4.5 the values of the most important input parameters to the two test calculations on PES 4 are shown. In both cases the number of Chebyshev terms in (4.33) has been chosen in such a manner that the Bessel expansion coefficient with the largest n was smaller than 1.0×10^{-17}.

The calculations on PES 5 were performed to compare the performance of the SAPS method with the PS method. In the comparison the initial state $(v=0, j=0, m_j=0)$ of H_2 was chosen, for the 0.3 to 1.15 eV range of normal incidence energies, in both calculations. For the PS calculation the diffractional basis set was $-11 \leq n \leq 12$ with $-11 \leq m \leq 12$, whereas in the SAPS calculation it was taken to be $|n| \leq 13$ and $|m| \leq 13$. In both cases the maximum rotational level included was $j_{max} = 28$. The cut-off on the potential was taken to be 5.5 eV in the SAPS method, giving a spectral range parameter of $\Delta H = 8.54$ eV. For the SPO propagator in the PS calculation, the time step was taken to be 5.0 atomic units of time. The values of the other most important input parameters are given in Table 4.5.

To obtain the $\chi_{vj}(r)$, a numerical method based on FFTs[118] was used to construct the Hamiltonian matrix of H_2 in the gas phase, which was subsequently diagonalised. Care was taken that the diagonaliser routines did not introduce an arbitrary phase choice in the calculated gas phase eigen vectors to avoid ambiguities in the signs of the S-matrix elements for rotationally and/or vibrationally inelastic scattering.

All four test calculations have been performed on a 1024 CPU SGI Origin 3800 machine, which is based on cc-NUMA architecture. Both the SAPS and the PS codes have been parallelized using the OpenMP standard. The SAWP code has been parallelized using the MPI standard. In all calculations the number of CPUs used was set to 16 except for the PS calculation. For the latter 32 CPUs had to be used due to the larger amount of memory required. Moreover, all three codes have been implemented to use the scsl library for FFTs, present on the SGI machine.

Parameter	Description	PES 4 $v=0,j=4,m_j=0$ H$_2$ initially		PES 5 $v=0,j=0,m_j=0$ H$_2$ initially	
		SAWP	SAPS	PS	SAPS
N_r	# of grid points in r.	40	40	40	40
Δr	Spacing of r grid (a_0).	0.150	0.150	0.150	0.150
R_{start}	Start value of grid in r (a_0).	0.522	0.522	0.522	0.522
N_z	# of grid points in Z.	90	90	96	96
ΔZ	Spacing of Z grid (a_0).	0.140	0.140	0.150	0.150
Z_{start}	Start value of grid in Z (a_0).	-1.00	-1.00	0.00	0.00
N_{z_sp}	# of specular grid points.	144	144	128	128
J_{max}	Maximum j value in basis set.	28	28	28	28
$N_x = N_y$	# of X and Y grid points.	-	-	24	-
O_{diff}	Maximum diffraction order.	11	-	-	-
nm_{max}	Maximum diffraction state.	-	11	-	13
N_{basis}	Total scattering basis set (million).	17	31	962	111
N_{dvr}	Total # of points in DVR (million).	-	82	1828	287
t_{tot}	Total propagation time (a.u.).	30000	30000	30000	30000
Δt	Time step of propagator (a.u.).	-	-	5.0	-
Δt_{an}	Time step for analyses (a.u.).	40.0	40.0	20.0	20.0
α	Surface lattice constant (a_0).	4.822	4.822	4.824	4.824
V_{max}	Cut-off potential (eV).	16.0	6.00	-	5.50
K_{max}	Cut-off kinetic operators (eV).	5.50	5.50	-	5.50
N_{cheby}	# of Chebyshev terms.	15531	9990	-	9654
ΔH	Spectral range parameter (eV).	13.85	8.85	-	8.54
A_r	Strength optical V of r grid.	0.200	0.200	0.0400	0.200
V_{r_min}	Start optical V of r grid (a_0).	4.000	4.000	3.822	3.822
V_{r_max}	End optical V of r grid (a_0).	6.372	6.372	6.372	6.372
A_Z	Strength optical V of Z grid.	0.050	0.050	0.0040	0.050
V_{Z_min}	Start optical V of Z grid (a_0).	6.84	6.84	9.00	9.00
V_{Z_max}	End optical V of Z grid (a_0).	11.46	11.46	14.25	14.25
A_{Z_sp}	Strength optical V specular grid.	0.050	0.050	0.0040	0.050
$V_{Z\_min\_sp}$	Start optical V specular grid (a_0).	13.84	13.84	13.05	13.05
$V_{Z\_max\_sp}$	End optical V specular grid (a_0).	19.02	19.02	18.45	18.45
Z_0	Centre initial wave packet (a_0).	10.20	10.20	11.00	11.00
E_{range}	Normal incidence energy range initial wave packet (eV).	0.3 - 0.9	0.3 - 0.9	0.3 - 1.15	0.3 - 1.15
$Z\infty$	Location analysis line (a_0).	6.84	6.84	8.55	8.55

**Table 4.5:** The most relevant input parameters used in the four calculations.

4.3. Results and discussion

4.3.1. SAPS versus SAWP

In order to test the SAPS method, the $H_2+Cu(100)$ system was chosen, to also enable a comparison with the SAWP method. To this end, calculations have been performed for H_2 initially in the $(v=0, j=4, m_j=0)$ state scattering at normal incidence (0.3 to 0.9 eV) using the well studied PES 4[61,62,66]. PES 4 only contains the $V_{\Gamma_d=A_1, \Gamma_r=A_1}$ and the $V_{\Gamma_d=B_1, \Gamma_r=B_1}$ components and for initially $m_j=0$ (A_1 calculation) only the $\psi_{vjm_j}^{\Gamma=A_1, \Gamma_r=A_1}$ and the $\psi_{vjm_j}^{\Gamma=A_1, \Gamma_r=B_1}$ SA FBRs need to be propagated. The basis set size numbers in Table 4.5 take these considerations into account.

Because the SAWP and the SAPS method are closely related (they both make use of symmetry and, in their present implementation, the ABC Chebyshev propagator was used), the input parameters, shown in Table 4.5, only differ in the cut-off imposed on the potential in the SAPS calculation and in the size of the diffractional basis set used. The SAWP method uses a "diamond shaped" grid in momentum space so that $|n|+|m|\leq O$ so that $(O+1)(O+2)/2$ diffraction states are present in the SAWP basis set (78 in this calculation)[89]. In the SAPS method the diffraction basis set is composed from $|n|\leq|m|\leq nm_{max}$ and consists of $(nm_{max}+1)^2$ basis functions (144 in this calculation). The latter suggests that the SAWP method, especially for PES 4, should be more efficient.

In Figure 4.2A and Figure 4.2B the reaction probabilities and the rovibrationally elastic scattering probabilities are shown for the test calculations performed on PES 4. In Table 4.6 the rovibrational elastic diffractional S-matrix elements are shown at a normal incidence energy of 0.303 eV and for $|n|+|m|\leq 4$. The results presented are also typical for tests performed on other initial states of H_2 (A_2, B_1, B_2 and E calculations) and clearly show that the SAPS method yields accurate results.
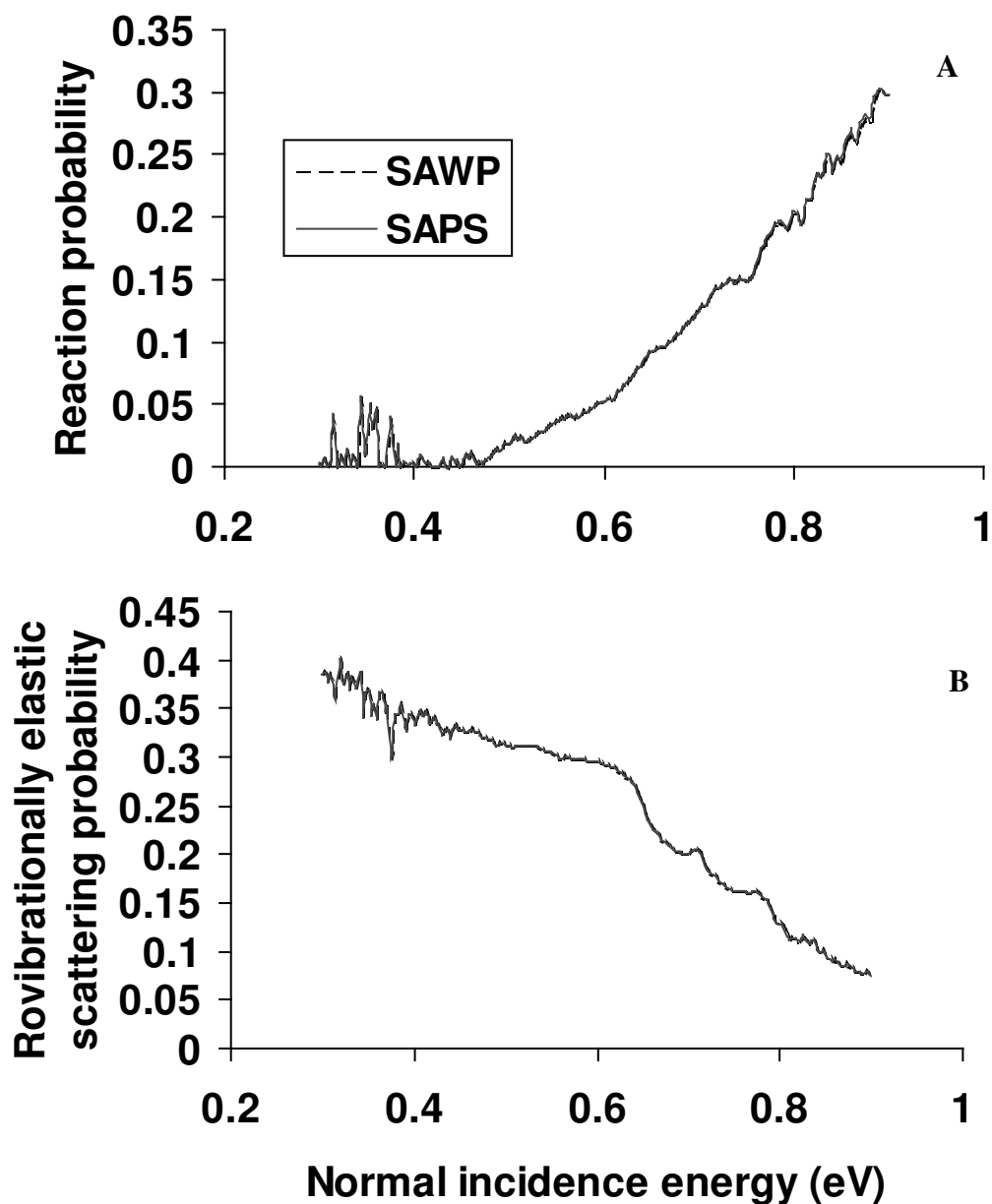
Figure 4.2: A) The reaction probability is shown as a function of the normal incidence energy for scattering of (v=0,j=4,m$_j$=0) H$_2$ from Cu(100) using PES 4. The dashed curve corresponds to the SAWP calculation, whereas the solid curve corresponds to the SAPS calculation. **B)** The rovibrationally elastic scattering probabilities from the same calculations.

H$_2$ (v=0,j=4,m$_j$=0) final diffraction state on PES 4	**SAWP Real**	**SAPS Real**	**SAWP Imaginary**	**SAPS Imaginary**
n=0, m=0	0.246081	0.246143	-0.308887	-0.308910
n=1, m=0	0.028706	0.028750	-0.005380	-0.005367
n=2, m=0	-0.054916	-0.054917	0.040142	0.040172
n=1, m=1	0.096572	0.096601	-0.028329	-0.028301
n=3, m=0	-0.020564	-0.020574	0.043201	0.043192
n=2, m=1	-0.104818	-0.104829	0.074166	0.074193
n=4, m=0	0.011729	0.011729	0.009229	0.009232
n=3, m=1	0.000015	0.000011	-0.015998	-0.016008
n=2, m=2	0.035664	0.035646	-0.058417	-0.058418

Table 4.6: The real and imaginary parts of the S-matrix elements are shown for rovibrationally elastic diffraction of (v=0,j=4,m$_j$=0) H$_2$ scattering from Cu(100) at an incidence energy of 0.303 eV, for normal incidence. Listed are results obtained with the SAWP and the SAPS methods.

SAWP Description	SAWP	SAPS		SAPS Description
Evaluating the Hamiltonian.	254 cpuh	254 cpuh		Evaluating the Hamiltonian.
Evaluating the kinetic energies.	86 cpuh	101 cpuh		Evaluating the kinetic energies.
Evaluating the potential.	168 cpuh	153 cpuh	69 cpuh	SA rotational transforms.
			32 cpuh	SA diffractional transforms.
			52 cpuh	SA potential multiplication.
Overhead.	25 cpuh	12 cpuh		Overhead.
Total time.	279 cpuh	266 cpuh		Total time.

Table 4.7: The timings of the SAWP and the SAPS calculations. See the text for the explanation of the different contributions.

In Table 4.7 the amount of cpu hours (cpuh) used in acting with the Hamiltonian, the potential and the kinetic energy operators (the Laplacian in all 6 degrees of freedom) on the wave function are listed. Also shown are the total cpu time, the different contributions to the potential operation in the SAPS method and the overhead. The latter is mostly due to the Chebyshev recursion and the application of the damping operator $\hat{\gamma}$ in (4.34). From the point of view of cpu time, for this potential (with 14 expansion terms and N_{coup}^{Γ}=102) the overall performance of the SAPS method is comparable to that of the SAWP method. As discussed below, for PES 4 the larger cost associated with the use of a

larger diffraction basis set in the SAPS method is offset by the lower cost associated with the reduced number of Chebyshev iterations needed in the SAPS method.

The SAPS diffractional basis set is 1.85 (144/78) times bigger. Employing a similar "diamond shaped" momentum grid in the SAPS method could reduce the number of FFTs needed to evaluate the kinetic energy operators in (r,Z) but also leads to a non-homomorphic SA DVR - SA FBR transform pair[94]. From a mathematical point of view (but not from the point of view of efficiency), the use of a "diamond shaped" momentum grid is as relevant as for the SAWP approach. One has simply to make sure that enough DVR points are used in the transforms along X and Y, in order to converge the underlying Gaussian quadratures of the matrix elements of the potential coupling matrix in the diffraction basis. This is equivalent to padding the FBR with zeros outside the "diamond shaped" basis. For the present calculation this would lead to an estimated reduction in the total CPU time of about 20%.

Whereas the larger diffraction basis set increases the cost of the SAPS calculation, its computational cost is reduced by the number of Chebyshev terms used in the propagator by a factor of 1.55. The latter is due to the possibility to impose a lower cut-off on the potential (of 6.0 eV) in the SAPS method, giving rise to a lower spectral range parameter (of $\Delta H = 8.85$ eV) (see also section II). Although the test calculations show that the SAPS method is less efficient than the SAWP method at performing a single Hamiltonian operation, this is counterbalanced by the possibility of reducing the spectral range of the potential operation so that less Chebyshev polynomials are required in (4.33).

Both tests have been performed with parallelised codes. The SAWP code has been parallelised using the MPI standard whereas at the moment only the OpenMP level of parallelisation is realised in the SAPS method. The effects of using different paralellisation schemes is not yet fully understood and might change the competition between the SAWP and the SAPS methods, but only slightly.

Looking at the different contributions of the time spent evaluating the potential operation in the SAPS method, one finds that the SA rotational transforms consume the most cpu time (see Table 4.7). One reason for this is that the SA diffractional transforms are performed very efficiently for this PES, i.e., the SA diffractional transforms of the two needed SA FBRs (the $\psi_{vjm_j}^{\Gamma=A_1,\Gamma_r=A_1}$ and the $\psi_{vjm_j}^{\Gamma=A_1,\Gamma_r=B_1}$) are performed in one step. The SA rotational transforms are not combined and thus two separate transforms are needed. More importantly the SA rotational transforms scale worse compared to the SA diffractional transforms due to the use of the Legendre matrix transform.

At first glance, it might seem odd that the potential multiplication in the SA DVR representation consumes more cpu time than the SA diffractional transforms. The larger expense of the potential multiplication can be partly understood by noting that the SA rotational transforms, which precede the potential multiplication, lead to an increase of the basis set by a factor of 2.6 mostly due to the non-direct product nature of the rotational SA FBRs and the direct product character of the SA DVRs. The difference in size is not the expected factor of 2 because of the use of the FCT transform algorithms in the SA transforms along ϕ (see the total SA DVR and SA FBR sizes in Table 4.5). The FFT, FCT and FST algorithms all need specific vector lengths for the algorithm to become fast.

Apart from the difference in size of the SA DVRs compared to the SA FBRs, the two components of $V_{\Gamma_d=\Gamma_r}$ needed in this SAPS calculation also contribute to the potential multiplication time. They lead to four products of $V_{\Gamma_d=\Gamma_r}$ and $\psi_{vjm_j}^{\Gamma,\Gamma_r}$ (each $\psi_{vjm_j}^{\Gamma,\Gamma_r}$ component needs to be multiplied with the two components of PES 4) and for each such product two multiplications per grid point using indirect memory references are needed to incorporate the symmetries of $V_{\Gamma_d=\Gamma_r}$ and $\psi_{vjm_j}^{\Gamma,\Gamma_r}$. The need to multiply $\psi_{vjm_j}^{\Gamma,\Gamma_r}$ with more than one $V_{\Gamma_d=\Gamma_r}$ may well shift the balance of relative scaling in favour of the SA transforms for general PESs, because for a general PES 28 or 46 products of $\psi_{vjm_j}^{\Gamma,\Gamma_r}$ and $V_{\Gamma_d=\Gamma_r}$ are needed for the

$\Gamma \in \{A_1, A_2, B_1, B_2\}$ and the $\Gamma = E$ calculations respectively, as can be deduced by using Table 4.4.

4.3.2. SAPS versus PS

To test the SAPS method on a general PES, two test calculations on PES 5 have been performed (PES 5 contains products of all irreducible representations). Both calculations address the scattering of $(v=0, j=0, m_j=0)$ H_2 from the Cu(100) surface for a normal incidence energy range of 0.3 to 1.15 eV. No results have been published yet on the dynamics of H_2+Cu(100) on PES 5, the two test calculations therefore also represent new results on the system as such.

Because the PS method does not make use of symmetry, one would expect the SAPS method to enjoy a clear advantage, in terms of both cpu time and memory requirements. As Table 4.5 shows for the initial state considered (which has $m_j=0$), the PS method requires an FBR which is a factor 8.7 times bigger than the size of the combined SA FBRs needed in the SAPS method. The difference for the DVR is less dramatic, a factor of 6.4 in favour of the SAPS method. This is due to the use of FCT transforms in the SAPS method for the X, Y and ϕ degrees of freedom as explained before.

In Figure 4.2A and Figure 4.2B, the reaction probabilities and rovibrationally elastic scattering probabilities computed with the PS and the SAPS methods are compared. These results show that the SAPS method yields correct results (as was also demonstrated in the PES 4 tests). For other initial states of H_2 (A_1, A_2, B_1, B_2 and E calculations, not shown here), our calculations similarly showed good results.

In Table 4.8, S-matrix elements are compared for rovibrationally elastic diffraction with $|n|+|m| \leq 4$ for a normal incidence energy of 0.303 eV. The correspondence between the S-matrix elements is not as good as it was in the SAWP versus SAPS test. This can be understood from two reasons. The first is that in the PS method a third order

approximation propagator, the SPO, is being used, which is much less accurate than the ABC Chebyshev propagator.
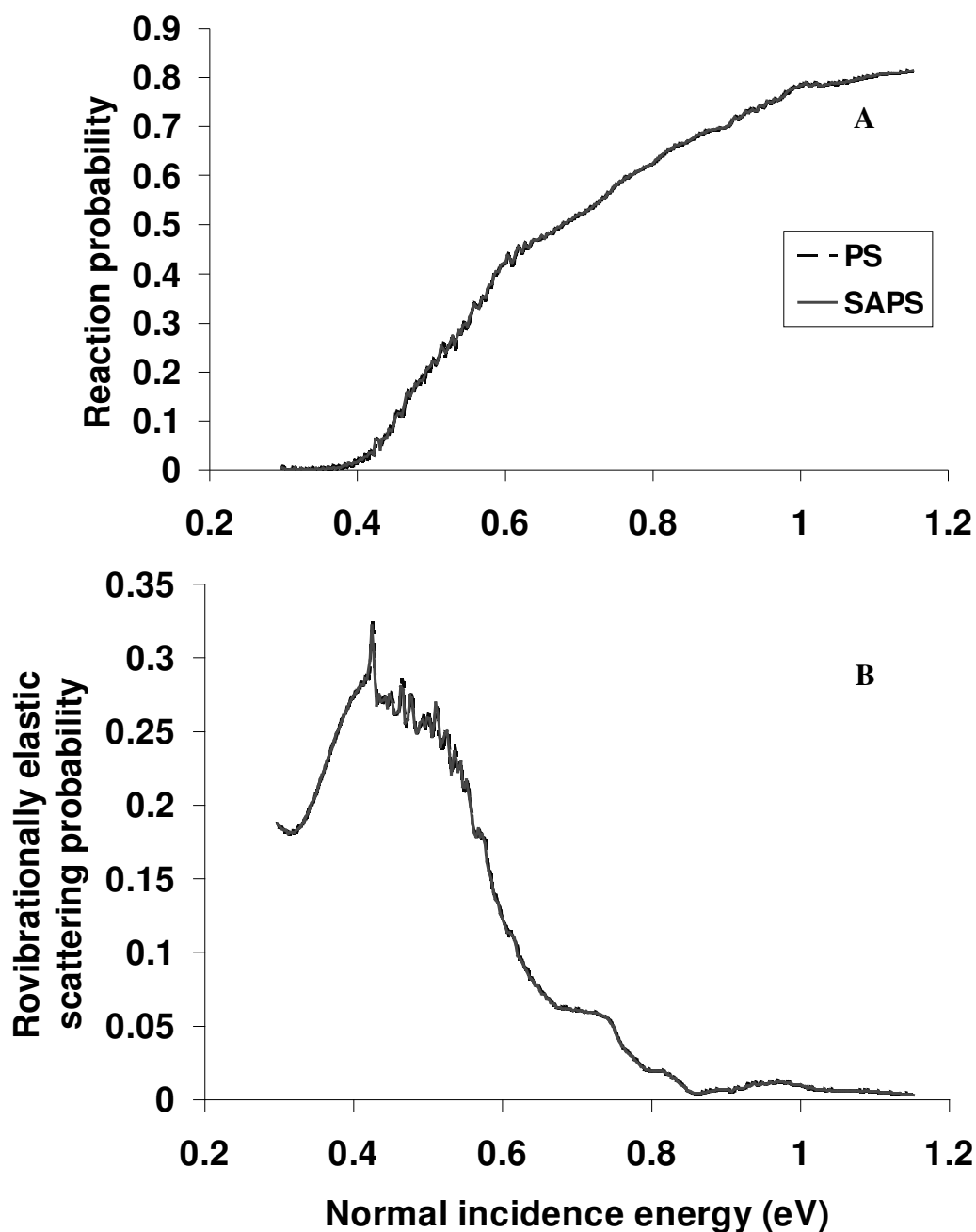
Figure 4.3: A) The reaction probability is shown as a function of the normal incidence energy for scattering of (v=0,j=0,m$_j$=0) H$_2$ from Cu(100) using PES 5. The dashed curve corresponds to the PS calculation, whereas the solid curve corresponds to the SAPS calculation. **B)** The rovibrationally elastic scattering probabilities from the same calculations.

H_2 v=0,j=0,m_j=0 final diffraction state on PES 5	PS Real	SAPS Real	PS Imaginary	SAPS Imaginary
n=0, m=0	0.076142	-0.088696	-0.079486	0.064500
n=1, m=0	-0.009612	-0.007033	-0.081439	-0.081705
n=2, m=0	0.032023	0.032490	-0.016270	-0.015413
n=1, m=1	0.021990	0.022562	-0.006416	-0.005793
n=3, m=0	-0.021077	-0.021666	0.020488	0.020322
n=2, m=1	0.037717	0.037445	0.022390	0.023316
n=4, m=0	0.012123	0.012073	0.002884	0.003030
n=3, m=1	-0.043915	-0.043080	-0.031499	-0.032543
n=2, m=2	-0.012340	-0.012314	0.012504	0.012093

Table 4.8: The real and imaginary parts of the S-matrix elements are shown for rovibrationally elastic diffraction of (v=0,j=0,m_j=0) H_2 scattering from Cu(100) at an incidence energy of 0.303 eV, for normal incidence. Listed are results obtained with the PS and the SAPS methods.

PS	SAPS	Description
6000	9654	Number of Hamiltonian operations.
11092 cpuh	1881 cpuh	Evaluating the Hamiltonian.
5338 cpuh	640 cpuh	Evaluating the kinetic energies.
1682 cpuh	262 cpuh	Rotational transforms.
2009 cpuh	277 cpuh	Diffractional transforms.
984 cpuh	694 cpuh	Potential multiplication.
119 cpuh	86 cpuh	Overhead.
11211 cpuh	1967 cpuh	Total time.

Table 4.9: The timings of the PS and the SAPS calculations. Also listed is the total number of Hamiltonian operations performed in each calculation.

The second reason is that the specular channel, (v=0,j=0,m_j=0,n=m=0) is also treated differently in both methods. In the PS method the analysis of the specular channel takes place at Z_∞=12.90 a_0, in contrast to the other channels which are analysed at the listed Z_∞=8.55 a_0. In the SAPS method the analysis line of the specular channel is located at the same place as for the other channels, at Z_∞=8.55 a_0. The analytical correction term in (4.8a) is used to cancel the effect of the initial wave packet passing the analysis line when moving towards the surface. In the PS method no such correction term is used and the result is that phase differences, which are due to the inaccuracy of the SPO propagator, are to be especially expected for the specular channel.

In Table 4.9 the timings (the total number of cpu hours used) of the two test calculations are shown (note that for the PS calculation 32 instead of 16 CPUs were needed to obey the memory requirements of the computer used). The number of effective Hamiltonian operations differs by a factor of 1.6 in favour of the PS method. The PS calculation using the SPO propagator took 6000 time steps of Δt=5.0 a.u.t to reach the total propagation time of t_{tot}=30000 a.u.t. With the SAPS method and the cut-offs used, 9654 ABC Chebyshev recursion steps, each contributing a single Hamiltonian operation, needed to be done to reach the same t_{tot}=30000 a.u.t within machine's precision.

Table 4.9 also shows that in total the SAPS method took a factor of 5.7 less time than the PS method. Taking into account the number of effective Hamiltonian operations, the SAPS method took approximately 0.2 cpuh whereas the PS method took approximately 1.8 cpuh of time per Hamiltonian operation. The use of symmetry therefore led to a speedup of approximately a factor of 9 in performing the Hamiltonian operation. Note that this is approximately equal to the factor gained by the FBR sizes in the SAPS method (8.7 in favour of the SAPS method). Note that the initial (v=0,j=0,m_j=0) H_2 state is a very favourable initial state for the SAPS method. The wave packet propagation needs to be performed for only one irrep (Γ=A_1). For initial states with m_j≠0, a factor of two increase in cpu time is expected.

Looking at the different contributions to the SAPS timings in Table 4.9, it is noted that the time spent on performing the potential multiplications in the SA DVRs is bigger by a factor of 1.3 compared to the time spent on all the SA transforms. This can be explained by the number (28) of $V_{\Gamma_d=\Gamma_r}$ and $\psi^{\Gamma,\Gamma_r}_{vjm_j}$ products needed in the SAPS method for this PES and by the fact that the combined SA DVR is about 2.6 times bigger than the combined SA FBR. Nonetheless, the SAPS potential operation in the SA DVRs is approximately 2.3 times faster per Hamiltonian operation than the point wise multiplication needed in the PS method on a grid that is 6.4 times bigger. The use of symmetry in the SA DVRs therefore also led to an overall reduction of memory and cpu costs for the potential operation, despite the overhead introduced by the number of products of $V_{\Gamma_d=\Gamma_r}$ and $\psi^{\Gamma,\Gamma_r}_{vjm_j}$,

the extra multiplications and indirect memory references in each such product in the SAPS potential operator.

The SA rotational transforms took less time than the SA diffractional transforms, despite the less favourable scaling law of the Legendre matrix transform. This can be partly understood by the fact that the SA diffractional basis set was about a factor of 1.2 bigger than the average SA rotational basis set in (4.19) (in the example of section 4.3.1. the rotational basis set was larger). On average, a direct product of 80 SA diffractional and 66 SA rotational basis functions is taken in each of the five SA FBR components of the present SAPS test calculation.

4.4. Summary

In this study a new method, called the symmetry adapted pseudo-spectral (SAPS) method, has been presented and tested. The SAPS method is a wave packet method for performing six dimensional quantum dynamical calculations on reactive scattering of diatomic molecules from square surfaces at normal incidence. A method which is especially efficient for reaction at normal incidence is relevant to surface reactions because many molecule-surface reactions obey normal energy scaling[105].

In the SAPS method, the quasi-linear scaling of the potential operation, as is obtained in direct product pseudo-spectral (PS) methods[11-16,54,55,63-65,77-79,94-99], is combined with the advantages of using the symmetry of the square surface. The use of the symmetry of the square surface, for normal incidence calculations, has already been shown to be effective in a method known as the SAWP method[56,88,89]. In the latter method, the wave packet was treated in a hybrid approach, i.e. a close coupling representation was used for four of the six degrees of freedom (symmetry adapted basis functions were used for the rotational and diffractional degrees of freedom) and a grid representation was used for the other two degrees of freedom. In the SAPS method, a finite basis representation is used as the

primary representation for all the degrees of freedom and the potential operation is performed in a three step procedure: first the individual symmetry adapted finite basis representations (SA FBRs) are transformed to the corresponding individual symmetry adapted discrete variable representations (SA DVRs), then the point wise multiplications associated with the potential operation are performed in the SA DVRs and finally $V\psi$ as expressed in the SA DVRs is transformed back to the corresponding SA FBRs. To transform the SA FBRs to their SA DVRs and back, the Gauss Legendre transform[13], as used in the PS method[54,55,63-65], has been symmetry adapted employing Fast Cosine transforms (FCTs) and Fast Sine transforms (FSTs) for the ϕ degree of freedom. FCTs and FSTs are also used for the transforms along the X and Y degrees of freedom.

To ensure a sparse potential coupling matrix (a requirement for the SAWP method to be efficient), a restriction on the PES is that it needs to be fitted to a limited number of symmetry adapted basis functions[89]. For the H_2+Cu(100) system such a PES, known as PES 4, was previously constructed (using 14 symmetry adapted basis functions) and already used in several studies[52,61]. For the PS and the SAPS methods no such fit to a limited number of symmetry adapted basis functions is needed to obtain good scaling and a general PES can be used with both methods. PES 5, also for the H_2+Cu(100) system, was also constructed in a previous study and is based on an accurate interpolation of DFT data, i.e. on the corrugation reduction scheme[50]. Although PES 5 is a more accurate fit, its use would lead to a bad performance of the SAWP method because this PES cannot be expressed in a limited number of symmetry adapted basis functions.

To compare the performance of the SAPS method with that of the SAWP method, calculations for reactive scattering of (v=0,j=4,m_j=0) H_2 have been done, using PES 4, for the normal incidence energy range 0.3 to 0.9 eV. The results of the two calculations show that the SAPS method yields accurate results and that, for the initial state considered, its efficiency is comparable to that of the SAWP method, in terms of cpu costs. For the PES considered, which gave rise to a potential coupling matrix in which only 2% of the matrix elements were non-zero, the higher cost associated with the need of using a larger diffraction basis set in the SAPS method was offset by the possibility to

impose a tighter cut-off on the potential, so that less Chebyshev terms were required in the propagation. The spectral range of the potential operator can be reduced more efficiently in the SAPS method than in the SAWP method because the potential is stored on grid points in the SAPS method and not in the form of a potential coupling matrix, as is done in the SAWP method.

To test the performance of the SAPS method on a general PES, SAPS and PS calculations have been done on the reactive scattering of $(v=0,j=0,m_j=0)$ H_2, using PES 5, for the normal incidence energy range 0.3 to 1.15 eV. The results showed that the SAPS method not only gives correct results but that its efficiency is also superior to that of the PS method, both in memory requirements and in computational costs. It was shown that the memory required for the SAPS wave function in the FBR is a factor of 8.7 smaller than that needed for the PS wave function for the initial state of H_2 considered, and the computational cost of the SAPS calculation was a factor of 5.7 less than that of the PS calculation.

The cost of a Hamiltonian operation in the SAPS method was actually 9 times smaller than the cost in the PS method, but with the propagator used in the PS method (the SPO propagator) less Hamiltonian operations were required than in the SAPS method, which used the ABC-Chebyshev propagator. The use of this propagator allows one to take advantage of the fact that the initial wave function can be taken real in the SAPS method and this propagator yields highly accurate results. The SPO propagator allows reliable but less accurate results to be obtained using less Hamiltonian operations, but requires complex rather than real algebra in the expensive part of the calculation.

The initial H_2 states considered (with $m_j=0$) were especially suitable for using the symmetry of the square surface for normal incidence: only one one-dimensional irrep (A_1) is contained in the initial wave packet. It is expected that, for a general PES, considering initial H_2 states with $m_j=0$, the SAPS method will be a factor of 6 faster and will use about 8 times less memory than the PS method. For initial H_2 states with $m_j{\neq}0$, considering a general PES, the SAPS method is expected to be about 3 times faster, at the

same time using a factor of about 4 (Γ=E, m_j=odd) or about 8 ($\Gamma \in \{A_1, B_1, A_2, B_2\}$, m_j=even but non-zero) less memory than the PS method. Less memory is required for the m_j=even calculations because the two calculations that are required can be done consecutively. Calculations performed by us (but not described further here) for mj≠0 and for H_2+Cu(100) confirm these expectations, which are based on symmetry considerations.

4.5. References

1   R. B. Gerber, A. T. Yinnon, and R. Kosloff, Chem. Phys. Lett. 105, 523 (1984).
2   R. B. Gerber, R. Kosloff, and M. Berman, Comput. Phys. Rep. 5, 59 (1986).
3   M.-N. Carre and D. Lemoine, J. Chem. Phys. 101, 5305 (1994).
4   A. T. Yinnon and R. Kosloff, Chem. Phys. Lett. 102, 216 (1983).
5   A. T. Yinnon, R. Kosloff, and R. B. Gerber, Surf. Sci. 148, 148 (1984).
6   B. Jackson, J. Chem. Phys. 97, 6792 (1992).
7   R. C. Mowrey and D. J. Kouri, Chem. Phys. Lett. 119, 285 (1985).
8   R. C. Mowrey and D. J. Kouri, J. Chem. Phys. 84, 6466 (1986).
9   R. C. Mowrey and D. J. Kouri, J. Chem. Phys. 86, 6140 (1987).
10   R. C. Mowrey, Y. Sun, and D. J. Kouri, J. Chem. Phys. 91, 6519 (1989).
11   D. Lemoine and G. C. Corey, J. Chem. Phys. 92, 6175 (1990).
12   D. Lemoine and G. C. Corey, J. Chem. Phys. 94, 767 (1991).
13   G. C. Corey and D. Lemoine, J. Chem. Phys. 97, 4115 (1992).
14   D. H. Zhang and J. Z. H. Zhang, J. Chem. Phys. 101, 1146 (1994).
15   J. Z. H. Zhang, J. Chem. Phys. 92, 324 (1990).
16   J. Z. H. Zhang, Comput. Phys. Commun. 63, 28 (1991).
17   J. Q. Dai, J. Sheng, and J. Z. H. Zhang, J. Chem. Phys. 101, 1555 (1994).
18   J. Q. Dai and J. Z. H. Zhang, Surf. Sci. 319, 193 (1994).
19   J. Q. Dai and J. Z. H. Zhang, J. Chem. Phys. 102, 6280 (1995).
20   G. R. Darling and S. Holloway, Faraday Discuss. 96, 43 (1993).
21   G. R. Darling and S. Holloway, J. Chem. Phys. 101, 3268 (1994).
22   G. R. Darling and S. Holloway, Surf. Sci. 304, L461 (1994).
23   G. R. Darling, M. Kay, and S. Holloway, Phys. Rev. Lett. 78, 1731 (1997).
24   G. R. Darling, M. Kay, and S. Holloway, Surf. Sci. 400, 314 (1998).
25   G. A. Gates and S. Holloway, Surf. Sci. 307, 132 (1994).
26   M. R. Hand and S. Holloway, J. Chem. Phys. 91, 7209 (1989).
27   G. R. Darling and S. Holloway, Surf. Sci. 268, L305 (1992).
28   G. R. Darling and S. Holloway, J. Chem. Phys. 97, 734 (1992).
29   G. R. Darling and S. Holloway, J. Electron Spectrosc. Relat. Phenom. 64-65, 517 (1993).
30   G. R. Darling and S. Holloway, Surf. Sci. 307, 153 (1994).

31   J. Sheng and J. Z. H. Zhang, J. Chem. Phys. 97, 6784 (1992).
32   J. Sheng and J. Z. H. Zhang, J. Chem. Phys. 99, 1373 (1993).
33   S. Thiel, M. Pykavy, T. Kluner, R. Kosloff, and V. Staemmler, Phys. Rev. Lett. 87, 077601 (2001).
34   S. Borowski, S. Thiel, T. Kluner, H.-J. Freund, R. Tisma, and H. Lederer, Comput. Phys. Commun. 143, 162 (2002).
35   S. Thiel, T. Kluner, D. Lemoine, and H.-J. Freund, Chem. Phys. 282, 361 (2002).
36   B. Jackson and H. Metiu, J. Chem. Phys. 86, 1026 (1987).
37   D. Halstead and S. Holloway, J. Chem. Phys. 93, 2859 (1990).
38   U. Nielsen, D. Halstead, S. Holloway, and J. K. Nørskov, J. Chem. Phys. 93, 2879 (1990).
39   A. C. Luntz and J. Harris, Surf. Sci. 258, 397 (1991).
40   C. Engdahl, B. I. Lundqvist, U. Nielsen, and J. K. Nørskov, Phys. Rev. B 45, 11362 (1992).
41   C. Engdahl and U. Nielsen, J. Chem. Phys. 98, 4223 (1993).
42   K. Gundersen, K. W. Jacobsen, J. K. Nørskov, and B. Hammer, Surf. Sci. 304, 131 (1994).
43   B. Jackson, M. Persson, and B. D. Kay, J. Chem. Phys. 100, 7687 (1994).
44   J. Q. Dai and J. C. Light, J. Chem. Phys. 107, 1676 (1997).
45   J. Q. Dai and J. C. Light, J. Chem. Phys. 108, 7816 (1998).
46   M.-N. Carre, B. Jackson, and D. Lemoine, J. Chem. Soc., Faraday Trans. 93, 949 (1997).
47   M.-N. Carre and B. Jackson, J. Chem. Phys. 108, 3722 (1998).
48   B. Hammer, M. Scheffler, K. W. Jacobsen, and J. K. Nørskov, Phys. Rev. Lett. 73, 1400 (1994).
49   P. Kratzer, B. Hammer, and J. K. Nørskov, Surf. Sci. 359, 45 (1996).
50   R. A. Olsen, H. F. Busnengo, A. Salin, M. F. Somers, G. J. Kroes, and E. J. Baerends, J. Chem. Phys. 116, 3841 (2002).
51   J. A. White, D. M. Bird, M. C. Payne, and I. Stich, Phys. Rev. Lett. 73, 1404 (1994).
52   G. Wiesenekker, G. J. Kroes, and E. J. Baerends, J. Chem. Phys. 104, 7344 (1996).
53   S. Wilke and M. Scheffler, Phys. Rev. B 53, 4926 (1996).
54   H. F. Busnengo, E. Pijper, M. F. Somers, G. J. Kroes, A. Salin, R. A. Olsen, D. Lemoine, and W. Dong, Chem. Phys. Lett. 356, 515 (2002).
55   S. M. Kingma, M. F. Somers, E. Pijper, G. J. Kroes, R. A. Olsen, and E. J. Baerends, J. Chem. Phys. 118, 4190 (2003).
56   G. J. Kroes, E. J. Baerends, and R. C. Mowrey, J. Chem. Phys. 107, 3309 (1997).
57   G. J. Kroes, E. J. Baerends, and R. C. Mowrey, Phys. Rev. Lett. 78, 3583 (1997).
58   D. A. McCormack, G. J. Kroes, E. J. Baerends, and R. C. Mowrey, Faraday Discuss. 110, 267 (1998).
59   D. A. McCormack, G. J. Kroes, R. A. Olsen, E. J. Baerends, and R. C. Mowrey, J. Chem. Phys. 110, 7008 (1999).
60   D. A. McCormack, G. J. Kroes, R. A. Olsen, E. J. Baerends, and R. C. Mowrey, Phys. Rev. Lett. 82, 1410 (1999).
61   D. A. McCormack, G. J. Kroes, R. A. Olsen, J. A. Groeneveld, J. N. P. v. Stralen, E. J. Baerends, and R. C. Mowrey, Faraday Discuss. 117, 109 (2000).

62   D. A. McCormack, G. J. Kroes, R. A. Olsen, J. A. Groeneveld, J. N. P. v. Stralen, E. J. Baerends, and R. C. Mowrey, Chem. Phys. Lett. 328, 317 (2000).

63   E. Pijper, G. J. Kroes, R. A. Olsen, and E. J. Baerends, J. Chem. Phys. 117, 5885 (2002).

64   E. Pijper, M. F. Somers, G. J. Kroes, R. A. Olsen, E. J. Baerends, H. F. Busnengo, A. Salin, and D. Lemoine, Chem. Phys. Lett. 347, 277 (2001).

65   M. F. Somers, S. M. Kingma, E. Pijper, G. J. Kroes, and D. Lemoine, Chem. Phys. Lett. 360, 390 (2002).

66   M. F. Somers, D. A. McCormack, G. J. Kroes, R. A. Olsen, E. J. Baerends, and R. C. Mowrey, J. Chem. Phys. 117, 6673 (2002).

67   E. Watts, G. O. Sitz, D. A. McCormack, G. J. Kroes, R. A. Olsen, J. A. Groeneveld, J. N. P. v. Stralen, E. J. Baerends, and R. C. Mowrey, J. Chem. Phys. 114, 495 (2001).

68   R. Bisseling and R. Kosloff, J. Comput. Phys. 59, 136 (1985).

69   S. Das and D. J. Tannor, J. Chem. Phys. 92, 3403 (1990).

70   R. A. Friesner, J. A. Bentley, M. Menou, and C. Leforestier, J. Chem. Phys. 99, 324 (1993).

71   S. K. Gray, J. Chem. Phys. 96, 6543 (1992).

72   R. Heather and H. Metiu, J. Chem. Phys. 86, 5009 (1987).

73   D. K. Hoffman, M. Arnold, and D. J. Kouri, J. Phys. Chem. 97, 1110 (1993).

74   B. Jackson, J. Chem. Phys. 99, 8299 (1993).

75   A. P. J. Jansen, J. Chem. Phys. 99, 4055 (1993).

76   G. J. Kroes and R. C. Mowrey, J. Chem. Phys. 101, 805 (1994).

77   D. Lemoine, Chem. Phys. Lett. 224, 483 (1994).

78   D. Lemoine, J. Chem. Phys. 101, 3936 (1994).

79   D. Lemoine, J. Chem. Phys. 101, 4343 (1994).

80   U. Manthe, H.-D. Meyer, and L. S. Cederbaum, J. Chem. Phys. 97, 3199 (1992).

81   R. C. Mowrey, J. Chem. Phys. 94, 7098 (1991).

82   D. Neuhauser, J. Chem. Phys. 93, 7836 (1990).

83   D. Neuhauser, Chem. Phys. Lett. 200, 173 (1992).

84   D. Neuhauser and M. Baer, J. Chem. Phys. 92, 3419 (1990).

85   D. Neuhauser and M. Baer, J. Chem. Phys. 91, 4651 (1989).

86   D. Neuhauser, M. Baer, and D. J. Kouri, J. Chem. Phys. 93, 2499 (1990).

87   O. Sharafeddin and J. Z. H. Zhang, Chem. Phys. Lett. 204, 190 (1993).

88   G. J. Kroes, J. G. Snijders, and R. C. Mowrey, J. Chem. Phys. 102, 5512-5524 (1994).

89   G. J. Kroes, J. G. Snijders, and R. C. Mowrey, J. Chem. Phys. 103, 5121 (1995).

90   G. J. Kroes, G. Wiesenekker, E. J. Baerends, and R. C. Mowrey, Phys. Rev. B 53, 10397 (1996).

91   G. J. Kroes, G. Wiesenekker, E. J. Baerends, R. C. Mowrey, and D. Neuhauser, J. Chem. Phys. 105, 5979 (1996).

92   R. C. Mowrey, G. J. Kroes, G. Wiesenekker, and E. J. Baerends, J. Chem. Phys. 106, 4248 (1997).

93   R. C. Mowrey, G. J. Kroes, and E. J. Baerends, J. Chem. Phys. 108, 6906 (1998).

94   A. S. Dickinson and P. R. Certain, J. Chem. Phys. 49, 4209 (1968).

95   D. Kosloff and R. Kosloff, J. Comput. Phys. 52, 35 (1983).

96   R. Kosloff, J. Phys. Chem. 92, 2087 (1988).
97   D. Lemoine, J. Chem. Phys. 101, 10526 (1994).
98   J. C. Light, I. P. Hamilton, and J. V. Lill, J. Chem. Phys. 82, 1400 (1985).
99   J. V. Lill, G. A. Parker, and J. C. Light, Chem. Phys. Lett. 89, 483 (1982).
100   M. D. Feit, J. A. Fleck, and A. Steiger, J. Comput. Phys. 47, 412 (1982).
101   G. C. Corey, J. W. Tromp, and D. Lemoine, in Numerical grid methods and their applications to Schrodinger equation, Vol. 412, edited by C. Cerjan (Kluwer Academic, Dordrecht, 1993), pp. 1-23.
102   I. P. Hamilton and J. C. Light, J. Chem. Phys. 84, 306 (1986).
103   D. Lemoine, Comput. Phys. Commun. 97, 331 (1996).
104   A. Gross, S. Wilke, and M. Scheffler, Phys. Rev. Lett. 75, 2718 (1995).
105   G. R. Darling and S. Holloway, Rep. Prog. Phys. 58, 1595 (1995).
106   T. J. Park and J. C. Light, J. Chem. Phys. 85, 5870 (1986).
107   H. Tal-Ezer and R. Kosloff, J. Chem. Phys. 81, 3967 (1984).
108   V. A. Mandelshtam and H. S. Taylor, J. Chem. Phys. 103, 2903 (1995).
109   G. G. Balint-Kurti, R. N. Dixon, and C. C. Marston, J. Chem. Soc. Faraday T. 86, 1741 (1990).
110   G. G. Balint-Kurti, R. N. Dixon, and C. C. Marston, Int. Rev. Phys. Chem. 11, 317 (1992).
111   L. Jansen and M. Boon, Theory of Finite Groups. Applications in Physics. (North-Holland, Amsterdam, 1967).
112   D. A. McCormack, G. J. Kroes, R. A. Olsen, J. A. Groeneveld, J. N. P. v. Stralen, E. J. Baerends, and R. C. Mowrey, Chem. Phys. Lett. 346, 347 (2001).
113   Numerical Recipes in FORTRAN 77 (Cambridge University Press, 1992).
114   A. Besprozvannaya and D. J. Tannor, Comput. Phys. Commun. 63, 569 (1991).
115   Y. Shi and D. J. Tannor, J. Chem. Phys. 92, 25172 (1990).
116   A. Vibok and G. G. Balint-Kurti, J. Phys. Chem. 96, 8712 (1992).
117   G. J. Kroes and D. Neuhauser, J. Chem. Phys. 105, 8690 (1996).
118   C. C. Marston and G. G. Balint-Kurti, J. Chem. Phys. 91, 3571 (1989).

Chapter 5

Six-dimensional quantum dynamics of scattering of (v=0,j=0)

H$_2$ and D$_2$ from Cu(111): test of two LEPS potential energy

surfaces

Abstract

We present six-dimensional quantum dynamics calculations on scattering of (v=0,j=0) H$_2$ and D$_2$ from Cu(111), at normal incidence. Theoretical results for dissociative chemisorption and vibrationally inelastic scattering, which were obtained using two different LEPS potential energy surfaces, are compared to experiment. The theoretical probabilities for vibrational excitation are too low by about an order of magnitude. The lack of competition with vibrational excitation leads to reaction probabilities which are probably too high at large collision energies. These discrepancies are related to the LEPS PESs used in the calculations and possible improvements are discussed.

5.1. Introduction

The dissociative chemisorption of H_2 on Cu(111) is perhaps the most studied reaction in surface science. A wealth of experimental[1-9] and theoretical[10-17] information is available. In particular, results of molecular beam and associative desorption experiments[5,6] have been fitted to sigmoid-shaped functions of the collision energy:

$$R_i(E_n) = \frac{A_i}{2}\left(1 + \text{erf}\left(\frac{E_n - E_i^0}{W_i}\right)\right)$$

(5.1)

In equation (5.1), R denotes a reaction probability and E_n the collision energy normal to the surface. Furthermore, A is the value at which the reaction probability saturates at large collision energies, E^0 is the collision energy at which the reaction probability becomes A/2 (E^0 is also called the dynamical barrier height) and W is a width parameter. Molecular beam experiments have resulted in parameters that are initial state (i) resolved with respect to the vibrational state v of H_2. Associative desorption experiments have yielded parameters which are resolved with respect to v as well as the rotational angular momentum quantum number j. Parameters are available for both D_2 + Cu(111)[3,5] and H_2 + Cu(111)[6]. The parameters for D_2 are based on collision energies (up to 0.83 eV) that are much higher than could be achieved for H_2 (up to about 0.5 eV).

The vibrationally inelastic scattering of H_2 from Cu(111) has also been studied in molecular beam experiments[4,18-21]. The experiments found that vibrational excitation probabilities P(v=0→v=1,j') could be fitted to the same functional relationship, equation (5.1), as the reaction probability and that vibrational excitation is remarkably efficient (A was found to be 0.28 for j'=3[20]). The vibrational excitation was attributed to an electronically adiabatic mechanism in which the molecule is stretched as it approaches the transition state to dissociative adsorption[19].

The experimental research has been parallelled by a large theoretical effort. In reduced dimensionality quantum dynamics studies, the effects of parallel translational motion[10,15], rotational motion[10,13,14] and vibrational motion[11,12] on reaction were studied. In six-dimensional (6D) quantum dynamics calculations, which modelled motion in all six molecular degrees of freedom, the effects of vibration[16], rotation and reactant rotational alignment[17] on reaction were studied. However, no quantitative comparison was made between the 6D initial-state resolved reaction probabilities and experimental results. Futhermore, no 6D results were reported yet concerning the vibrationally inelastic scattering of H_2 from Cu(111).

The present work represents an attempt to fill these gaps. Reaction probabilities and probabilities for vibrational excitation are calculated for (v=0,j=0) H_2 scattering from Cu(111) at normal incidence and directly compared to experiment. The computational results are derived from two different LEPS potential energy surfaces (PESs)[14,22], which are both based on calculations using density functional theory (DFT). To arrive at a firm conclusion regarding the size of the reaction probability at large collision energies, we have also performed calculations for (v=0,j=0) D_2 + Cu(111). Because these calculations are much more cpu intensive than those for H_2 (by about an order of magnitude), they were only performed for the PES[22] which yielded reaction probabilities in best agreement with the experiments for H_2 + Cu(111) .

The quantum dynamics method is discussed briefly in section (5.2.1). The two LEPS PESs are discussed in section (5.2.2). Results are presented and discussed in section (5.3). section (5.4) gives our conclusions.

5.2. Method

5.2.1. Dynamics method

In the quantum dynamics calculations, we make the Born-Oppenheimer approximation and assume that the reaction takes place on the ground state PES. We also make the approximation of freezing the positions of the surface Cu atoms to their equilibrium positions. The validity of both approximations is discussed in e.g. reference 23.
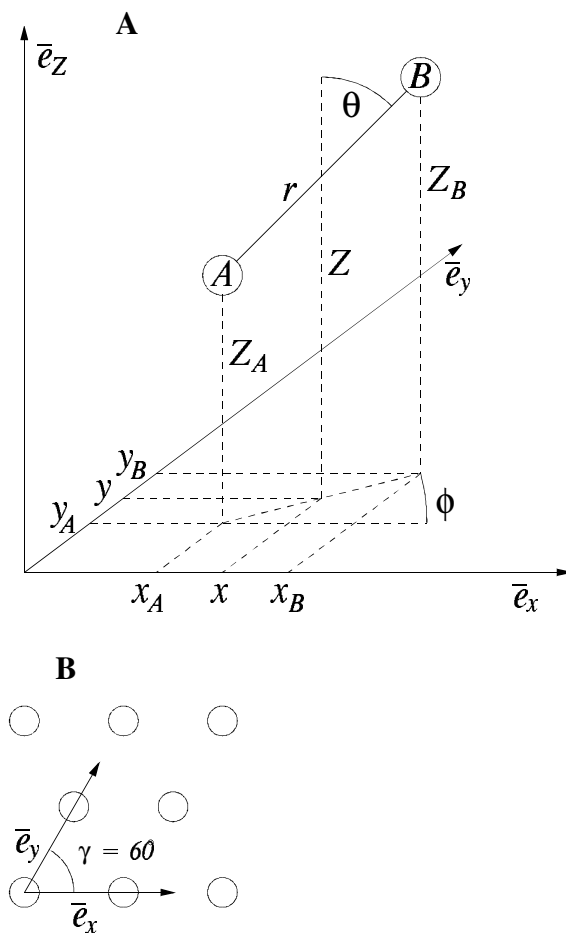
Figure 5.1: The coordinate system used in this study. In **(A)** the H_2 center of mass coordinates (x,y, and Z), the H_2 bond distance r and the two orientational angles θ and ϕ are indicated together with the coordinates of hydrogen atoms A and B. A coordinate system with a skewing angle $\gamma = 60$ degrees between the x- and y-axes has been used **(B)**.

The motion in the remaining six degrees of freedom is treated essentially without approximations. The coordinate system and the surface unit cell are shown in Figure 5.1. For the Cu(111) surface, a system of skewed coordinate axes x and y is used for the molecular motion parallel to the surface. The other four coordinates used are the distance of the molecule to the surface Z, the H-H distance r and the molecular orientation angles θ and ϕ.

The method we use to perform the quantum dynamics calculations is similar to the implementation of the time-dependent wave packet (TDWP) method[24] employed by Dai and Light for $H_2 + Cu(111)$[16]. However, to represent the dependence of the wave function on θ and ϕ, we use a non-direct product finite basis representation (FBR) in the spherical harmonics $Y_{jm_j}(\theta,\phi)$, employing a method developed by Corey and Lemoine[25,26]. For both PESs, the values of the most important parameters of the wave packet calculations are given in Table 5.1. Additional computational details will be given elsewhere[27], along with results for a larger set of initial states.

Parameter	Description	DZ PES, H_2	ER PES, H_2	ER PES, D_2
Z_0	starting value on Z grid (a_0)	0.0	0.0	0.0
ΔZ	grid spacing in Z (a_0)	0.15	0.15	0.106
N_Z	number of grid points in Z	128	90	128
r_0	starting value on r grid (a_0)	0.5	0.5	0.5
Δr	grid spacing in r (a_0)	0.20	0.25	0.177
N_r	number of grid points in r	40	32	48
$N_x(N_y)$	number of grid points in x (y)	12	16	24
a	surface lattice constant (a_0)	4.84	4.757	4.757
j_{max}	max. value of j in rotational FBR	28	28	40
N_{tot}*	size scattering basis set	321 million	321 million	2750 million**
T	total propagation time (atomic units)	25,000	15,000	20,000

* N_{tot} is the number of rotational channels in the FBR $\times N_Z N_r N_x N_y$
** A maximum of 28 was imposed on $|m_j|$ in the FBR.

**Table 5.1**: Input parameters of the wave packet calculation.

5.2.2. LEPS potential energy surfaces

The two PESs that were tested in the present work are based on the LEPS form, as first adapted for molecule-surface reactions by Sato[28] and by McCreery and Wolken[29]. The LEPS potential reduces to a modified Morse potential for H_2 for both H-atoms far away from the surface and to modified Morse potentials for H-atoms interacting with the surface for large H-H distances.

The first PES we studied was taken from the work of Dai and Zhang[14]. Their LEPS-PES (henceforth called the DZ PES) was based on density functional calculations performed using a super cell model of the surface-adsorbate system[30] and employing a generalized gradient approximation (GGA) to compute the exchange-correlation energy[31]. The aim of these DFT calculations was to describe dissociative chemisorption of H_2 on Cu(111). Dai and Zhang made the atom-surface potential parameters dependent on the surface site to describe the corrugation of the PES. The two Sato-parameters were adapted to reproduce the barrier height (0.72 eV in the LEPS-PES vs. 0.73 eV in the DFT calculations) and the barrier location (r=1.1 Å, Z=1.2 Å) for the bridge-to-center dissociation geometry, for which Hammer et al. found the lowest reaction barrier[30]. A known defect of this PES is that the minimum barrier to dissociation is too high: although 0.73 eV is the result obtained for the DFT basis set with which the PES was mapped out, convergence tests indicated that the DFT-GGA barrier should be lower by about 0.2 eV[30].

The second PES was taken from the research of Persson et al.[22], who modelled the Eley-Rideal reaction of H with H on Cu(111). We will henceforth call this PES the ER PES to emphasize that its purpose was the description of the Eley-Rideal reaction. The basic DFT approach (use of super cell and GGA employed) was the same as in the calculations of Hammer et al.[30], but the details of the DFT calculations differed. Persson et al. also introduced a surface site dependence into the parameters describing the atom-surface interaction to model the corrugation of the PES, based on a site-dependent DFT study of the atom-surface interaction. In a new development, they introduced an improvement that leads to a faster decay of the molecule-surface interaction for large molecule-surface

distances. Their potential yields a better value for the height of the bridge-to-center barrier to reaction (0.54 eV), although the barrier is located at a value of the H-H distance (1.0 Å) that is somewhat too small (it should be 1.1 Å[30]).
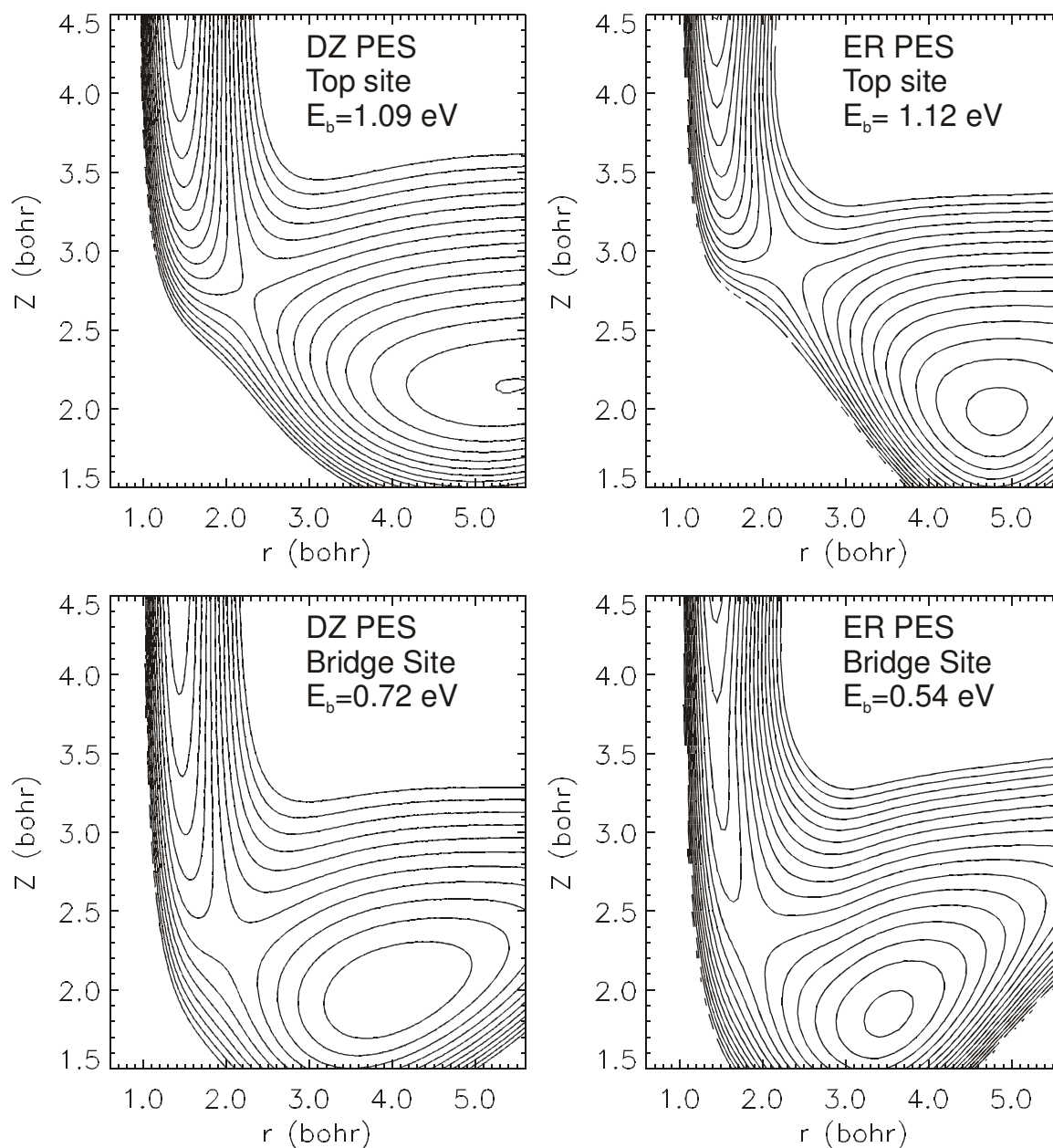
Figure 5.2: Two-dimensional cuts through the LEPS-PESs are shown for the DZ PES[14] and the ER PES[22], for the bridge-to-center and the top-to-bridge dissociation routes. In all cases, H_2 is parallel to the surface. The energy is relative to the minimum of the H_2 gas phase potential and contour lines are drawn for intervals of 0.1 eV.

Two-dimensional cuts through the two LEPS-PESs are shown in Figure 5.2. As stated before, the bridge-to-center reaction barrier (0.72 eV) of the DZ PES should be too high by about 0.2 eV. The DZ PES also somewhat overestimates the corrugation that is associated with the height of the barrier (the minimum barrier height for dissociation above the top site exceeding that for the bridge site by 0.37 eV in the DZ PES, compared to 0.25 eV in the DFT calculations[30] on which the PES was based). The height of the bridge-to-center reaction barrier (0.54 eV) is in quite good agreement with converged DFT calculations[30] in the ER PES[22], but this PES overestimates the corrugation of the barrier to reaction even more (the minimum barrier height for dissociation above the top site exceeding that for the bridge site by 0.57 eV in the ER PES, compared to 0.25 eV in the DFT calculations[30]).

5.3. Results and discussion

5.3.1 H_2 + Cu(111)

Reaction probabilities for H_2 (v=0,j=0) + Cu(111) computed for the DZ PES[14] and the ER PES[22] are compared with fitted experimental reaction probabilities[6] in Figure 5.3. In making the comparison, a choice had to be made whether the comparison to experiment should be with fits to associative desorption experiments, which are initial state-selective for v as well as j, or adsorption measurements, which are initial state-selective with respect to v only. The former results are for a higher surface temperature (T_s = 925 K compared with 120 K for the adsorption measurements). The latter results include an averaging over the initial rotational H_2 states that are populated in the beam, which is rotationally quite hot. Both effects should lead to a somewhat larger width of the reaction probability curve than would be measured for (v=0,j=0) H_2 reacting with a 0 K surface, as simulated in the calculations. We decided to make the comparison to the adsorption experiments because only these yield absolute reaction probabilities. However, the fitted

curve for (v=0) H_2 reaction from adsorption measurements for T_s = 120 K is quite similar to the fit for (v=0,j=0) H_2 reaction from associative desorption measurements for T_s = 925 K and interchanging the fits would not alter our conclusions regarding the comparison to the calculations.

We first consider the results for the DZ PES[14]. For E_n up to about 0.73 eV, the computed reaction probability curve appears to be shifted upwards relative to experiment by about 0.1 eV, and it rises to a much higher value than the fit. As further discussed in reference 27, these observations suggest that the barriers in the PES are too high by at least 0.1 eV and that the computational curve should be shifted to lower energies by at least this
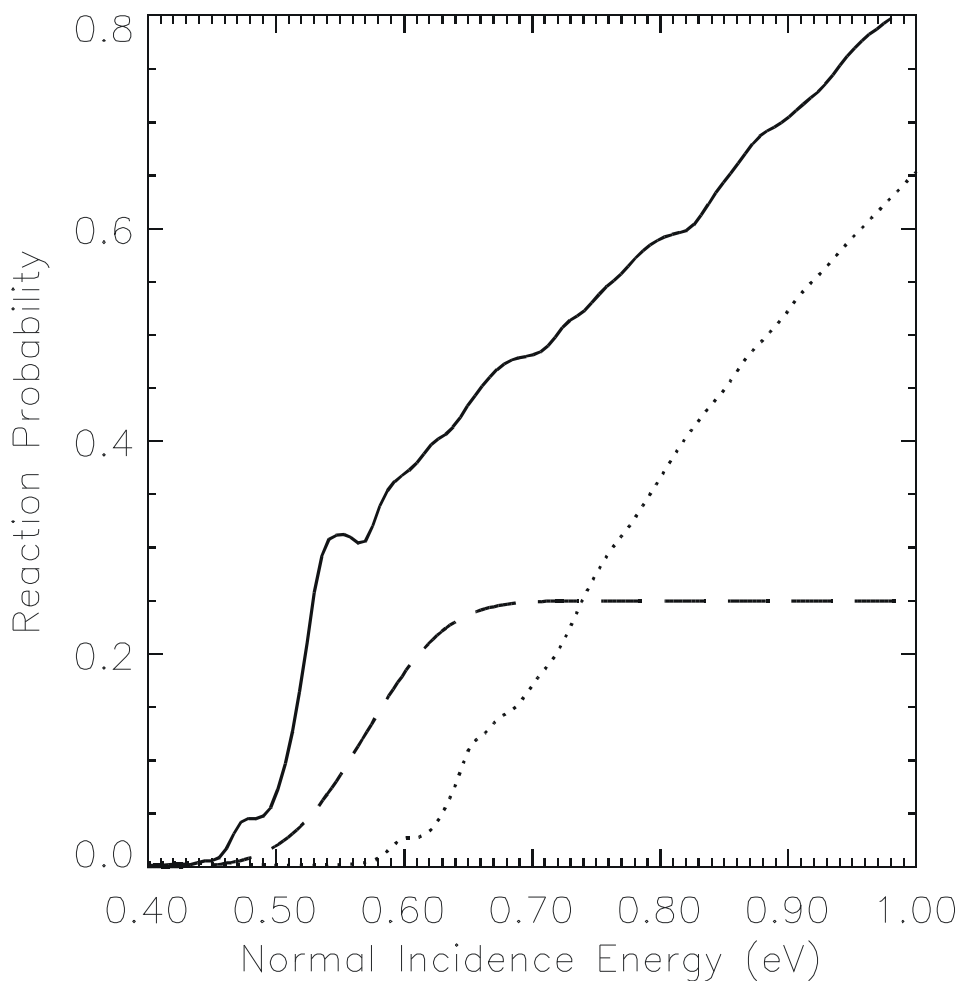
Figure 5.3: Reaction probabilities computed for the DZ PES[14] (dotted line) and the ER PES[22] (solid line) are compared with reaction probabilities fitted to dissociative chemisorption measurements[6] (dashed line), for H_2 + Cu(111). The results are shown as a function of normal incidence energy. The calculations are for reaction of H_2 in its (v=0,j=0) initial state. The fit to experiments is for reaction of H_2 in its (v=0) state and for a surface temperature of 120 K.

amount. This observation is consistent with the defect of the DZ PES that we discussed before, i.e., that the height of the minimum barrier to dissociation in the fit is too high by about 0.2 eV compared to the DFT-GGA data[30]. Our conclusion regarding barrier heights is also in agreement with conclusions reached in five-dimensional quantum dynamics calculations on H_2 + Cu(111) performed by Gross et al.[15], employing a PES based on the same DFT results[30] as the DZ PES.

The reaction probability obtained using the DZ PES rises to a much higher value than the fit (A=0.25). The experimentalists pointed out that equally good fits could be obtained with A in the range 0.15-0.5, but the computed reaction probabilities fall outside this range for large collision energies. The large uncertainty in A is due to the fact that for pure H_2 beams the collision energies that can be achieved do not extend much beyond 0.5 eV. However, in experiments on D_2 + Cu(111) using antiseeding in H_2, collision energies up to 0.83 eV were achieved[3]. We can compare the theoretical results for the DZ PES for H_2 + Cu(111) to the experimental results for D_2 + Cu(111) if we make the assumption that the computational results for H_2 should not be very different from those for D_2 (this assumption will be discussed in section (5.3.2)). Fits to the experiments for D_2 suggest the reaction probability to be no higher than 0.32 for $E_n \leq 0.83$ eV[3,19]. If the computational curve is shifted to lower energies by 0.1 eV, a much higher reaction probability of 0.57 is found for the highest E_n of 0.83 eV. We conclude that the DZ PES yields reaction probabilities for H_2 + Cu(111) that are probably too high and that the barriers in the PES are too high by at least 0.1 eV.

We next consider the reaction probabilities computed for the ER PES[22]. Near threshold, the results are in better agreement with experiment (see Figure 5.3), presumably because the lowest barrier in the PES is more realistic (it is in better agreement with converged DFT results, as pointed out in section (5.2)). However, like the DZ PES, at high collision energies the ER PES yields reaction probabilities which are much too high when compared with the experimentally fitted reaction probability curve. Whether the reaction probability computed for H_2 is indeed too high at large E_n remains uncertain for the reasons mentioned above; this point is discussed further in section (5.3.2). For now, we

conclude that the ER PES yields reaction probabilities for H_2 + Cu(111) that are probably too high at large collision energies.

At low collision energies (< 0.6 eV), the reaction probability curve for the ER PES has a higher slope than both the experimentally fitted curve and the curve for the DZ PES. We attribute this to the bridge-to-center barrier being too early in the ER PES. This should lead to the anisotropy of the PES being too low at the minimum barrier geometry, enabling reaction for molecules that are not optimally oriented at too low energies for collisions with the bridge site. Another way to say this is that the window of reactive orientations increases too fast with the collision energy, because the anisotropy of the potential is too low at the minimum barrier geometry. Furthermore, at high collision energies (> 0.6 eV) the slope of the curve obtained for the ER PES is lower than the slope of the curve obtained with the DZ PES. We attribute this difference to the large energetic corrugation of the reaction barrier of the ER PES, as discussed in section (5.2.2).

A likely deficiency of both PESs is that they yield reaction probabilities that are too high for large collision energies. To investigate whether this might be due to a lack of competition with vibrational excitation, we also computed vibrational excitation probabilities $P(v=0,j=0\rightarrow v=1)$. The computed vibrational excitation probabilities are quite low for both PESs (< 0.008 for the ER PES, and < 0.012 for the DZ PES for the entire range of collision energies). This is to be contrasted with the vibrational excitation probabilities measured for H_2 + Cu(111): fits of $P(v=0\rightarrow v=1,j=3)$ using an expression analogous to equation (5.1) yielded a maximum vibrational excitation probability of 0.28[20].

A direct comparison between our theoretical data (for j=0 only) and experiment is not possible because our theoretical vibrational excitation probabilities are *initial state-selective* with respect to j, whereas the experimental result is *final-state selective* with respect to j, representing an average over the (v=0,j) levels that were populated in the molecular beam. Furthermore, the maximum final-state selective vibrational excitation probabilities were found to decrease by a factor 3 going from final j=0 to 7[19]. Quantum

dynamics calculations on H_2 + Cu(100) which were based on a DFT PES showed an increase of the initial-state selective vibrational excitation probability P(v=0,j→v=1) by 30% when going from j=0 to j=4[32]. Even if an allowance is made for these dependencies of the vibrational excitation probability on the initial and final value of j, the present comparison does suggest that both PESs yield vibrational excitation probabilities that are much too low, by about an order of magnitude. Given the size of the experimentally measured vibration excitation probability, it is also quite likely that the ensuing lack of competition with reaction should result in reaction probabilities that are too high at large collision energies, as further discussed in section (5.3.2).

Rettner, Auerbach and coworkers attributed the efficient vibrational excitation they observed to a mechanism in which H_2 becomes stretched as it reaches the barrier, so that the molecule may emerge vibrationally excited if reflected from the barrier[4,19,20]. No significant dependence on surface temperature could be observed for the range T_s = 250-700 K[19]. Subsequent calculations performed by Darling and Holloway showed that efficient vibrational excitation can indeed occur in an electronically adiabatic mechanism if the PES features a reaction path with a strong curvature in front of an especially late barrier[11,12]. Subsequent quantum dynamics calculations on the analogous H_2 + Cu(100) system employing PESs that were accurate fits to DFT/GGA data confirmed the possibility of efficient vibrational excitation[32-34], which was shown to be due to collisions with the top site. For H_2 + Cu(100), the reaction path for dissociation on the top site contains the features that are necessary for efficient vibrational excitation (large curvature in front of an especially late barrier).

It is likely that the reaction path for dissociation of H_2 over the top site of Cu(111) should exhibit the same features (large curvature in front of an especially late barrier)[33] for vibrational excitation to be as efficient as observed experimentally. Apparently, the two LEPS potentials investigated here do not correctly describe these features. At present, it is not clear whether this is due to limitations that are inherent to the LEPS expression. The ER PES[22] was not based on DFT data for geometries relevant to dissociative chemisorption. Both the DZ[14] and the ER PES[22] contained only two Sato-parameters,

which can be used to fit the location and height of the barrier. An obvious improvement would be to further generalize the LEPS expression by making one or both of the Sato-parameters dependent on the surface site, which should allow one to *simultaneously* adapt the height and location of the barrier at *different* surface sites. Whether this improvement would be sufficient to describe the efficient vibrational excitation observed experimentally remains to be seen, because this should also require a correct description of the shape (curvature) of the reaction path in front of the barrier. Future research should be able to show whether the LEPS expression rests on a firm enough physical basis to accomplish this description once the Sato-parameters correctly describe the corrugation of the height and the location of the reaction barrier.

5.3.2. D_2 + Cu(111)

To eliminate uncertainties as much as possible in our conclusions regarding the size of the reaction probability at large collision energies, we have also performed calculations for D_2 (v=0,j=0) scattering from Cu(111). Reaction probabilities computed for D_2 using the ER PES are compared with reaction probabilities computed for H_2 in Figure 5.4. The theoretical reaction probabilities are compared with experimental values in Figure 5.5.

We first consider the comparison to experiment for the ER PES (Figure 5.5). At $E_n > 0.6$ eV, the computed reaction probability is much higher than the reaction probabilities measured directly in the seeded beam experiments, and than the reaction probability fitted for v=0 (for (v=0), Rettner et al. report parameters $A_0 = 0.32$, $E_0^0 = 0.72$ eV, and $W_0 = 0.07$ eV, for equation (5.1) with the error function replaced by a hyperbolic tangent function[19]). For the highest E_n (0.83 eV) for which the reaction probability was measured, we compute a reaction probability of 0.53, which is much higher than the experimental saturation value (0.32). This strongly suggests that for large collision energies the ER PES yields reaction probabilities which are too high. This conclusion is still somewhat uncertain because the entire experimentally fitted curve for (v=0) appears to be shifted to higher energies with respect to the theoretical results for (v=0,j=0) D_2 (by 0.1-0.2 eV). In

later work, Michelsen et al.[5] reported an uncertainty of 0.1 eV in E_0^0, and we also note that the experimentally fitted curve for (v=0) D_2 appears shifted relative to the experimental curve for (v=0) H_2[6] by 0.1-0.15 eV. As discussed below, this shift is somewhat larger than found in our calculations using the ER PES (Figure 5.4).

Finally, we compare the reaction probability computed for (v=0,j=0) H_2 with that computed for (v=0,j=0) D_2, using the ER PES. Over the entire range of E_n for which we have results, the reaction probability of D_2 is lower than that of H_2. For $E_n > 0.65$ eV, the reaction probability curve for D_2 is shifted to higher energies by 0.05-0.09 eV relative to that of H_2. The sign of the difference is consistent with the difference in the experimental values of E_0^0, but the magnitude is not (E_0^0=0.59 eV for H_2[6] and 0.72 eV for D_2[5]). The origin of the differences between the curves computed for H_2 and D_2 will be discussed in reference 27, where we will present results for reaction of v=1 H_2.
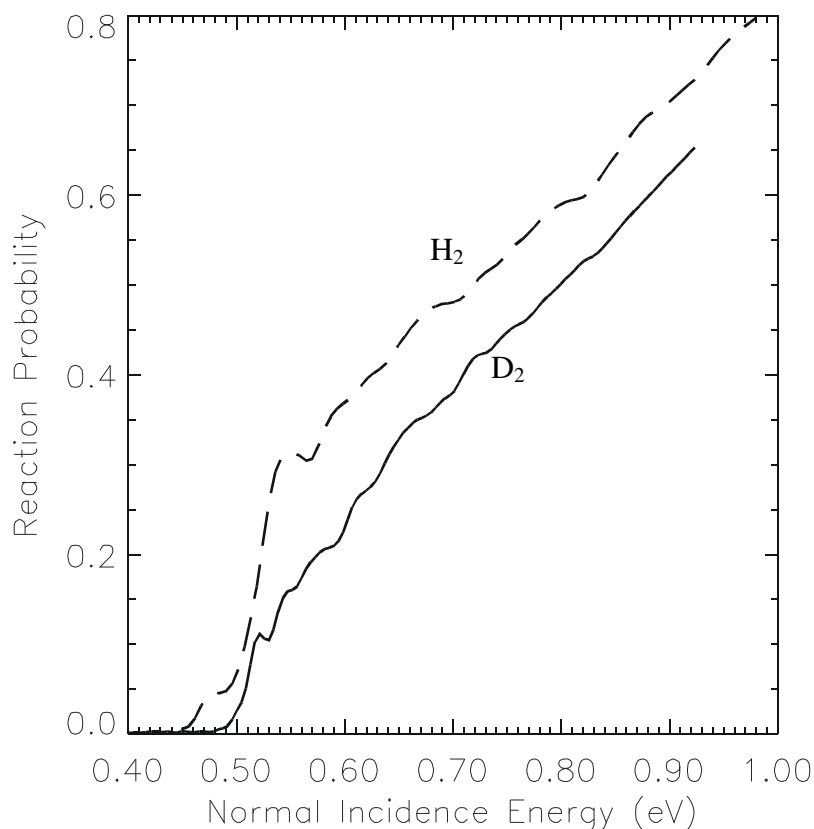
Figure 5.4: Reaction probabilities computed for (v=0,j=0) D_2 (solid line) are compared with reaction probabilities calculated for (v=0,j=0) H_2 (dashed line). In the calculations, the ER PES[22] was used.
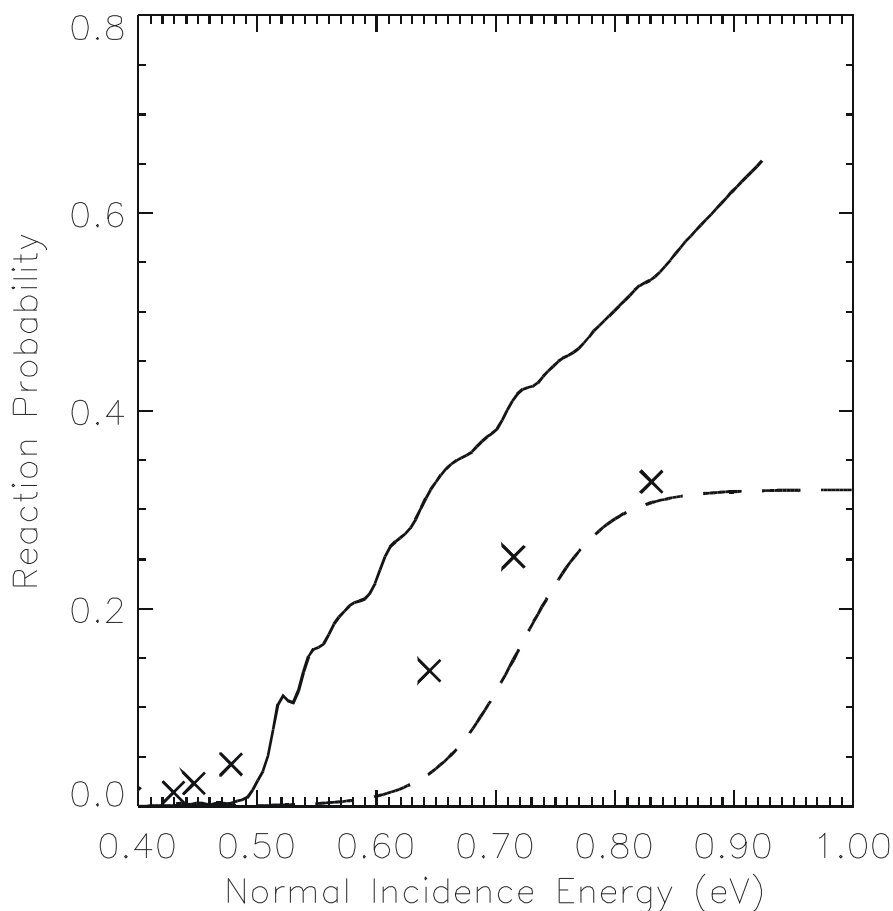
Figure 5.5: Reaction probabilities computed using the ER PES[22] (solid line) are compared with reaction probabilities fitted to dissociative chemisorption measurements[3,19] (dashed line), for D_2 + Cu(111). The results are shown as a function of normal incidence energy. The calculations are for reaction of D_2 in its (v=0,j=0) initial state. The fit to experiments is for reaction of D_2 in its (v=0) state. We also plot the reaction probabilities ($\times$) measured directly in seeded beam experiments on D_2 + Cu(111) performed at normal incidence (taken from figure 1 of reference 3; note that, where possible, we selected the results for the lowest nozzle temperature). These reaction probabilities also contain contributions from v>0.

At E_n = 0.83 eV, the computed reaction probability of D_2 is lower than that of H_2 by 0.07 (Figure 5.4). If we use this number to correct the reaction probability that would be obtained for D_2 using the DZ PES at E_n = 0.83 eV using the energy shifting procedure discussed in section (5.3.1), a reaction probability of 0.50 is obtained. Again, this is much higher than the experimental maximum value of 0.32. This is consistent with our

conclusion that, for large collision energies, the DZ PES yields reaction probabilities which are probably too high.

5.4. Conclusions

We have performed six-dimensional quantum dynamics calculations on the scattering of (v=0,j=0) H_2 and D_2 from Cu(111). The goal of the calculations was to test the accuracy of two different LEPS-PESs[14,22] in describing dissociative chemisorption and vibrational excitation. Both PESs were based on DFT calculations performed within a super cell approach and using the GGA in the calculation of the exchange-correlation energy.

The comparison of the computed reaction probabilities with experimentally fitted reaction probabilities shows that the LEPS-PESs yield reaction probabilities that are probably too high for large collision energies. For H_2, the comparison also suggests that the barriers in the DZ PES[14] are too high by at least 0.1 eV.

The comparison of computed vibrational excitation probabilities with experimentally fitted vibrational excitation probabilities strongly suggests that the LEPS-PESs yield vibrational excitation probabilities that are too low, by about an order of magnitude. The ensuing lack of competition with reaction could well lead to reaction probabilities that are too high at large collision energies, as suggested by the comparison of computed reaction probabilities with experimental values. Future research is needed to establish whether the LEPS potential is able to provide a good representation of both reaction and vibrationally inelastic scattering of H_2 colliding with a copper surface. Possibly, improved results can be obtained by introducing corrugation into the Sato-parameters describing the height and the location of the reaction barrier.

The present comparison shows a clear need for the development of a PES for H_2 + Cu(111) that is an accurate global fit to DFT data, for enough geometries to be useful in

calculations on dissociative chemisorption and vibrational excitation of H_2 and D_2. The enormous experimental effort that has been invested in describing the reaction has left us with a large amount of data that is still in need of detailed interpretation and this would well justify the effort needed to develop such an accurate PES. Also, global fit methods for the accurate representation of DFT data are now available for the interaction of a diatomic molecule with a static surface (see for instance reference 35). Finally, calculations on an accurate PES can perhaps clarify the large difference between the experimentally fitted adsorption probability of v=0 H_2 and D_2 reacting on Cu(111), as noted here.

5.5. References

1   H. A. Michelsen and D. J. Auerbach, J. Chem. Phys. 94, 7502-7520 (1991).
2   H. A. Michelsen, C. T. Rettner, and D. J. Auerbach, Phys. Rev. Lett. 69, 2678 (1992).
3   C. T. Rettner, D. J. Auerbach, and H. A. Michelsen, Phys. Rev. Lett. 68, 1164 (1992).
4   D. J. Auerbach, C. T. Rettner, and H. A. Michelsen, Surf. Sci. 283, 1 (1993).
5   H. A. Michelsen, C. T. Rettner, D. J. Auerbach, and R. N. Zare, J. Chem. Phys. 98, 8294-8307 (1993).
6   C. T. Rettner, H. A. Michelsen, and D. J. Auerbach, J. Chem. Phys. 102, 4625 (1995).
7   D. Wetzig, M. Rutkowski, R. David, and H. Zacharias, Europhys. Lett. 36, 31 (1996).
8   H. Hou, S. J. Gulding, C. T. Rettner, A. M. Wodtke, and D. J. Auerbach, Science 277, 80-82 (1997).
9   M. J. Murphy and A. Hodgson, J.Chem.Phys. 108, 4199 (1998).
10   U. Nielsen, D. Halstead, S. Holloway, and J. K. Nørskov, J. Chem. Phys. 93, 2879-2884 (1990).
11   G. R. Darling and S. Holloway, J. Chem. Phys. 97, 734 (1992).
12   G. R. Darling and S. Holloway, Surf. Sci. 307-309, 153-158 (1994).
13   G. R. Darling and S. Holloway, J. Chem. Phys. 101, 3268-3281 (1994).
14   J. Dai and J. Z. H. Zhang, J. Chem. Phys. 102, 6280-6289 (1995).
15   A. Gross, B. Hammer, M. Scheffler, and W. Brenig, Phys. Rev. Lett. 73, 3121 (1994).
16   J. Dai and J. C. Light, J. Chem. Phys. 107, 1676-1679 (1997).
17   J. Dai and J. C. Light, J. Chem. Phys. 108, 7816-7819 (1998).
18   A. Hodgson, J. Moryl, P. Traversaro, and H. Zhao, Nature 356, 501-504 (1992).

19   C. T. Rettner, D. J. Auerbach, and H. A. Michelsen, Phys. Rev. Lett. 68, 2547 (1992).
20   C. T. Rettner, H. A. Michelsen, and D. J. Auerbach, Chem. Phys. 175, 157 (1993).
21   A. Hodgson, P. Samson, A. Wight, and C. Cottrell, Phys. Rev. Lett. 78, 963 (1997).
22   M. Persson, J. Strömquist, L. Bengtsson, B. Jackson, D. V. Shalashilin, and B. Hammer, J. Chem. Phys. 110, 2240-2249 (1999).
23   G. J. Kroes, Prog. Surf. Sci. 60, 1-85 (1999).
24   R. Kosloff, J. Phys. Chem. 92, 2087-2100 (1988).
25   G. C. Corey and D. Lemoine, J. Chem. Phys. 97, 4115 (1992).
26   D. Lemoine, J. Chem. Phys. 101, 10526 (1994).
27   S. Nave, D. Lemoine, M. F. Somers, S. M. Kingma, E. Pijper, and G. J. Kroes, J. Chem. Phys. in preparation (2002).
28   S. Sato, J. Chem. Phys. 23, 592 (1955).
29   J. McCreery and G. Wolken, J. Chem. Phys. 63, 2340 (1975).
30   B. Hammer, M. Scheffler, K. W. Jacobsen, and J. K. Nørskov, Phys. Rev. Lett. 73, 1400-1403 (1994).
31   J. P. Perdew, J. A. Chevary, S. H. Vosko, K. A. Jackson, M. R. Pederson, D. J. Singh, and C. Fiolhais, Phys. Rev. B 46, 6671-6687 (1992).
32   D. A. McCormack, G. J. Kroes, R. A. Olsen, E. J. Baerends, and R. C. Mowrey, Phys. Rev. Lett. 82, 1410 (1999).
33   G. J. Kroes, G. Wiesenekker, E. J. Baerends, and R. C. Mowrey, Phys. Rev. B 53, 10397-10401 (1996).
34   G. J. Kroes, E. J. Baerends, and R. C. Mowrey, Phys. Rev. Lett. 78, 3583-3586 (1997).
35   H. F. Busnengo, A. Salin, and W. Dong, J. Chem. Phys. 112, 7641-7651 (2000).

Chapter 6

Diffractive and reactive scattering of (v=0,j=0) HD from Pt(111): six-dimensional quantum dynamics compared with experiment

Abstract

We present results of (v=0,j=0) HD reacting on and scattering from Pt(111) at off-normal angles of incidence, treating all six molecular degrees of freedom quantum mechanically. The six-dimensional (6D) potential energy surface (PES) used was obtained from density functional theory (DFT), using the generalized gradient approximation (GGA) and a slab representation of the metal surface. Diffraction and rotational excitation probabilities are compared with experiment for two incidence directions, at normal incidence energies between 0.05-0.16 eV and at a parallel translational energy of 55.5 meV. The computed ratio of specular reflection to non-specular in-plane diffraction for HD + Pt(111) is lower than found experimentally, and lower for HD + Pt(111) than for H_2 + Pt(111) for both incidence directions studied. The calculations also show that out-of-plane diffraction is much more efficient than in-plane diffraction, underlining that results from experiments that solely attempt to measure in-plane diffraction are not sufficient to show the absence of surface corrugation. Discrepancies in rotational excitation and diffraction probabilities between theory and experiment are discussed, as well as possible future improvements in the dynamical model and in the calculation of the PES.

6.1. Introduction

Since the early 1980's, the reactive, the rotationally elastic and inelastic, and the diffractive scattering of molecular hydrogen from metal surfaces have been studied extensively, both experimentally[1-17] and theoretically[17-28]. Much attention has been devoted to HD scattering from Pt(111) because of, *inter alia*, the high probabilities for rotational excitation to only a limited number of accessible rotational states. Experimental efforts by Cowin and co-workers[1,2] have been followed by several theoretical studies of this system, employing either Wigner R-matrix theory[27,29] or Engdahl-Moiseyev-Maniv T-matrix methods[28] to obtain rotationally inelastic scattering probabilities. In all of these calculations, it was assumed that the system could be treated accurately by neglecting vibration and dissociative chemisorption and conserving the magnetic rotational quantum number, m_j, of incident HD. Furthermore, diffraction, and thus translation in X and Y, was neglected, leading to a two-dimensional Hamiltonian depending only on the molecule-surface distance Z and polar angle of orientation θ (the angle between the molecular axis and the surface normal). The potential energy surface (PES) in these studies was approximated by a Morse potential that was adapted to allow for anisotropy in θ. These approximations were considered justified, because Pt(111) was thought to be a non-corrugated ("flat") surface, as was suggested by Cowin *et al.* on the basis of their molecular beam experiments in which no significant (in-plane) diffraction was observed[2]. The main aim of these theoretical calculations was to reproduce the bound level resonances of the HD + Pt(111) physisorption interaction potential that were encountered by Cowin *et al*[1].

The reaction of H_2 on Pt(111) has likewise received attention. In 1990, Luntz *et al.*[12] concluded from their molecular beam study of dissociative chemisorption of H_2 and D_2 on Pt(111) that the PES must be rather corrugated, since the reaction probability was found to depend on the initial parallel momentum, instead of scaling with normal translational energy. The latter finding and the observation of little diffraction in the

experiments of Cowin *et al.*[2] represent a paradox[30]: the experiments on reaction suggest a corrugated surface, whereas the experiments on diffraction suggest a flat surface.

This controversy has been addressed in several theoretical studies[31-33] on H_2 scattering from Pt(111). In a study treating all six molecular degrees of freedom quantum mechanically[33] and employing a PES based on density functional theory (DFT)[34,35], it was found that reaction does not obey normal energy scaling, and that the diffraction is substantial, supporting the conclusion of Luntz *et al*[12]. It was suggested that the experiments by Cowin *et al.*[1,2] failed to find proof of the corrugation of the surface because they measured only in-plane diffraction and did not consider diffraction out of the plane of incidence (the out-of-plane diffraction was predicted to be substantial by the theory). Nevertheless, the calculations yielded more in-plane diffraction (relative to non-diffractive reflection) than Cowin's experiment. It was suggested that this difference might be due to a difference between HD and H_2: rotational excitation is expected to be more efficient for HD than for H_2, and therefore increased competition of rotational excitation with diffraction might lead to lower diffraction probabilities for HD.

Our work addresses this question by comparing six-dimensional quantum dynamics results with experiment, thus offering the first results of dynamics calculations on a *heteronuclear* diatomic molecule scattering from a surface in which all molecular degrees of freedom are treated quantum mechanically. The dynamics method and the PES used are discussed in sections (6.2.1) and (6.2.2), respectively. In sections (6.3.1)-(6.3.3), reaction, rotational excitation and diffraction results are discussed and, where possible, compared with experiment. Section (6.4) offers a summary of our findings.

6.2. Method

6.2.1. Dynamics

In the quantum dynamics calculations, the Born-Oppenheimer approximation was used and it was assumed that the reaction takes place on the ground state PES only, thereby neglecting electron-hole pair excitations. The surface Pt atoms were frozen to their equilibrium positions, thereby neglecting the possibility of energy transfer involving phonons. For a discussion of these approximations, and a review of quantum dynamics methods for molecule-surface reactions, see references 36-38.

The motion in the remaining six degrees of freedom (those of HD) was treated essentially without approximations. The coordinate system and the surface unit cell are shown in Figure 6.1 and Figure 6.2. The translational coordinates X, Y, and Z are the coordinates of the center-of-mass of the molecule. A system of skewed coordinate axes X and Y, with a skewing angle of 60°, was used to describe motion parallel to the surface. The coordinate Z describes the distance to the surface. The internal coordinates r, θ and ϕ represent the H-D distance and the polar and the azimuthal angles of orientation of the HD axis.

The calculations were performed using the same implementation of the time-dependent wave packet (TDWP) method[39] as used before to study H_2 + Pt(111)[33]. We employed the split-operator formalism[40] in which the propagator is symmetrically split into two kinetic energy parts and one potential energy part. The wave function was represented by an expansion in a finite non-direct product basis set (FBR) of spherical harmonics $\mathbf{Y}_{jm_j}(\theta,\phi)$ with expansion coefficients $c_{jm_j}(X,Y,Z,r)$, where X, Y, Z and r are points on Fourier grids with constant spacings ΔX, ΔY, ΔZ and Δr.

The action of the translational and vibrational kinetic energy operator part of the propagator on the wave function, $c_{jm_j}(X,Y,Z,r)$, was implemented using Fast Fourier transforms[41] in X, Y, Z and r. For the rotational energy operator, no transforms were necessary, since the spherical harmonics are eigenfunctions of this operator.
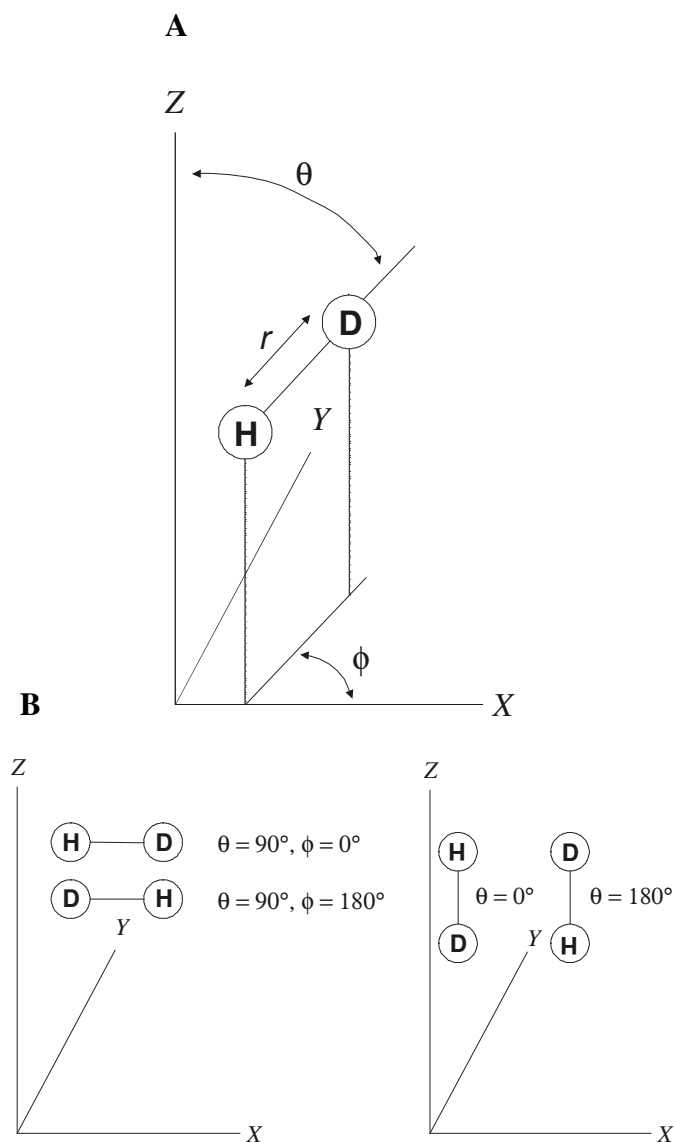
Figure 6.1: The co-ordinate system used in this study. In **(A)** the HD center of mass co-ordinates (X, Y and Z), the HD bond distance r and the two orientational angles θ and φ are indicated. In **(A)** and **(B)**, the conventions adopted for θ and φ are illustrated.
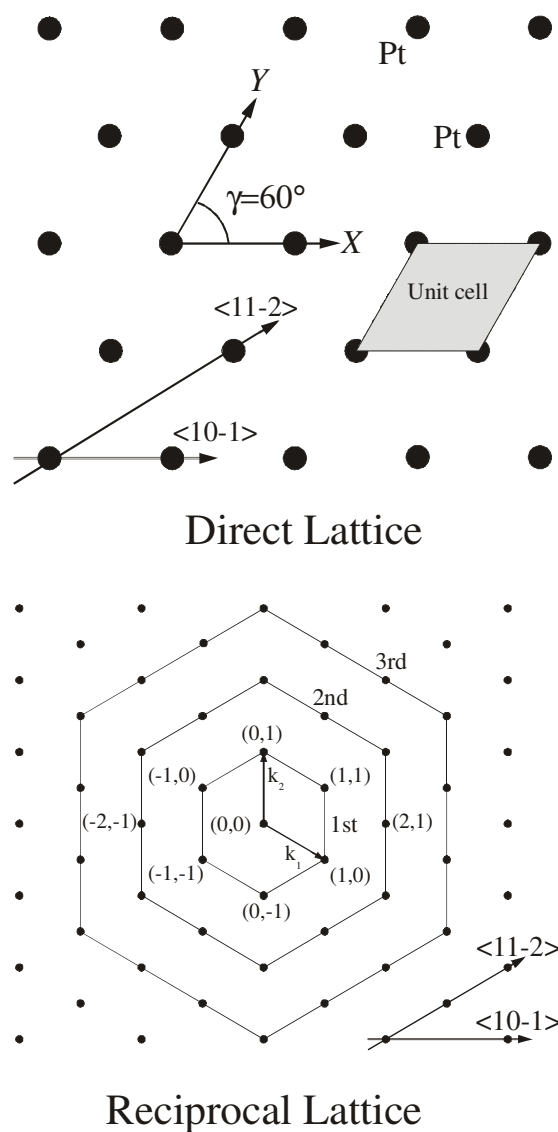
Figure 6.2: The direct lattice (top) and reciprocal lattice (bottom) of the Pt(111) surface. The direct lattice shows the unit cell (shaded area) and the X and Y co-ordinate axes used. The skewing angle γ equals 60°. Points on the reciprocal lattice correspond to diffraction states allowed during scattering. The hexagonal rings define the diffraction order. In both figures, the $<10\overline{1}>$ and $<11\overline{2}>$ directions are indicated.

In evaluating the action of the potential energy operator part of the propagator on the wave function, a Gauss-Associated-Legendre method developed by Corey and Lemoine[42,43] was used to transform the $c_{jm_j}(X, Y, Z, r)$ from the FBR in j and m_j to a discrete variable representation (DVR) in θ and ϕ, and back to the FBR (after multiplication with the potential energy).

The scattering amplitude formalism[44,45] was used to compute state-to-state scattering probabilities for the range of initial translational energies in Z contained in the wave packet (0.05-0.16 eV). Reaction probabilities were calculated by subtracting the summed scattering probabilities from unity. We performed calculations for (v=0,j=0) HD incident along the $<10\bar{1}>$ and $<11\bar{2}>$ directions (Figure 6.2) with an initial translational energy parallel to the surface of 55.5 meV. This corresponds to an incidence angle of 45° with the surface normal at an initial translational energy in Z of 55.5 meV, thus exactly reproducing the conditions of one of the experiments of Cowin *et al.*[2] for this incidence energy. The most relevant parameters used in the calculations are listed in Table 6.1.

6.2.2. Potential energy surface

The six-dimensional PES used in these calculations was originally developed for the H_2 + Pt(111) system, using the program BAND[46] for performing density functional theory (DFT) calculations for H + Pt(111) and H_2 + Pt(111) systems, employing the generalized gradient approximation (GGA)[47,48]. Relativistic effects, which are important for Pt, are taken into account by the zeroth-order regular approximation (ZORA)[49]. The "corrugation reduction" scheme by Salin and co-workers[35] was used to construct the H_2 + Pt(111) PES from a number of two-dimensional PESs. More information on the construction of this PES has been published in references 34 and 50.

Parameter	Description	Value
$E_{\parallel}$	Parallel incidence energy (eV)	0.0555
	Normal incidence energy range (eV)	0.05-0.16
Z_0	Location of center of wave packet on Z grid (a_0)	11.0
Z_{min}	Starting value of Z grid (a_0)	-1.0
N_Z	Number of grid points in Z	90
ΔZ	Grid spacing in Z (a_0)	0.15
N_r	Number of grid points in r	40
Δr	Grid spacing in r (a_0)	0.20
r_{min}	Starting value of r grid (a_0)	0.40
N_X	Number of grid points in X	16
N_Y	Number of grid points in Y	16
a	Surface lattice constant (a_0)	5.23966
j_{max}	Maximum value of j in rotational FBR	16
N_{tot}^{*}	Size scattering basis set	266 million
Δt	Size of time step in propagation (atomic units)	2.5
T_{max}	Total propagation time (atomic units)	35000

[*] N_{tot} is the number of rotational channels in the FBR multiplied by

$N_Z N_r N_X N_Y$.

Table 6.1: Input parameters of the wave packet calculations for HD scattering from Pt(111).

Within the Born-Oppenheimer approximation, a PES developed for H_2 is equally fit for calculations on an isotopomer, *in casu* HD. The symmetry with respect to the center-of-mass which exists in H_2, however, is absent in HD. This is because in HD, the center-of-mass is closer to the D atom than to the H atom. The potential energy for an HD molecule with center-of-mass coordinates $(X, Y, Z, r, \theta, \phi)$ is equal to the potential energy of an H_2 molecule with coordinates $(X', Y', Z', r, \theta, \phi)$, where X', Y' and Z' are given by:

$$X' = X + \frac{r}{2}\left[\frac{\sin(\gamma - \phi)}{\sin\gamma}\sin\theta\right]\left[\frac{m_D - m_H}{m_D + m_H}\right] \tag{6.1}$$

$$Z' = Z + \frac{r}{2}\cos\theta\left[\frac{m_D - m_H}{m_D + m_H}\right] \tag{6.2}$$

$$Y' = Y + \frac{r}{2}\left[\frac{\sin\phi}{\sin\gamma}\sin\theta\right]\left[\frac{m_D - m_H}{m_D + m_H}\right] \tag{6.3}$$

In these equations, m_D and m_H represent the masses of D and H, respectively, and γ is the skewing angle $(0° < \gamma \leq 90°)$: $60°$ in the case of the Pt(111) surface. Extra conventions have to be adopted for θ and ϕ: rotations of $180°$ over θ no longer leave the molecule-surface interaction invariant and the same applies to rotations of $180°$ over ϕ for an orientation of the molecule parallel to the surface. The conventions adopted are implied by the expressions above and shown in Figure 6.1.

6.3. Results and discussion

6.3.1. Reaction

In Figure 6.3, the dissociative chemisorption probabilities of HD and H_2[33] are plotted as a function of normal incidence energy, for a parallel translational energy of 55.5 meV, and for incidence along the $<10\bar{1}>$ and $<11\bar{2}>$ directions. No significant dependence of reaction on the incidence direction was found for either isotopomer. Over the entire energy range, H_2 dissociation is more efficient than HD dissociation. This difference is most probably due to greater competition between reaction and rotational excitation in HD. As the inset to Figure 6.3 shows, the total probability for rotational excitation is much larger for HD than for H_2. One reason that rotational excitation is so efficient for
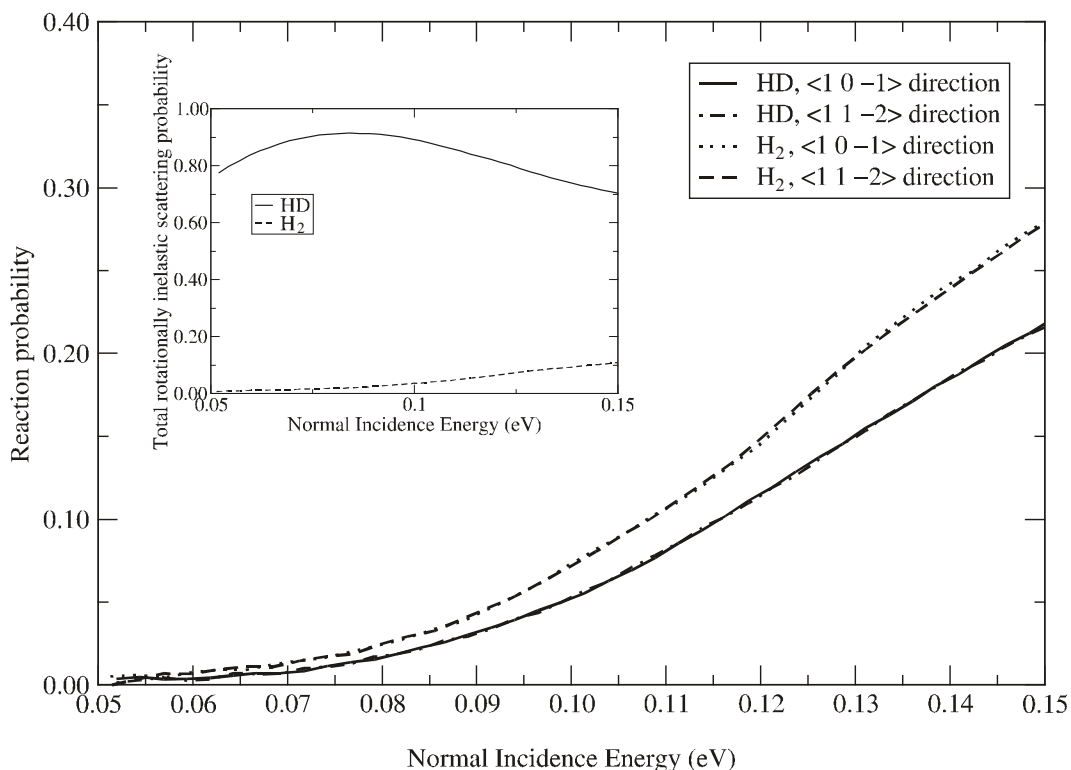
Figure 6.3: Dissociative chemisorption probabilities for (v=0,j=0) HD (present work) and H_2[33] as a function of normal incidence energy, for an initial parallel translational energy of 55.5 meV. Results for both the $<10\bar{1}>$ and $<11\bar{2}>$ incidence directions are shown. The inset shows the total rotationally inelastic scattering probabilities P(v=0,j=0 $\rightarrow$ v'=0,j'≠0) for H_2 and HD for the $<11\bar{2}>$ incidence direction at a parallel translational energy of 55.5 meV, as a function of normal incidence energy.

HD is that HD is a heteronuclear molecule, the j=1 and j=3 states being accessible from the rotational ground state; many molecules return to the gas phase in these states (see below), which are not accessible to (homonuclear) j=0 H_2. The energy transferred to rotation is subsequently no longer available for traversing the barrier to dissociation. Furthermore, because the center-of-mass of HD is not situated halfway between the nuclei, orientations that differ in the polar angle by 180 degrees are not equivalent, and therefore, the potential for HD is more anisotropic than for H_2 (Figure 6.4), which is expected to result in more rotational excitation and less reaction. Finally, the energy spacing between the rotational levels of HD is smaller than in H_2, thereby again enhancing rotational excitation and inhibiting reaction.

Cowin *et al.* did not measure reaction (sticking) probabilities for HD + Pt(111). In an attempt to account for lost flux, they did, however, remark that reaction could play a significant role in the attenuation of their signal. Since the reaction probability at the
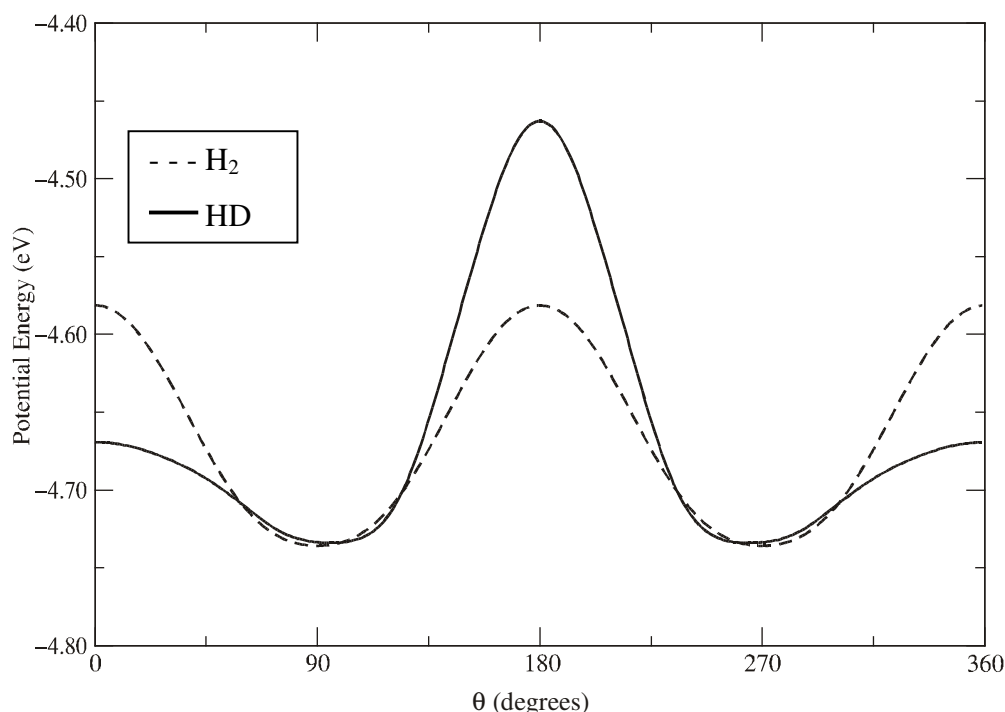
Figure 6.4: Plot of the potential energy as a function of θ for HD and H_2 at the top site (X=Y= 0.0 a_0). The center-of-mass of the molecule is fixed at the H_2 barrier location (r=1.46 a_0, Z=4.25 a_0) with ϕ=120°. The difference between the highest and lowest values of the potential energy when rotating over θ is greater for HD (0.27 eV) than for H_2 (0.15 eV).

energy considered has been shown to be relatively small in both theoretical calculations[33] and experiments on H_2 and D_2 on Pt(111)[12,13], it is more likely that the greater part of the loss of flux in Cowin's experiment should be attributed to other causes, such as out-of-plane diffraction (see section (6.3.3) below).

6.3.2. Rotational excitation

In Figure 6.5, rotationally elastic and inelastic excitation probabilities P(v=0,j=0 → v=0,j=j') are presented as a function of initial normal incidence energy, for j'=0-3 and for an initial parallel energy of 55.5 meV along the $<11\overline{2}>$ direction. At an incidence angle of 45° (i.e. at an initial translational energy in Z of 55.5 meV), the excitation probabilities are 0.68 and 0.11 for the j=0 → j'=1 and j=0 → j'=2 transitions, respectively. As already explained in section (6.3.1), rotational excitation of HD is expected to be more efficient than that of H_2 because HD is asymmetric and has more closely spaced energy levels. An additional explanation for these large rotational excitation probabilities at low collision energies has been suggested in previous theoretical[17,33,51] and experimental[7,17] studies: because the threshold energy to reaction is equally low, molecules are able to approach the barrier closely at these low energies, where they experience a high anisotropy of the potential energy, allowing efficient rotational excitation.

Cowin *et al.* found virtually identical rotational excitation probabilities for the two incidence directions at this energy (cf. figure 4 of reference 2). They considered this result an illustration of the weak corrugation of the surface[1,2]. Our computed results are also practically identical for the $<10\overline{1}>$ and $<11\overline{2}>$ directions. We believe, however, that this result can be understood from somewhat different arguments, which are similar to those used in references 33 and 30: because the parallel momentum of the molecules is small, they will be scattered by the first barrier they encounter, instead of experiencing the full range of the variation of the anisotropy in the plane of incidence. The calculations of reference 33 have shown that for greater parallel momentum, rotational excitation

probabilities start to differ significantly for the two incidence directions: rotational excitation for incidence along the $<10\bar{1}>$ direction roughly obeys normal energy scaling, whereas for incidence along the more corrugated $<11\bar{2}>$ direction, rotational excitation is coupled more strongly to parallel motion. The incidence direction-independent results for HD + Pt(111) obtained by Cowin *et al.*[2] and by us for a low parallel energy are therefore only typical for small parallel energies.
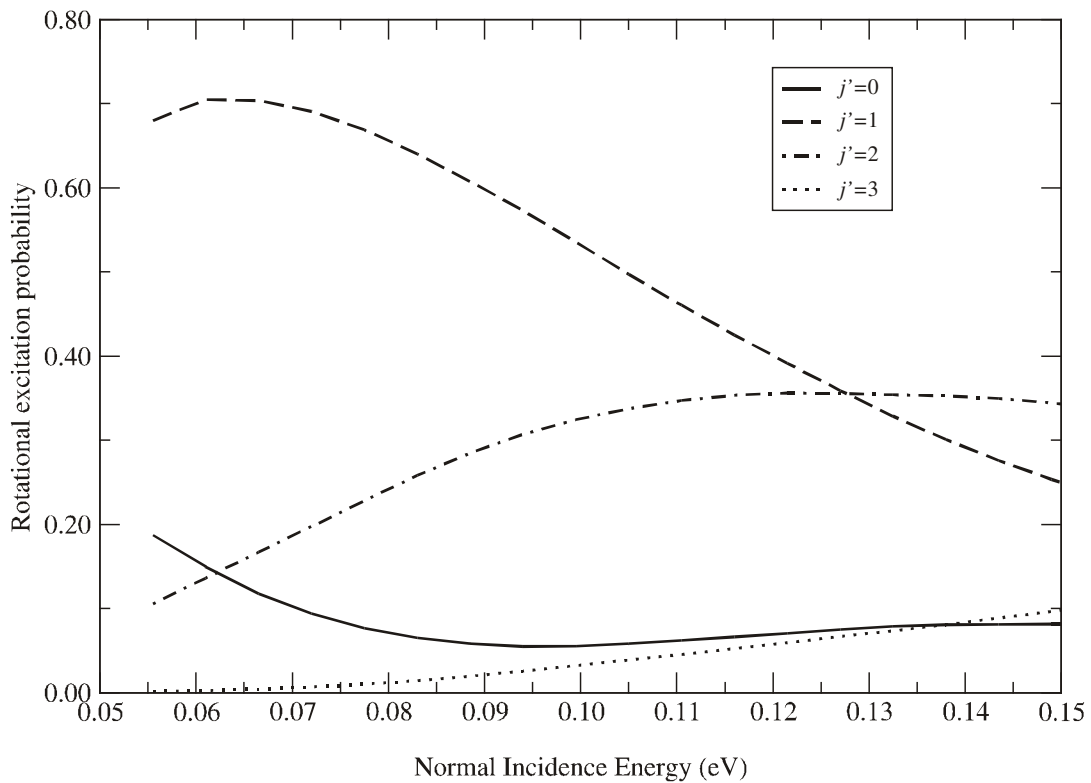
Figure 6.5: Absolute rotational excitation probabilities for (v=0,j=0) HD scattering from Pt(111) as a function of normal incidence energy, for incidence along the $<11\bar{2}>$ direction. The initial parallel translational energy is 55.5 meV, reproducing the experimental conditions of Cowin's experiment[2] for 55.5 meV translational energy in Z (i.e., at an incidence angle of 45°). The probabilities have been summed over all diffraction states and m_j channels. Incidence along the $<10\bar{1}>$ direction yields virtually the same results, which are not shown in the plot.

A quantitative comparison of the results of our calculations with the experimental results can only be performed for a normal incidence energy of 55.5 meV; together with an equal amount of parallel translational energy, the total energy of 111 meV of Cowin's beam is then reproduced. A comparison over the entire energy range is not possible, because the experiments were performed for various incidence angles and fixed total translational energy[2], whereas our calculations were performed for fixed parallel energy and a range of normal translational energies.

Although our results agree qualitatively with the results of Cowin *et al.*[2] in that we also found identical rotational excitation probabilities for the two incidence directions, our results do not agree quantitatively with their results. In Table 6.2, the rotational excitation probabilities calculated in our study are compared with the *relative* excitation probabilities of Cowin *et al*. To make this comparison meaningful, our probabilities have been normalized to unity to yield *relative* numbers as well. Furthermore, the experimental rotational excitation probabilities represent probabilities for phonon-elastic, non-diffractive scattering $(G = 0)$[2]. In particular, although the measurements were performed for a surface temperature $T_S = 500$ K, a Debye-Waller attenuation model was used to extrapolate the results to a 0 K surface, in order to allow the data to be compared with theoretical calculations on a rigid surface[2]. In Table 6.2, we therefore compare our rigid surface results for rotational excitation with $G = 0$ with the experimental rotational excitation probabilities.

	j=0 → j'=0	j=0 → j'=1	j=0 → j'=2
Cowin et al.[2]	0.03	0.40	0.57
This work	0.16	0.72	0.12

Table 6.2: Rotational excitation probabilities for $(G = 0)$ scattering of (v=0,j=0) HD from Pt(111), for incidence along the $<10\overline{1}>$ direction at a normal incidence energy of 55.5 meV and equal parallel translational energy. The probabilities have been normalized to unity.

In our calculations, the majority of the molecules scatter back to the gas phase in the j'=1 state, whereas in Cowin's experiment, the j'=1 and j'=2 states are both highly populated. This discrepancy can be due to inaccuracies in the PES and in the dynamical model. Inaccuracies in the PES can be due to approximations inherent in DFT as well as to small errors that were made in the interpolation of the DFT data to obtain a global PES. With respect to the latter, we note that extensive tests have shown that the representation of the DFT data by the PES is accurate to within 30 meV in both the entrance and barrier regions of the PES[34]. The representation of the DFT data by the PES should therefore be much more accurate than for the H_2 + Cu(100) case, for which Watts *et al.* recently published a comparison with experimental data for rotational excitation[17]. Although it cannot be ruled out that small errors resulting from the interpolation procedure affect the present results, we believe that the results are probably more affected by approximations now made in DFT. For instance, it is known that the GGA[47,48] used in the construction of the PES[50] does not yield a correct description of the attractive van der Waals interaction between the molecule and the surface. This means that the van der Waals physisorption well, which has an estimated depth of 55 meV[52], the estimation being based on rotationally mediated selective adsorption[1,52], is absent from our PES. The incorrect description of the van der Waals energy could well result in errors in the location of the barriers in the PES, which in turn could lead to errors in the anisotropy of the PES in the region near the barrier, which is thought to be important for rotational excitation. For this reason, we believe that attempts to improve the PES to obtain a better description of rotational excitation of HD on Pt(111) should focus on correctly incorporating the van der Waals interaction in the DFT description of the PES. Over the past few years, density functionals for calculating van der Waals interaction energies have been developed[53-57], and perhaps these or other yet to be developed methods can be used in future research to improve the accuracy of the PES.

We now turn to possible shortcomings in the dynamical model, such as the neglect of phonons and of electron-hole pair excitations. With respect to the former, we note that Cowin *et al.* did make an attempt to extrapolate their experimental results to 0 K in order to obtain phonon-elastic excitation probabilities, which could presumably be compared to

theoretical results employing a rigid surface approximation. However, as they note themselves, the Debye-Waller model they applied for extrapolating their results to 0 K was developed for single molecule-surface bounces, and at their experimental normal collision energy (55 meV), many collisions are likely to suffer multiple Debye-Waller attenuation, due to trapping in the van der Waals physisorption well[2]. The increased importance of energy exchange with phonons under conditions where trapping may occur has been pointed out in a recent theoretical study of rotational excitation of H_2 on Pd(111)[58]. Experiments on H_2 + Pd(111)[59] as well as on H_2 + Cu(100)[16] have shown that substantial amounts of energy may be exchanged with the surface in rotationally inelastic scattering. Because an improved description of the competition of phonon-inelastic scattering with phonon-elastic scattering should yield a better description of phonon-elastic scattering, we believe that incorporating phonons in the dynamical model would represent another important step towards an improved description of rotationally inelastic scattering of HD from Pt(111).

We do not believe that the neglect of electron-hole pair excitations represents a serious approximation. In recent experiments, Gergen *et al.*[60] found that the probability of exciting electron-hole pairs shows a power law dependence on the adsorption energy, low adsorption energies correlating with low excitation probabilities. In particular, they estimate an excitation probability of about 6% for an adsorption energy of about 0.2 eV, which is still larger than the estimated physisorption well depth for HD + Pt(111) of 55 meV. Probabilities for rotational excitation together with electron-hole pair excitation would then be expected to be at the few percent level, so that the incorporation of electron-hole pair excitations in the dynamical model should not lead to important improvements in the description of rotationally inelastic scattering of HD from Pt(111).

A qualitative difference with experiment is that no resonances were found in the calculations. This is probably due to two causes. First, we did not perform calculations for the energies at which the resonances occur most strongly (< 40 meV translational energy in Z). Quantum dynamics calculations on reaction of H_2 on Pd(100)[22] and on reaction and rotational excitation of H_2 on Pd(111)[61], which used DFT PESs in a similar way to the present work, and which were performed for even lower energies, showed

scattering resonances at these energies due to energy transfer to rotational and parallel motion, and the opening up of new scattering channels. Second, and more importantly, as previously mentioned, the generalized gradient approximation of DFT used in creating the 6D PES lacks a physically correct description of the attractive van der Waals interactions, which means that the van der Waals forces causing the resonances (through rotationally mediated selective adsorption in the physisorption well[1]) have not been incorporated in the PES.

6.3.3. Diffraction

In Table 6.3, the computed ratios of specular to non-specular in-plane diffraction of HD are compared with the experimental values of Cowin *et al.*[2], and to the values computed for H_2 + Pt(111) in reference 33. In this table, G denotes the momentum vector associated with diffraction: (G=0) corresponds to scattering without a change in parallel momentum and (G≠0) denotes diffractive scattering. Note that the ratios discussed here are for probabilities that represent sums over rotationally elastic and inelastic scattering.

	System	<1 0 -1>, in-plane $P(G=0) / P(G{\neq}0)$	<1 1 -2>, in-plane $P(G=0) / P(G{\neq}0)$
Cowin et al.[2]	HD + Pt(111)	approx. 100	approx. 10
Reference 33	H_2 + Pt(111)	20.0	4.71
This work	HD + Pt(111)	13.8	3.39

Table 6.3: Ratio of specular reflection (G=0) to in-plane diffraction (G≠0) of HD scattering from Pt(111) at a normal incidence energy of 55.5 meV and equal parallel translational energy. In computing the ratios, diffraction probabilities have been summed over all rotational channels.

As discussed in the introduction, the authors of reference 33 suggested that the difference between experiment for HD + Pt(111) and theory for H_2 + Pt(111) might be due to stronger competition between rotational excitation and diffraction in HD as compared with H_2, because of the expected higher rotational excitation probability of the former species. Our calculations show that this is not the case. For the conditions of Cowin's experiment, even smaller ratios were computed for HD (13.8 for incidence along the $<10\bar{1}>$ direction and 3.39 for the $<11\bar{2}>$ direction) than for H_2 (20.0 and 4.71, respectively). A possible explanation for the fact that we computed larger $G{\neq}0$ probabilities for HD than for H_2 is that, since the mass of HD is greater than the mass of H_2, the energy gaps between HD diffraction channels are smaller, which is expected to lead to larger probabilities for diffractive scattering.

Above, the comparison between theoretical results for HD + Pt(111) and H_2 + Pt(111) does not yet explain the discrepancies between the experimental and theoretical ratios (G=0 scattering) / (G≠0 in-plane scattering) for HD + Pt(111). We attribute these discrepancies to the same deficiencies of the PES and the model that are likely to cause the discrepancies between experimental and theoretical rotational excitation probabilities. The absence of a correct description of the attractive van der Waals interaction by the DFT functionals we used[47,48], and the absence of an explicit description of energy exchange with surface phonons are most likely responsible for the present disagreement between theory and experiment for in-plane diffractive scattering of HD from Pt(111).

Cowin *et al.*[2] only measured in-plane scattering. As already mentioned, they found very little G≠0 in-plane scattering (1-10 % compared with specular reflection) and hence concluded that the surface must be rather flat. Furthermore, they estimated that the total G≠0 scattering would roughly equal three times the total G≠0 in-plane scattering.
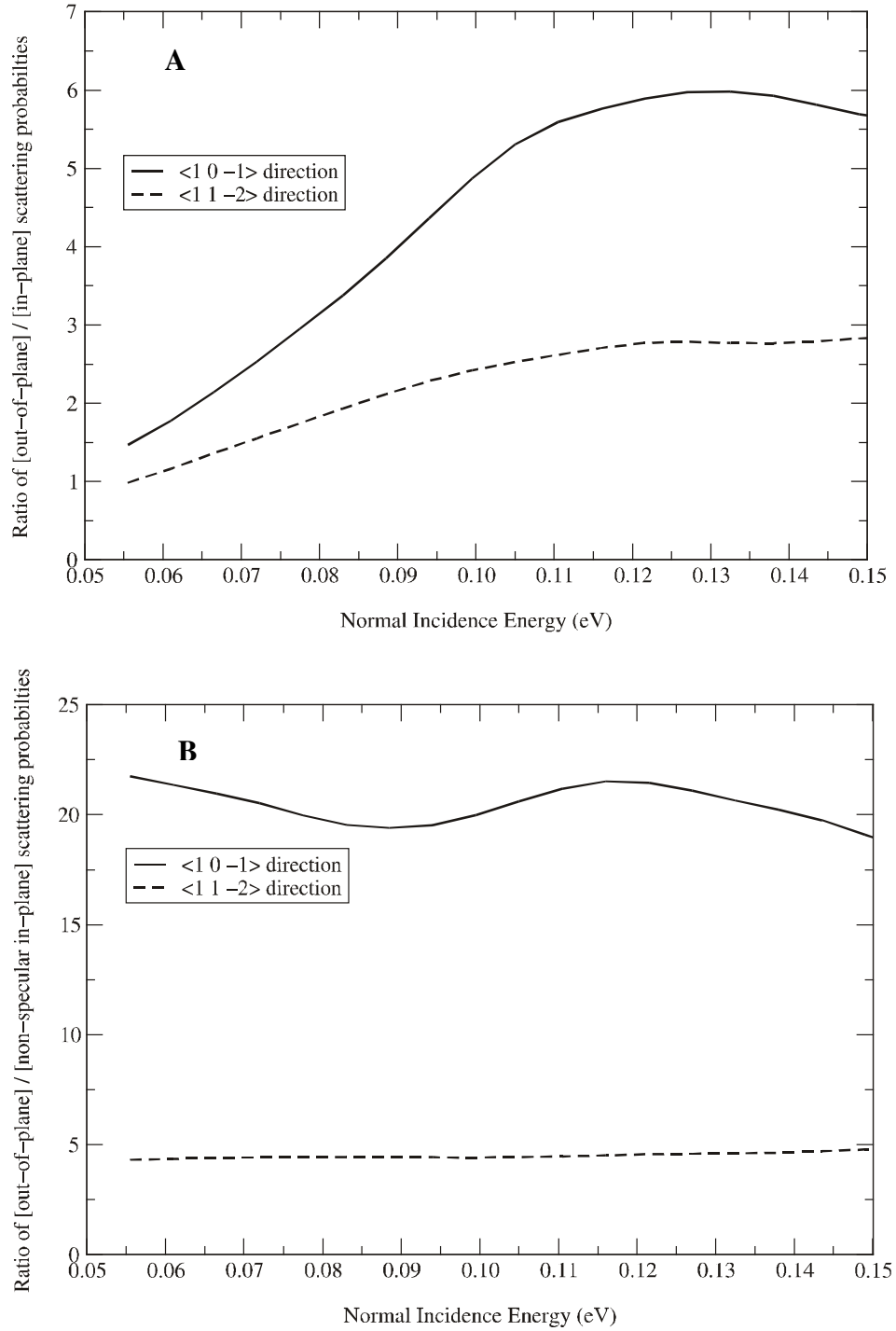
Figure 6.6: Figure **(A)** shows a plot of the ratio of total out-of-plane to total in-plane (including G=0 scattering) scattering probabilities of the HD + Pt(111) system for both the $<10\overline{1}>$ and $<11\overline{2}>$ incidence directions, as a function of normal incidence energy. Figure **(B)** shows the ratio of total out-of-plane to G≠0 in-plane scattering probabilities. In both figures, the initial parallel translational energy is 55.5 meV.

For a parallel translational energy of 55.5 meV and both incidence directions considered, our calculations show that over the entire range of energies, out-of-plane scattering out-competes in-plane scattering (*including* scattering with G=0) by a factor varying between approximately 1 and 6 (Figure 6.6A). The ratio of total out-of-plane to in-plane scattering is greater for the $<10\bar{1}>$ than for the $<11\bar{2}>$ direction. This is due to the non-availability of first-order in-plane diffraction channels in the former direction, as discussed in references 32 and 33. The ratio of out-of-plane to G≠0 in-plane scattering (Figure 6.6B) produces an even more impressive illustration of the importance of measuring out-of-plane scattering: for the $<10\bar{1}>$ direction, more than 20 times as much out-of-plane diffraction is found in the calculations. Thus, out-of-plane scattering is much more important than suggested by the experimentalists[2], who assumed that the total G≠0 scattering would roughly equal three times the G≠0 in-plane scattering, and were at a loss to explain the observed loss of flux in their experiments[2]. In particular, the extrapolation of the experimental results to T_S = 0 K suggested that 28% of the molecules is scattered with G=0, and Cowin *et al.*[2] estimated that only 6% of the molecules should be diffracted. According to the present theoretical results, for the $<10\bar{1}>$ incidence direction, 37% of the molecules is scattered with G=0 and 60% is diffracted, 58% of the scattering being due to out-of-plane scattering. Our results therefore strongly support the statement of reference 33 that conclusions about the corrugation of the surface should not be based on scattering experiments that only look at in-plane diffraction. Experimental techniques able to measure out-of-plane scattering are available[62-64] and it would be interesting to see whether the computed high out-of-plane diffraction probabilities are reproduced by such experiments.

6.4. Summary

We have presented results of 6D quantum dynamics calculations on the dissociative adsorption of HD on, and the rotationally inelastic and diffractive scattering of HD from Pt(111) at off-normal incidence (with a parallel translational energy of 55.5 meV) along

the $<10\bar{1}>$ and $<11\bar{2}>$ surface directions, for a normal incidence energy range of 0.05-0.15 eV. The calculations were motivated by a discrepancy between experimental results for HD + Pt(111)[2] and theoretical results for H_2 + Pt(111)[33], the experiments for HD showing much less in-plane G≠0 scattering relative to G=0 scattering than the calculations for H_2. The main goal of the calculations was to determine whether the computed ratio of G=0 to G≠0 in-plane scattering would be higher for HD + Pt(111) than for H_2 + Pt(111), explaining the above difference between theory and experiment. This was expected from the higher rotational excitation probabilities of HD, which could lead to more competition of rotational excitation with diffraction. The calculations showed, however, that for HD the ratio was lower rather than higher, i.e. that G≠0 scattering is more probable, relative to specular scattering, than in H_2. We have suggested that this result could be explained by the lower energy gaps between diffraction channels in HD, which is caused by its greater mass.

The present calculations on HD + Pt(111) show a ratio of out-of-plane diffractive scattering to in-plane diffractive scattering that is much higher than assumed by the experimentalists[2]. Out-of-plane diffractive scattering may well account for much of the "lost flux" observed in their experiments[2]. Like previous studies[31-33], the present calculations indicate that experiments only looking at in-plane diffraction are not well suited for probing the corrugation of the molecule-surface PES.

The reaction probability of HD is lower than that of H_2 over the energy range studied. This difference can be attributed to rotational excitation competing more strongly with reaction for HD than for H_2 reacting on Pt(111).

The computational results for rotational excitation of HD on and for in-plane diffractive scattering of HD from Pt(111) do not yet agree quantitatively with the experimental results. The deficiencies in the PES and in the dynamical model which are most likely responsible for the lack of agreement are the absence of a correct description of the attractive van der Waals interaction in the DFT-PES and the absence of an explicit description of energy exchange with phonons in the model. To improve the agreement

between theory and experiment for scattering of HD from Pt(111), improvement of these two aspects should be the goal of future theoretical work.

6.5. References

1   J. P. Cowin, C. F. Yu, S. J. Sibener, and J. E. Hurst, J. Chem. Phys. 75, 1033 (1981).
2   J. P. Cowin, C. F. Yu, S. J. Sibener, and L. Wharton, J. Chem. Phys. 79, 3537 (1983).
3   H. A. Michelsen, C. T. Rettner, D. J. Auerbach, and R. N. Zare, J. Chem. Phys. 98, 8294 (1993).
4   M. Beutl, M. Riedler, and K. D. Rendulic, Chem. Phys. Lett. 247, 249 (1995).
5   B. E. Hayden and C. L. A. Lamont, Phys. Rev. Lett. 63, 1823 (1989).
6   A. Hodgson, J. Moryl, P. Traversaro, and H. Zhao, Nature 356, 501 (1992).
7   A. Hodgson, P. Samson, A. Wight, and C. Cottrell, Phys. Rev. Lett. 78, 963 (1997).
8   D. Wetzig, M. Rutkowski, H. Zacharias, and A. Gross, Phys. Rev. B 63, 205412 (2001).
9   H. Hou, S. J. Gulding, C. T. Rettner, A. M. Wodtke, and D. J. Auerbach, Science 277, 80 (1997).
10   C. T. Rettner, D. J. Auerbach, and H. A. Michelsen, Phys. Rev. Lett. 68, 2547 (1992).
11   C. T. Rettner, D. J. Auerbach, and H. A. Michelsen, Phys. Rev. Lett. 68, 1164 (1992).
12   A. C. Luntz, J. K. Brown, and M. D. Williams, J. Chem. Phys. 93, 5240 (1990).
13   P. Samson, A. Nesbitt, B. E. Koel, and A. Hodgson, J. Chem. Phys. 109, 3255 (1998).
14   M. Gostein, E. Watts, and G. O. Sitz, Phys. Rev. Lett. 79, 2891 (1997).
15   M. Gostein, H. Parkikhteh, and G. O. Sitz, Phys. Rev. Lett. 75, 342 (1995).
16   E. Watts and G. O. Sitz, J. Chem. Phys. 114, 4171 (2001).
17   E. Watts, G. O. Sitz, D. A. McCormack, G. J. Kroes, R. A. Olsen, J. A. Groeneveld, J. N. P. van Stralen, E. J. Baerends, and R. C. Mowrey, J. Chem. Phys. 114, 495 (2001).
18   J. Dai and J. C. Light, J. Chem. Phys. 107, 1676 (1997).
19   J. Dai and J. Z. H. Zhang, J. Chem. Phys. 102, 6280 (1995).
20   G. R. Darling and S. Holloway, J. Chem. Phys. 101, 3268 (1994).
21   M. Dohle and P. Saalfrank, Surf. Sci. 373, 95 (1997).
22   A. Gross, S. Wilke, and M. Scheffler, Phys. Rev. Lett. 75, 2718 (1995).
23   A. Gross, S. Wilke, and M. Scheffler, Surf. Sci. 357-358, 614 (1996).
24   A. Gross and M. Scheffler, Phys. Rev. B 57, 2493 (1998).
25   B. Hammer, M. Scheffler, K. W. Jacobsen, and J. K. Nørskov, Phys. Rev. Lett. 73, 1400 (1994).
26   G. J. Kroes, E. J. Baerends, and R. C. Mowrey, Phys. Rev. Lett. 78, 3583 (1997).

27   K. B. Whaley, J. C. Light, J. P. Cowin, and S. J. Sibener, Chem. Phys. Lett. 89, 89 (1982).
28   U. Peskin and N. Moiseyev, J. Chem. Phys. 96, 2347 (1992).
29   K. B. Whaley and J. C. Light, J. Chem. Phys. 81, 2144 (1984).
30   G. R. Darling and S. Holloway, Surf. Sci. Lett. 304, L461 (1994).
31   E. Pijper, G. J. Kroes, R. A. Olsen, and E. J. Baerends, J. Chem. Phys. 113, 8300 (2000).
32   E. Pijper, G. J. Kroes, R. A. Olsen, and E. J. Baerends, J.Chem.Phys. 116, 9435 (2002).
33   E. Pijper, G. J. Kroes, R. A. Olsen, and E. J. Baerends, J. Chem. Phys. 117, 5885 (2002).
34   R. A. Olsen, H. F. Busnengo, A. Salin, M. F. Somers, G. J. Kroes, and E. J. Baerends, J. Chem. Phys. 116, 3841 (2002).
35   H. F. Busnengo, A. Salin, and W. Dong, J. Chem. Phys. 112, 7641 (2000).
36   G. R. Darling and S. Holloway, Rep. Prog. Phys. 58, 1595 (1995).
37   G. J. Kroes, Prog. Surf. Sci. 60, 1 (1999).
38   A. Gross, Surf. Sci. Rep. 32, 291 (1998).
39   R. Kosloff, J. Phys. Chem. 92, 2087 (1988).
40   M. D. Feit, J. A. Fleck, and A. Steiger, J. Comput. Phys. 47, 412 (1982).
41   J. W. Cooley and J. W. Tukey, Math. Computation 19, 297 (1965).
42   G. C. Corey and D. Lemoine, J. Chem. Phys. 97, 4115 (1992).
43   D. Lemoine, J. Chem. Phys. 101, 10526 (1994).
44   G. G. Balint-Kurti, R. N. Dixon, and C. C. Marston, J. Chem. Soc. Faraday Trans. 86, 1741 (1990).
45   R. C. Mowrey and G. J. Kroes, J. Chem. Phys. 103, 1216 (1995).
46   G. ter Velde and E. J. Baerends, Phys. Rev. B 44, 7888 (1991).
47   A. D. Becke, Phys. Rev. A 38, 3098 (1988).
48   J. P. Perdew, Phys. Rev. B 33, 8822 (1986).
49   P. H. T. Philipsen, E. v. Lenthe, J. G. Snijders, and E. J. Baerends, Phys. Rev. B 56, 13556 (1997).
50   R. A. Olsen, G. J. Kroes, and E. J. Baerends, J. Chem. Phys. 111, 11155 (1999).
51   A. J. Cruz and B. Jackson, J. Chem. Phys. 94, 5715 (1991).
52   J. P. Cowin, C. F. Yu, and L. Wharton, Surf. Sci. 161, 221 (1985).
53   Y. Andersson, D. C. Langreth, and B. I. Lundqvist, Phys. Rev. Lett. 76, 102 (1996).
54   T. A. Wesolowski, Y. Ellinger, and J. Weber, J. Chem. Phys. 108, 6078 (1998).
55   J. F. Dobson and J. Wang, Phys. Rev. Lett. 82, 2123 (1999).
56   E. Hult, Ph.D. Thesis, Chalmers University of Technology, 1999.
57   H. Rydberg, Ph.D. Thesis, Chalmers University of Technology and Göteborg University, 2001.
58   H. F. Busnengo, W. Dong, P. Sautet, and A. Salin, Phys. Rev. Lett. 87, 127601 (2001).
59   E. Watts and G. O. Sitz, J. Chem. Phys. 111, 9791 (1999).
60   B. Gergen, H. Nienhaus, W. H. Weinberg, and E. W. McFarland, Science 294, 2521 (2001).
61   H. F. Busnengo, E. Pijper, M. F. Somers, G. J. Kroes, A. Salin, R. A. Olsen, D. Lemoine, and W. Dong, Chem. Phys. Lett. 356, 515 (2002).

62   J. P. Toennies, in Surface Phonons, Vol. 21 (Springer, Berlin, 1991), pp. 111.
63   D. Farías and K. H. Rieder, Rep. Prog. Phys. 61, 1575 (1998).
64   J. R. Buckland and W. Allison, J. Chem. Phys. 112, 970 (2000).

Samenvatting

Zes-dimensionale quantumdynamica van dissociatieve chemisorptie van waterstof op metaaloppervlakken

In dit proefschrift worden berekeningen besproken aan verstrooiing en reactie van moleculaire waterstof, en zijn isotopomeren, aan de overgangsmetaaloppervlakken Cu(100), Cu(111) en Pt(111). Het doel van deze berekeningen is beter te begrijpen hoe moleculen zoals H_2, D_2 en HD, reageren op metaaloppervlakken. Een fundamenteel begrip van dit onderwerp is belangrijk voor vele praktische toepassingen in de industrie en het dagelijks leven. Hierbij kan, bijvoorbeeld, gedacht worden aan de hydrogenatie van stikstof in de productie van ammonia in de industrie en aan de autokatalysator die tegenwoordig niet meer weg te denken is. Een ander doel van de berekeningen is verklaringen te vinden voor onbegrepen experimentele waarnemingen, gevonden in experimenten aan de reactie en verstrooiing van waterstof aan overgangsmetaaloppervlakken. Een stap verder die genomen wordt is het voorspellen van fenomenen, die belangrijke elementen van reactiemechanismen zouden kunnen aantonen, maar wel experimenteel nog bevestigd moeten worden.

Vanuit theoretisch oogpunt bezien zijn de H_2 + metaaloppervlaksystemen ook erg interessant. Ze vormen een ideaal model voor reactieve verstrooiing aan een metaaloppervlak opgevat als een statisch geheel. Door de metaalatomen vast te zetten op hun plaats blijven er zes vrijheidsgraden over die corresponderen met de vrijheidsgraden van het twee-atomige molecuul. Deze zes vrijheidsgraden zijn volledig

quantumdynamisch te beschrijven onder de aanname dat de reactie beschreven kan worden met gebruik van de Born-Oppenheimer-benadering. De Born-Oppenheimer-benadering gaat er van uit dat de bewegingen van de elektronen en de kernen ontkoppeld kunnen worden. Dit kan omdat de elektronen vele malen lichter zijn en de kernen dus relatief langzaam bewegen. Een bijkomstige benadering, voortvloeiend uit de Born-Oppenheimer-benadering, is dat de dynamica van moleculair waterstof, te beschrijven is in een enkel krachtveld corresponderend met de elektronische grondtoestand, dat door de kernen en alle elektronen gegenereerd wordt en dit brengt een voordeel met zich mee: het benodigde krachtveld voor de dynamica kan verkregen worden met conventionele dichtheidsfunctionaaltheorie (DFT).

DFT is een methode die gebaseerd is op een theorema van Hohenberg en Kohn: van een systeem van N wisselwerkende deeltjes, in een externe potentiaal, is de energie van de veel-deeltjes-grondtoestand, mits deze niet ontaard is, te schrijven als een functionaal van de deeltjesdichtheid. Als de echte exacte functionaal van de energie bekend zou zijn, zou DFT als een echte *ab initio*-methode gezien kunnen worden. Echter, de exacte functionaal is niet bekend en in de praktijk worden benaderingen gebruikt. Deze benaderde functionalen kunnen getoetst worden door dynamicaberekeningen uit te voeren met een DFT-potentiaaloppervlak als invoer en de daaruit verkregen resultaten te vergelijken met experimenten. Op deze manier leveren de berekeningen aan de reactie van moleculair waterstof op metaaloppervlakken een bijdrage aan de theoretische chemie. Vele experimenten zijn gedaan aan dit soort systemen en de dynamica kan volledig quantummechanisch aangepakt worden. Omdat de in de dynamica gebruikte benaderingen goed gemotiveerd kunnen worden, wordt de vergelijking van dynamica resultaten met experimentele resultaten in principe een betrouwbare test voor de kwaliteit van DFT.

De dynamicaberekeningen beschreven in dit proefschrift zijn gebaseerd op tijdsafhankelijke golfpakketmethodes. In deze methodes wordt een golfpakket gebruikt om een bundel van moleculen te beschrijven die naar een metaaloppervlak toe bewegen. Het golfpakket wordt in de tijd gepropageerd door middel van de tijdafhankelijke

Schrödingervergelijking. Als het golfpakket aankomt bij het oppervlak kan een deel van de moleculen de barrière tot reactie over gaan. Het restant van het golfpakket dat niet over de barrière gaat, gaat terug naar de gasfase. Dit wordt verstrooiing genoemd. Het verstrooiingsproces kan gepaard gaan met energie-uitwisseling tussen de zes vrijheidsgraden van het molecuul: rotationeel en / of vibrationeel in-elastische diffractieve verstrooiing.

Ondanks dat de dynamica van reactieve verstrooiing van moleculair waterstof aan metaaloppervlakken volledig quantummechanisch aangepakt kan worden, blijven de dynamicaberekeningen een uitdagende taak, zelfs voor de computers van vandaag. Verschillende tijdafhankelijke golfpakketmethoden zijn ontwikkeld om het rekenwerk doenbaar te maken. De verschillen tussen de gebruikte golfpakketmethoden uiten zich voornamelijk in de representatie die gebruikt wordt voor het golfpakket. De representatie van het golfpakket bepaalt namelijk hoe efficiënt de methode is in computertijd en geheugen-gebruik.

Verschillende representaties zijn mogelijk, waaronder de close-coupling-representatie. Hierbij wordt het golfpakket geëxpandeerd in een basisset en de bewegingsvergelijkingen voor de expansiecoëfficiënten opgesteld die volgen uit de tijdsafhankelijke Schrödingervergelijking. Het gebruik van een close-coupling-representatie leidt tot het gebruik van een potentiaalkoppelingsmatrix in de propagatie van de golffunctie. In de close-coupling-representatie is men echter vrij om een geschikte basisset te kiezen. Een mogelijke keuze is het gebruik van symmetrie-aangepaste basisfuncties om zo het rekenprobleem te reduceren en de potentiaalkoppelingsmatrix uit te blokken. De "symmetry adapted wave packet" (SAWP) methode is daar een voorbeeld van dat is gebruikt in het werk beschreven in dit proefschrift.

Een andere mogelijke representatie is gebaseerd op het duale karakter van de quantummechanica. In de quantummechanica kunnen operatoren, zoals delen van de Hamilton-operator, in twee verschillende representaties geformuleerd worden: de coördinaat-representatie of de impuls-representatie. In hoogstens een van deze

representaties is de operator eenvoudig toe te passen. Door nu het golfpakket heen en weer te transformeren tussen de twee mogelijke representaties, kunnen de acties van de verschillende operatoren van de Hamilton-operator op de golffunctie eenvoudig achterelkaar uitgerekend worden. Deze methode van aanpak wordt pseudo-spectraal (PS) genoemd en is eveneens gebruikt in het werk beschreven in dit proefschrift. De twee geconjugeerde representaties van het golfpakket in de pseudo-spectrale methoden worden ook wel de "finite basis representation" (FBR) en de "discrete variable representation" (DVR) genoemd. De FBR is daarbij equivalent aan de impuls-ruimte en de DVR aan de coördinaat-ruimte.

In het algemeen is de close-coupling-methode efficiënt in rekentijd- en geheugen-gebruik als slechts één van de vrijheidsgraden in een basisset gerepresenteerd wordt. Worden er meerdere vrijheidsgraden geëxpandeerd in een basisset, zoals in de SAWP-methode gebeurt die rotationele en diffractionele symmetrie-aangepaste basisfuncties gebruikt, dan is de close-coupling-methode alleen efficiënt als de potentiaalkoppelingsmatrix veel nullen bevat ("sparse" is). De sparseness van de potentiaalkoppelingsmatrix kan, onder andere, bereikt worden door de potentiaal, die het krachtveld waarin de waterstofatomen zich bewegen beschrijft, te expanderen in een beperkt aantal van de basisfuncties die gebruikt zijn in de close-coupling-representatie. Dit legt echter wel een beperking op aan het krachtenveld, die de pseudo-spectrale methoden niet kennen. De pseudo-spectrale methoden gebruiken het potentiaaloppervlak (PES) dat direct gedefiniëerd is op roosterpunten in de DVR. De specifieke vorm van de PES doet er dan niet toe en een efficiënte manier voor het laten werken van de potentiaaloperator op de golffunctie, een deel van uitwerken van $\hat{H}\Psi$, maakt gebruik van transformaties tussen de FBR en de DVR.

Het werk dat beschreven is in dit proefschrift bestaat niet alleen uit toepassingen van bestaande dynamicamethoden op verstrooiing en reactie van moleculair waterstof aan metaaloppervlakken. Een gedeelte van dit proefschrift behandelt de implementatie van symmetrie, zoals die ook is gebruikt in de SAWP-methode, in een pseudo-spectrale methode. Ter voorbereiding wordt in **hoofdstuk 2** de theorie van tijdsafhankelijke

golfpakketmethoden behandeld, tezamen met eerder gebruikte representaties van het golfpakket. Het verband tussen de close-coupling-representatie en de algemene pseudo-spectrale aanpak behoort ook daarbij. Daarnaast wordt er ook een korte introductie in de dichtheidsfunctionaaltheorie gegeven en in de verschillende interpolatie- en / of fit-methoden die gebruikt zijn om de verschillende potentiaaloppervlakken te representeren die gebruikt zijn in de andere hoofdstukken van dit proefschrift.

In **hoofdstuk 3** worden berekeningen aan reactie van H_2 op Cu(100) gepresenteerd, gebruikmakende van de SAWP-methode en PES 4. De berekende reactieplaats-specifieke reactiewaarschijnlijkheden laten zien dat, in het algemeen, voor lage j (j=0-5), de H_2-moleculen die het oppervlak naderen in de vibrationele grondtoestand (v=0) het liefst op de "bridge-site" reageren, terwijl de moleculen die het oppervlak naderen in de (v=1)-toestand het liefst op de "top-site" reageren, bij lage energieën. Ook laten diezelfde resultaten zien dat voor de moleculen die op de "top-site" reageren, een duidelijke afhankelijkheid van de initiële rotatietoestand aanwezig is in de reactiewaarschijnlijkheid: hoe hoger het initiële draaiimpulsmomentquantumgetal j van het molecuul, hoe hoger de reactiewaarschijnlijkheid. Deze effecten kunnen worden gerelateerd aan specifieke eigenschappen van PES 4 bij de barrière van de "top-site": de hoge kromming in het reactiepad en de late barrière van de "top-site" zorgen ervoor dat de vibrationeel aangeslagen moleculen een groot deel van de extra vibratie-energie kunnen gebruiken om de barrière voor reactie te overbruggen. De late barrière leidt tegelijkertijd tot rotationele versterking van de reactie; doordat de rotatieconstante, geassociëerd met het molecuul, lager wordt naarmate het molecuul de barrière dichter nadert kan er energie vloeien van de rotatie- naar de reactie-coördinaat. In hoofdstuk 3 wordt beargumenteerd dat dit rotationele versterkingseffect gebruikt kan worden in experimenten aan associatieve desorptie, om indirect bewijs te verkrijgen met betrekking tot de plaats op het oppervlak waar waterstof reageert.

Naast het rotationele versterkingseffect op de reactie bij de "top-site", laten berekeningen ook zien dat een eerder verkregen experimenteel verifiëerbare signatuur, gebaseerd op de rotationele "quadrupole alignment", niet in het algemeen geldt voor de lage

rotatieniveaus. De rotationele "quadrupole alignment" is een maat voor de voorkeur van reactie van "helicopters" ($|m_j|=j$) boven "cartwheels" ($m_j=0$), en eerder onderzoek toonde aan dat de "alignment" van reagerend ($v=1,j=4$) H_2 hoger is dan die van reagerend ($v=0,j=4$) H_2 voor lage translatie-energieën. Dit laatste geeft aan dat op de "top-site" sterker de voorkeur gegeven wordt aan de reactie van de "helicopters" voor de ($v=1,j=4$) H_2 moleculen. Dit kon verklaard worden door de rotationele hinderingseffecten die optreden en gerelateerd konden worden aan de specifieke eigenschappen van PES 4 bij de "top-site"-barrière: de hoge anisotropie in θ en de lage anisotropie in ϕ. De in hoofdstuk 3 gepresenteerde berekeningen aan initiëel ($j=2$) waterstof laten echter zien dat de rotationele "quadrupole alignment" voor reagerend ($v=1,j=2$) H_2 lager is dan die van reagerend ($v=0,j=2$)-H_2, terwijl de "top-site" de geprefereerde reactieplaats blijft voor ($v=1,j=2$) H_2. De berekeningen aan initiëel ($j=3$)-H_2 geven aan dat de "alignments" van reagerend ($v=0,j=3$) en ($v=1,j=3$) H_2 ongeveer gelijk zijn voor de lage translatie-energieën. Deze bevindingen zijn niet te verklaren met de rotationele hinderingsmechanismen, zoals ze voor ($j=4$) gebruikt werden en een verklaring is gevonden door twee verschillende rotationele versterkingseffecten in de beschouwing mee te nemen: elastische en in-elastische rotationele versterking.

Het elastische rotationele versterkingsmechanisme vindt zijn oorsprong in het verlagen van de rotatieconstante geassociëerd met het molecuul als het een late barrière nadert. Het in-elastische rotationele versterkingsmechanisme wordt geassociëerd met een rotationele overgang als het molecuul een barrière nadert die anisotropie in θ heeft. De overgang van een hogere j naar een lagere j op weg naar de barrière levert energie op die gebruikt kan worden om de barrière te overbruggen. In hoofdstuk 3 wordt beargumenteerd dat het elastische versterkingsmechanisme niet direct een verschil in reactiviteit tussen de "helicopters" en de "cartwheels" oplevert. Van het in-elastiche rotationele versterkingseffect wordt wel een sterke afhankelijkheid van de specifieke initiële rotationele toestand verwacht en dus een duidelijk verschil in reactiviteit van "helicopters" en "cartwheels" gevonden voor ($j=2$): de hoge anisotropie in θ en de lage anisotropie in ϕ van PES 4 bij de "top-site" leiden ertoe dat de ($j=2,m_j=0$)$\rightarrow$($j'=0,m_j'=0$) overgang efficiënt is en de reactiviteit van de ($j=2$) "cartwheels" hoger zal zijn dan van de

(j=2) "helicopters" (bij de overgang moet gelden Δj=even en Δm$_j$≈0). Op basis van dit argument kan begrepen worden dat de "alignment" van reagerend (v=1,j=2) H$_2$ lager is dan voor (v=0,j=2) H$_2$: de (v=0) moleculen reageren het liefst op de "bridge-site" waar een hogere anisotropie in ϕ en een lagere anisotropie in θ in PES 4 gevonden wordt dan op de "top-site", waar vooral de (v=1) moleculen met m$_j$=0 reageren.

Ondanks dat de eerder gevonden experimenteel verifiëerbare signatuur, gebaseerd op de rotationele "quadrupole alignment" van de reagerende waterstofmoleculen, niet algemeen blijkt te zijn, kan het meten van de "alignment" in associatieve desorptie-experimenten nog steeds bewijs leveren voor de plaatsafhankelijkheid van de reactie van H$_2$ in verschillende (v,j) toestanden en het rotationele in-elastische versterkingsmechanisme dat voornamelijk bij reactie aan de "top-site" plaatsvindt. De uitvoering van zulke associatieve desorptie-experimenten, waarin de rotationele "quadrupole alignement" wordt gemeten en die reeds eerder voor H$_2$ + Cu(111) gedaan zijn, zou de voorspellingen die gedaan worden in hoofdstuk 3 kunnen toetsen en er wordt daarom sterk gepleit voor het eveneens uitvoeren van dit soort metingen voor H$_2$ + Cu(100). Ze zouden wellicht indirect experimenteel bewijs kunnen leveren voor de "top-site"-reactiviteit van initiëel (v=1) H$_2$.

De berekeningen van hoofdstuk 3 zijn gedaan met gebruik van de SAWP golfpakketmethode. Zoals al vermeld was, levert het gebruik van SAWP-methode een beperking op aan de PES die gebruikt kan worden: de PES moet worden geëxpandeerd in een beperkt aantal symmetrie-aangepaste functies. Ook is al duidelijk gemaakt dat de pseudo-spectrale golfpakketmethoden die restrictie niet kennen en de potentiaal in de DVR op een rooster gebruiken. In **hoofdstuk 4** worden de symmetrie-technieken, zoals ze in de SAWP-methode gebruikt zijn, in een pseudo-spectrale methode toegepast voor verstrooiing van een twee-atomig molecuul, bij normale inval, aan een oppervlak dat vierkant is. Deze nieuwe methode wordt de symmetrie-aangepaste pseudo-spectrale methode (SAPS-methode) genoemd.

In de SAPS-methode wordt het golfpakket, net zoals in de SAWP-methode, geëxpandeerd in een symmetrie-aangepaste rotatie-diffractie basis set. De C_{4v} symmetrie-aangepaste rotatie- en diffractie-basissets worden verkregen door groepentheorie en projectie-operatoren toe te passen op de niet symmetrie-aangepaste rotatie- en diffractie-basissets. Echter, in plaats van gebruik te maken van een potentiaalkoppelingsmatrix, zoals dat in de SAWP-methode gedaan wordt, worden de expansiecoëfficiënten (de symmetrie-aangepaste FBR) naar symmetrie-aangepaste DVRs getransformeerd alvorens er met de potentiaal geopereerd word. Na het toepassen van de potentiaaloperator in de volledige DVR wordt het verkregen resultaat weer terug getransformeerd naar de symmetrie-aangepaste FBRs. Efficiënte transformatiealgoritmen voor de symmetrie-aangepaste diffractiebasissets zijn geïmplementeerd door gebruik te maken van "fast sine transforms" (FSTs) en "fast cosine transforms" (FCTs). Om de rotationele golffunctie te transformeren, is de Gauss-Legendre-transformatie, zoals die ontwikkeld is door D. Lemoine *et al.*, symmetrie-aangepast in ϕ door ook gebruik te maken van FSTs en FCTs.

Om de nieuwe SAPS-methode te testen zijn twee testberekeningen gedaan aan $(v=0, j=4, m_j=0)$ H_2 + Cu(100), gebruik makende van PES 4. Een berekening is gedaan met de nieuwe SAPS-methode, de andere met de SAWP-methode. PES 4 is speciaal geschikt voor de SAWP-methode en de vergelijking tussen de SAWP- en SAPS-resultaten laat zien dat de SAPS-methode competitief is met de SAWP-methode ondanks dat voor PES 4 de SAWP-methode zeer efficiënt geacht wordt en er in de SAPS-berekening een grotere diffractiebasisset wordt gebruikt. De reden hiervoor is dat in de SAPS-methode de PES direct in de DVR op een rooster gebruikt wordt. Een betere reductie van de "spectral range" van de potentiaal kan behaald worden, welke zorgt voor een efficiëntere propagatie als de aangepaste Chebyshev-propagator gebruikt wordt. In hoofdstuk 4 wordt geconcludeerd dat als er in de SAPS-methode eenzelfde ruitvormige diffractiebasisset gebruikt zou worden als in de SAWP-methode gebruikt is, de SAPS-methode nog efficiënter zou worden in gebruik van geheugen en rekentijd.

Om de SAPS-methode te testen op een algemene PES zijn voor hoofdstuk 4 ook nog twee berekeningen gedaan aan (v=0,j=0) H_2 + Cu(100) met gebruik van PES 5. PES 5 is een potentiaaloppervlak dat gebaseerd is op de corrugatie-reductie-interpolatiemethode van H.F. Busnengo *et al.* De vergelijking tussen de SAPS-resultaten en de algemene (niet-symmetrie-aangepaste) PS-resultaten, laat zien dat de SAPS-methode, in het algemeen, minstens 3 keer zo efficiënt is in gebruik van geheugen en rekentijd dan de PS-methode. Daarnaast werden er met de SAPS-methode nauwkeurigere resultaten behaald dan met de PS-methode, omdat een nauwkeurigere propagator (de aangepaste Chebyshev-propagator) werd gebruikt. In onze implementatie maakte de algemene PS-methode gebruik van de split-operator-propagator, die een 3e orde propagator is en niet, zoals de aangepaste Chebyshev-propagator, een fout in de orde van grootte van de machineprecisie kan leveren.

Ondanks dat de SAPS-methode voor de reactieve verstrooiing van twee-atomige moleculen bij normale inval op vierkante oppervlakken efficiënter is dan de standaard PS-methode, kunnen berekeningen aan niet vierkante oppervlakken of bij niet normale inval op dit moment alleen met de PS-methode gedaan worden. In **hoofdstuk 5**, dat de reactieve verstrooiing van initiëel (v=0,j=0) H_2 en D_2 op Cu(111) behandelt, is gebruik gemaakt van de standaard PS-methode om twee verschillende aangepaste LEPS-potentialen, die voor het H_2 + Cu(111) systeem beschikbaar zijn, te testen. Ondanks dat Dai *et al.* al eerder zes-dimensionale berekeningen op hun aangepaste LEPS-PES (DZ-PES) hebben gedaan en er ruimschoots experimenten gedaan zijn aan dit systeem, waren de resultaten, gebaseerd op de DZ-PES, nog niet vergeleken met de experimentele data, voor zowel de reactie als de vibrationeel in-elastische verstrooiing. Voor de andere LEPS-PES (ER-PES), die door Persson *et al.* geconstrueerd is, waren nog geen zes-dimensionale reactieve verstrooiingsberekeningen gedaan. De resultaten voor initiëel (v=0,j=0) H_2 verstrooiend aan Cu(111) laten, voor beide LEPS-potentiaaloppervlakken, zien dat er te weinig vibrationeel in-elastische verstrooiing plaatsvindt en dat daarom de reactiewaarschijnlijkheid te hoog uitvalt bij hogere bewegingsenergieën. Verder laten de berekeningen zien dat de reactiewaarschijnlijkheid berekend met de ER-PES de experimentele fit bij de drempel van reactie beter benadert. In hoofdstuk 5 wordt

beargumenteerd dat dit waarschijnlijk komt omdat de ER-PES op DFT-data gebaseerd is die beter geconvergeerd zijn.

Omdat de experimentele fit gebaseerd is op metingen bij botsingsenergieën niet hoger dan 0.5 eV, is er een extra berekening aan (v=0,j=0) D_2 + Cu(111) gedaan, met gebruik van de ER-PES. Voor D_2 + Cu(111) was, in moleculaire bundelexperimenten, een botsingsenergie behaald van 0.83 eV. De vergelijking tussen de experimentele en de berekende resultaten voor D_2 + Cu(111) laten ook duidelijk zien dat er te veel reactie gevonden wordt in de berekening. De suggestie voor verbetering die gegeven wordt in hoofdstuk 5, is het oppervlakteplaats-afhankelijk maken van de fitparameters (Sato-parameters) in de aangepaste LEPS-fit-formule. Dit laatste zou ervoor kunnen zorgen dat de kromming van het reactiepad en de locatie van de barrière mogelijk beter beschreven wordt voor de "top-site", waar vibratie-excitatie concurreert met reactie. Dit zou dan moeten leiden tot meer vibrationeel in-elastische verstrooiing en een verlaging van de reactiewaarschijnlijkheid bij hogere botsingsenergieën. Of deze suggestie, om de Sato-parameters oppervlakteplaats-afhankelijk te maken, voldoende is moet blijken uit verder onderzoek. Misschien moet er zelfs afgestapt worden van het gebruik van aangepaste LEPS-potentialen.

In **hoofdstuk 6** is de standaard PS-methode gebruikt om de reactieve verstrooiing van (v=0,j=0) HD aan Pt(111) te bestuderen onder de invalsrichtingen $<10\overline{1}>$ en $<11\overline{2}>$. In deze berekeningen is ook gebruik gemaakt van een PES voor H_2 + Pt(111) die gebaseerd is op de corrugatie-reductie-interpolatiemethode van H.F. Busnengo *et al.* Door een massamiddelpuntstransformatie uit te voeren, is de PES voor H_2 + Pt(111), binnen de Born-Oppenheimer benadering, ook voor HD + Pt(111) te gebruiken. Eerdere berekeningen aan H_2 + Pt(111), die gebruik maken van dezelfde PES en uitgevoerd zijn door Pijper *et al.*, hebben geholpen bij het oplossen van een experimentele paradox. Experimenten met moleculaire bundels aan reactie, gedaan door Luntz *et al.,* hadden aangetoond dat het H_2 + Pt(111)-systeem niet aan "normal energy scaling" voldoet. Dit laatste betekent dat de translationele energie parallel aan het oppervlak van belang is en een effect heeft op de reactiewaarschijnlijkheid en dat het oppervlak niet vlak kan zijn.

Echter, de experimentele resultaten van Cowin *et al.*, die experimenten met moleculaire bundels gedaan hadden aan verstrooiing van HD aan Pt(111) en alleen naar de verstrooiing in het vlak van inval keken in de $<10\bar{1}>$ invalsrichting, suggereerden dat het oppervlak vlak moest zijn omdat er weinig diffractie in het vlak van inval plaatvond. De eerdere berekeningen aan H_2 + Pt(111) van Pijper *et al.* gaven hier een mogelijke verklaring voor: in het vlak van inval is eerste orde diffractie niet mogelijk voor de $<10\bar{1}>$ richting en is de speculaire reflectie ongeveer 20 keer groter dan diffractie in het vlak van inval. Verder bleek ook uit de berekeningen dat de diffractie uit het vlak van inval aanzienlijk was voor inval in de $<10\bar{1}>$ richting, onder de omstandigheden van de experimenten van Cowin *et al.*, en dat experimenten die enkel en alleen naar diffractie in het vlak van inval kijken geen uitspraak kunnen doen over de corrugatie van een oppervlak. De berekeningen aan H_2 verstrooiend aan Pt(111) gaven echter nog te veel diffractie in het vlak van inval vergeleken met de experimenten van Cowin *et al.* Zij vonden een verhouding van (speculaire reflectie) / (diffractie in het vlak van inval) van ongeveer 100 voor HD + Pt(111) ten opzichte van 20 in de berekeningen. De vraag of dit te maken had met het simuleren van H_2 in plaats van HD verstrooiend aan Pt(111) is het onderwerp van hoofdstuk 6. Voor HD liggen de rotatieniveaus minder ver uit elkaar in energie, de PES voor HD + Pt(111) heeft meer anisotropie en zowel even als oneven j-niveaus kunnen bezet worden in HD. De verwachte toename in rotatieneel in-elastische verstrooiing zou in competitie met de diffractie in het vlak van inval, de laatste kunnen verlagen en zo de verhouding (speculaire reflectie) / (diffractie in het vlak van inval) kunnen doen toenemen.

De berekeningen in hoofdstuk 6 laten echter zien dat, ondanks dat de verwachte toename in de rotatieneel in-elastische verstrooiing optrad, de verhouding (speculaire reflectie) / (diffractie in het vlak van inval) niet hoger maar zelfs lager is voor (v=0,j=0) HD + Pt(111) dan voor H_2 + Pt(111). Als verklaring hiervoor wordt gegeven dat de energieverschillen tussen de diffractietoestanden van HD ook kleiner moeten zijn dan bij H_2 en dat diffractieve verstrooiing daarom ook hoger voor HD dan voor H_2 is. De berekende resultaten voor in-elastische rotationele verstrooiing in het vlak van inval voor HD laten echter weer zien dat er te weinig moleculen in de hogere j' toestanden (j' ≥ 2)

terugverstrooien. De experimenten van Cowin *et al.* gaven wel aanzienlijke terugverstrooiing in de j'=2 rotationele toestand. Beargumenteerd wordt dat dit verschil twee oorzaken kan hebben: i) het verwaarlozen van de fononen in het dynamische model, en ii) het afwezig zijn van de van der Waals fysisorptieput in de PES, welke een diepte van ongeveer 55 meV behoort te hebben. De toevoeging van een fysisorptieput in de PES zou de barrière iets dichter naar het oppervlak kunnen verschuiven en daardoor voornamelijk de anisotropie van de PES in θ bij de barrière verhogen. Op basis van deze toename van anisotropie zou men verwachten dat rotationeel in-elastische verstrooiing toeneemt vooral voor verstrooiing naar de hogere j' rotatieniveaus. Er wordt daarom gesuggereerd in hoofdstuk 6 dat het construeren van een PES, die gebaseerd is op DFT data op basis van DFT functionalen die de van de Waals-interacties beschrijven, en het gebruik van die PES in dynamicaberekeningen, logische volgende stappen zijn in het onderzoek naar de rotationeel in-elastische verstrooiing van HD aan Pt(111).

List of publications

1. *On the competition between photoionisation and photodissociation of molecular deuterium after (3+1) resonance-enhanced-multiphoton excitation via the $B^1\sum_u^+$ state*, C.R. Scheper, M.F. Somers, C.A. de Lange, Journal of electron spectroscopy and related phenomena **108** (2000), 123-133.

2. *Six-dimensional quantum dynamics of scattering of (v=0,j=0) H_2 from Pt(111): comparison to experiment and to classical dynamics results*, E. Pijper, M.F. Somers, G.J. Kroes, R.A. Olsen, E.J. Baerends, H.F. Busnengo, A. Salin and D. Lemoine, Chem. Phys. Lett. **347** (2001), 277-284.

3. *Constructing accurate potential energy surfaces for a diatomic molecule interacting with a solid surface: H_2 + Pt(111) and H_2 + Cu(100)*, R.A. Olsen, H.F. Busnengo, A. Salin, M.F. Somers, G.J. Kroes, E.J. Baerends, J. Chem. Phys. **116** (2002), 3841-3855.

4. *Six-dimensional quantum and classical dynamics study of H_2 (v=0,j=0) scattering from Pd(111)*, H.F. Busnengo, E. Pijper, M.F. Somers, G.J. Kroes, A. Salin, R.A. Olsen, D. Lemoine and W. Dong, Chem. Phys. Lett. **356** (2002), 515-522.

5. *Six-dimensional quantum dynamics of scattering of (v=0,j=0) H_2 and D_2 from Cu(111): test of two LEPS potential energy surfaces*, M.F. Somers, S.M. Kingma, E. Pijper, G.J. Kroes and D. Lemoine, Chem. Phys. Lett. **360** (2002), 390-399. Chapter 5 of this thesis.

6. *Diffractive and reactive scattering of (v=0,j=0) HD from Pt(111): six-dimensional quantum dynamics compared with experiment*, S.M. Kingma, M.F. Somers, E. Pijper, G.J. Kroes, R.A. Olsen, and E.J. Baerends, J. Chem. Phys. **118** (2003), 4190-4197. Chapter 6 of this thesis.

7. *Signatures of site-specific reaction of H_2 on Cu(100)*, M.F. Somers, D.A. McCormack, G.J. Kroes, R.A. Olsen, E.J. Baerends and R.C. Mowrey, J. Chem. Phys. **117** (2002), 6673-6687. Chapter 3 of this thesis.

8. *Performance and application of a symmetry adapted pseudo-spectral method for scattering of a diatomic molecule from a square surface: H_2+Cu(100)*, M.F. Somers, D. Lemoine and G.J. Kroes, Chem. Phys. submitted. Chapter 4 of this thesis.

Curriculum Vitae

Mark Frans Somers is geboren op 18 augustus 1975 te Heerlen. Nadat hij zijn HAVO-diploma heeft behaald op de scholengemeenschap Godelinde te Naarden in 1993, heeft hij zijn VWO-diploma twee jaar later op diezelfde school behaald. In datzelfde jaar, 1995, startte hij met zijn studie Scheikunde aan de Universiteit van Amsterdam. Na zijn bul in de fysische chemie behaald te hebben in 1999, mede op basis van een onderzoeksstage in de groep van Prof. dr. C.A. de Lange, werd hij aangenomen als promovendus aan het Leids Instituut voor Chemisch Onderzoek (LIC) van de Universiteit Leiden. Onder begeleiding van Prof. dr. G.J. Kroes heeft hij zes-dimensionale quantumdynamische berekeningen gedaan aan verstrooiing van waterstof aan metaaloppervlakken zoals Cu(100), Cu(111) en Pt(111). Daarnaast is, in diezelfde periode, onder begeleiding van Prof. dr. G.J. Kroes en dr. D. Lemoine, een programma ontwikkeld, gebaseerd op het gebruik van symmetrie, om soortgelijke zes-dimensionale quantumdynamische verstrooiingsberekeningen uit te voeren, met een nieuwe, efficiëntere methode.

Nawoord

Zo, de laatste woorden van dit proefschrift. De laatste maanden heb ik uren achter de computer moeten doorbrengen om ze op papier te krijgen, maar hier staan ze dan en een last vloeit van mijn schouders. Een taak vervul ik nog graag, namelijk het noemen van de mensen waarmee ik heb samengewerkt en die mij het leven de afgelopen jaren, zowel hier als in het buitenland, aangenaam hebben gemaakt.

Ik wilde beginnen met de kamergenoten die ik in die periode heb gehad: Ernst Pijper, Rob van Harrevelt, Ayman al-Halabi, Girts Barinovs, Jonathan Vincent, Sikke Kingma, Rogier van Willigen en Joris Kuipers. Zij allen hebben te maken gehad met mijn gedrag dat naar boven komt zodra de muziek op de koptelefoon aan gaat. De mensen die op de andere kamer zaten: Harry Sommerdijk, Cedric Crespos, Devon Gardner, Stefan Andersson, Rosendo Valero en Loradana Valenzano. Regelmatig ben ik langs gewandeld om vragen te stellen of te melden dat het echt tijd voor een koffie-pauze was. Ik heb verder op prettige wijze samengewerkt met Didier Lemoine, Drew McCormack, Roar Olsen en Marc van Hemert. Als laatste de mensen die hier een tijdje doorgebracht hebben in Leiden: Antoine Salin, Fabio Busnengo, Sven Nave en Cristina Diaz. Ook met hen heb ik op prettige wijze samengewerkt.

Ik kijk met plezier terug naar de tijd die ik op het Gorlaeus en in Lille heb doorgebracht en ik had het voor geen goud willen missen.